SURFACE PRESSURE MEASUREMENTS ON A ROTATING CONTROLLED DIFFUSION BLADE

By

Andrew Falck Cawood

A THESIS

Submitted to
Michigan State University
in partial fulfillment of the requirements
for the degree of

MASTER OF SCIENCE

Mechanical Engineering

2012

ABSTRACT

SURFACE PRESSURE MEASURMENTS ON A ROTATING CONTROLLED DIFFUSION BLADE

By

Andrew Falck Cawood

A method for quantifying fluctuating pressure magnitudes on the surface of a Controlled Diffusion (CD) blade was utilized to identify characteristics of the flow structure of the boundary layer at various streamwise and spanwise locations. This research effort explored the fundamental aspects of an axial fan flow field - a supplement to and a continuation of the work performed by Douglas Neal (2010). The work is driven by the motivation to identify flow structures within the boundary layer of the CD blade and characterize similarities between the results for rotating and stationary blades. These results are expected to be valuable for those working in the areas of aeroacoustics and noise prediction. Streamwise and spanwise surface pressures were measured along the surface of a stationary and a rotating CD blade. Additional trailing edge velocity wake surveys identify boundary layer features of the rotating and stationary blades. Surface pressure statistics, spectral characteristics, and correlations distinguish elements of the boundary layer from the stationary and rotating CD blades. Further results from correlations and spectral analysis on the airfoil trailing edge region identify spatial and temporal decay rates as well as parameters useful for trailing edge aeroacoustic noise prediction. An off-design operating point was evaluated to expand the context of this experiment; significant differences were observed. The fluctuating wall pressure observations are consistent with those made of a flat plate boundary layer (Willmarth and Woolridge 1962) and of the CD geometry by Moreau and Roger (2005).

Many men go fishing all their lives not knowing it is not fish they are after.
— Henry David Thoreau —

To my father, the man who taught me to fish

ACKNOWLEDGMENTS

On account of being at the MSU for so many years, as a student and as a local resident, I have encountered so many wonderful friends, colleagues, and strangers.

I would first like to extend thanks to Dr. John Foss and my committee members. Dr. Foss had the audacity to pick me up as an undergraduate and hired me in his laboratory. Most impressive, two years later he convinced me to stay at MSU for my Masters and managed to coax the following document out of me ("on-schedule"). Dr. Foss has been a truly outstanding mentor though the years - I have had the pleasure of working closely with him and experiencing the finest of his anecdotal advice.

I have also had the pleasure of working with so many great friends and colleagues. The invaluable advice and guidance from Prof. Scott Morris of Notre Dame and Prof. Stéphane Moreau of The Université de Sherbrooke made most of this work possible. I was fortunate enough to follow the work of Dr. Douglas Neal; I served as his assistant through the latter part of his Ph.D. and learned more than I ever imagined about the nuances of experimental fluid mechanics, coffee, and kayaking. Doug laid the groundwork for the present work and provided me many hours of feedback and guidance on a personal and professional level. I had the opportunity to work with many other great people: To Al, Kyle, Rohit, and Jason, thank you for the unending support. Your technical and practical skills made this work possible. Your friendships made it gratifying. I owe a big thanks to Daniel Höwer, without whom I would still be looking for answers. Daniel was critical for the computational development of the boundary layer results.

A special thanks goes to the Craigs of the ME department - The two people in the department who always have the right answers. I always knew who to go to if I needed advice, guidance, or say, last-minute tech support for a thesis defense. Gunn: Modern usage of the Oxford comma and ad hoc racquetball games - I'm still confidant I know the rules of neither - Thanks! Somerton: You couldn't be more correct - It's the little things that make lasting impressions! To my machine shop friends, Roy and Ken for providing a haven from the insanity of school (as well as arguably the worlds best chili recipe)! To the friends I've met through baja - these are probably the only people that can tolerate me driving them across Montana blaring calypso music that "only old people like".

To those who have given me a great deal of support through my undergraduate and graduate years. The secretarial staff, without whom I would cease to function: To Aida and Mary who somehow managed to wade through the mountains of paperwork I've caused and to Jill and Suzanne who have always been willing to lend a helpful ear.

To my friends, you've been more important to me than you'll ever know. From karaoke nights, long bike rides, and tolerating me talking through any movie, you've kept me (somewhat) sane through this process. For those who I have neglected and for total strangers, know that your kindness was not forgotten. A special thanks goes to my team of editors who laughed with me at my egregious and often obvious mispellings.

And finally, I want to send the most sincerest of thanks to my family. You have literally been there every step of the way. Thank you for your unending support!

On a personal level: For those that will continue reading this document, note that this is merely the quantitative aspect my degree program. This has been a truly formative journey - a special thanks is needed for those who kept me motivated and on task but knew when I needed a break - I am in debt to all of you beyond words. I wish you all the best in your future adventures. Remember: work hard, be kind, and amazing things will happen!

TABLE OF CONTENTS

LIST OF TABLES

LIST OF FIGURES

KEY TO SYMBOLS AND ABBREVIATIONS

ABBREVIATIONS

AFRD........................Axial Fan Research and Development

CD............................Controlled Diffusion

RCDB........................Rotating Controlled Diffusion Blade

ROMAN SYMBOLS

A(f), B(f)....................Fourier transform of random sinusoidal processes *a(t), b(t)*

A(x), B(x)...................Random variable

C_p..............................Static pressure coefficient

C_l...............................Lift coefficient

Kurt...........................Kurtosis - 4th moment (1.16)

L_{11},L_{22}.......................Integral length scale at $t=0$ of R_{11} and R_{22}

P(x)............................Probability density function (1.12)

R_{11},R_{22}.......................Streamwise and spanwise autocorrelation

R_{aa}, R_{bb}.....................Cross-correlation of random processes *a(t), b(t)* where *a(t)=b(t)*

R_{ab}............................Cross-correlation of random processes *a(t), b(t)* (1.20)

R_{pp}............................Cross-correlation of pressure (1.1)

Re_c............................Chord based Reynolds Number ($Re_c = u_\infty c/\upsilon$)

Skew..........................Skewness - 3rd moment (1.15)

T_{ij}..............................Lighthill's tensor (1.6)

U................................RCDB angular velocity (Figure 2.1)

U_c..............................Convection velocity (1.2, 3.2)

V................................RCDB inlet velocity in the stationary reference frame (Figure 2.1)

$\vec{V}_{a/b}$ ....Velocity of air with respect to the blade

$\vec{V}_{a/g}$ ....Velocity of air with respect to the ground

$\vec{V}_{b/g}$ ....Velocity of the blade with respect to the ground

Var ....Variance - 2nd moment (1.14)

W ....RCDB inlet velocity in the rotating reference frame (Figure 2.1)

$a(t)$, $b(t)$ ....Random sinusoidal process

c ....Chord length

c_o ....Speed of sound in air

d ....Microphone diameter

d^+ ....Microphone diameter in wall units

f ....Frequency

f^+ ....Frequency in wall units

$\bar{k}$ ....Characteristic wavenumber of turbulent motions

$\dot{m}$ ....Mass flow rate

$p(x_1,x_2)$ ....Pressure along airfoil surface

p_∞ ....Atmospheric pressure

r,θ,z ....Radial coordinates

t ....Time

u_i,u_j ....Fluctuating velocity vector

u_∞ ....Freestream velocity: Stationary - CD

u_τ ....Friction velocity

w_∞ ....Freestream velocity: Rotating - RCDB

x,y,z ....Cartesian coordinates

x_1, x_2 .... Blade surface streamwise and spanwise directions

$\Delta x_1, \Delta x_2$ .... Blade surface streamwise and spanwise tap separations (see h_1, h_2)

GREEK SYMBOLS

$\Lambda_{11},\Lambda_{22}$ .... Integral length scale at $t=0$ of R_{11} and R_{22}

Φ_{aa},Φ_{bb} .... Power spectral density for random processes $a(t)$, $b(t)$ (1.17)

Φ_{ab} .... Cross spectral density

Φ_{pp} .... Wall pressure power spectral density (1.8)

$\Phi_{p,rad}$ .... Radiated acoustic power spectral density (1.9)

Ω .... Rotational speed

α .... Geometric angle of attack

α_c .... Camber angle

α_i .... Aerodynamic angle of attack

γ_{ab} .... Coherence function (1.18)

δ .... Boundary layer thickness

δ^* .... Displacement thickness

δ_{ij} .... Kronecker delta

η .... Directionless correlation distance

η_1,η_2 .... Streamwise and spanwise correlation lengths

λ .... Wavelength

λ_w .... Eddy wavelength (1.4) - Charactistic wavelength of turbulent motions

μ .... Mean - 1st moment (1.13)

υ .... Kinematic viscosity of air

ρ .... Density of air

σ................................Standard deviation (1.14)

σ_{ij} ....Reynolds stress tensor

t ....Correlation time delay

Δt ....Time delay between correlation peaks

τ_w................................Wall shear stress

f ....Phase factor (1.19)

ω................................Angular frequency

ϖ ....Characteristic frequency of turbulent motions

1.0 Introduction

1.1 Motivation

This research effort explored the fundamental aspects of an axial fan flow field - a supplement to and continuation of the work performed by Douglas Neal (2010). A planar, Controlled Diffusion (CD) airfoil was cast into a rotating axial fan blade and attached to the rotating hub of the Axial Fan Research and Development (AFRD) facility at Michigan State University. The acronym: RCDB (Neal 2010) - Rotating CD Blade - is used to describe the experimental configuration. The RCDB results are compared with a stationary CD blade by way of mean and fluctuating surface pressures. Fluctuating pressure measurements can be used to comparatively infer boundary layer properties by implementing statistical, spectral, and correlative analysis. The purpose is to identify properties of the turbulent boundary layer of the fan blade surface and compare the rotating fan to the stationary airfoil at matched flow conditions. Additionally, the fan is operated at an off-design flow condition to better quantify boundary layer behavior. Ultimately, this project is part of a larger study whose goal is the reduction of noise from axial fans and similar devices. This work provides experimental verification of the rotating analog and baseline measurements to the aeroacoustic prediction community.

Aeroacoustics has received expanded attention in the last few decades and has become an important discipline within aeronautics. Modern commercial demands require larger and faster vehicles, bigger structures and higher efficiencies. The environmental and societal impact of these structures and vehicles has been under more serious investigation as population growth increases; the development of on-shore wind turbines has been limited due to noise issues with those residing in populated areas (Dassan et al. 1997). Noise abatement and the design of quieter air vehicles and structures are essential to the continued growth of these industries. A characteristic self-noise-generation condition that occurs in these application areas is the low Mach number turbulent boundary layer that is formed over and separates from a surface. Lifting and control surfaces are of particular importance in this regard.

1.2 Pressure Fluctuations in Turbulent Boundary Layers

This document is focused on characterizing the boundary layer along the surface of a controlled diffusion airfoil. A typical boundary layer on the airfoil suction surface will begin in the laminar state and transition to turbulence some distance downstream (see Figure 1.1). The controlled diffusion airfoil is known to have an early transition to turbulence and a well established boundary layer near the trailing edge.

It is instructive to discuss some of the governing aspects of boundary layer pressure fluctuations and to introduce more modern computational methods. Previous experimental surface pressure boundary layer studies focused primarily on simplified geometries; a carefully developed flat plate boundary layer ensures a well developed and stable flow field. The pressure fluctuations of a flat boundary layer are well discussed by Willmarth and Woolridge (1962), Bull (1967), and Gravante et al. (1998). An excellent summary of previous research is provided by Bull (1996).

Willmarth defines several data reduction methods and parameters that are useful for characterizing the boundary layer; he identifies the wall pressure fluctuations as a stationary random variable that is a function of time and position. Since the pressure fluctuations are statistically stationary, Willmarth proposes expressing the fluctuations along the surface in terms of their root-mean-square (RMS) pressure; he identifies an increase in RMS pressure as an

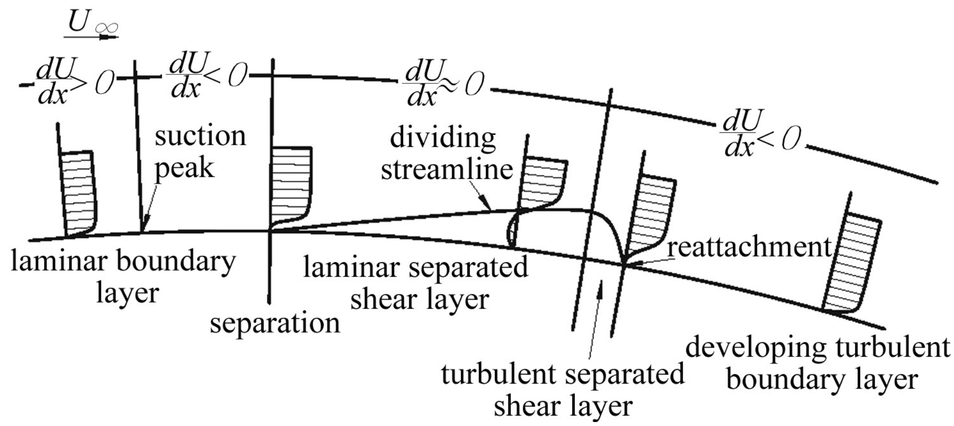

Figure 1.1 Airfoil boundary layer (Gerakopulos and Yarusevych 2012)

indicator for a boundary layer transition[1]. Further interpretations of the boundary layer are accomplished through the implementation of space-time cross-correlations.

The cross-correlation of a pressure signal is defined as

$$R_{pp}(x_1, x_2, t) = \frac{\overline{p(x_1, x_2, t) \cdot p(x_1 + \Delta x_1, x_2 + \Delta x_2, t + \tau)}}{\sqrt{\overline{p^2(x_1, x_2, t)} \cdot \overline{p^2(x_1 + \Delta x_1, x_2 + \Delta x_2, t + \tau)}}} \quad \mathbf{1.1}$$

where x_1 and x_2 are the spanwise and streamwise pressure tap coordinates, Δx_1 and Δx_2 are the streamwise and spanwise pressure tap separations, and τ is the correlation time delay between pressure measurements.

Willmarth used the space-time cross-correlation to “track” motions of selected frequency bands. The thought behind filtering the fluctuating pressure signal into frequency bands is to specify frequency regions and identify their role and impact on the boundary layer. Figure 1.2 shows the streamwise space-time correlation of a high and low frequency band. The ordinate shows the correlation coefficient and the abscissa shows the time delay

1. It is noteworthy to mention that the RMS is equal to the standard deviation when the mean of the signal is zero (the square root of the 2nd statistical moment), as it is for microphone measurements.

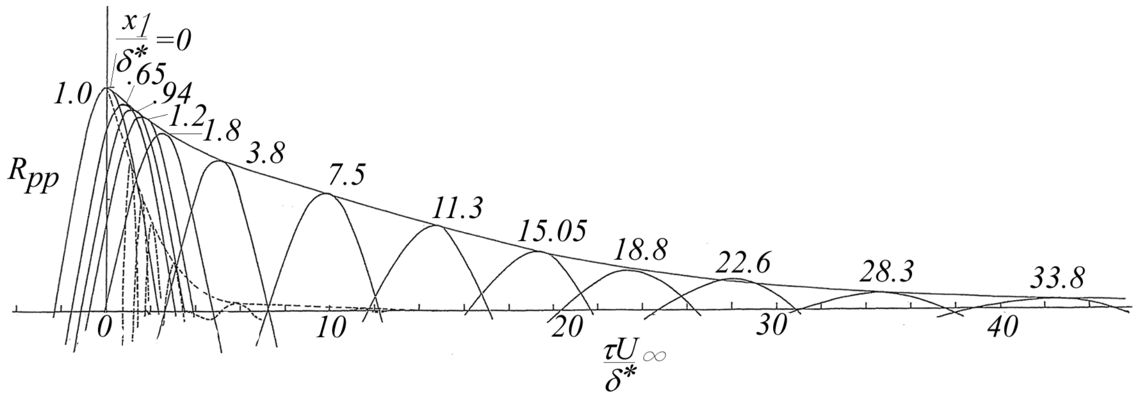

Figure 1.2 Streamwise space-time correlation (Willmarth and Woolridge 1962)
Solid line: 300Hz < *f* < 700Hz
Dashed line: 3000Hz < *f* < 5000Hz

normalized by the free-stream velocity (u_∞) and boundary layer displacement thickness (δ^*). Each parabola shape in the figure represents the peak segment of the cross-correlation for a given a downstream pressure tap and an upstream reference tap. Note that the numbers along the peaks identify the location of the downstream pressure tap (x_1/δ^*, reference tap at: $x_1=0$).

Willmarth proposed using the gross time delay between correlation peaks ($\Delta\tau$) to define the convection velocity U_c of the boundary layer

$$U_c = \frac{\Delta x}{\Delta \tau} \tag{1.2}$$

Convection velocity is an implicit function of frequency when the fluctuating pressure signal is filtered following Willmarth's method. Willmarth suggests defining an average frequency and an average wavenumber for a given frequency band

$$\bar{k} = \frac{\bar{\omega}}{U_c} = \frac{\omega_{low} + \omega_{high}}{2U_c} \tag{1.3}$$

The idea of a characteristic wavelength follows:

$$\lambda_w = \frac{2\pi}{\bar{k}} = \frac{2U_c}{\omega_{low} + \omega_{high}} \quad \textbf{1.4}$$

The eddy wavelength is a descriptor of the length scale of the convecting pressure fluctation.

Gravante et al. (1998) identify several key parameters for accurate measurements at low frequencies and in noisy facilities. Additionally, they explored the effects of sensor averaging on attenuation at high frequencies. It is ideal to have a very small sensor diameter for measuring the fluctuating pressures; if the sensor diameter is too large, the smallest scales of the flow cannot be resolved since frequency scales are the inverse of the wavelength. It is suggested that to avoid spectral attenuation for resolving frequencies up to $f^+ = \frac{f\upsilon}{u_\tau^2} = 1$ a pinhole sensor with dimensions $d^+ = \frac{du_\tau}{\upsilon} < 18$ should be used. In the present experiment, a pinhole *d=0.5mm* corresponds to $6.5 < d^+ = \frac{du_\tau}{\upsilon} < 12.5$ in the trailing edge region. The sensor diameter is well within the acceptable range for a maximum frequency of ~35kHz (well beyond the frequency range of interest).

More recent experiments have the advantage of more computational power and improved transducers with respect to the pioneering work of the 1960s. Boutilier and Yarusevych (2012) considered the surface pressure fluctuations as did Willmarth but used a more complex geometry: a NACA0018 airfoil. Boutilier combines simultaneous hot-wire and surface pressure measurements, spectral analysis, space-time correlations (pressure-pressure and pressure-velocity), and lower-order statistical moments to characterize the airfoil boundary layer. Moreau and Roger (2005), using the same stationary controlled diffusion airfoil considered in this report, quantified the boundary layer in terms of pressure spectra, coherence, and phase with applications to noise prediction.

1.3 Aeroacoustics

Airfoil self-noise results from an unsteady-flow interaction with the airfoil, the interaction is often with its own boundary layer and/or wake. Five mechanisms for producing airfoil self-noise are shown in Figure 1.3 (Brooks et al. 1989):

- *Trailing edge bluntness – vortex shedding noise:* Vortex shedding noise resulting from a small separated region aft of the trailing edge
- *Tip vortex formation noise:* Noise resulting from highly turbulent vortices that are shed from the lateral edge of an airfoil blade.
- *Separation/stall noise:* At higher angles of attack, the boundary layer can separate near the trailing edge, producing noise from the shed turbulent vorticity. At even higher angles of attack, full stall can occur, or large-scale separation. This typically produces low-frequency noise similar to what a bluff body produces in a similar flow
- *Turbulent boundary layer – trailing edge noise:* At high chord Reynolds numbers, a turbulent boundary layer forms over most of the airfoil and produces noise as it passes over the trailing edge of the airfoil.
- *Laminar boundary layer – vortex shedding noise:* At low chord Reynolds numbers, laminar boundary layers form across most of the airfoil and typically produce a Von-Karman vortex street aft of the trailing edge. This contributes mostly to tonal noise.

The primary flow geometry and associated noise mechanism of interest for the present study is the turbulent boundary layer – trailing edge noise. It has been demonstrated that if sufficient pressure information is known about the convecting turbulent

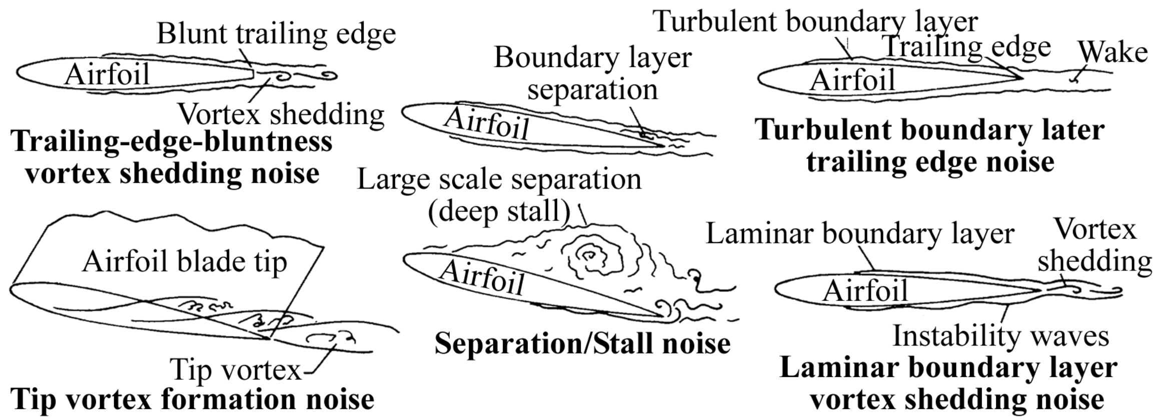

Figure 1.3 Airfoil self-noise (Brooks et al. 1989)

boundary layer, the trailing edge noise pattern can be predicted from acoustical models (Roger and Moreau 2004).

As the principal airfoil noise contribution in homogeneous stationary flows, trailing edge noise is a matter of particular interest when discussing noise production from fans, airfoils, and turbines. A demand exists within industrial applications for reliable, but realistic, prediction tools of noise intensity with respect to frequency and radiation angles. Analytical models, in the context of incompressible flow computations and experiments, allow for this noise prediction with varying degrees of accuracy according to the acoustic analogy (Singer et al. 2000).

The most practical aeroacoustic analysis relies on Lighthill's 'acoustic analogy' – a novel method pioneered by M. J. Lighthill in 1951. The Lighthill analogy makes a connection between flow-physics and acoustics by casting the Navier-Stokes equations into an inhomogeneous wave equation. The Lighthill analogy considers a free flow where the non-stationary fluctuations are represented by quadrupole sources (Oberai et al. 2002). the wave equation in an undisturbed medium at rest or, Lighthill's equation (Howe 1978) is

$$\frac{\partial^2 \rho'}{\partial t^2} - c_0^2\left(\frac{\partial^2 \rho'}{\partial x_i \partial x_i}\right) = \frac{\partial^2 T_{ij}}{\partial x_i \partial x_j} \qquad \textbf{1.5}$$

where T_{ij}, Lighthill's Tensor, is given as

$$T_{ij} = \rho u_i u_j - \sigma_{ij} + (p - \rho c_0^2)\delta_{ij} \qquad \textbf{1.6}$$

where $\rho u_i u_j$ is a Reynolds Stress term, σ_{ij} describes the sound generated by shearing, and $(p - \rho c_0^2)\delta_{ij}$ describes non-linear processes associated with internal energy. It is typical to assume $\sigma_{ij} = 0$, neglecting the effects of viscosity and heat transfer; then, $T_{ij} \approx \rho u_i u_j$. The quadrupole source term $\left(\frac{\partial^2 T_{ij}}{\partial x_i \partial x_j}\right)$ accounts for the noise generated by the non-linearities in the flow (Howe 2001).

Lighthill's work was modified by Curle in 1955 to include a dipole (i.e., a loud-speaker) source term, which takes into account the noise generated by the interaction of the fluid with a non-moving boundary. Ffowcs, Williams and Hawkings corrected the Lighthill and Curle formulations in 1969 further to include a monopole (i.e., a siren) noise source to predict the noise generated by the interaction of the fluid with a moving boundary. Monopole noise is generated due to unsteady volume displacement of the fluid volume. Curle's formulation and Ffowcs Williams and Hawkings corrections yield (Howe 2001)

$$\frac{\partial^2 \rho'}{\partial t^2} - c_0^2\left(\frac{\partial^2 \rho'}{\partial x_i \partial x_j}\right) = \frac{\partial \dot{m}}{\partial t} - \frac{\partial(f_i + \dot{m} u_i)}{\partial x_i} + \frac{\partial^2 T_{ij}}{\partial x_i \partial x_j} \qquad \textbf{1.7}$$

where $\frac{\partial(f_i + \dot{m} u_i)}{\partial x_i}$ is the additional dipole source term and $\frac{\partial \dot{m}}{\partial t}$ is the additional monopole source term. It is important to note that Lighthill's equation, Curle's formulation, and Ffowcs Williams and Hawkings corrections are exact for the conditions they describe.

The Ffowcs Williams and Hawkings method is the most general approach of the acoustic analogy and is therefore the most suitable for computing the trailing edge acoustic field, noting that the equations are derived directly from the continuity and momentum equations and formally solved using a half-plane Greens function (Roger and Moreau 2004)

Computational solutions to the far field fluctuating pressure field can be computationally expensive as they are primarily calculated in conjunction with direct numerical simulations. It is often simpler to compute a large-eddy simulation or perform experimental measurements to determine the fluctuating wall pressure spectrum and apply a semi-empirical model to predict far-field noise.

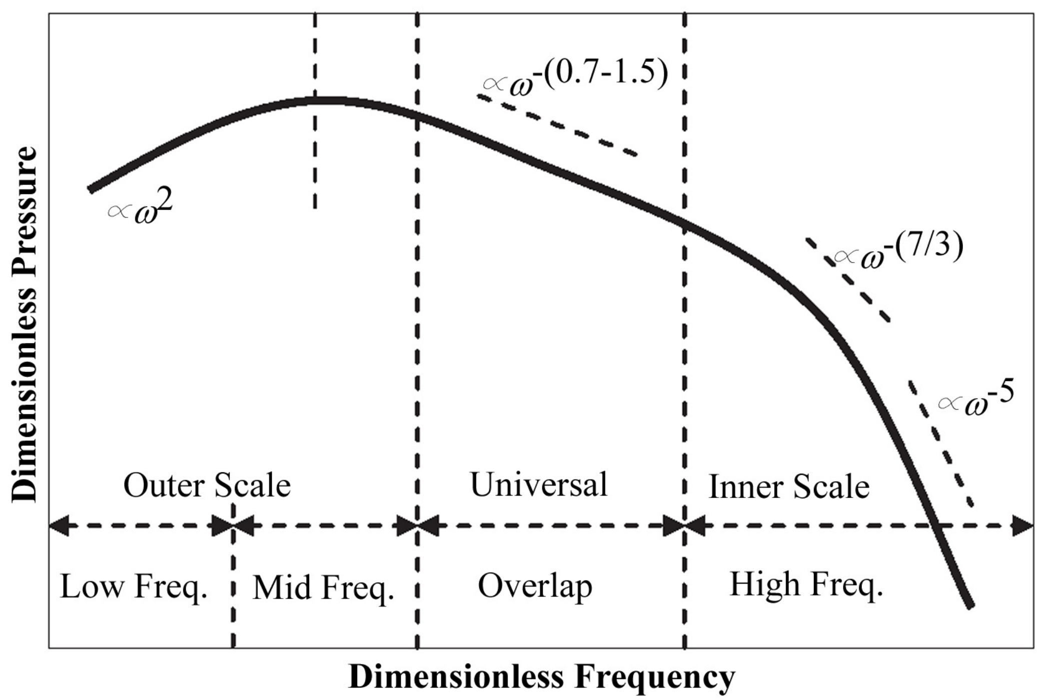

Figure 1.4 Spectral characteristics of a turbulent boundary layer (Hwang et al. 2009)

The ideal semi-empirical model describes the fluctuating wall pressure field beneath a turbulent boundary layer using practical data and theoretical knowledge. There is no uniform single scaling law that collapses experimental data for all frequencies, rather, there exists a multitude of models each optimized for a specific purpose. The goal of the semi-empirical model is to combine the following scaling ranges into one model:

Low frequency range: Characterized by a spectral scaling of ω^2

Mid frequency range: Characterized by a maximum in the spectra

Overlap range: Characterized by a spectral scaling of $\omega^{-(0.7\sim1.5)}$

High frequency range: Characterized by ω^{-5}, particularly at high frequencies

Figure 1.4 shows the different scales used to collapse the data from different frequency ranges. These spectral characteristics combine to define the descriptive model used for calculating the frequency spectrum. The following discussion describes the application of unsteady pressure data for predictive purposes and draws from semi-empirical models that have been fitted to the descriptive model empirically, but with theoretical guidance. The Goody model represents the most recent developments in spectral modeling, benefitting from recent measuring techniques and experimental data previously unavailable (Hwang et al. 2009).

$$\frac{\Phi_{pp}(\omega)u_\infty}{\tau_w^2\delta} = \frac{C_2(\omega\delta/u_\infty)^2}{\left\{(\omega\delta/u_\infty)^{0.75} + C_1\right\}^{3.7} + \left\{(\omega\delta/u_\infty)\cdot C_3R_T^{-0.57}\right\}^{3.7}} \qquad \textbf{1.8}$$

where R_T is the ratio of the outer to inner boundary layer time scale and C_1, C_2, and C_3 are empirical constants with recommended values of 0.5, 3, and 1.1 respectively. The ratio of C_1 and $C_3R_T^{-0.57}$ determines the size of the overlap region, which may be very thin at low

Reynolds numbers since $R_T \propto (u\delta/\upsilon)$. The Goody model is valid for a large range of Reynolds numbers, 1400 to 23400, and be extrapolated to higher Reynolds numbers due to the Reynolds number dependent factor R_T (Hwang et al. 2009).

It is intuitively reasonable that as more experimental measurements become available, empirical constants can be calculated more accurately, leading to better predictions. The semi-empirical models are developed further for use in the aeroacoustic community; predictive capabilities expand to predicting far-field pressure spectra, the acoustic production from the airfoil. This is accomplished by combining concepts from Lighthill's analogy to the semi-empirical model. Blake's model for trailing edge noise prediction is a common model used in the aeroacoustic community (Blake 1986)

$$\Phi_{p_{rad}}(\omega) = \frac{U_c L_2 \Lambda_2}{2\pi^2 c_o r^2} \Phi_{pp}\left(\frac{\omega\delta^*}{u_\infty}\right) \cos^2\left(\frac{\theta}{2}\right) |\sin\phi| \qquad \textbf{1.9}$$

where $\Phi_{p_{rad}}(\omega)$ is the power spectra of the acoustic radiation, L_2 and r are measured lengths associated with the spanwise length of the trailing edge and the distance from the trailing edge to the location of predicted acoustic radiation, c_o is the acoustic wavespeed, and U_c and Λ_2 are calculable quantities that represent the convection velocity and the spanwise correlation length scale. U_c and Λ_2 are typically estimated since accurate measurements that enable their calculation are often unavailable. Λ_2 is defined by Pope (2000) as the integral of the autocorrelation function

$$\Lambda_2 = \int_0^\infty R_{22}(\eta_2, t) dr \qquad \textbf{1.10}$$

$\Phi_{pp}\left(\frac{\omega\delta^*}{u_\infty}\right)$ is the local non-dimensional wall pressure spectra, directly measured by fast-response surface pressure transducers. θ and ϕ are directivity variables which describe the pattern of the far-field acoustic radiation. Note the appearance of the cardioid pattern $cos^2(\theta/2)$. The cardioid can be seen as a bounding envelope for the directivity patterns, emphasizing that trailing edge sources have dipole characteristics.

The contributions from this document to the aeroacoustic community are not within the scope of defining new prediction methods. Rather, the focus is to characterize the boundary layer using high-speed pressure sensors to resolve the fluctuating pressures along the airfoil surface. Additionally, this document will present, demonstrate, and discuss the capability of the current experiment for the future implementation into noise models.

1.4 Definitions of the Computational Methods Utilized in this Document

For use within this report it is instructive to define a few computational methods for random data analysis. A background in random process theory is needed to accurately assess conditions of the turbulent boundary layer of the present study. The following methods quantify random processes as defined by Munson et al. (1998) and Bendat & Piersol (1986).

The static pressure coefficient (C_p), a nondimensional form of pressure, is defined as the ratio of surface static pressure and free stream dynamic pressure (Equation 1.11). C_p is a useful expression for quantifying the static pressure along an airfoil independent of body size.

$$C_p = \frac{[p(x_1, x_2) - p_\infty]}{\frac{1}{2}\rho u_\infty^2} \quad \textbf{1.11}$$

The probability density function (PDF) of the fluctuating pressure is a expression that describes the relative intensities as a function of their probability. The PDF *P(x)*, for a random variable *x(k)*, where *k* is a set of possible outcomes such that *x(k)<x*, is

$$P(x) = \lim_{\Delta a \to 0}\left[\frac{Prob[x < x(k) \le (x + \Delta x)]}{\Delta x}\right] \quad \mathbf{1.12}$$

Statistical moments are identified to quantify the shape of the PDF with a singular variable; the calculation of moments allows for a simplified representation of a complex pressure field. Moments one through four are of interest in this experiment. The first moment is the mean of the signal for a function *A(x)*

$$\mu = \int_{-\infty}^{\infty} xA(x)dx \quad \mathbf{1.13}$$

The second moment is the variance of the signal is defined by Equation 1.14. Variance is a measure of the ‘spread’ of the PDF.

$$Var(A) = \int_{-\infty}^{\infty} (x-\mu)^2 fA(x)dx = \sigma^2 \quad \mathbf{1.14}$$

where σ is the standard deviation. The third moment is the skewness of the signal is defined by Equation 1.15. Skewness is a measure of the bias (positive or negative) of the PDF.

$$Skew(A) = \int_{-\infty}^{\infty} (x-\mu)^3 A(x)dx \quad \mathbf{1.15}$$

The fourth moment is the kurtosis of the signal is defined by EQ. Kurtosis is a measure of the ‘flatness’ or ‘peakedness’ of the PDF (Equation 1.16). A normal distribution has a kurtosis equal to 3.

$$Kurt(A) = \int_{-\infty}^{\infty} (x-\mu)^4 A(x)dx \quad \mathbf{1.16}$$

The power spectral, or autospectral, density (PSD) function of a fluctuating pressure signal describes the average frequency content of a random process *a(t)*. By use of Fourier transform methods, the PSD is given as

$$\Phi_{aa} = 2E[|A(f)|^2] \qquad \mathbf{1.17}$$

where E is an ensemble average for fixed frequency *f*.

The coherence function is a measure of the relationship between two signals as the square of the absolute value of the cross-spectral density function to the product of the autospectral density functions of the two signals.

$$\gamma_{ab}^2(f) = \frac{|\Phi_{ab}(f)|^2}{\Phi_{aa}(f)\Phi_{bb}(f)} \qquad \mathbf{1.18}$$

where $0 \le \gamma_{ab}^2(f) \le 1$.

The phase factor, or simply, phase, is a measure of the phase lag of the representative sinusoidal signal calculated using Fourier transfer methods. Defined as the angular component ϕ of the Fourier transform

$$e^{i\phi} = \cos\phi + i\sin\phi \qquad \mathbf{1.19}$$

where i is the imaginary unit.

The cross-correlation function is the measure of the product of two sinusoidal signals *a(t)* and *b(t)* at time *t* and time *(t+τ)* for an averaging time *T*

$$R_{ab}(\tau) = \frac{1}{T}\int_0^T a(t)b(t+\tau)dt \qquad \mathbf{1.20}$$

The autocorrelation is a special case where *a(t)=b(t)*.

Note that all the mentioned methods are valid only when applied to a stationary stochastic process. It it determined that the data presented in this document are statistically invariant with respect to translations in time. These data are sufficiently well converged so that they are considered stationary and stochastic.

2.0 Experimental Equipment and Procedure

2.1 RCDB Fan Development

The Rotating Controlled Diffusion Blade (RCDB) is derived as a rotating analog of a stationary Controlled Diffusion airfoil; the present work is a continuation of Neal (2010). The intent of the RCDB investigation is to study fundamental flow properties by making a direct translation - between stationary and rotating reference frames - of a known airfoil geometry. Given the equivalent operating conditions, valuable physical information on the effects of rotation can be inferred from flow-field measurements. See Neal (2010) for further details.

To reduce complexities and appropriately cast the CD airfoil into a rotating frame, the RCDB was designed without common fan and turbomachinery features that would have improved performance, efficiency, noise production, etc. It is important for several parameters to remain constant between the stationary and rotating experiments: a constant chord of $c=133.9mm$ across the entire blade span, a geometric angle of attack α of $8°$, a chord Reynolds number $(Re_c = 1.5\times10^5)$ based on the relative incident velocity $w_\infty = 16m/s$ and an equivalent aerodynamic loading.

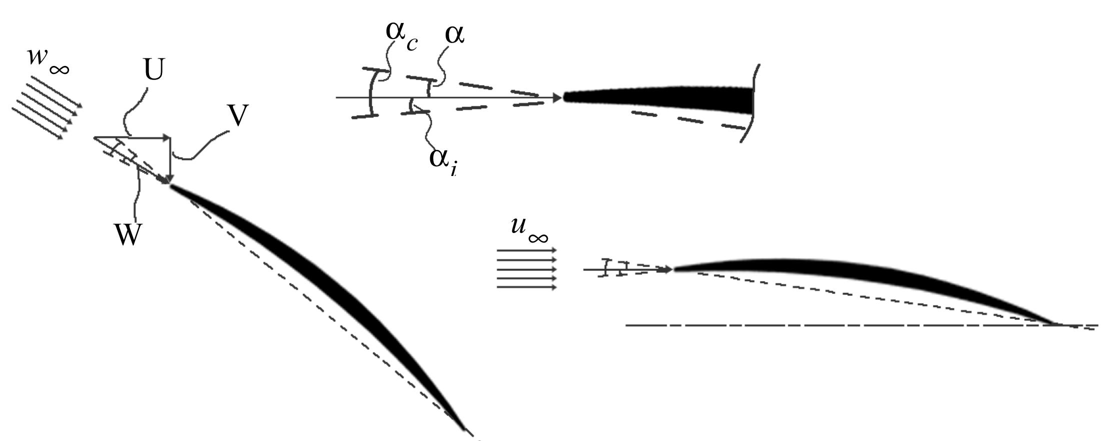

Figure 2.1 Flow geometry schematic (left - rotating; right - stationary)

It is instructive to note the difference between geometric and aerodynamic angle of attack for this geometry (Figure 2.1). The geometric angle of attack (α) is defined by the chord line with respect to the incident flow direction. The aerodynamic angle of attack (α_i) is defined as the tangent of the mean camberline at the leading edge of the airfoil - referred to as the camber angle (α_c) (Lakshminarayana 1996).

The RCDB was designed with a blade twist so that the angle of the incident velocity $\vec{V}_{a/b}$ was maintained across the leading edge of the blade; consequently, the magnitude increases linearly with respect to the radius as a result of the increased tangential velocity (rΩ) toward the tip. The relation between absolute inlet velocity and incident tip velocity is best expressed as:

$$\vec{V}_{a/b} = \vec{V}_{a/g} - \vec{V}_{b/g} \qquad \textbf{2.1}$$

where *a/g, a/b,* and *b/g* are the relative velocities of air with respect to a fixed reference frame (ground), air with respect to the rotating blade, and the rotating blade to the fixed reference frame. It is common to rewrite Equation 2.1 in more specific turbomachinery terms where $\vec{V}_{b/g}$ is written as the tangential velocity: $\vec{U} = \vec{\Omega} \times \vec{r}$, and $\vec{V}_{a/b}$ is written as the incident velocity W. Inlet velocity can be rewritten as:

$$\vec{W} = \vec{V} - \vec{U} \qquad \textbf{2.2}$$

Schematics of the incident velocity vectors for the CD airfoil and the RCDB are shown in Figure 2.1. Consequently, the Reynolds number is non-constant radially; the Reynolds number is matched to the CD airfoil at the midspan of the RCDB where $w_\infty = u_\infty = 16$ m/s.

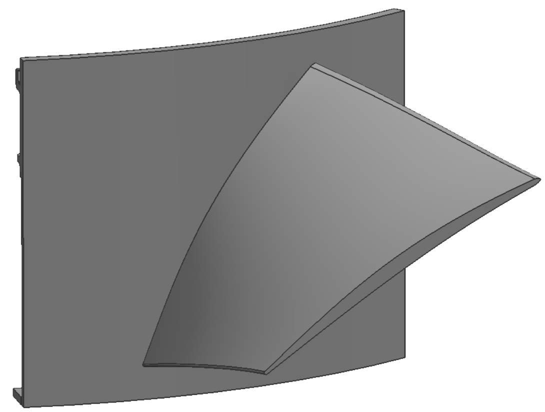

Figure 2.2 Modular blade section

Great care was taken to ensure proper matching of the CD airfoil and RCDB flow conditions as well as to minimize three-dimensional effects. The design target of the RCDB was first generated with RANS CFD simulations (Neal 2010). As shown in Figure 2.3, a converging inlet nozzle and centerbody create an annulus of uniform velocity $\vec{V} = 8$ m/s. Additionally, the exit radial velocity is minimized to nearly 3% of the relative inlet velocity (approximately 0.5m/s). Due to added three-dimensional and tip effects, compromises in the blade design and minor corrections in the operating conditions (mass flowrate and rotational speed) are required (Section 2.3.1). Additional trade-offs and details of the design iteration are discussed further in the Neal 2010 dissertation.

The final design of the RCDB experiment consists of a modular hub, which was designed and fabricated such that the rotor can accommodate any combination between 2 and 9 blades. Experiments were run to determine the C_p distribution for a range of blade solidity conditions. The final configuration was selected based on which solidity condition matched the blade loading of the CD airfoil.

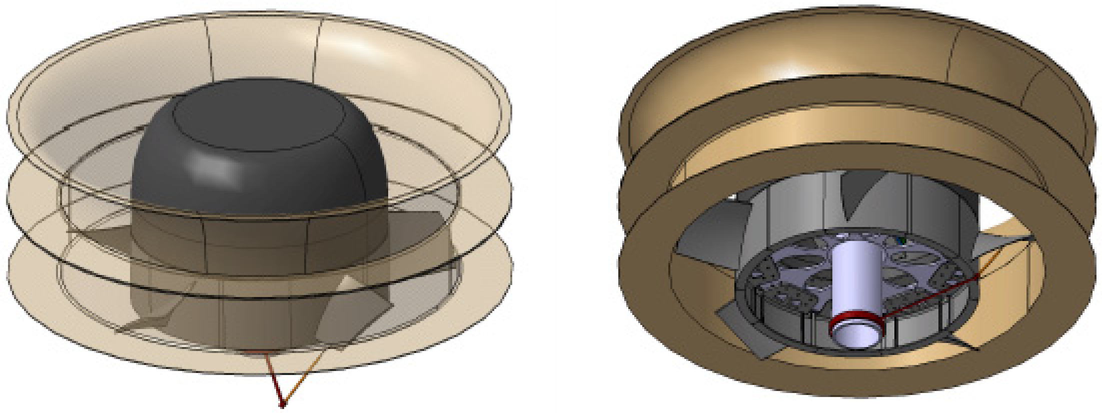

Figure 2.3 RCDB 5-blade CAD rendering (left - upstream; right - downstream) Neal (2010)
For interpretation of the references to color in this and all other figures, the reader is referred to the electronic version of this thesis

It is noteworthy that the C_p distribution for the stationary airfoil is highly dependent on the inlet nozzle width; it is suggested that the solidity of the rotating fan system is analogous to the nozzle width of the CD airfoil (Neal 2010). To determine which configuration had the best agreement with the stationary CD airfoil, physical experiments were conducted on several blade configurations (Figure 2.4). The blade loading was matched relatively closely between the CD airfoil and RCDB with three blades attached to the rotating hub. A consequence of the inherently different boundary conditions was apparent in the leading edge separation region and the general pressure distribution on the pressure side of the blade. While imperfect, the 3-blade RCDB configuration had the best agreement with the CD airfoil (Figure 2.5).

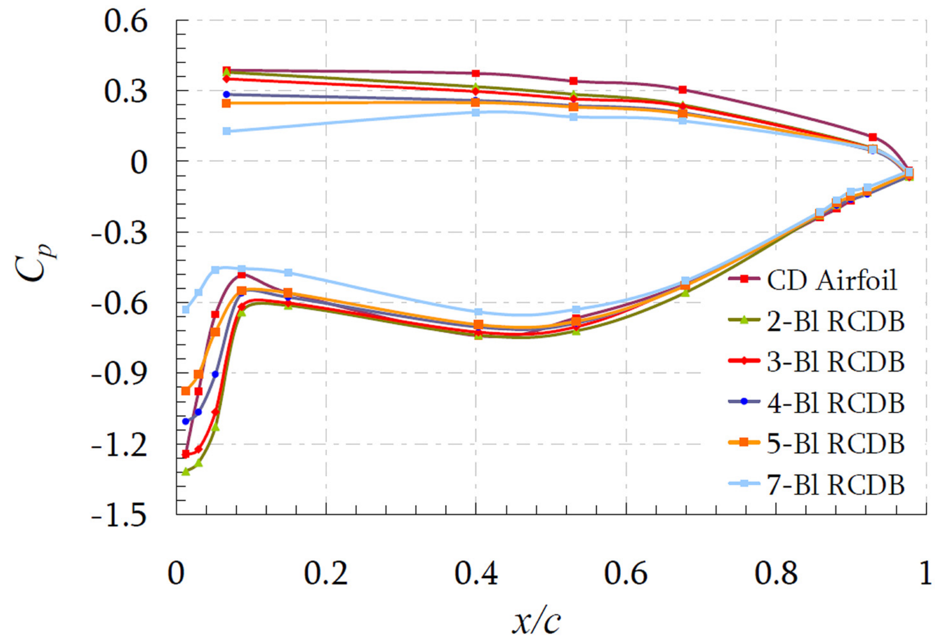

Figure 2.4 RCDB C_p comparison for several blade configurations
Neal (2010)

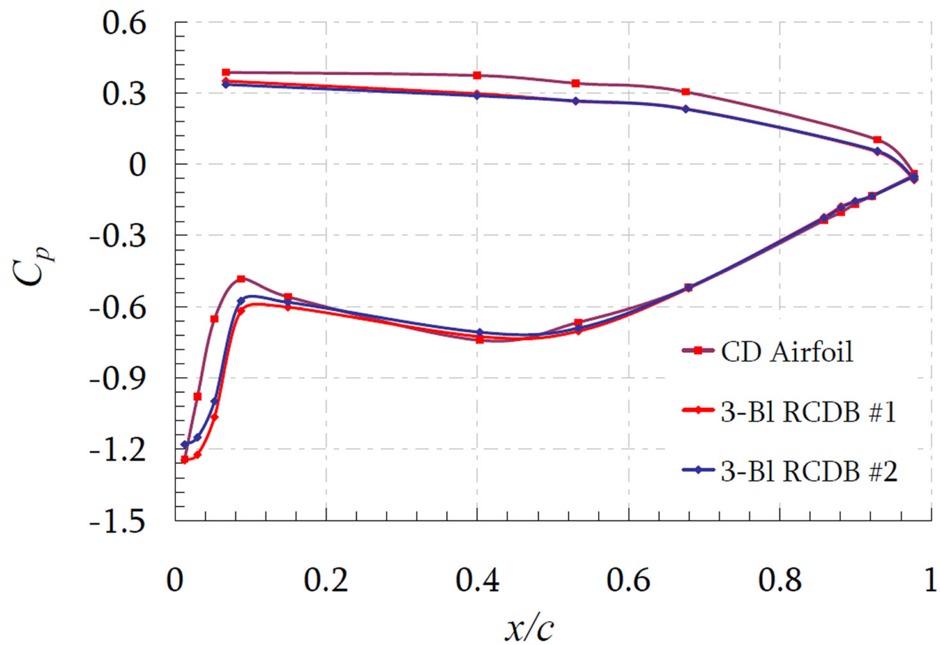

Figure 2.5 Final RCDB C_p configuration and CD airfoil
Neal (2010)

2.2 Experimental Configuration/Facility

2.2.1 Axial Flow Research and Development (AFRD) Facility

The Axial Research and Development (AFRD) facility was used for the RCDB experiments. Originally designed to measure integral quantities of volume flowrate, pressure rise, and input power as well as wake measurements, the AFRD has since been used for a variety of low-speed axial fan experiments (Morris and Foss 2001, Neal and Foss 2007, Dusel 2005, Neal 2010).

The AFRD facility, shown in Figure 2.6, is a vertical wind tunnel that draws atmospheric air into an upper receiver (D). The RCDB fan assembly (A) and prime mover (K, Chicago Design 36 SISW SQA Airfoil) are responsible for the flow through the facility. Air is moved from the upper receiver into the lower receiver (H) through a set of delivery nozzles (E) and turning vanes (F). The 90-degree turning action results in a net moment-of-momentum flux that is proportional to the mass flow rate; this net flux is balanced by the moment of a force transducer (G) about a pivot point. The flow inlet (I) to the prime mover is located in the lower receiver. The flow rate is controlled with a throttle plate (J) at the exhaust of the prime mover. A wall tap in the upper receiver of the AFRD facility is used to measure the pressure differential across the test fan.

The RCDB fan assembly was mounted on a vertical shaft cantilevered 60cm above a bearing support to avoid any aerodynamic blockage of the wake from support members. The shaft was driven by a Reliance Electric 11.2 kW (15 HP) electric D.C. motor. An optical encoder provided an angular location and rotational speed. A slip ring is used to make an electrical connection from the stationary frame to the rotating assembly. A built-in traverse system (C) allows for radial, axial, and azimuthal positioning of hot-wire and similar probes downstream of the fan.

The integral flow metering apparatus was calibrated separately using both metering nozzles and the inlet nozzle for the RCDB. Knowing the discharge coefficient and the pressure differential across the N nozzle(s), it is a simple matter to determine the mass air flow following Equation 2.3.

$$\dot{m} = \rho \times N \times A_{nozzle} \times C_d \sqrt{\frac{2}{\rho}(p_{atm} - p_{receiver})} \qquad \textbf{2.3}$$

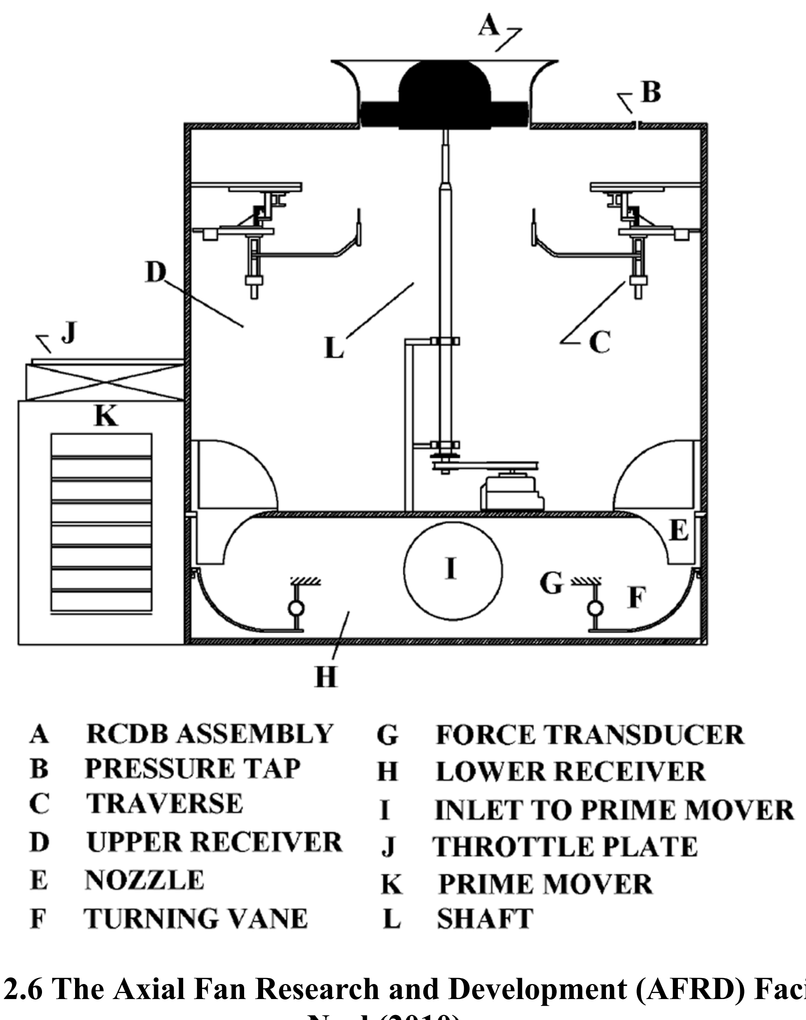

Figure 2.6 The Axial Fan Research and Development (AFRD) Facility Neal (2010)

The AFRD inlet was retrofitted to accommodate the modular hub, aerodynamic centerbody, and an inlet contraction. These components were designed to meet the RCDB and CD design targets as discussed in Section 2.1. The final installation is shown in Figure 2.7

2.2.2 Rotating Controlled Diffusion Blade (RCDB) Assembly

Salient features of the RCDB are shown in Figure 2.7. The RCDB assembly has a hub-tip ratio of 0.655 (hub diameter of 480mm), a 4mm tip clearance, and a shroud diameter of 740mm. One of the three blades in the current RCDB configuration is instrumented with 21 surface pressure taps at the midspan of the blade (Figure 2.9).

The particularly large hub section makes the RCDB well suited for onboard instrumentation and data acquisition. All measurements of the RCDB occur in the rotating hub, necessitating an intricate instrumentation package of OEM and custom transducers and components. The details of the blade and instrumentation package required to support the present experiment are outlined in the following sections.

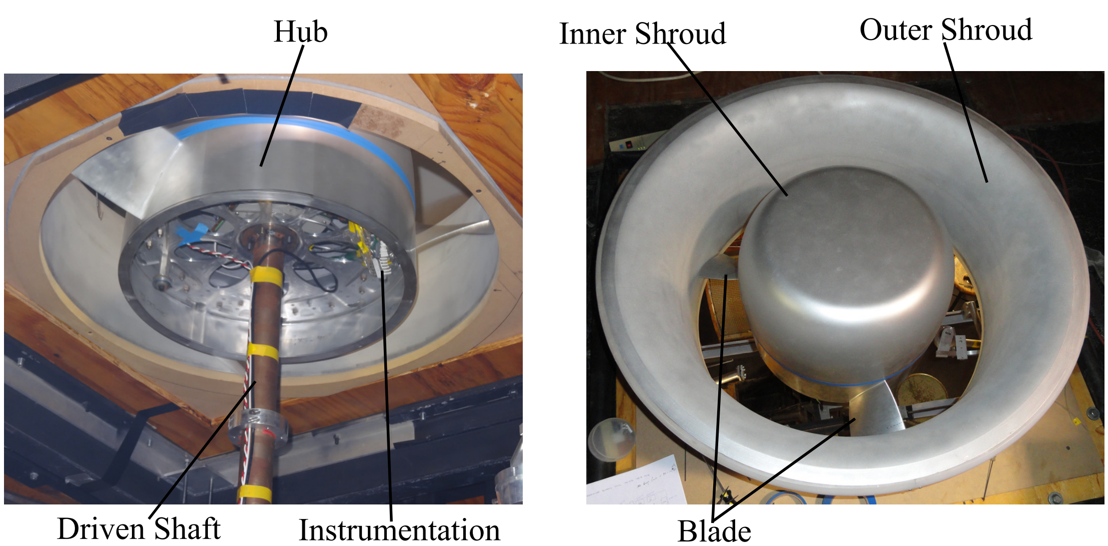

Figure 2.7 RCDB assembly installed in AFRD Facility

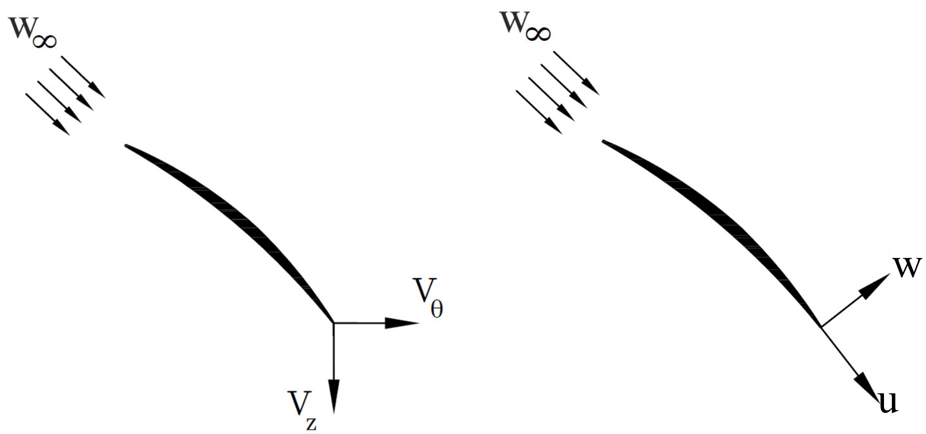

Figure 2.8 RCDB coordinate systems (left - r–θ–z; right - x-y-z) (Neal 2010)

2.2.2.1 Coordinate System

The RCDB assembly is described and data are collected in the traditional polar turbomachinery coordinate system: r-θ-z (Figure 2.8), where r is the radial line normal to the axis of rotation z and θ is the polar angle or azimuth. Typically, the coordinate system is recast into one similar to the CD blade: a Cartesian u-v-w. This transform allows for direction comparison with the CD airfoil. However, due to limited trailing edge surveys, wake data are presented in polar coordinates within this document. See Figure 2.8 for a visual representation of the difference.

2.2.2.2 Instrumented Blade

Due to the thin profile of the RCDB and the need for high spatial resolution, it is impractical to embed pressure transducers directly in the surface of the blade. Instead, 1mm OD, 0.5mm ID stainless steel tubing was embedded flush into small channels milled in the blade surface. Each tube had a small pinhole drilled at the midspan of the blade and at a unique chord location as shown in Figure 2.9. Eighteen streamwise taps and three trailing edge spanwise taps exist in the current experiment; each tap is assigned a unique number shown in Figure 2.10 and Tables 2.1, 2.2, and 2.3(Moreau and Roger 2005, Neal 2010). Note that the gaps in the numbering sequence exist to maintain consistent numbering with previous investigations.

The 21 taps will be used for mean and unsteady surface pressure measurements. See further discussion in Section 2.2.2.6 and Section 2.2.3.

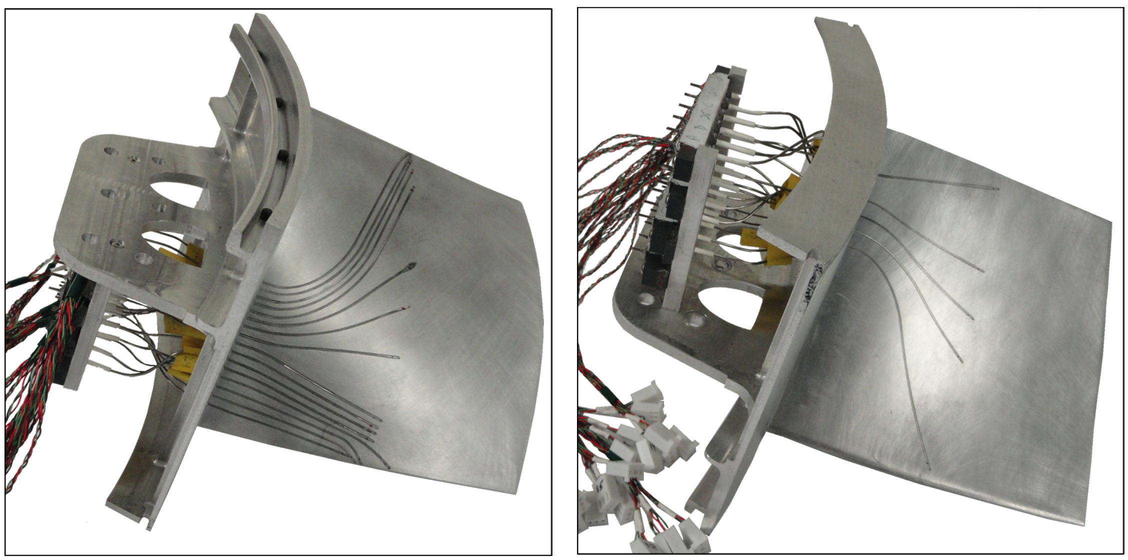

Figure 2.9 RCDB instrumented pressure taps
Left: Suction side (top); Right: Pressure side (bottom)

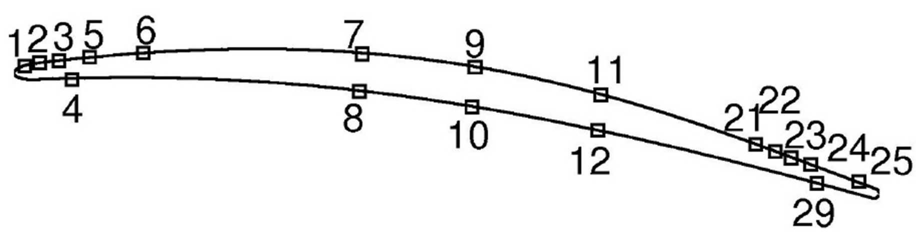

Figure 2.10 Surface pressure tap locations

Table 2.1 Suction side taps (y/*l*=0.5)

Tap	1	2	3	5	6	7	9	11	21	22	23	24	25
x/c	.013	.030	.052	.087	.149	.403	.534	.679	.858	.881	.899	.922	.978

Table 2.2 Pressure side taps (y/*l*=0.5)

Tap	4	8	10	12	29
x/c	.067	.400	.530	.675	.929

Table 2.3 Trailing edge spanwise taps (x/c=0.978)

Tap	25A	25B	25	25C
y/*l*	.454	.477	.500	.577

2.2.2.3 Data Acquisition

Measurements of the RCDB experiment were digitally sampled by two synchronized analog-to-digital (A/D) acquisition boards. The primary A/D (IOTech Inc. WaveBook/516E) measures variables in the stationary reference frame and provides a sync signal used to clock the secondary A/D. The secondary A/D (IOTech Inc. DaqBoard/3035USB) is rigidly mounted in the rotating hub of the RCDB. The stationary A/D can sample up to 16 differential 16-bit channels at 1 MHz and has the capability for advanced TTL triggering and external clocking, making it well suited for high-speed, downstream, stationary measurements, as well as serving as a master clock. The rotating board can sample 64 single-ended 16-bit channels at 1MHz; it is clocked externally via a sync signal from the stationary A/D.

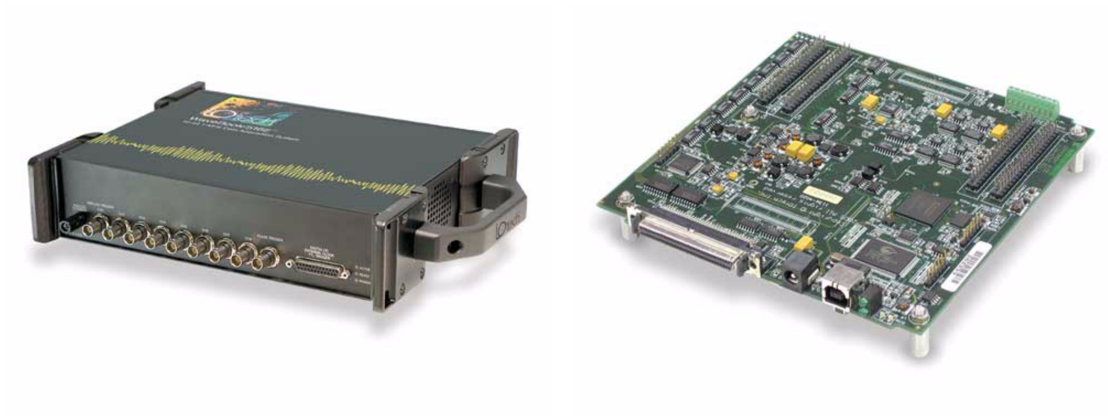

Figure 2.11 Data acquisition boards (photos: www.mccdaq.com)

Its compact design (15cm x15cm), as well as its simple interface (power and data transfer via USB 2.0), make it particularly suitable for implementation in the RCDB assembly.

2.2.2.4 Signal Transmission

It is inherently difficult to maintain electrical connections between rotating and stationary reference frames. To transfer power and data between the RCDB and lab environment, a slip ring assembly was mounted on the end of the rotating fan shaft (Figure 2.12). The slip ring (SR20M by Michigan Scientific Corporation) allows 20 channels of data to be transferred from the rotating environment. Each channel has a maximum current rating of 500mA, a typical contact resistance of 0.05 ohms, and contact life of 200 million revolutions. The SR20M is ideally suited to this experiment because of its low noise characteristics and low maintenance requirements.

As discussed in Section 2.2.2.3, the onboard data acquisition board requires only USB 2.0 for power and data transmission. In addition to USB 2.0, a digital sync signal and DC power for the instrumentation package is transferred through the slip ring.

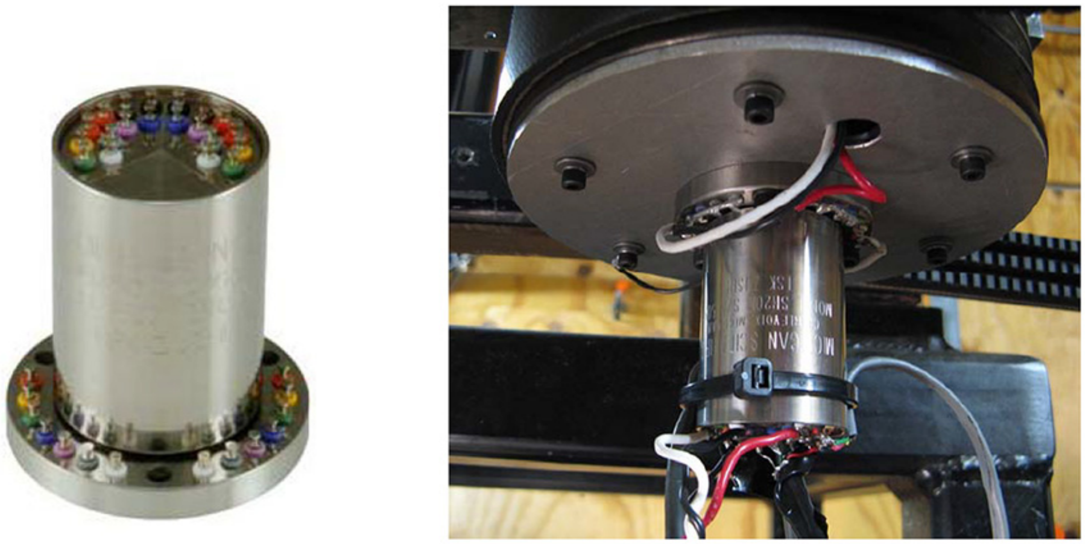

Figure 2.12 Slip ring assembly (Neal 2010)

The digital signals of USB 2.0 and the sync signal are not as susceptible to noise effects from the slip ring assembly as are analog signals; and, therefore, they are well suited for uncorrupted data transfer. DC power (±24 V) is split between multiple channels to meet the current ratings and conditioned with onboard electronics to remove any electrical noise.

2.2.2.5 Temperature Measurements

Temperature measurements were made possible by two IC amplifiers with integrated cold junction compensators (Analog Devices AD595). The fast response type-T thermocouples are used for temperature compensation of hot-wire measurements as well as temperature monitoring of the instrumentation cluster. The ICs were mounted in a custom circuit board that interfaced directly with the rotating A/D (see Figure 2.17 for an instrumentation and data path schematic).

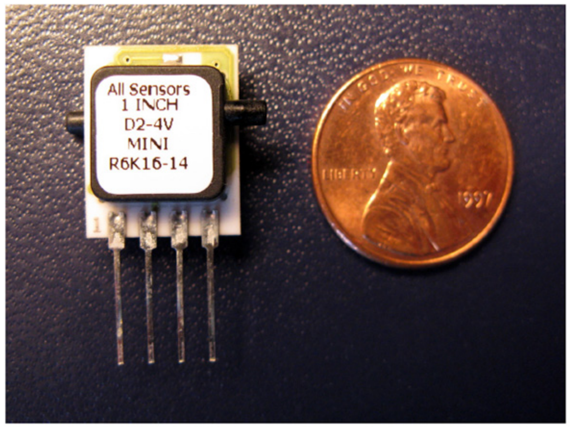

Figure 2.13 MEMS pressure transducer (Neal 2010)

2.2.2.6 Time-Mean Pressure Measurements

Pressure measurements are made in the rotating reference frame by 22 small MEMS pressure transducers (model-type 1-INCH-D2-4V-MINI manufactured by All Sensors, Figure 2.13) installed in the hub of the RCDB assembly. These relatively slow response transducers are responsible for measuring the time-mean surface pressure. All 22 transducers share a common reference pressure P_{atm}. Measuring P_{atm} in a rotating reference frame presents a challenge. An isobaric reference chamber provides a known, and equal, reference for all 22 pressure transducers (Figure 2.16). The isobaric chamber is open so that the pressure in the chamber is the same as the AFRD upper receiver pressure.

The pressure transducers are susceptible to adverse rotational effects due to their internal construction: the inner diaphragm may be displaced by centrifugal forces leading to a false pressure reading. To avoid this, great care was taken in mounting the transducers so that the diaphragm would be normal to the axis of rotation, preventing any unwanted displacement. In addition to centrifugal forces acting on the transducer membrane, issues arise from the centrifugal forces acting on the air that is present in the connecting tube. The measured pressure will be different due to the radial separation between the transducer and the pressure tap (Figure 2.14). To account for this rotation-induced pressure gradient, a simple correction of the measured differential pressure $\Delta P_{measured}$ to the actual differential pressure $[P_{taps} - P_{ref}]$ is proposed as follows (Neal 2010):

$$\Delta P_{corr1} = \frac{\rho\omega^2 (r_{taps}^2 - r_{sensor}^2)}{2} \qquad \textbf{2.4}$$

where ΔP_{corr1} is the correction between the pressure transducer (r_{sensor}) and the pressure taps on the blade ($r_{taps} = 303$ mm). Equation 2.4 corrects the positive side of the differential pressure transducer which is connected to the surface taps.

$$\Delta P_{corr2} = \frac{\rho\omega^2 (r_{sensor}^2 - r_{ref}^2)}{2} \qquad \textbf{2.5}$$

where ΔP_{corr2} is the correction between the isobaric reference chamber ($r_{ref} = 0$ mm) and the pressure transducer (r_{sensor}). Equation 2.5 corrects the negative (reference) side of the differential pressure transducer. Applying the corrections, the expression for the actual pressure $[P_{taps} - P_{ref}]$ becomes

$$[P_{taps} - P_{ref}] = \Delta P_{measured} + \Delta P_{corr1} + \Delta P_{corr2} \qquad \textbf{2.6}$$

or

$$[P_{taps} - P_{ref}] = \Delta P_{measured} + \frac{\rho\omega^2 r_{taps}^2}{2} \qquad \textbf{2.7}$$

Correcting to atmospheric pressure where $P_{ref} = P_{receiver}$,

$$[P_{taps} - P_{atm}] = \Delta P_{measured} + \frac{\rho\omega^2 r_{taps}^2}{2} + [P_{receiver} - P_{atm}] \qquad \textbf{2.8}$$

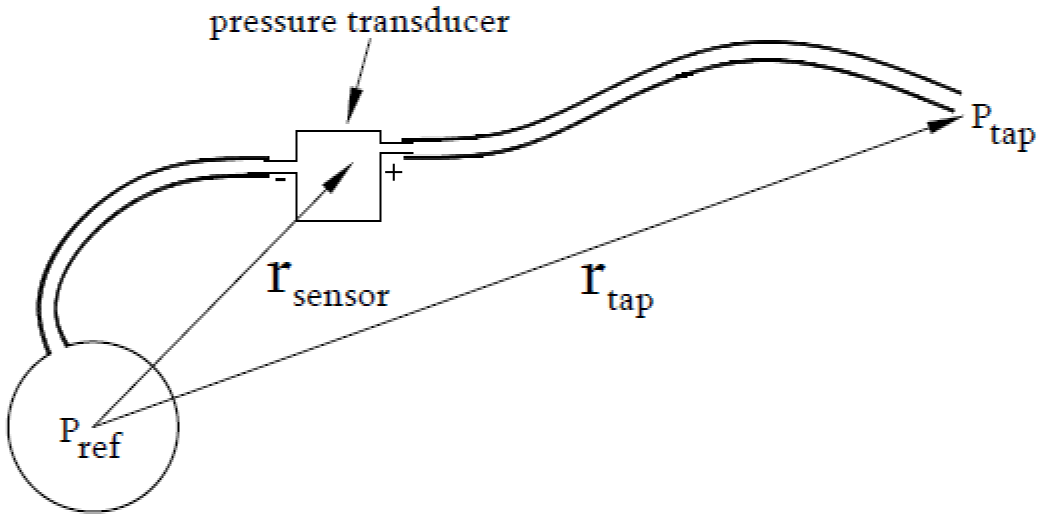

Figure 2.14 Pressure transducer schematic (Neal 2010)

Equation 2.8 shows the reduced relationship between the measured differential pressure and the actual differential pressure. Note that the r_{sensor} term is eliminated; accordingly, the pressure transducer can be placed at an arbitrary radial location within the hub.

2.2.2.7 Constant Temperature Hot-Wire Anemometry

Two hot-wire channels were installed in the RCDB instrumentation package for fast response ($f_r > 20kHz$) velocity measurements (Figure 2.16). TSI 1750 anemometers were chosen for their small size and sufficient frequency response, with the custom probes used in the rotating reference frame measurements. See Section 2.2.4 for further discussion of the hot-wire technique.

2.2.2.8 Microphone Amplifiers

A series of microphone amplifiers are mounted in the instrumentation package. These IC operational amplifiers (Texas Instruments OPA4134) support 21 electret condenser microphones (Knowles FG-23329) used for unsteady surface pressure measurements. Figure 2.15 shows a schematic of the amplifier and microphone system. See Section 2.2.3 for further information on microphone development and implementation

2.2.2.9 Hub Instrumentation Package

The final assembly of the instrumentation package is shown in Figure 2.16. Relevant features are:

A) Level 1: A/D board
B) Level 2: Mezzanine level board which houses thermocouples, pressure transducers, and microphone amplifiers. This is a non-OEM part.
C) Level 3: Hot-wire constant temperature anemometers and power conditioning circuitry
D) Level 4: Isobaric pressure reference chamber

A detailed schematic of the instrumentation package and signal paths is shown in Figure 2.17.

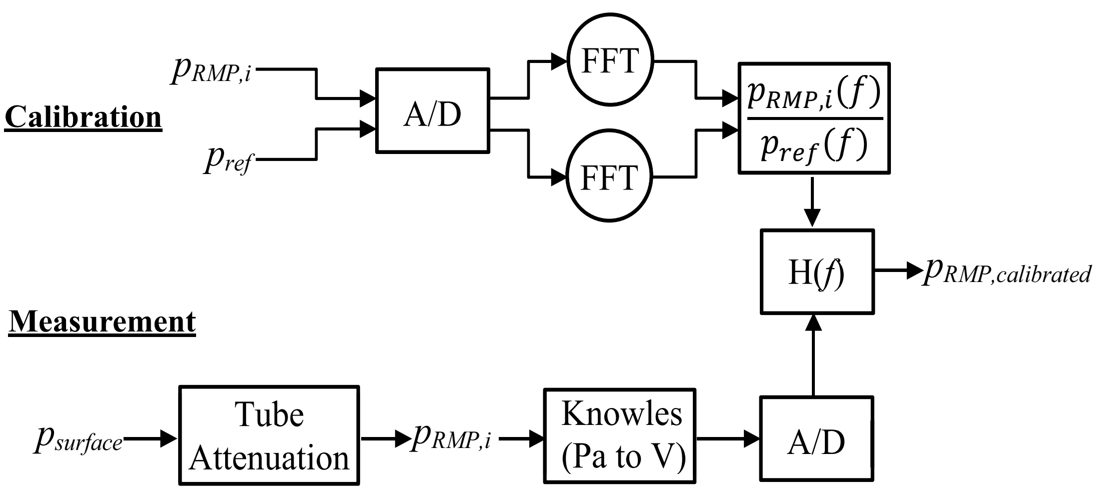

Figure 2.15 Amplifier and microphone system

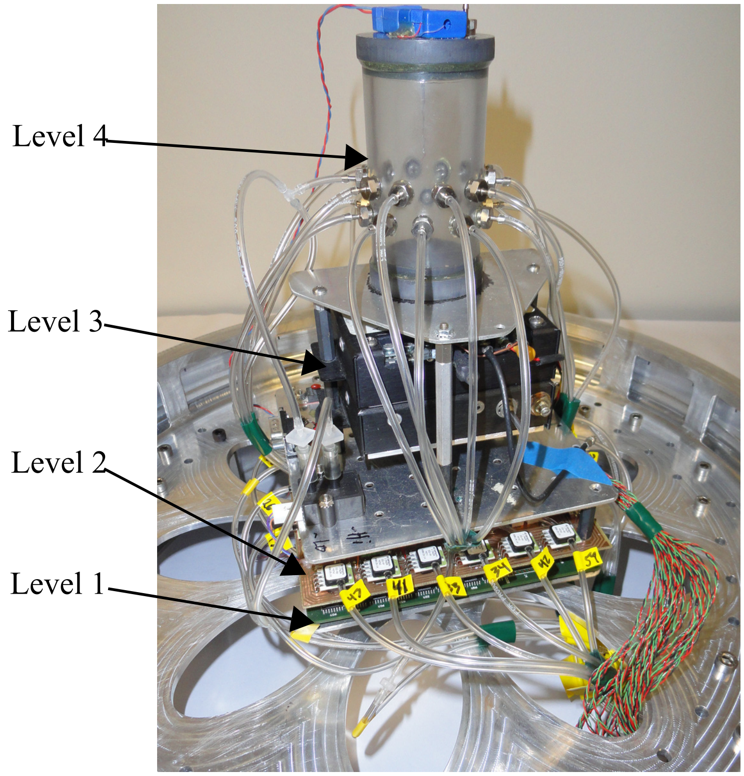

Figure 2.16 Hub instrumentation package

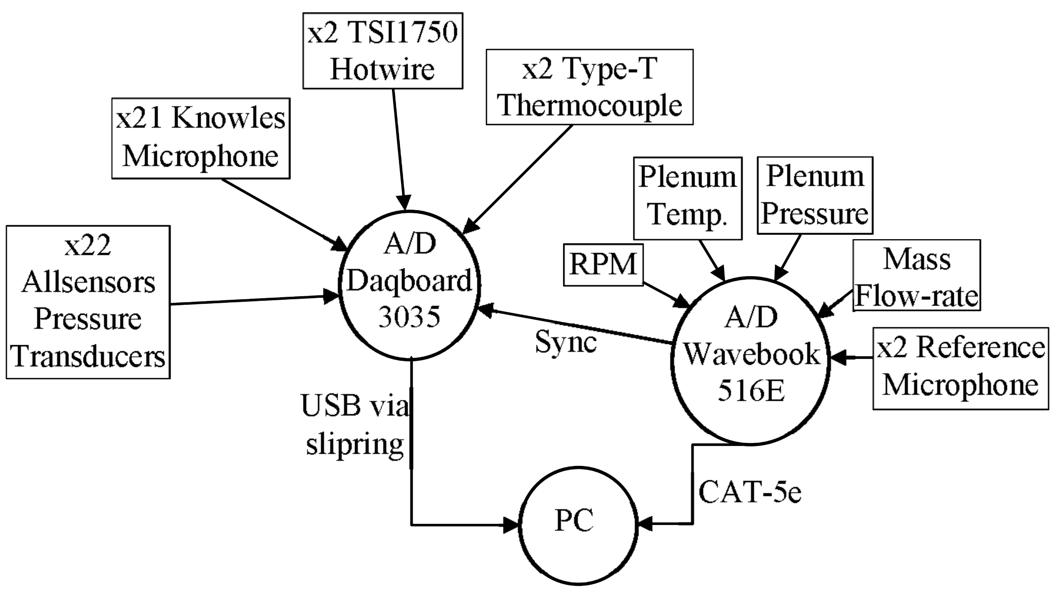

Figure 2.17 Data path schematic (RCDB)

2.2.3 Remote Microphone Probes (RMPs)

Information regarding the pressure fluctuations, in addition to the time-mean pressures, is important in representing the flow over the stationary and rotating CD airfoils. The latter ($\bar{p}$) measurements are obtained by connecting the open, static taps to the MEMS pressure transducers. For these data, it is assumed that the time-mean voltage output represents the time-mean pressure at the tap. The former ($p'(t) = p(t) - \bar{p}$) measurement requires that a "fast-response transducer", a microphone, is connected to the static tap in such a manner that the amplitude and phase of its response can be processed to yield an acceptably accurate representation of *p'(t)* at the airfoil surface.

The thin airfoil and the desire for good spatial resolution make it imperative that the microphones are located at some physical (remote) distance from the tap itself. The associated challenges to fabricate, install, and calibrate the RMP system are presented in the following sections.

2.2.3.1 Technique

Pérennès and Roger (1998) developed a unique RMP for measuring surface pressures using capillary tubes in thin airfoils. High spatial resolution and a thin airfoil mandated the remote measurement of the surface pressures with the bulky microphone transducers. The RMP concept evolved for use in the work of Moreau and Roger (2005), a study where the RMPs were installed in the CD airfoil geometry - the stationary analog of the RCDB.

The present experiment is equipped with 21 embedded taps, 18 of which are located at a common radial coordinate and 4 of which are located at the same chord location (Tap 25, x/c=0.9776) but distributed spanwise along the trailing edge. The taps are drilled into stainless steel tubing that is embedded in the blade surface. The present form of the RMP is predicted to have a maximum frequency response of 20-25kHz but has been modified procedurally and physically from the previous applications of Pérennès and Roger to accommodate new techniques and technologies, updated hardware, and packaging requirements.

2.2.3.2 Fabrication/Implementation

The embedded stainless steel capillary tubing (Section 2.2.2.2) provides the transmission path for unsteady pressure propagations between the blade surface and the microphone transducers. The acoustic channel of stainless tubing is terminated with a small section of PVC tubing that extends to the MEMS pressure transducers (schematic shown in Figure 2.22). This PVC tubing acts to prevent reflections by attenuating high frequency pressure fluctuations and matching impedances to avoid acoustic resonances (Hoarau 2006).

The precise dimensions of this tubing allows for leak-proof splicing between segments to be made as shown in Figure 2.19. Specifically, a splice for the installed 0.5mm ID, 1.0mm OD tubing is accomplished by using a 1.0mm ID "sleeve" tube to mate the smaller steel tubes and heat-shrink tubing to seal the combined sections.

The microphones (Knowles FC-23329-C05: 2.56mm physical diameter, 0.76mm sensor diameter) are chosen for their small size, sensitivity, and cost (see Appendix A for specifications). The microphones are mounted in a support member that is placed between the surface tap and the MEMS pressure transducer. Since there is zero flow in the 0.5mm passage, the fluctuating pressure signal is transmitted from the open surface tap (and past) the opening that exposes the microphone element to the fluctuating pressure in the passage.

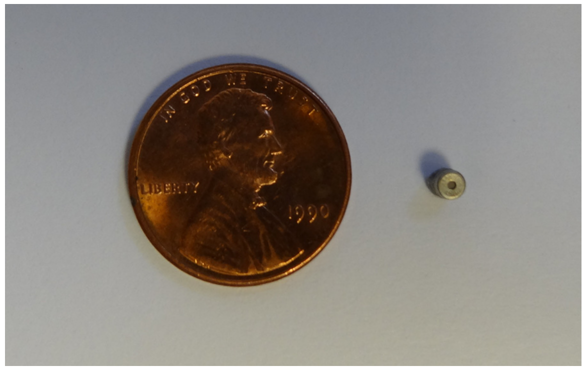

Figure 2.18 RMP microphone

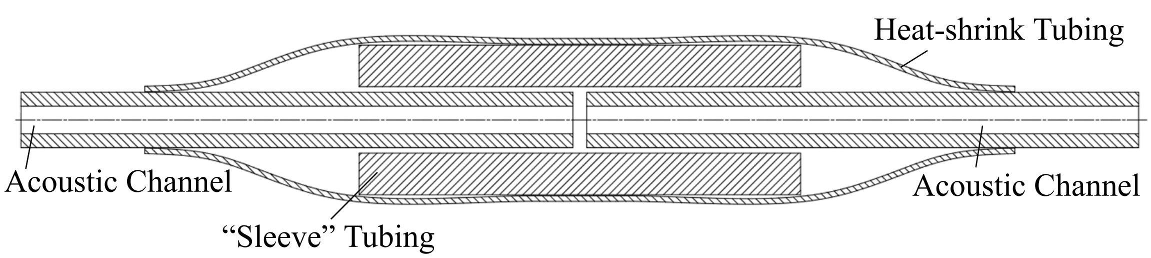

Figure 2.19 RMP tube splicing

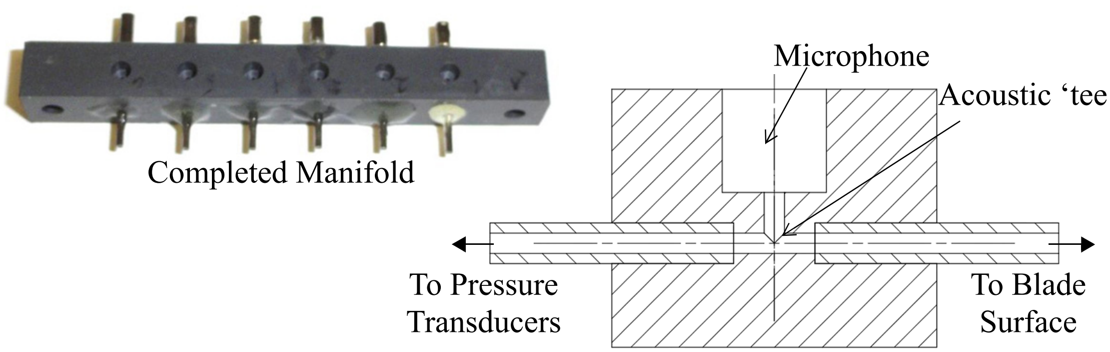

Figure 2.20 RMP manifold schematic

Figure 2.20 identifies salient features of the RMP support member. For ease of installation and packaging purposes, the RMPs were fit into a small PVC support manifold and easily spliced into the existing stainless steel tubing as shown in Figure 2.19. The PVC structure acts to passively damp vibrations and other external noise sources. This contributes to clearer and better resolved microphone data. The PVC manifold houses 6 RMP microphone assemblies; see Figure 2.21. It is necessary to realize that the acoustic properties of the microphones and tubing connected to each RMP are inherently unique. Each RMP additionally had a unique, unknown, electrical response. This mandate a routine to identify a known RMP response/transfer function between pressures measured at the microphone and pressures acting on the surface of the airfoil.

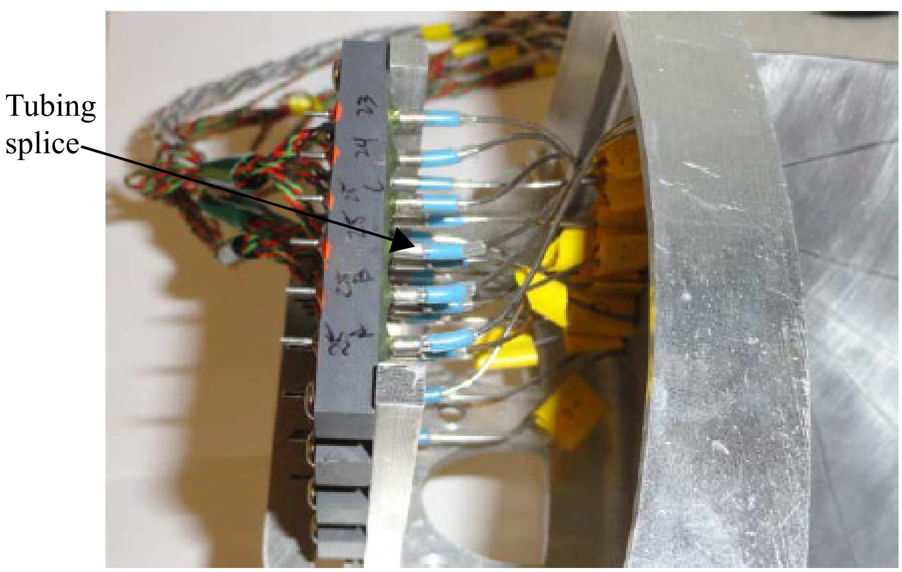

Figure 2.21 Installed RMP manifolds (Note spliced steel tubing)

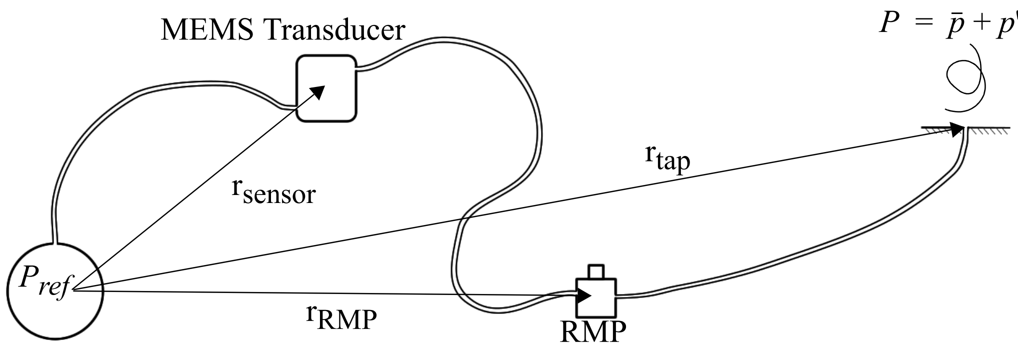

Figure 2.22 Pneumatic circuit of RMP system

2.2.3.3 Evaluation/Calibrations

It is apparent that a calibration will be required to relate the fluctuating pressure at the surface tap to the fluctuating pressure experienced by the microphone. That is, both the amplitude and the phase of the recovered signal must be related to those of a known signal at the surface tap via calibration data. The calibration will account for attenuation effects from the acoustic channel, including imperfections and blemishes in assembly and manufacturing, as well as accounting for individual microphone responses. For further details on the development of the calibration procedure, the reader is referred to Appendix A.

A plane wave tube (PWT) was fabricated with removable inserts at an x/L location of roughly 0.4 (Figure 2.23). The PWT is used to generate a uniform acoustic pressure signal along a given cross-section sufficiently downstream of the tube's opening (AED-1ID-1991). The PWT was used to evaluate and validate calibration routines and RMP manifold geometries.

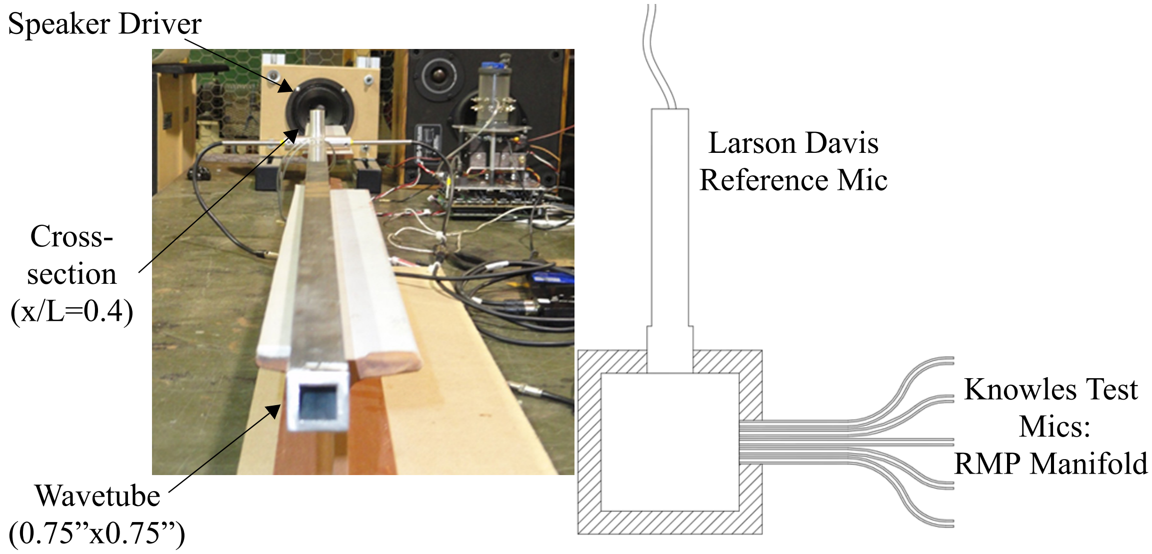

Figure 2.23 Wavetube experiment and schematic

The apparatus in Figure 2.23 allows for the simultaneous testing and subsequent calibration of five microphones within a given RMP manifold. Phase and magnitude transfer functions for each of the RMPs were obtained by comparing the five microphone signals to the concurrent output from the Larson Davis reference microphone (specifications in Appendix A). Calibrating the RMP microphones (i.e., applying the calculated transfer functions) accomplishes the effect of “matching” the RMPs to a known magnitude and phase response (measured by the Larson Davis reference microphone). The calibration algorithms and RMPs are tested on their ability to accurately recover known spectral properties when subjected to a known acoustic pressure field. It is evident in Figure 2.24 that the calibration functions provide a quite acceptable representation of the acoustic signal with exceptions near 6000Hz and 8000Hz. Additional measurements (not presented here - see Appendix A) suggest that the seemingly unreliable transfer functions are an artifact of the speaker-wavetube configuration.

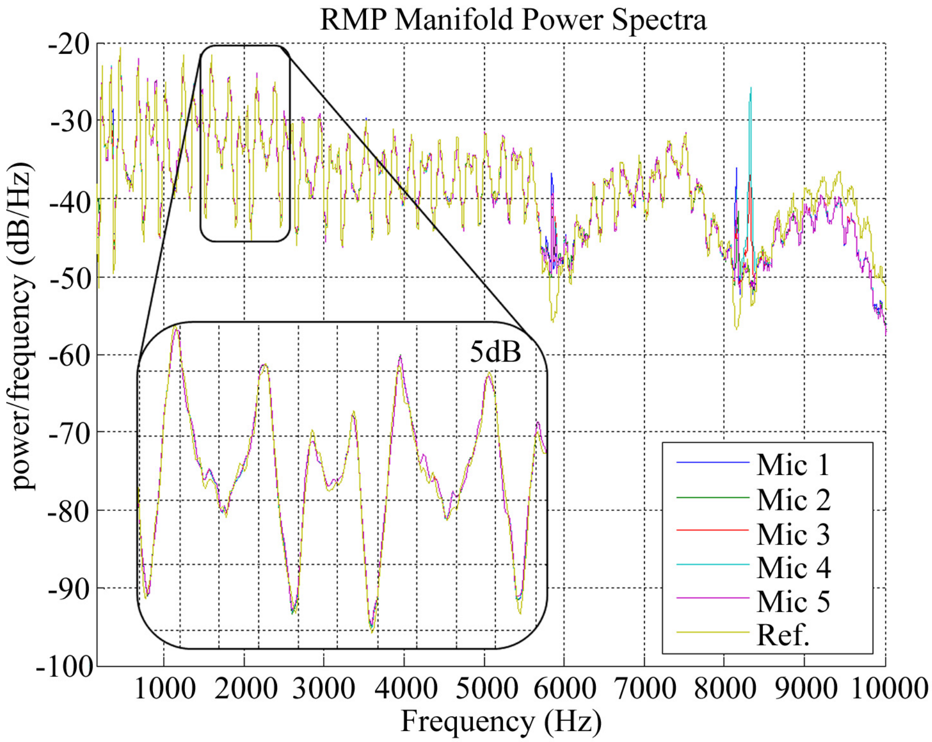

Figure 2.24 RMP manifold and reference spectra

While useful for characterization and testing, the PWT is not a practical device to calibrate microphones installed in the RCDB due to the inhibiting blade camber and sweep. Accordingly, an *in situ* method, where the reference microphone is held normal to the airfoil surface, offset roughly by 1mm and centered on a pressure tap, is used in lieu of the PWT. A sufficiently downrange set of speakers (low-range and mid-range) is used to generate a broad-spectrum acoustic pressure field - exciting the reference and RMP microphones simultaneously. The calculation of phase and magnitude transfer functions proceeds using the same analysis used for the PWT.

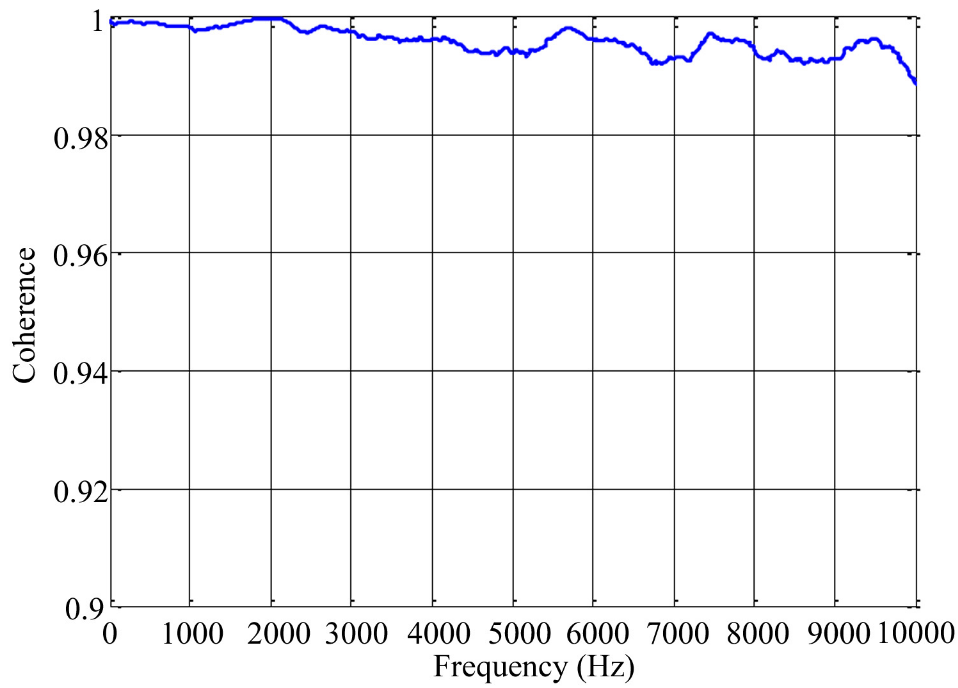

Figure 2.25 Larson-Davis comparison (*in situ* method)

This method is accurate to frequencies whose wavelengths are of order of the separation distance and microphone diameter (f>>10kHz, λ<<0.03m). This is verified in Figure 2.25 where two phase-matched Larson Davis reference microphones were tested in a simulated experiment. It is clear that there is excellent coherence across the frequency range of interest; this is validation that the *in situ* is appropriate to use for RMP calibrations.

The *in situ* method is time consuming; the microphones cannot be calibrated in bulk; therefore, a calibration rig containing indexed positions for all 21 microphones was developed to meet the needs of the calibration procedure. Accuracy, precision, and repeatability are critical for consistent calibrations (Figure 2.26).

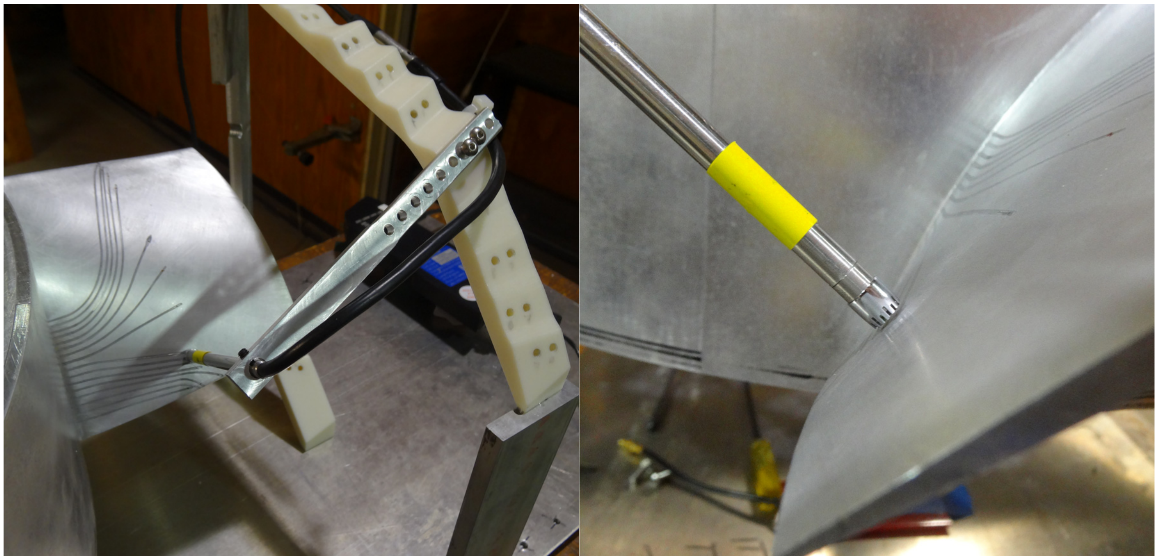

Figure 2.26 RCDB *in situ* microphone calibration rig

Each RMP calibration produces a unique set of transfer functions (Figure 2.27). The data of Figure 2.27 reveal two important aspects of the experimental procedures to recover fluctuating pressure information at the open taps on the RCDB surface. The first immediately clear message is that calibrations are very consistent with few day-to-day variations; this is a result of a very stable calibration routine. The second message relates to the identification of the physical processes at work in the p'(t) measurement scheme. This second message is based upon the properties of the "magnification-factor" and the phase as a function of the frequency of the incident sound waves. The magnification-factor and phase combined represent the response difference between the reference microphone, the literal representation of the pressure at the surface tap, and a given RMP, including the microphone response and the attenuation effects of the acoustic channel.

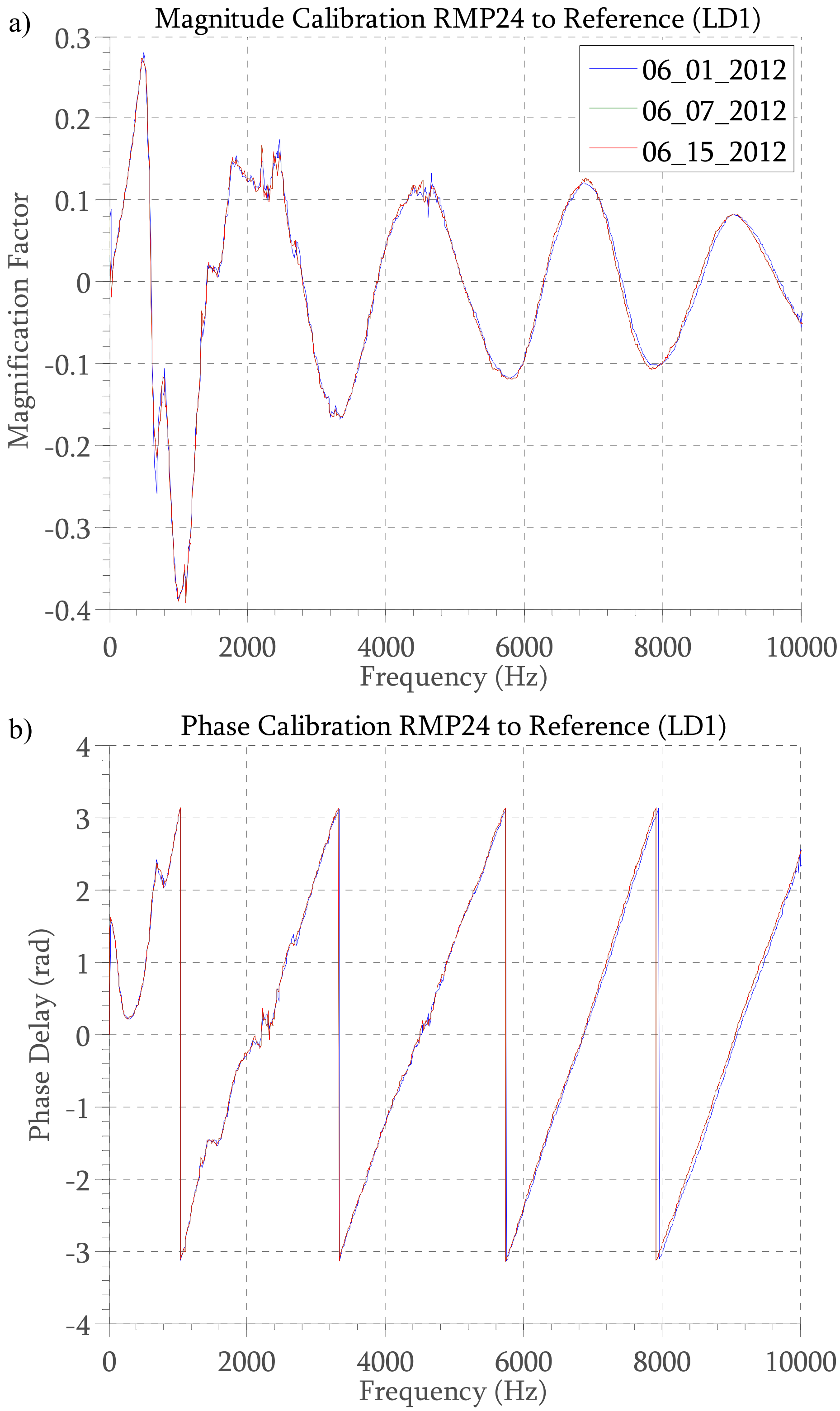

Figure 2.27 Transfer functions for RMP24 using *in situ* method

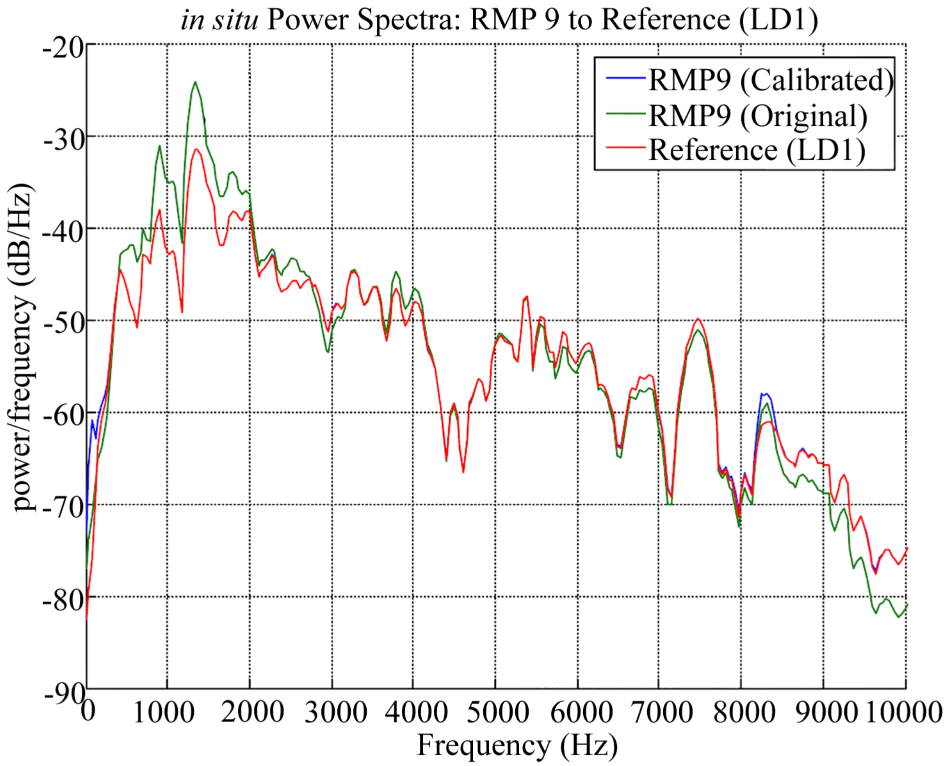

Figure 2.28 Original and calibrated RMP 9 spectra

Figure 2.28 compares the power spectrum of the reference microphone and RMP9, raw/original signal and calibrated signal, using a magnitude and phase transfer function method produced using the *in situ* calibration technique. Agreement between the reference and corrected RMP9 microphone is considered to be excellent.

2.2.3.4 Facility Noise Concerns

Due to the nature of the unsteady pressure measurement sensors, it is important to address radiated far-field acoustic noise produced by the AFRD flow facility. Since the flow-facility (AFRD) in use is non-anechoic, it was expected that vibrations and extraneous noise sources within the facility would pollute surface pressure sensors. In particular, the RMP microphones employed in the present experiment are traditionally used as acoustic sensors and are thus optimized for human sound perception; additionally, the sensors are particularly sensitive to secondary noise phenomena beyond the isolated mechanical wave propagation within the acoustic channel.

It was considered that the hydrodynamic pressures of the boundary layer might be of similar magnitude to the noise sources identified in the AFRD facility. A ground-level Larson-Davis microphone was used to characterize the strength of the ambient noise; the microphone was located within the upper receiver of the AFRD. Typical power spectra of the acoustic pressure (measured by the Larson Davis) and the hydrodynamic pressure (measured by an airfoil surface tap) are shown in Figure 2.29.

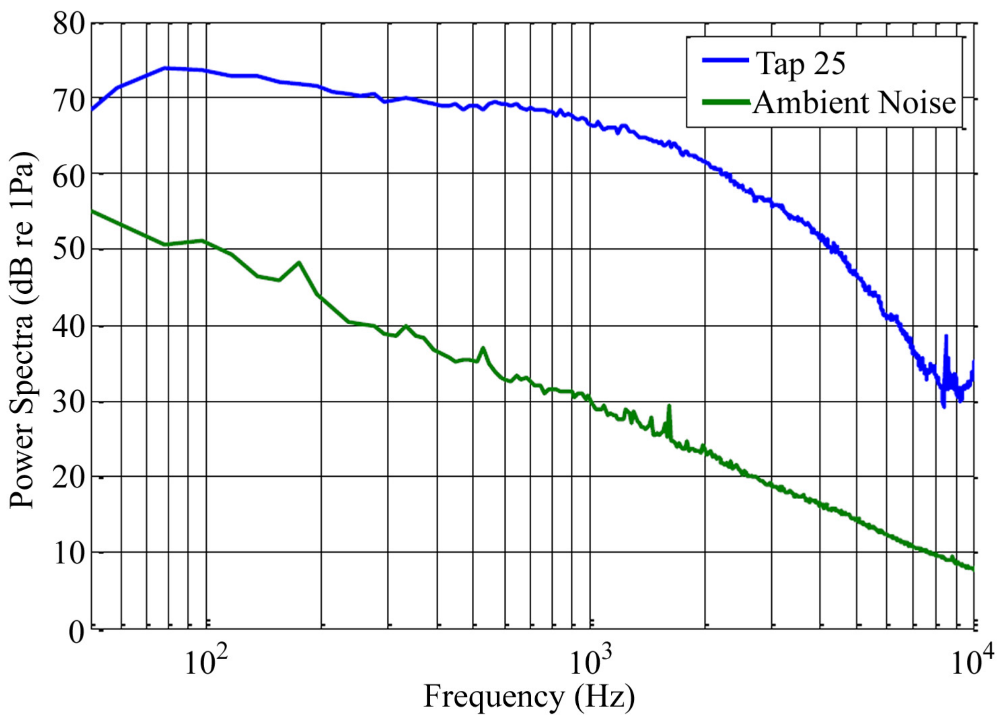

Figure 2.29 AFRD acoustic noise

It can be seen that the hydrodynamic pressure is approximately 100 times more powerful than the acoustic noise produced by the facility. It is well known that hydrodynamic pressures are typically orders of magnitude higher than acoustic pressures - acoustic pressures are a lower intensity, whereas hydrodynamic are higher intensity and local phenomena. This confirms that the microphone sensors are appropriate for accurately measuring the blade hydrodynamic surface pressures in a “noisy” environment; the measured intensity is well above the noise floor.

Additionally, correlated tonal noise between the ground-level ambient microphones and RMPs is attenuated using the Optimal Noise Cancellation (ONC) method suggested and provided by Professor Ahmed Naguib (see Appendix B). The ONC method is another way to ensure the integrity of the collected data in an otherwise noisy environment.

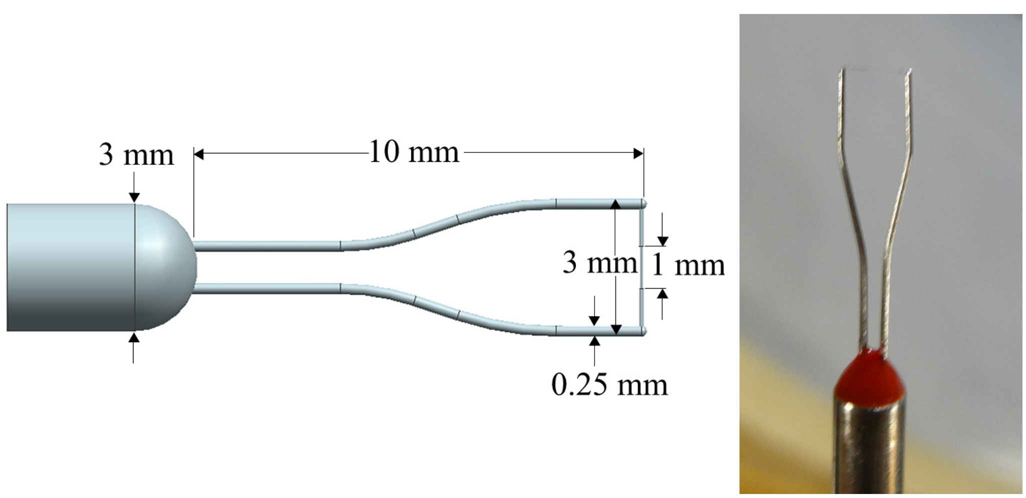

Figure 2.30 Schematic and image of SN hot-wire

2.2.4 Hot-Wire Measurements

Single sensor hot-wire probes (Straight-Normal: SN) were used to measure mean and fluctuating velocity magnitudes in the wake of the RCDB. (Figure 2.30). A special traverse was developed to support the SN probe in the rotating reference frame, enabling the measurement of time-resolved wake data and velocity spectra. TSI 1750 constant-temperature anemometers were used to drive the hot-wire probes. The anemometers were tuned to a typical frequency response greater than 20kHz at a flow velocity of *16m/s*. Post-processing temperature compensation of the hot-wires was accomplished using measurements from onboard thermocouple amplifiers (Analog Devices AD595).

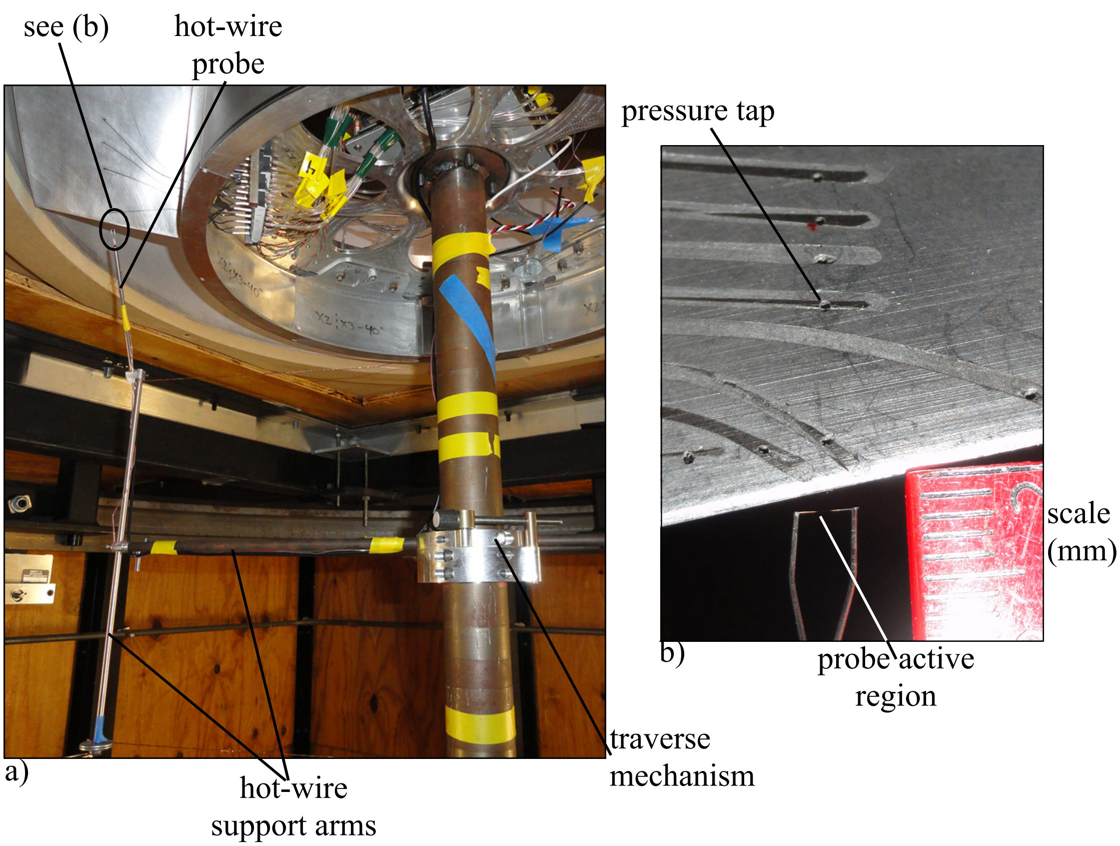

Figure 2.31 Hot-wire traverse
a) Overall view (not pictured: counter balance)
b) Trailing edge hot-wire location

2.2.4.1 Traverse

The “flying” hot-wire rig was designed to position the probe at the midspan of the blade and traverse azimuthally (θ) while maintaining a constant radial position. Limited adjustment exists radially and vertically. The rig was balanced so that it was dynamically stable, minimizing vibrations and flutter as well as maintaining the rotational balance of the entire RCDB assembly. Through a fine lead screw, the rig is capable of traversing with a resolution of $r\Delta\theta = 0.4$ mm at a radius of 303mm. (Figure 2.31).

Hot-wire wake surveys were performed in three r-θ planes downstream of the airfoil at $z = 1mm, 3mm, 8mm$. Each survey had ten azimuthal locations.

2.2.4.2 Probe Construction/Calibration

A custom hot-wire probe was developed specifically for use within the rotating frame. The active region of the tungsten wire sensor (D=5um) was L=1mm. L/D>200 satisfies the condition of a minimized end-conduction over the active region (Champagne et al. 1967). This probe is shown in Figure 2.30. An overheat ratio of 1.6 was used for all measurements.

A hot-wire calibration facility was used to produce a low disturbance and similar magnitude velocity to the expected experimental flow field. Laboratory air is drawn into the calibration facility where the disturbance level is minimized through a layer of filter material before passing through a well-characterized nozzle. The calibration facility is capable of holding a probe at angles of $(\pm 36)^\circ$ from center in 6° increments (SN is calibrated at one angle: 90°). A schematic of the facility is shown in Figure 2.32.

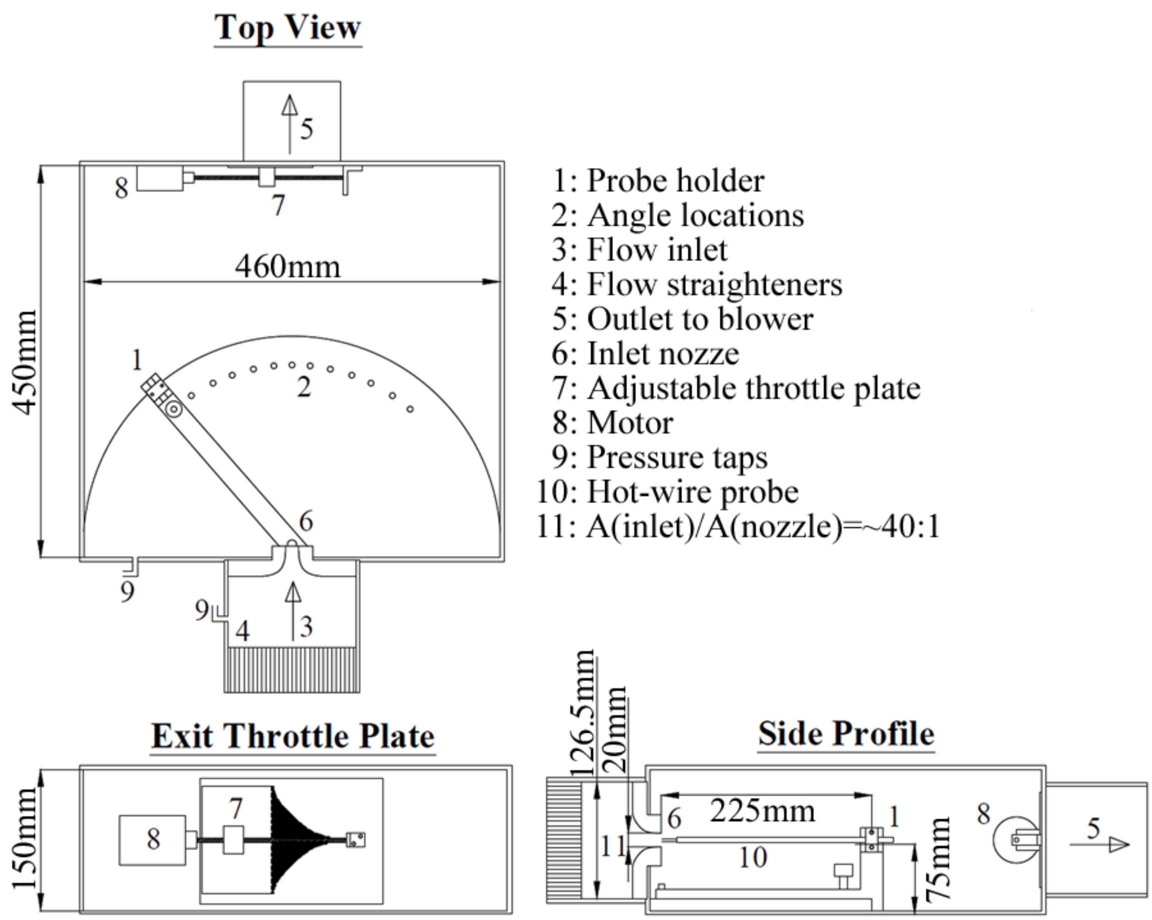

Figure 2.32 Hot-wire calibration unit

The calibration velocity is defined as the "Bernoulli velocity". Velocity is obtained by measuring the static pressure difference across the low disturbance nozzle and calculated following Equation 2.9, where air density ρ was calculated using the ideal gas law.

$$V_{cal} = \sqrt{\frac{2[p_{atm} - p_{cal}]}{\rho}} \qquad \textbf{2.9}$$

The calibration was made across a range of velocities using a "quasi-steady-state" condition where the velocity varies as a function of time but changes slowly enough such that the transients are within the response of the calibration transducers (Hellum 2006). A pre and post-calibration of the hot-wires was performed to identify variances, or drift, that may have occurred during hot-wire data acquisition. The typical drift was within 2% between pre and post-calibration.

It became evident during experiments that there was an inherent time lag between the on-board hot-wire anemometer channels and the rest of the data acquisition channels. The hot-wire was delayed on the order of 3000 time samples, or 0.075 seconds. This is identified to be a phenomenon of the electronics rather than an anomaly of the measured flow field. Hot-wire measurements are corrected for this by identifying the distance between the trailing edge and the hot-wire and subtracting the time-lag using a known wake velocity and convection velocity from the trailing edge pressure taps.

2.3 Experimental Parameters/Procedure

2.3.1 Experimental Operating Conditions

As previously discussed, the primary operating point (see Figure 2.33) was established to match the loading conditions of the experimental work performed by Moreau and Roger (2005). This target primary condition is defined by an incident velocity of 16m/s and a geometric angle of attack of 8°. Note that all stationary CD results presented in this report correspond to this operating condition.

In order to evaluate the behavior of the rotating CD blade, a new operating condition was defined that maintained similar features to the stationary blade. However, due to the complexities of the flow geometry and intricacies with casting a stationary 2D airfoil to a rotating reference frame, the experimental flow field of the RCDB is not identical to that of the CD blade.

Calculating the actual operating condition is limited by how well the angle of the twisted rotating blade can be identified (this was computed using CAD drawings) and how well the components of the inlet velocity triangle can be computed (angular and axial velocity). Presently, the angular velocity is fixed to a specific RPM for a given operating condition and the axial velocity is varied to match the target flow condition (angle and magnitude of the incident velocity). The axial velocity is varied by throttling the main blower in the AFRD facility; a Pitot tube measures the axial velocity just upstream of the fan to ensure the correct operating point is met.

Two operating points were established for the RCDB study: Case 1 and Case 2. Case 1 corresponds to a near-identical inlet condition to the CD blade with an incident velocity of 16.25m/s, a geometric angle of attack of 8°, and a mass flow-rate of *2.305kg/s* See Figure 2.33 for a schematic of the geometry and Figure 2.35 for details of the inlet velocity triangle. Note that the velocity is within 2% of the stationary experiment flow field.

The second operating condition (Case 2) is defined by an incident velocity of 16.4m/s, a geometric angle of attack of 15°, and a mass flow-rate of *1.799kg/s*. This operating condition was targeted to match an alternate flow field used in Moreau and Roger (2005). For purposes of this report, Case 2 represents an “off-design” condition; the “off-design” flow field provides an additional parameter to identify details of the RCDB boundary layer, specifically, new separation/reattachment regimes and different statistical behaviors. See Figure 2.34 for a schematic of the geometry and Figure 2.35 for details of the inlet velocity triangle.

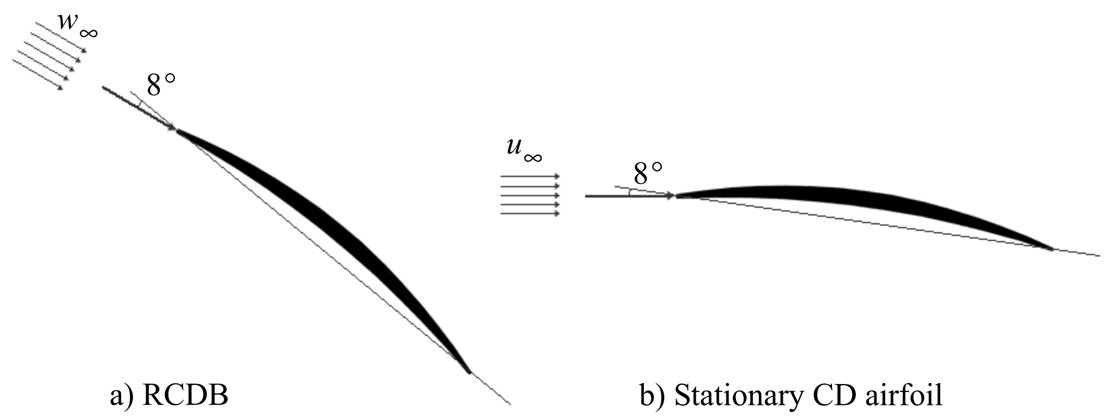

Figure 2.33 Flow geometry Case 1

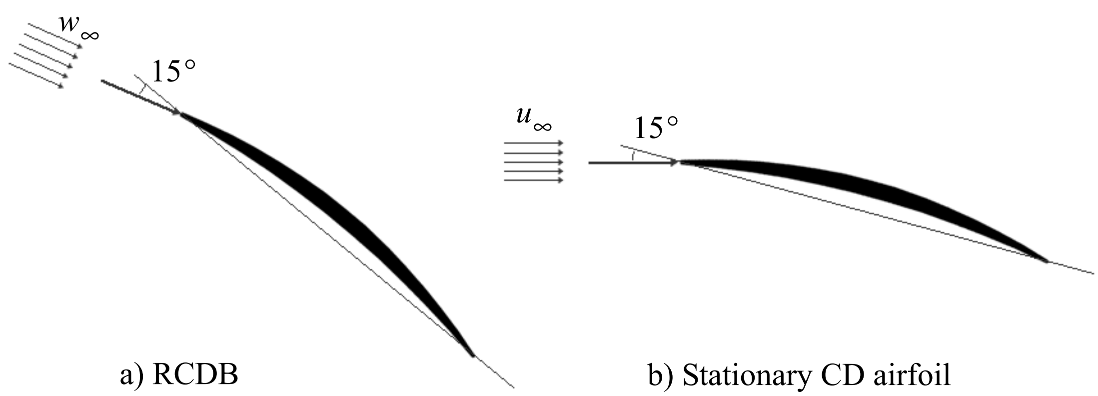

Figure 2.34 Flow geometry Case 2

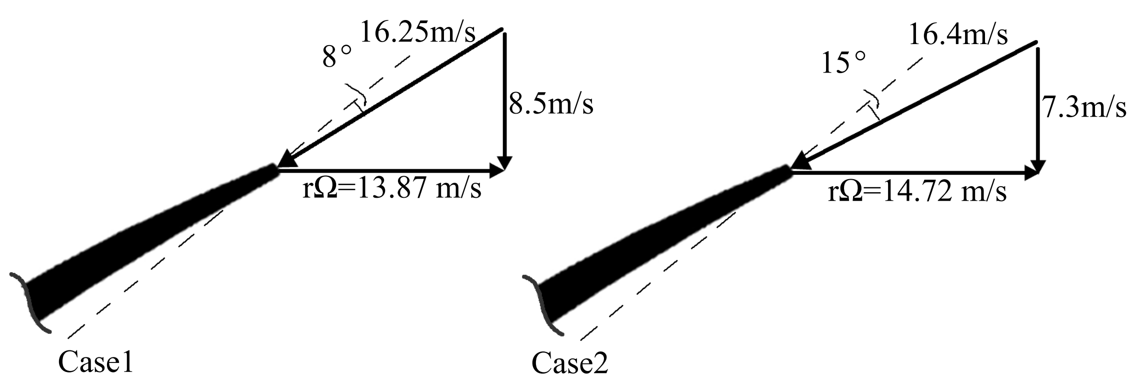

Figure 2.35 Flow geometry velocity triangles (Case 1 and Case 2)

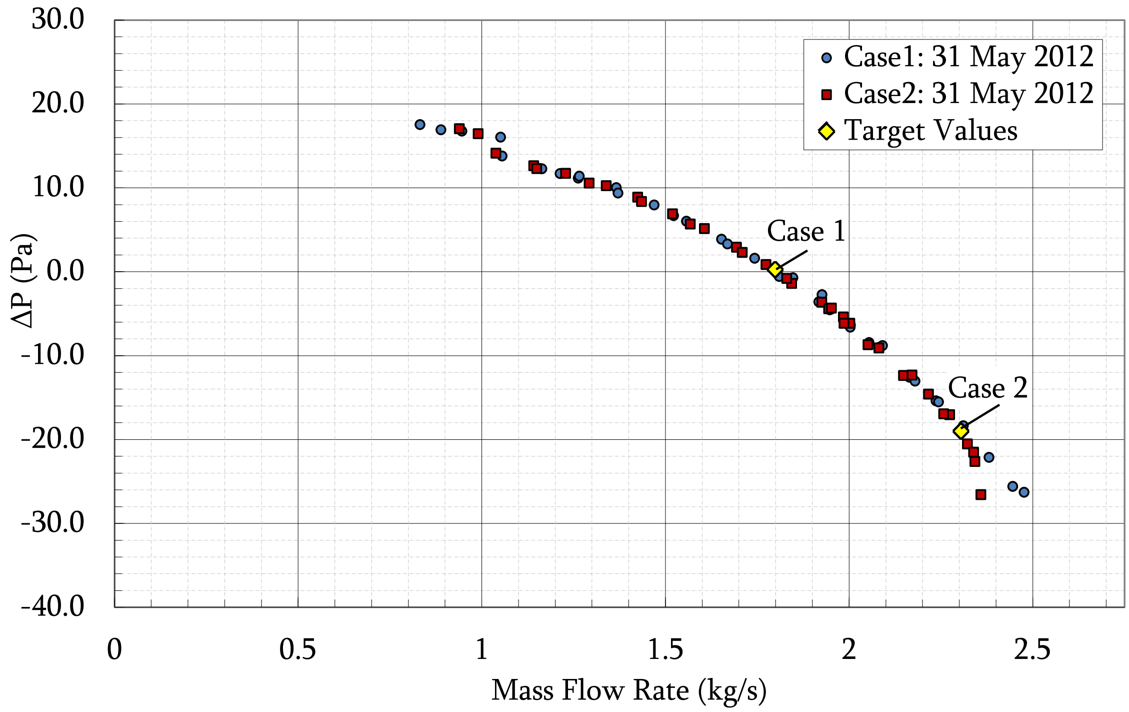

Figure 2.36 Performance curves for RCDB Case 1 and Case 2

Fan performance curves were derived experimentally to identify the associated pressure drop from the atmosphere to the upper receiver for a given flow rate, establishing facility parameters to match the operating conditions of the CD experiment. Figure 2.36 shows the performance curves for both fan conditions. The operating point of the AFRD facility is inferred from the known mass flow rate across the fan. The target operating point is marked on each curve. Each case has a unique RPM condition.

2.3.2 Data Acquisition

As mentioned previously, the rotating A/D board is clocked and triggered from the stationary A/D board. This ensures accurate and simultaneous data acquisition. The system samples at 40000Hz for 30 seconds, which is long enough to converge higher-order statistics. Due to the unsteady nature and sensitive operating point of the fan, a series of data files are taken for a particular target operating point where the main blower is throttled through various flow conditions. During post-processing, the file with the calculated operating conditions nearest to the target is selected for further post-processing.

2.4 Stationary Experiments

All data presented by Höwer from stationary experiments follow with similar procedures and equipment. Höwer performed his experiments in parallel to the RCDB experiment. Further procedures are well discussed in Höwer's Masters Thesis (2012).

In addition to stationary experimental data from Höwer, Moreau was kind enough to forward CD airfoil data from 2005. See Moreau and Roger (2005) for further reading.

3.0 Experimental Results and Discussion

This section focuses on identifying and describing the nature of the convecting pressure patterns along the airfoil surface as well as calculating and presenting the usefulness of parameters of interest to the aeroacoustic noise prediction community. For purposes of this report, it is useful to first recognize specific flow regimes associated with the airfoil boundary layer - identified by Moreau and Roger (2005) and Neal (2010). These are (for the suction side):

- Leading edge separation - identified as the region at the leading edge where the boundary layer separates from the surface. It is characterized by a very low pressure coefficient. Estimated to occur between x/c=0 and x/c=0.1.
- Reattachment - the region following the separated zone where the boundary layer transitions and reattaches as a turbulent boundary layer. Estimated to occur between x/c=0.05 and x/c=0.15.
- Mid-chord - the region where pressure increases (an effect of airfoil shape) and the turbulent boundary layer thickens as in an adverse pressure gradient flat plate boundary layer. Estimated to occur between x/c=0.2 and x/c=0.8.
- Trailing edge - the aft region of the airfoil where the boundary layer is similar to a well developed flat-plate boundary layer.
- Trailing edge (spanwise) - This region consists of 4 spanwise distributed taps at x/c=0.98. The region is an extension of the trailing edge region with the added purpose to investigate radial effects. Estimated to occur between x/c=0.8 and x/c=1.0.

The pressure side:

- The pressure side of the airfoil is treated as one region since the flow has laminar characteristics at and between the measurement locations. This "viscous dominated region" is distinguished with a quiescent pressure field. The last tap (Tap 29 x/c=0.93) begins to show evidence of a trailing-edge interaction.

With the lack of full-field data and the inherent unsteadiness of the geometry/flow field, it is difficult to identify the exact locations of the aforementioned regions. As mentioned previously, the exploration and quantification of the boundary layer properties necessitate the need for surface embedded steady and unsteady pressure transducers.

It is clear from known C_p data that there exist discrete flow regions along the airfoil - these can be further identified and studied through the application of mean and fluctuating surface pressure measurements. The following methods and techniques quantify the flow regions along the airfoil surface.

3.1 Pressure Coefficient

It is useful to first consider the mean pressure quantities on the fan blade. The blade loading is expressed in the form of a pressure coefficient (C_p), of which the integral will yield a non-dimensional lift coefficient. As discussed in Section 2.1, the pressure coefficient profile is critical for matching the blade loading conditions between the rotating and stationary Controlled Diffusion experiments.

Figure 3.1 shows the C_p distribution between the rotating and stationary experiments for the Case 1 operating condition. It can be seen that the general shape of the curves match well, but there is lower lift on the pressure side of the rotating airfoil. The non-dimensional lift coefficient, following Equation 3.1, yields 0.83 and 0.74 for the stationary and rotating blades respectively.

$$C_l = \int_0^1 (C_{p,\,lower} - C_{p,\,upper}) d\frac{x}{c} \qquad \textbf{3.1}$$

There is more total lift produced by the stationary blade, mostly from additional contributions from the pressure side. Note that there is an inherent unsteadiness in the leading-edge laminar separation and turbulent reattachment region; it was expected to see a strong difference between the two cases. As discussed previously, Figure 3.1 confirms similar operating conditions between the rotating and stationary experiments.

Figure 3.2 shows a comparison of the C_p distribution between Case 1 and Case 2 operating conditions of the RCDB. It is clear from the pressure distribution that the two cases have distinctly different flow conditions. The blade in Case 2 is more highly loaded as is evident from the integral (Equation 3.1) of the profile: 1.0 for Case 2 versus 0.74 for Case 1. There exists a higher magnitude pressure at the leading edge (x/c<0.2), but less pressure building across the midspan (0.2<x/c<0.8) of the blade for Case 2. The C_p distribution of RCDB Case 2 does not follow the characteristic curvature of the CD blade as the stationary and RCDB Case 1 does, this suggests that there exists a very thick boundary layer or a separation condition is occurring across the suction side of the Case 2 blade. While the RCDB Case 2 blade is more highly loaded, it is speculated from the distribution that a full or partial stall may be occurring. It is evident that the pressure side of the airfoil contributes more significantly to the integral loading of the blade. Note that the pressure coefficient along the trailing edge of the suction side of the blade is similar for each case.

It is clear the mean pressure profiles do not adequately describe the details of the near-wall pressure field. Further similarities and differences of the wall pressure field between the rotating and stationary CD blades are explored further through the measurement of the local fluctuating pressures.

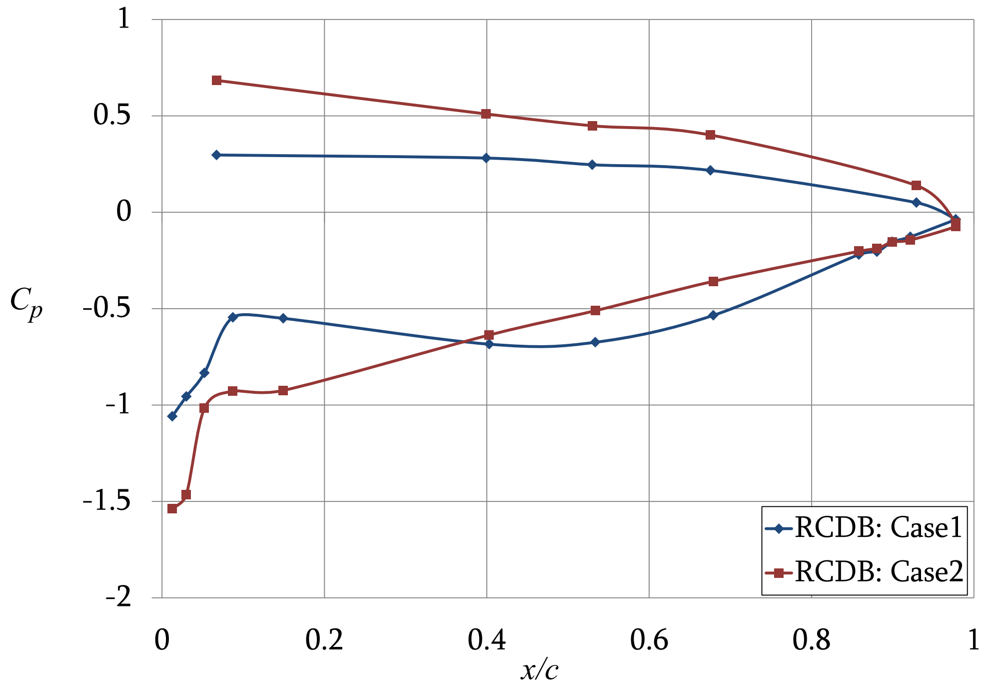

Figure 3.1 C_p distribution CD and RCDB Case 1

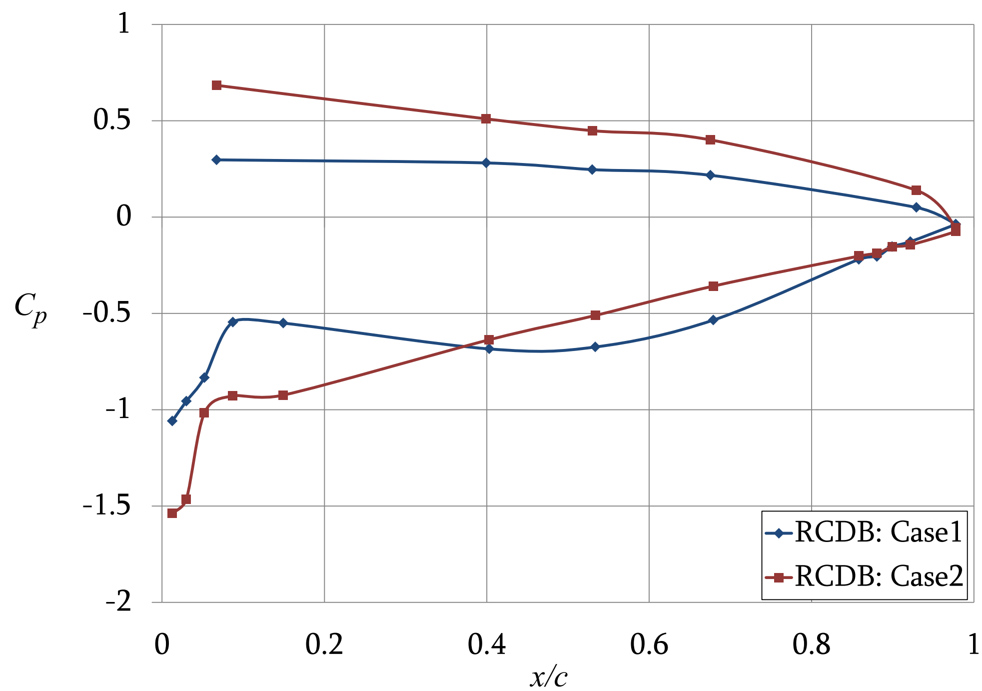

Figure 3.2 C_p distribution RCDB Case 1 and Case 2

3.2 Statistics

Mean pressure quantities do not adequately identify and characterize the details of the near-wall region pressure field. High speed - fast response - microphone transducer measurements are particularly well suited for quantifying some aspects of the boundary layer near to the airfoil surface by measuring the fluctuating pressures.

Regions of quiescence and regions of disorder are visibly identifiable along the airfoil surface from time-series data. Figure 3.3 shows a sample collection of time-series data for several locations on the blade surface. It is seen that taps in the leading edge region (Figure 3.3a) of the blade have stronger fluctuations than those in other regions. The separation region (Figure 3.3b) shows high magnitude fluctuations with rather large structures (evident by the intermittency and long time delay between peaks/valleys in the time-series). As the flow reattaches and transitions to a turbulent boundary layer ($x/c=0.1$), the flow maintains the larger structures and intermittency while evolving to include high frequency, intense fluctuations. The separation/reattachment region shows the strongest fluctuations on the blade surface. The fluctuations decay farther downstream and become more regular. The mid-chord region (Figure 3.3c) shows evidence of sporadic low frequency structures and evolve into a more uniform signal downstream near the trailing edge (Figure 3.3d). These are characterized by high frequency, low magnitude fluctuations. The pressure side mid-chord (Figure 3.3e) time-series is typical of all the measurement locations on that side of the blade; as suggested by Moreau and Roger (2005), the low magnitude and rolling signal is indicative of a viscous dominated boundary layer with minimal disturbances.

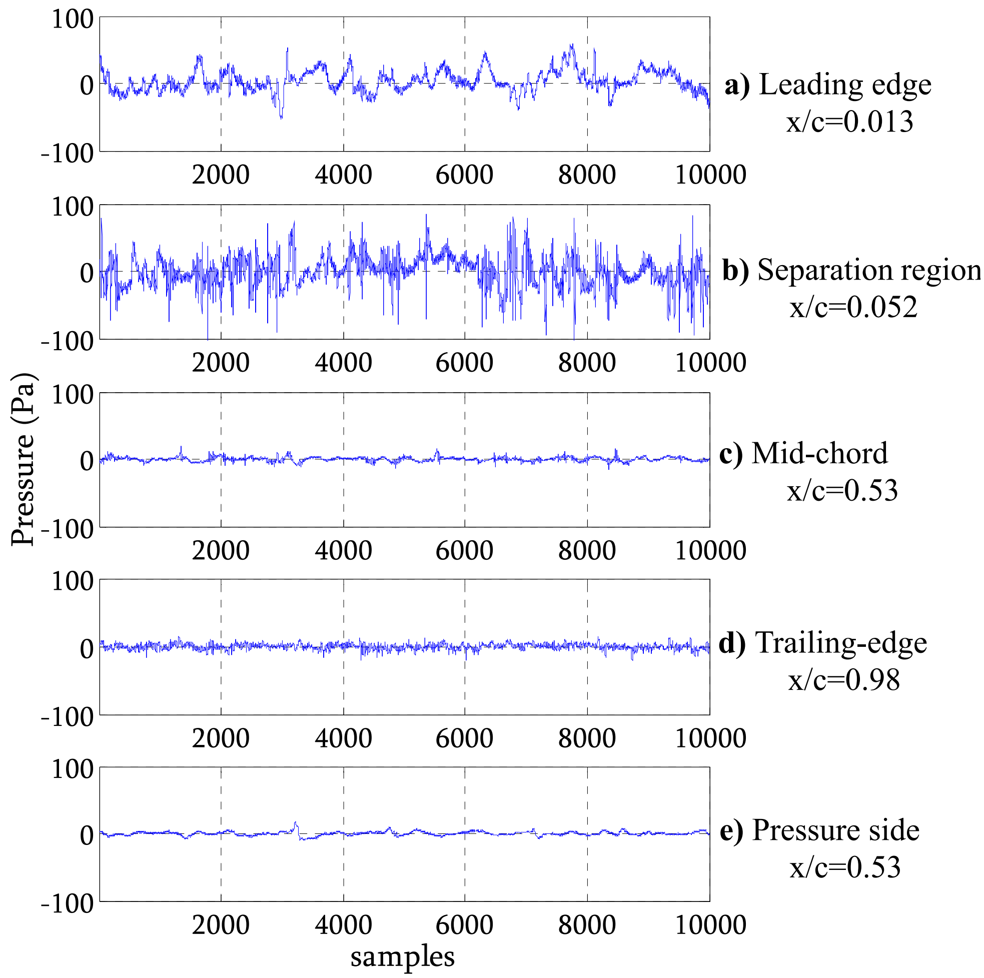

Figure 3.3 Sample time series RCDB Case 1

The collected unsteady pressure data are assumed to represent a continuous random variable. The probability density function (PDF)[1] supports further conclusions from the pressure field. The probability density functions represent the statistical likelihood of a random variable to take on a particular value; the PDF for a particular pressure tap reflects the statistical description of the wall pressure field. Several statistical quantities can be

1. It is recognized that the histograms of this thesis may not be fully converged as are required to fully justify the use of the term: probability density function. The latter is used for convenience with the adequate argument that the distributions are relatively smooth.

calculated from the PDF and used to infer and support conclusions on the condition of the flow field above the airfoil surface.

The PDF of the fluctuating pressure signal visually demonstrates the statistical distribution. Generally, a narrow PDF is indicative of a viscous dominated boundary layer. A wide PDF suggests the presence of a turbulent boundary later. There are varying degrees of distributions.

Figure 3.4 and Figure 3.5 show the PDFs of the suction side pressure taps for RCDB and CD Case 1. It is seen that the CD airfoil generally has a more narrow distribution across the entirety of the airfoil. The magnitude and narrowness of the leading-edge PDFs, Taps 1 and 2 (Figure 3.4a and Figure 3.4b), suggest a strong viscous dominated region. The PDF distributions are typically dissimilar between the RCDB and CD blades except the trailing edge spanwise region (Figure 3.6), where the acoustic production is significant (as discussed in Section 1.3). The pressure side PDFs (Figure 3.7) show the high peakedness of the pressure signal, particularly with the CD airfoil. The inconsistency with CD Tap 29 (Figure 3.7e) is attributed to a non-physical corruption of the microphone data.

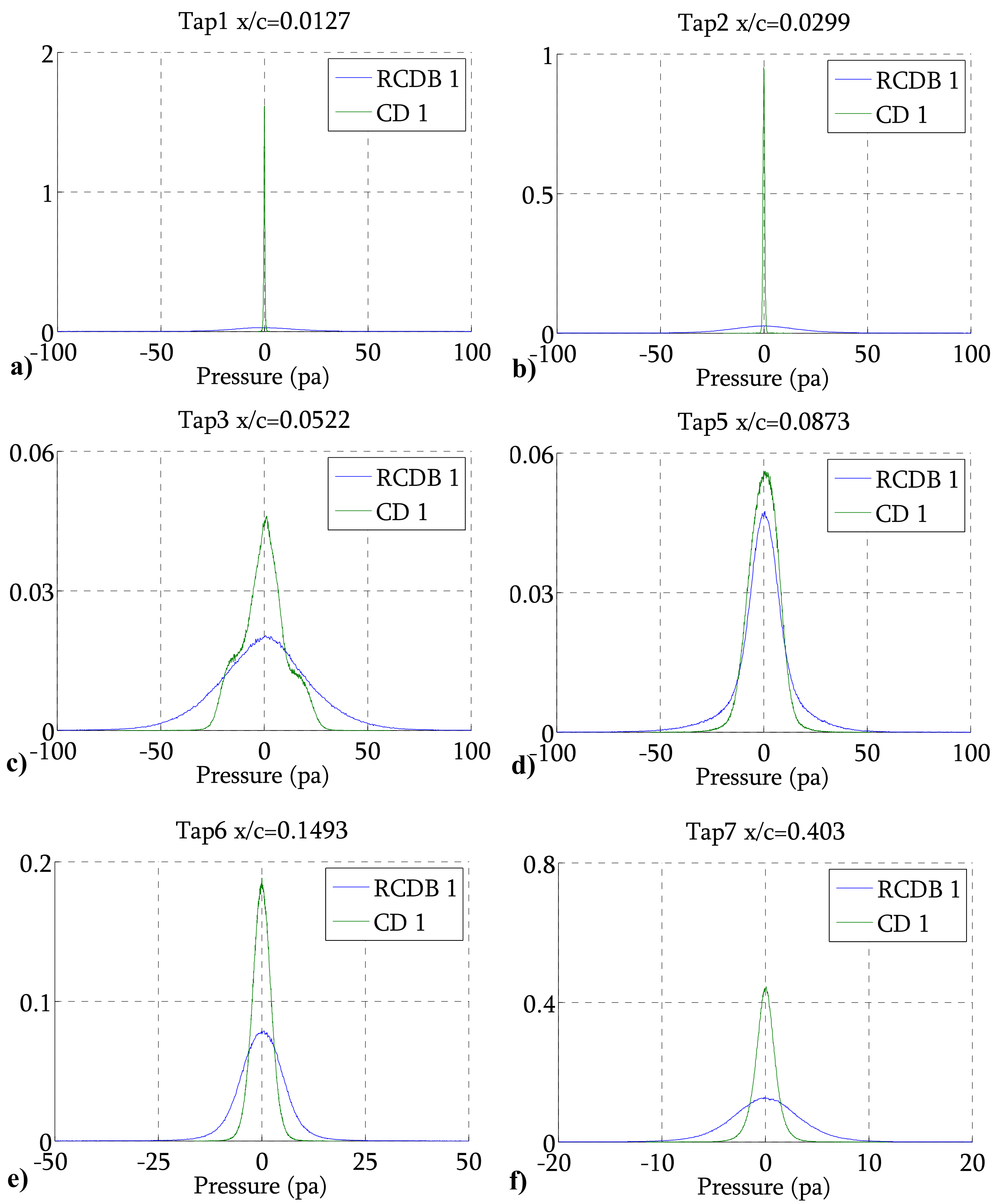

Figure 3.4 RCDB-CD Case 1 suction side PDFs

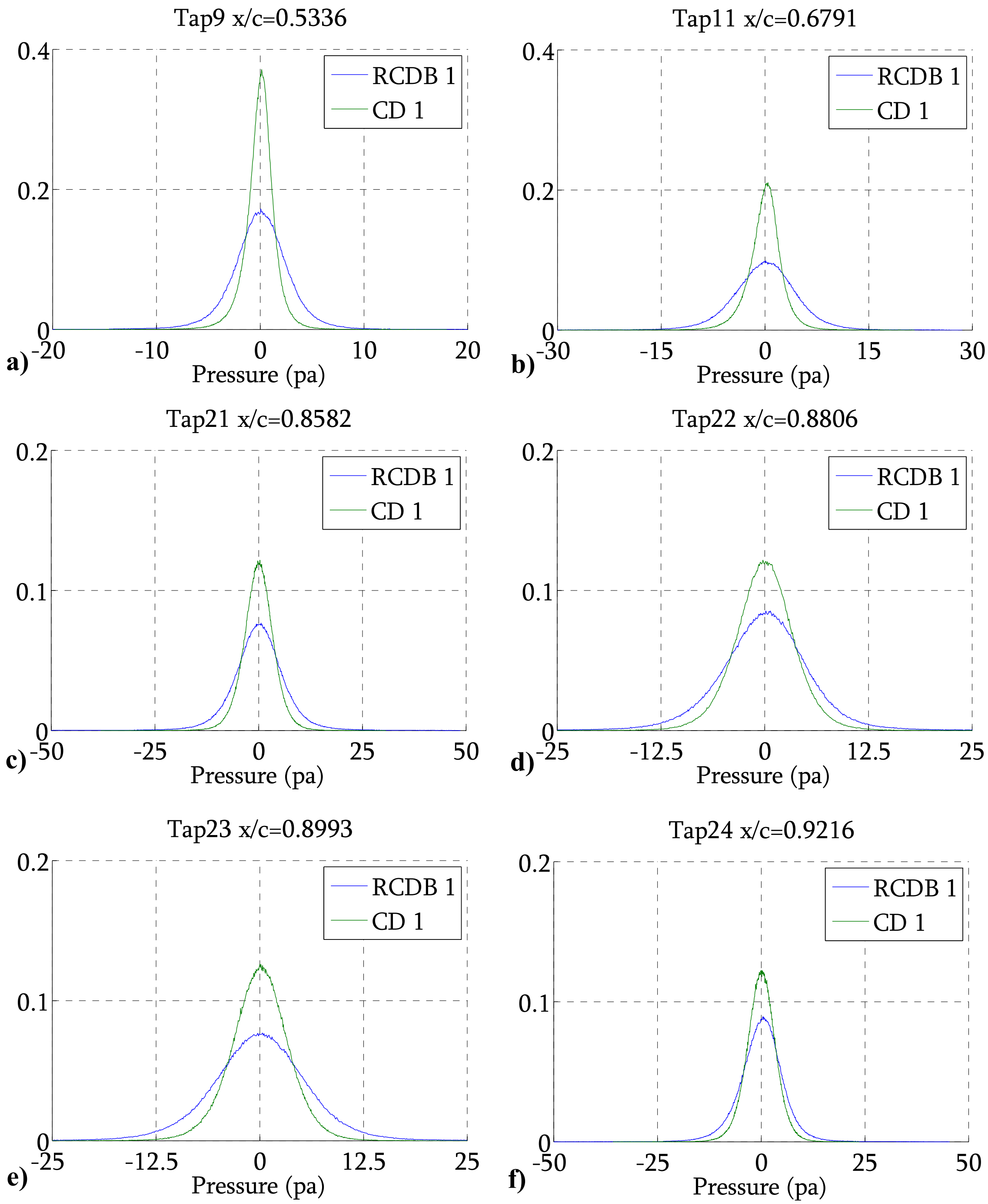

Figure 3.5 RCDB-CD Case 1 suction side PDFs continued

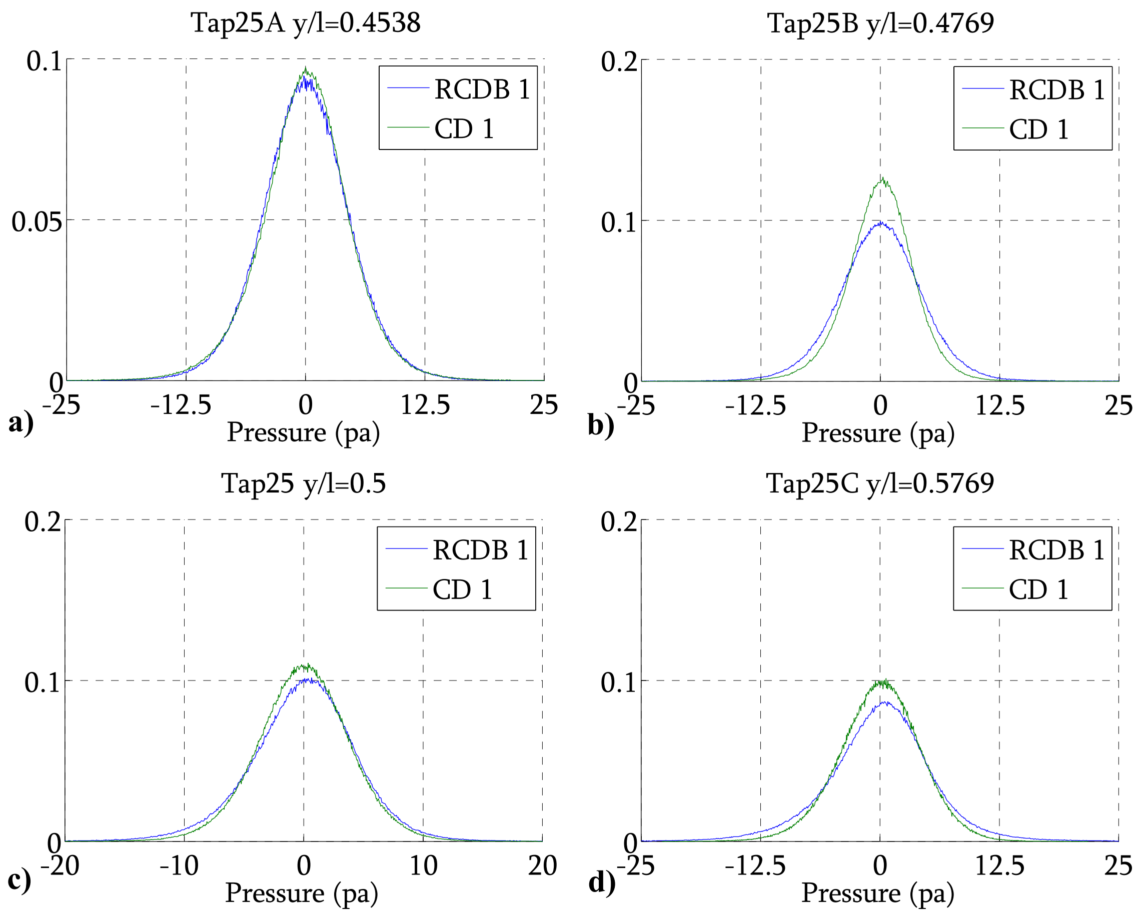

Figure 3.6 RCDB-CD Case 1 trailing edge spanwise PDFs

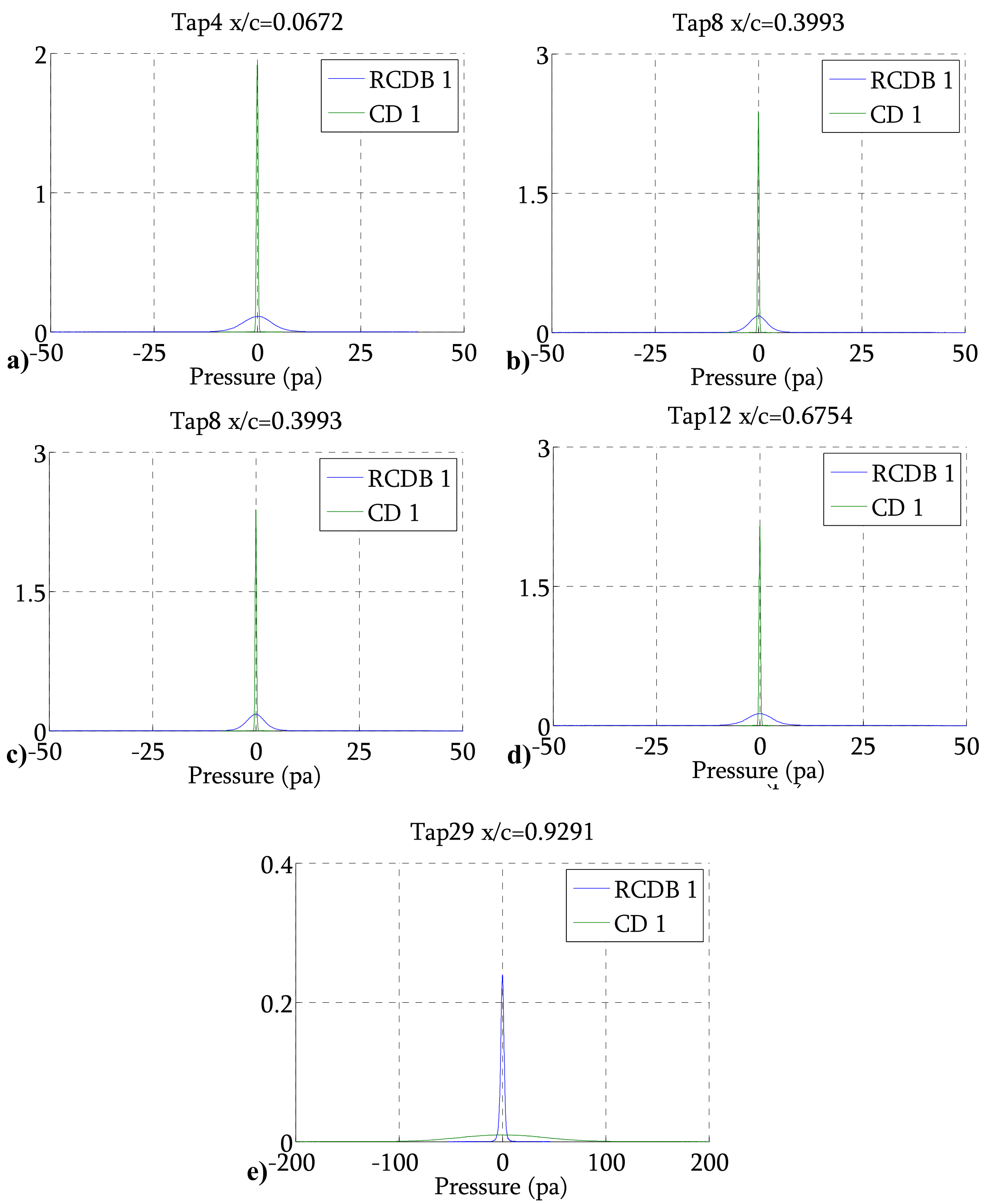

Figure 3.7 RCDB-CD Case 1 pressure side PDFs

Figure 3.8 and Figure 3.9 show the suction side PDFs of RCDB Case 1 and Case 2. From these distributions, it is clear that there are similarities and differences for the design point flow field and the off-design flow field. Most notably, there are wider PDF distributions for the off-design condition for most of the airfoil surface - this suggests a more energetic wall pressure field for the RCDB Case 2 flow field. Following stationary CD boundary layer survey results from Neal (2010), the more energetic wall pressure fluctuations of the RCDB Case 2 are inferred to be indicative of a more turbulent boundary layer. Additionally, the PDFs for the leading edge taps are skewed positively for the off-design condition - there is a higher tendency for negative pressures. Considering the trailing edge spanwise and pressure side PDFs (Figure 3.10 and Figure 3.11) the similar conclusion holds: the design-point condition (Case 1) is characterized by a more stable boundary layer with fewer fluctuations than the off-design condition.

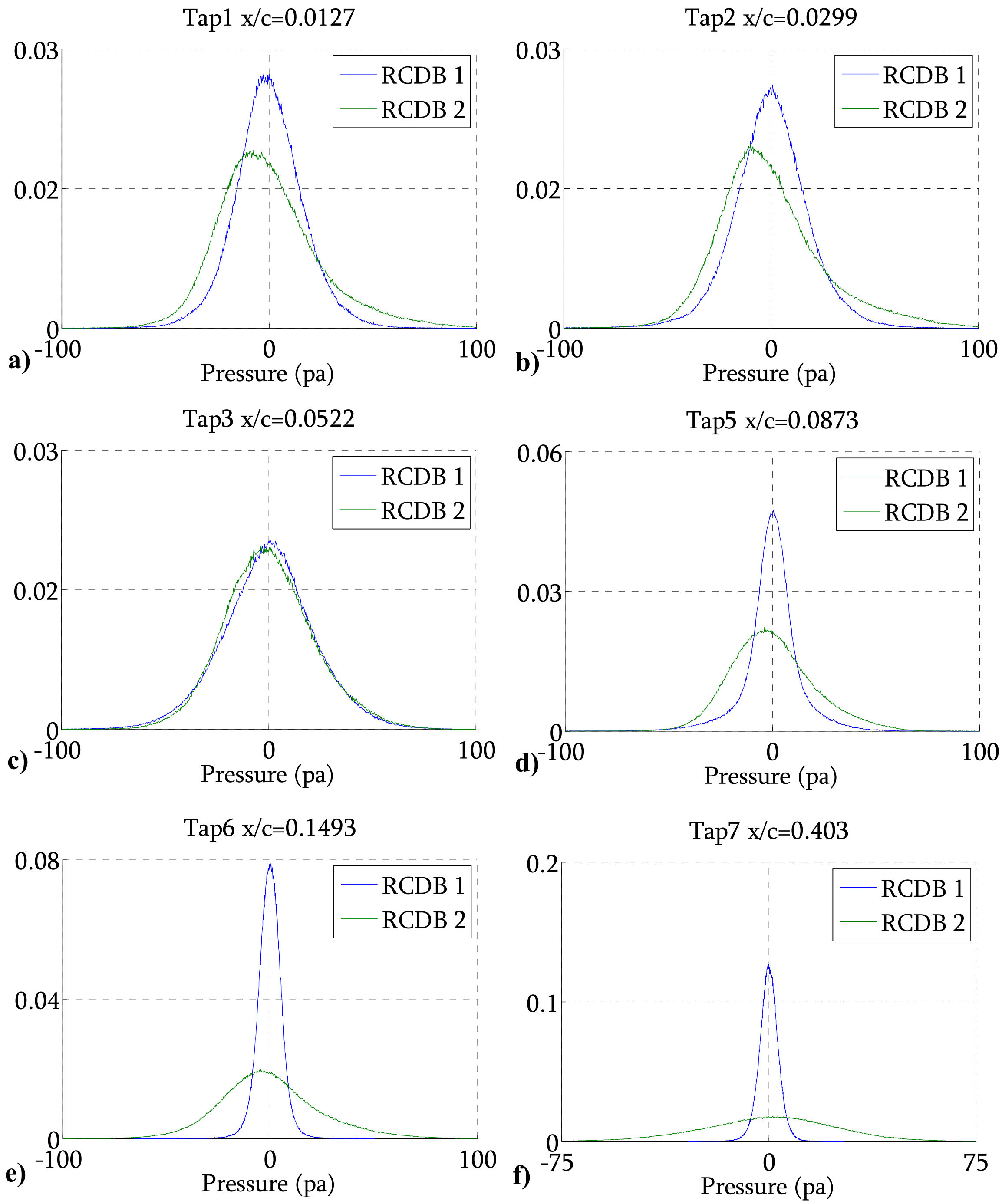

Figure 3.8 RCDB Case1-Case2 suction side PDFs

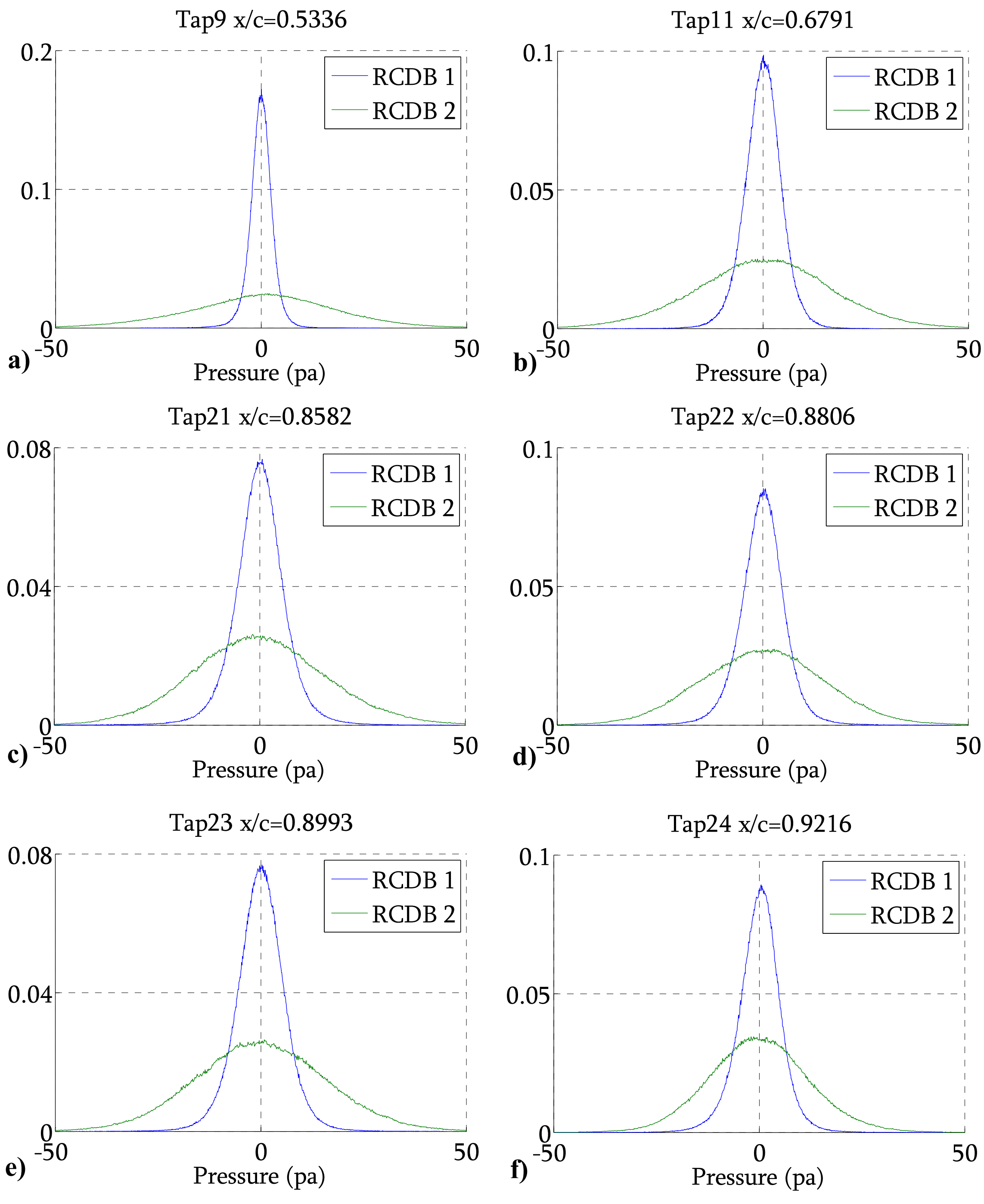

Figure 3.9 RCDB Case1-Case2 suction side PDFs continued

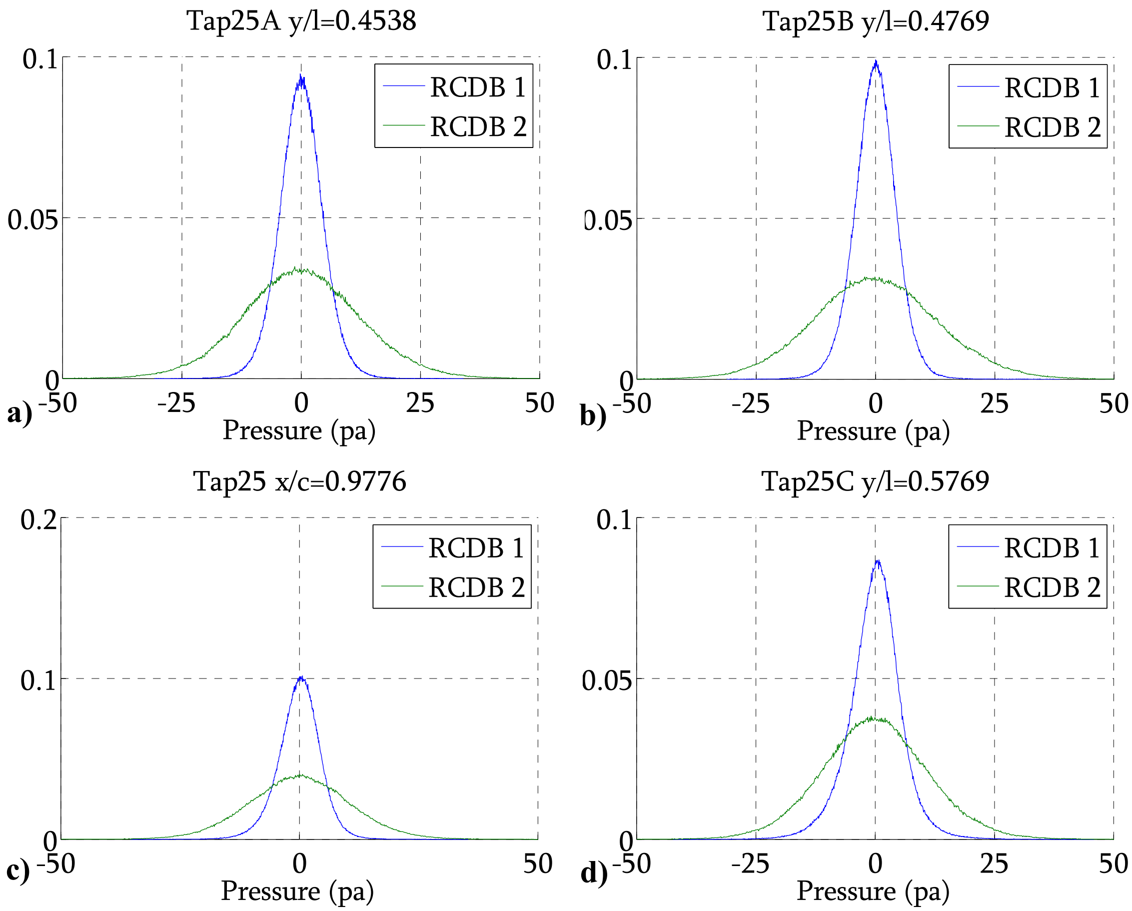

Figure 3.10 RCDB Case1-Case2 trailing edge spanwise PDFs

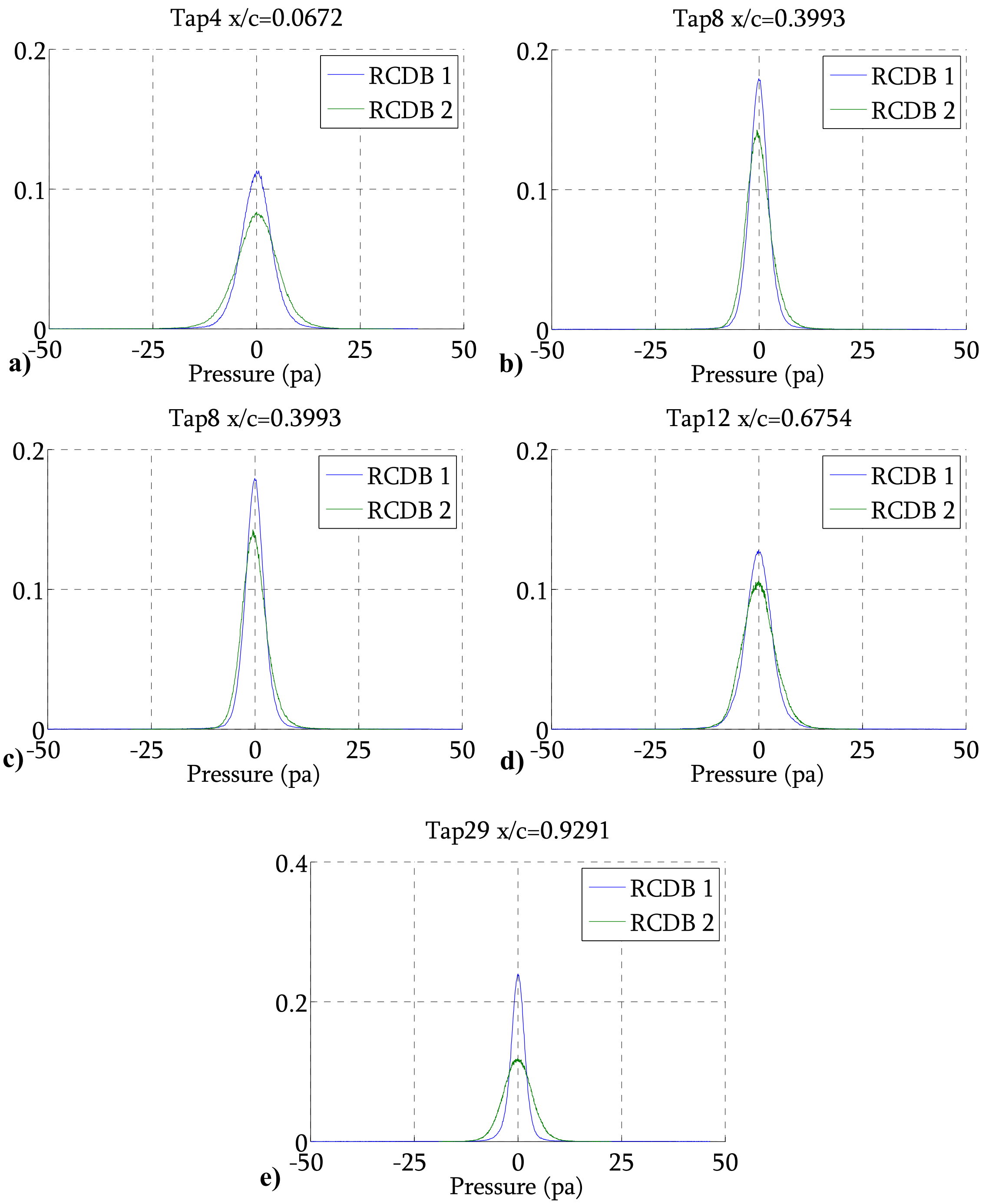

Figure 3.11 RCDB Case1-Case2 pressure side PDFs

In order to quantify time series data with standard statistical representations, the method of moments is applied to the unsteady pressure data to identify the parameters: mean, variance, skewness, and kurtosis (1st through 4th statistical moments - see Section 1.4). These statistical quantities numerically quantify the distribution of the PDF. The mean pressure is measured by the onboard pressure MEMS transducers where higher order statistics are calculated from the unsteady microphone measurements (note that the microphones only measure fluctuating pressures - i.e., the mean of microphone data is zero). The variance, 2nd moment, represents the width, or spread, of the fluctuating pressure amplitude. Skewness, the 3rd moment, indicates the bias of the pressure pattern - whether the fluctuations are biased positively or negatively. A skewed distribution often results if the variable is bounded on the high end (skewness is positive) or the low end (skewness is negative) of the mean. Kurtosis, the 4th moment, is commonly known as 'peakedness' - an expression of how peaked or flat the distribution is. A Gaussian distribution has a flatness of 3.0 (Bendat and Piersol 1986). This allows for a simple comparison to a Gaussian distribution.[1]

Figure 3.12 shows the 1st through 4th moments of the RCDB and CD Case 1 suction side. The agreement in the 1st moment (Figure 3.12a) C_p has been demonstrated previously, but it is worth comparing alongside higher moments for further understanding of the flow regimes. The suction side of the airfoil is characterized by a leading edge boundary layer transition. The separation and reattachment of the boundary layer ($0<x/c<0.15$) causes significant unsteadiness in the pressure field; the variance is high and the skewness

1. Note that the connecting lines in the following figures (Figure 3.12 to Figure 3.17) do not imply trends. The lines exist purely to identify and connect data points from adjacent measurement locations.

and kurtosis do not show a trend in the streamwise direction. Variance is highest at x/c=0.05, the expected peak of the separated region. The flow reattaches downstream (x/c>0.15), characterized by a decrease in the magnitude of C_p and variance as well as an increase in the relative spatial uniformity of higher order statistics from 0.15<x/c<1. Following separation, the mid-chord flow statistics remain relatively constant - supporting the Moreau and Roger (2005) idea of a boundary layer region analogous to an adverse pressure gradient flat-plate boundary layer. The trailing edge also exhibits similarly uniform streamwise statistics.

Figure 3.13 compares the moments for RCDB Case 1 and Case 2. The statistics of the off-design point suggest that there exists an energetic pressure field aft of the typical reattachment region (x/c=0.15). The variance (Figure 3.13b) is high across the entire surface, supporting the claim that the boundary layer is more energetic in Case 2 than Case 1. The off-design flow field shows a strong positive skewness (Figure 3.13c) near the leading edge of the airfoil (x/c<0.15). The skewness is generally higher across the suction side of RCDB Case 2 compared to RCDB Case 1. It is noteworthy to mention that the 4th moment is uniform across the majority of the airfoil surface while the other lower-order moments tend to vary more.

Figure 3.14 and Figure 3.15 show the pressure side statistics for RCDB-CD Case 1 and RCDB Case 1-Case 2, respectively. The pressure side has been characterized by a predominantly viscous dominated boundary layer. This is supported by the general consistency and low magnitudes for the 1st, 2nd, and 3rd moments. The lower order moments of Figure 3.14 show spatial homogeneity within their respective flow fields and show similar magnitudes and trends between the two flow fields for x/c<0.7. The high magnitude of the

4th moment in RCDB Case 1 is recognized but the interpretation is subject to uncertainty. It is noteworthy to mention the similarity of the pressure side moments between Case1 and Case 2 (Figure 3.15) compared to the differences shown in Figure 3.13. This suggests that the RCDB Case 2 flow field has a similar viscous dominated boundary layer.

It has been demonstrated previously (Neal 2010) that the stationary and rotating CD airfoils have minimal spanwise velocity components; therefore, it is expected that the stationary and rotating CD airfoils will have constant statistics in the spanwise direction. A comparison of the RCDB and CD Case 1 spanwise moments (Figure 3.16) show similar statistical properties. The moments show limited spatial variation along the span of each blade and the similar magnitudes demonstrate good agreement between the rotating and stationary blades. Additionally, a comparison of Case 1 and Case 2 spanwise statistics (Figure 3.17) demonstrates a similar consistency in the spatial variation of each flow field, but agreement between Case 1 and Case 2 statistics is poor. The relative spatial homogeneity of the spanwise boundary layer moments show that the wall pressure field fluctuations are not a strong function of local radial position; the flow field across the surface is fairly uniform in the radial direction.

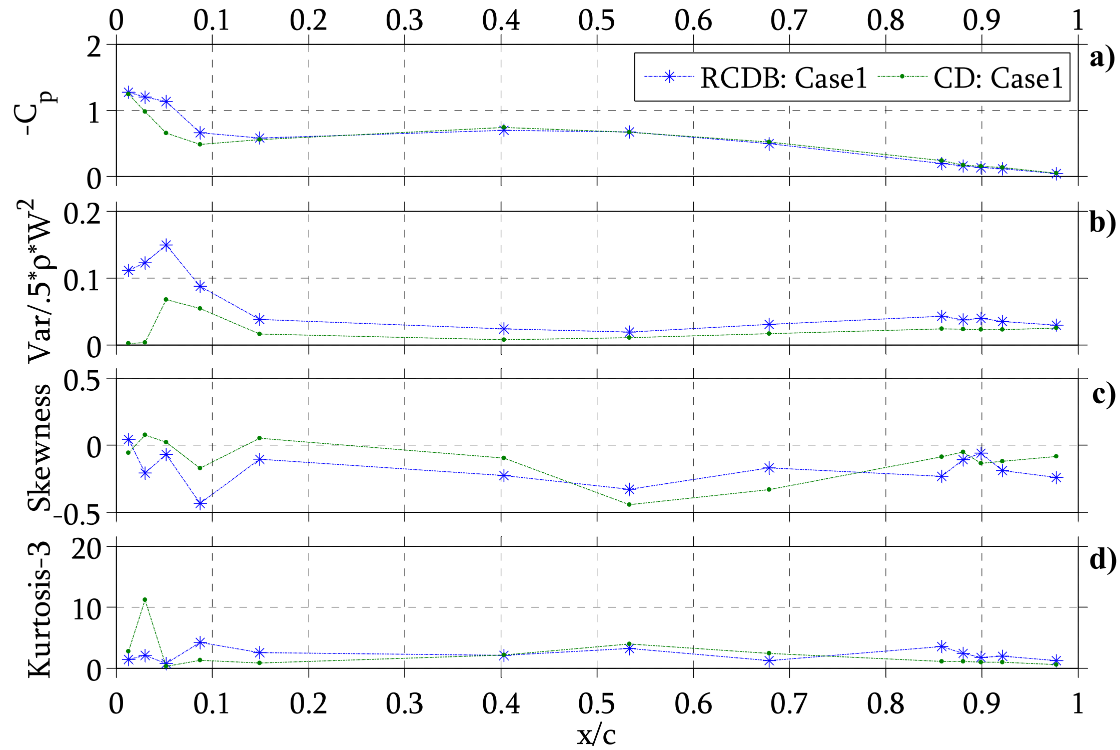

Figure 3.12 RCDB-CD Case 1 suction side moments

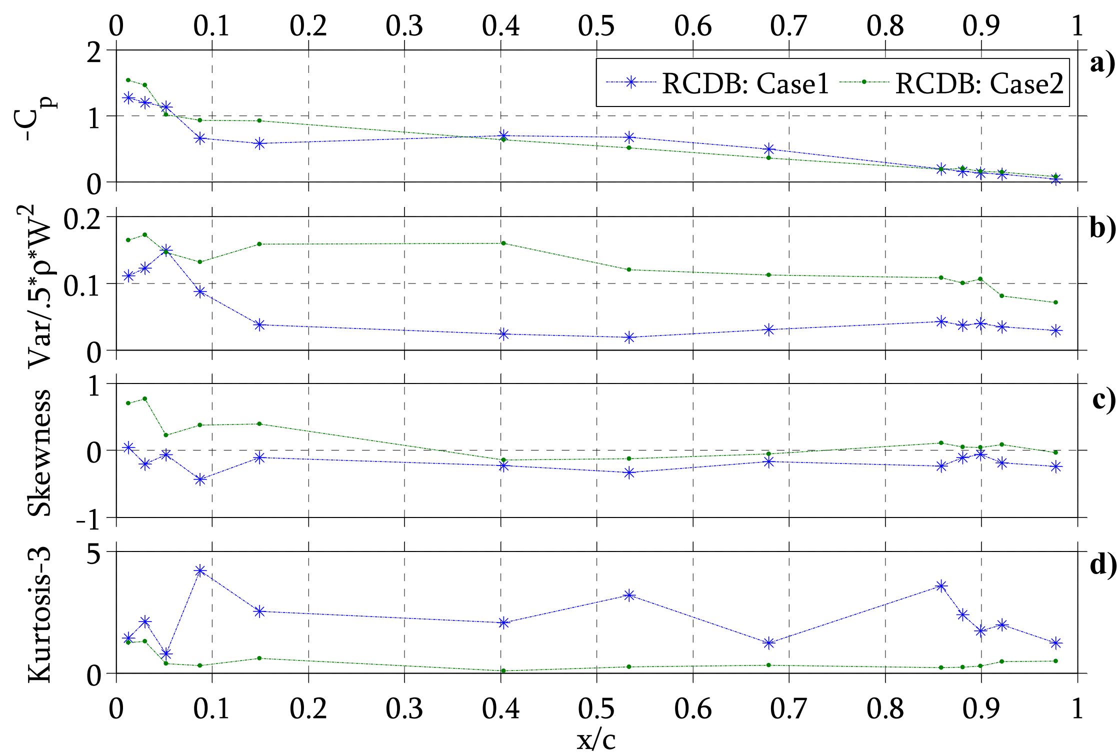

Figure 3.13 RCDB Case1-Case2 suction side moments

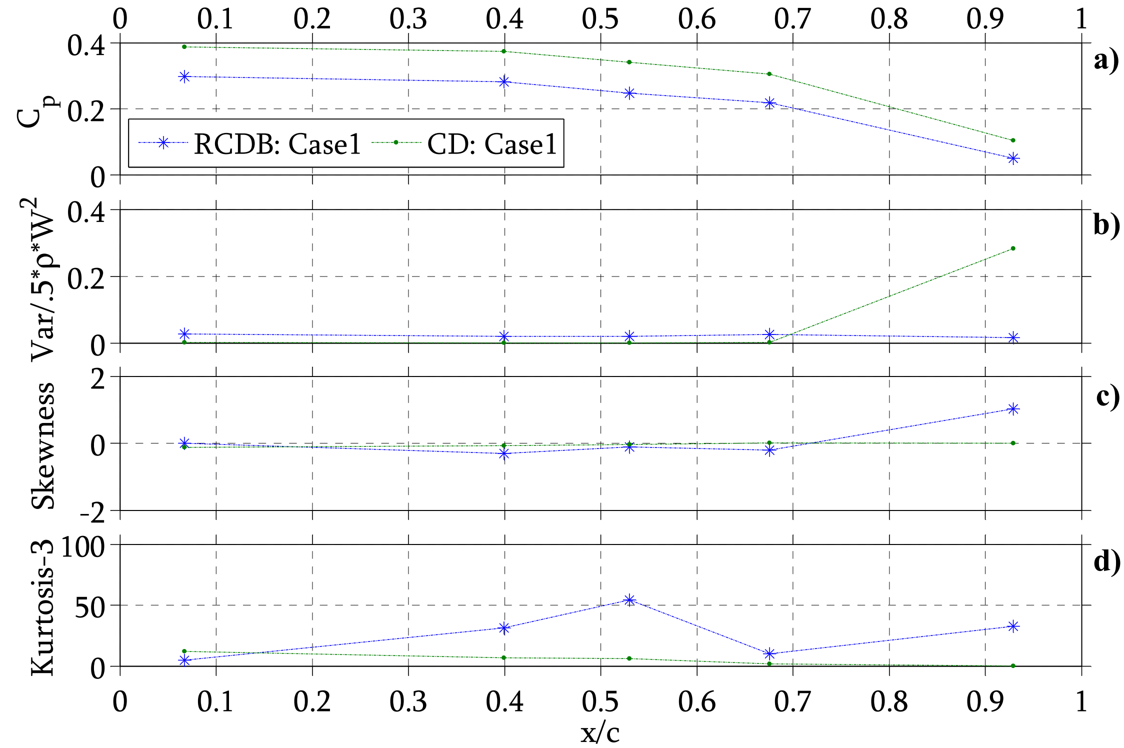

Figure 3.14 RCDB-CD Case 1 pressure side moments

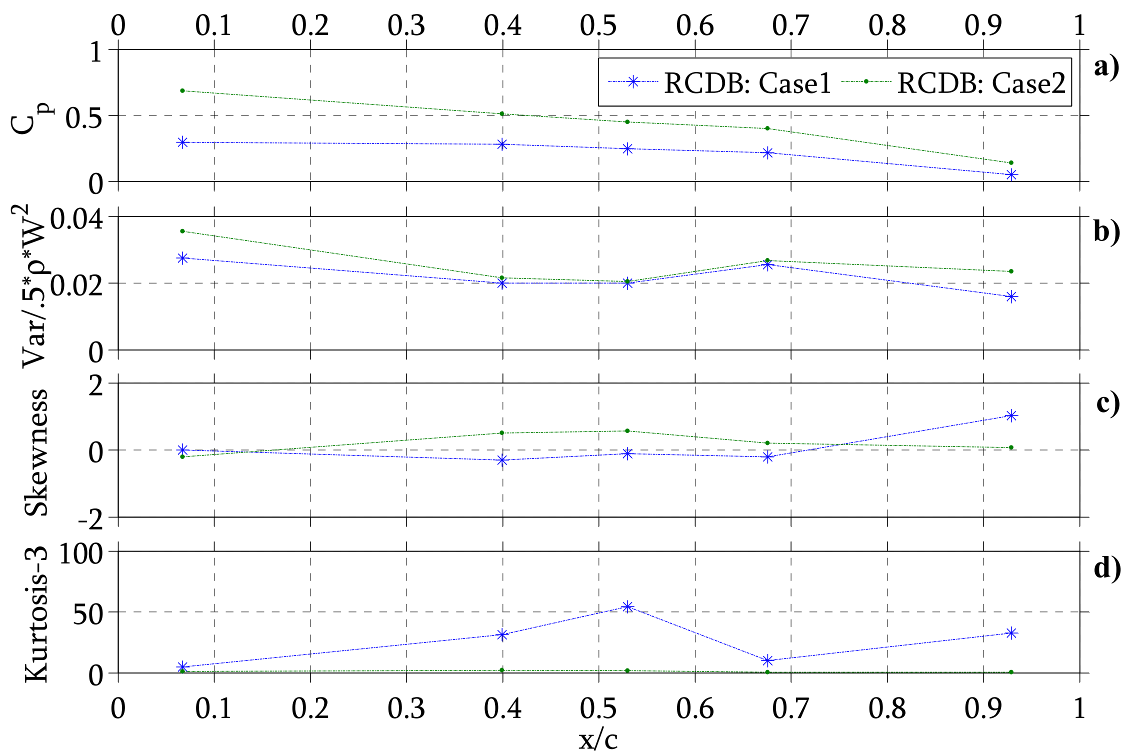

Figure 3.15 RCDB Case 1 - Case 2 pressure side moments

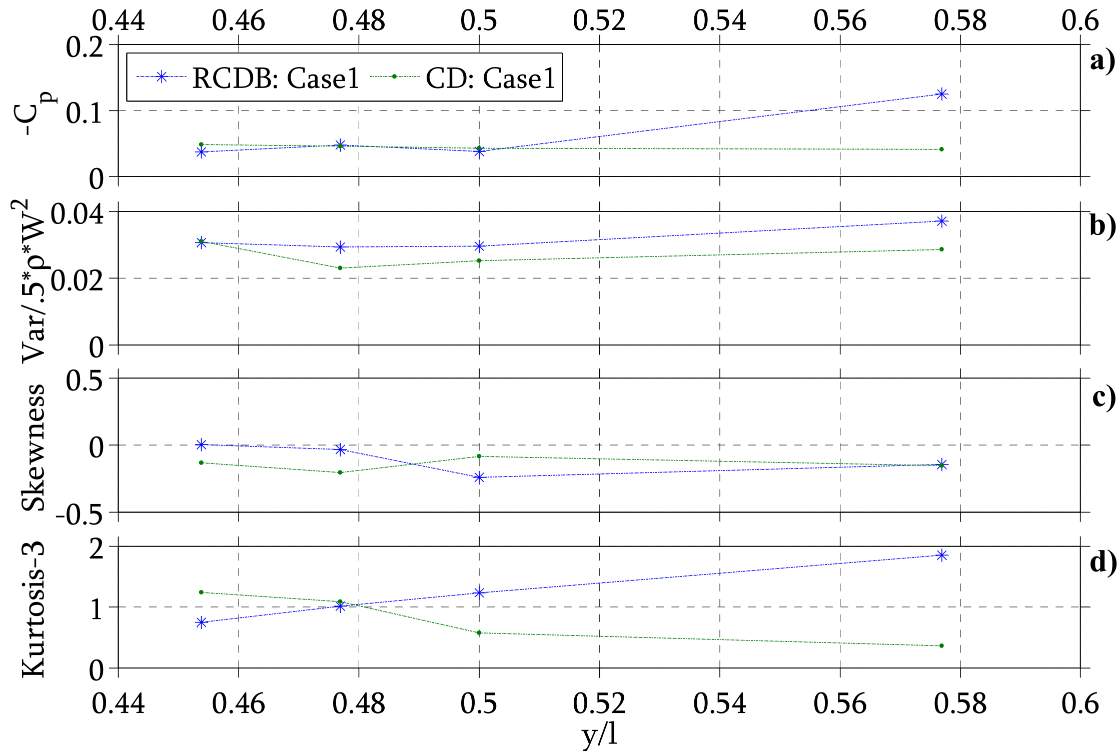

Figure 3.16 RCDB-CD Case 1 trailing edge spanwise moments

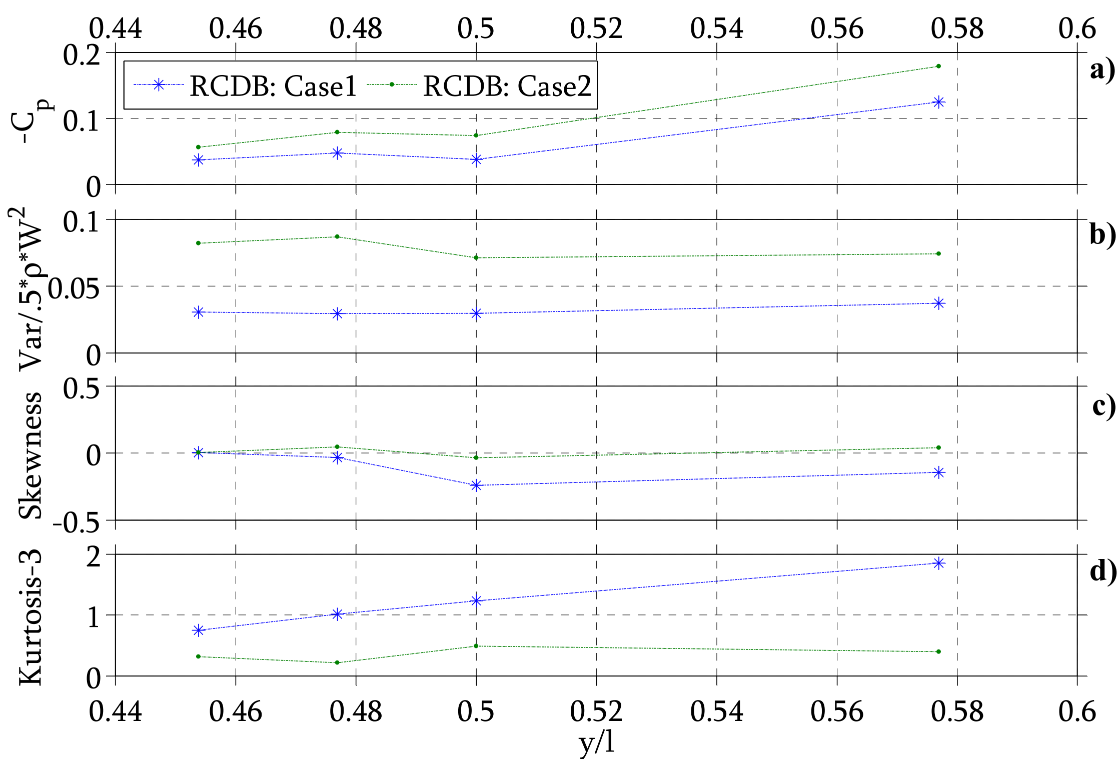

Figure 3.17 RCDB Case1 - Case2 trailing edge spanwise moments

3.3 Pressure Spectra

Continuing to characterize the boundary layer characteristics, a power spectral density of the wall pressure fluctuations (PSD, Φ_{pp}) is calculated to identify how the boundary layer pressure fluctuations vary as a function of frequency. The spectral calculations are generally repeatable between experiments within 2dB for all taps across the airfoil with the exception of the leading edge taps (Taps 1, 2, and 3) where there is an inherent instability associated with the separation/reattachment and transition of the boundary layer. Before comparing boundary layer regimes for a particular flow condition, it is useful to compare the wall pressure spectra of the Case 1 and Case 2 flow fields on a tap-by-tap basis. Figure 3.18 through Figure 3.59 show the wall pressure spectra for each surface tap and their corresponding operating conditions (RCDB: Case1, Case 2 and CD: Case 1).

Consider a comparison between RCDB Case 1 and CD Case 1 flow conditions (Figure 3.18 to Figure 3.38)[1]. The direct comparison of the stationary and rotating analog for a similar flow condition is instructive for demonstrating the properties of the fluctuations of surface pressure field. It is evident that the leading edge taps (Figure 3.18 to Figure 3.20) have widely varying spectral properties. This is attributed to the separation region unsteadiness and to fundamental differences in the flow geometry. Figure 3.18, representative of the furthest forward measurement location (x/c=0.013), shows a significant difference in spectral magnitude for frequencies $\omega c / u_\infty < 20$. The exact behavior of the separation/reattachment region is unknown between the rotating and stationary CD blades; the difference shown in Figure 3.18 demonstrates the inherent difference the two

1. Note that Höwer data is high pass filtered with a pass-band: $\omega c / u_\infty > 6$

geometries. The interpretation is subject to some uncertainty at this time. Note that it was expected that the Höwer and Moreau results be identical due to their similar geometries. Moreau and Höwer results agree better as the boundary layer develops farther downstream. The differences near the leading edge are associated to instabilities in the leading edge boundary layer separation/reattachment and flow facility differences (see Höwer 2012 for a more thorough analysis).

Following separation, the flow reattaches and becomes established as a turbulent boundary layer. The pressure spectra of the stationary and rotating CD blades become more uniform at measurement locations farther downstream. Mid-chord (0.2<x/c<0.8) measurements (Figure 3.18 to Figure 3.25) show strong spectral agreement for frequencies $\omega c/u_\infty > 20$. Low frequencies along the mid-chord indicate that the RCDB Case 1 contains more energy in larger flow structures than the CD blade. Power spectra of the trailing edge (0.1<x/c<1) indicate that energy from large structures is transferred to small structures. Stationary and rotating CD spectra in Figure 3.26 to Figure 3.30 show a systematic decrease in the low frequency ($\omega c/u_\infty < 10$) energy on order of 5-10dB from Tap 21 (x/c=0.858) to Tap 25 (x/c=0.978) where the mid-frequency ($10 < \omega c/u_\infty < 100$) shows an increase in energy along the same distance. Trailing edge spanwise spectra (Figure 3.30 to Figure 3.33) show similar differences to those seen in the trailing edge streamwise taps. Generally, the spectra of RCDB Case w are similar to CD Case 1 with the notable exception that the RCDB spectra is more biased toward lower frequencies.

The pressure side (Taps 4, 8, 10, 12, and 29) spectra show similar spectral shape between the stationary and rotating CD blades, noting that the RCDB Case 1 had a magnitude shift of approximately 10-20dB. There is a higher power in the RCDB pressure signal across the entire spectra; while typical of most of the measurements taken for the CD and RCDB geometries, it is worth considering the magnitude of the difference. Following Moreau and Roger (2005), the spectral shape seen on the pressure side is indicative of a viscous dominated boundary layer; the measurements are particularly susceptible to broadband noise due to the weak hydrostatic pressure signal. Moreau notes that the sensors on the pressure side of the blade likely act as acoustic sensors. Moreau's measurements reach the floor of the transducer's resolution at higher frequencies.

Consider a comparison between RCDB Case 1 and RCDB Case 2 flow conditions (Figure 3.39 to Figure 3.59). The comparison of the two operating conditions supports a deeper understanding of the RCDB boundary layer characteristics. Generally, the power of the Case 2 flow field is higher than Case 1 - this is a confirmation of the statistical measurements from Section 3.2, which suggested a more energetic disturbance in the Case 2 flow field. The leading edge measurements (Figure 3.39 to Figure 3.41) show similar spectral shapes in both cases. Following reattachment, toward the mid-chord of the airfoil, the Case 2 spectra develop more energy in all frequencies. Near the trailing edge (Figure 3.47 to Figure 3.51), the Case 2 spectra develops a more consistent profile, characterized by high power in the low frequencies and a steady, shallow decay. The low frequency content suggests generally larger flow structures due to a larger integral scale of the boundary layer. A comparison of the pressure side spectra (Figure 3.55 to Figure 3.59) yields little new information; the Case 2 power spectra have a generally constant magnitude shift relative to the Case 1 spectra.

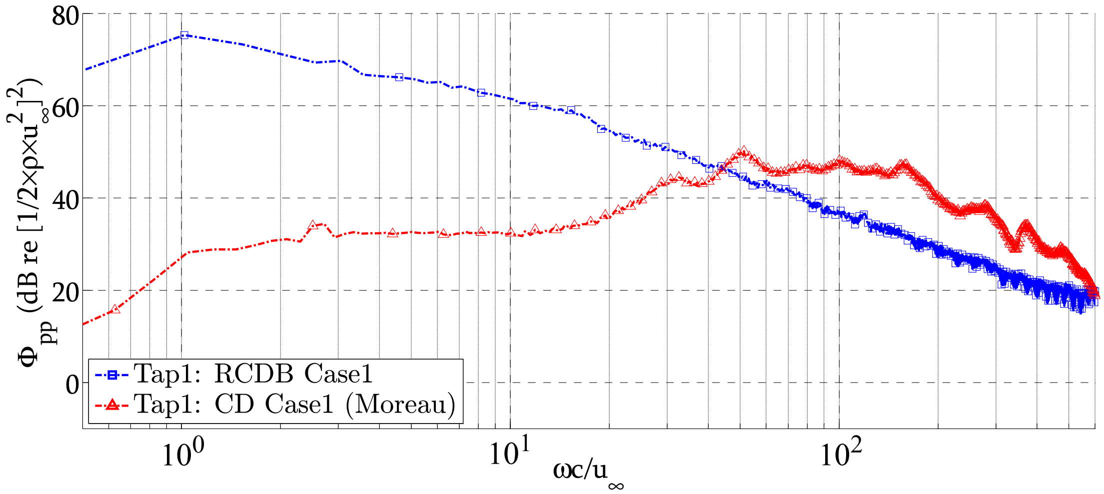

Figure 3.18 RCDB and CD Case 1 (Moreau) spectra: Tap1 (x/c=0.013)

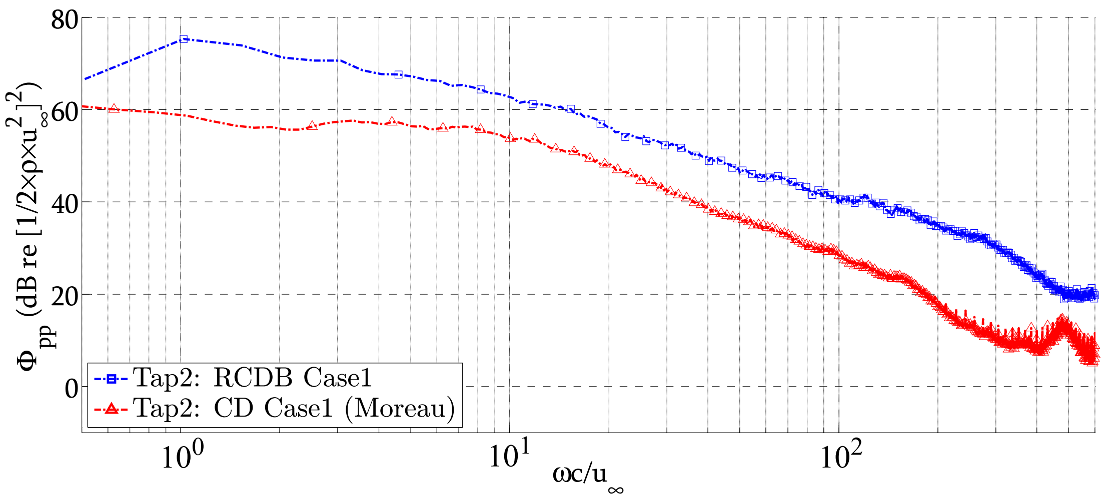

Figure 3.19 RCDB and CD Case 1 (Moreau) spectra: Tap2 (x/c=0.03)

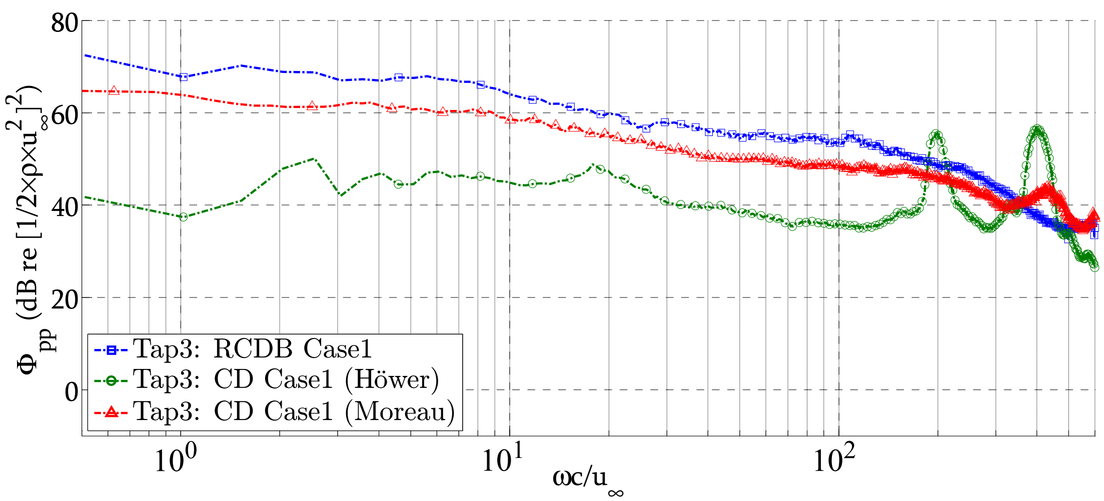

Figure 3.20 RCDB and CD Case 1 (Höwer and Moreau) spectra: Tap3 (x/c=0.052)

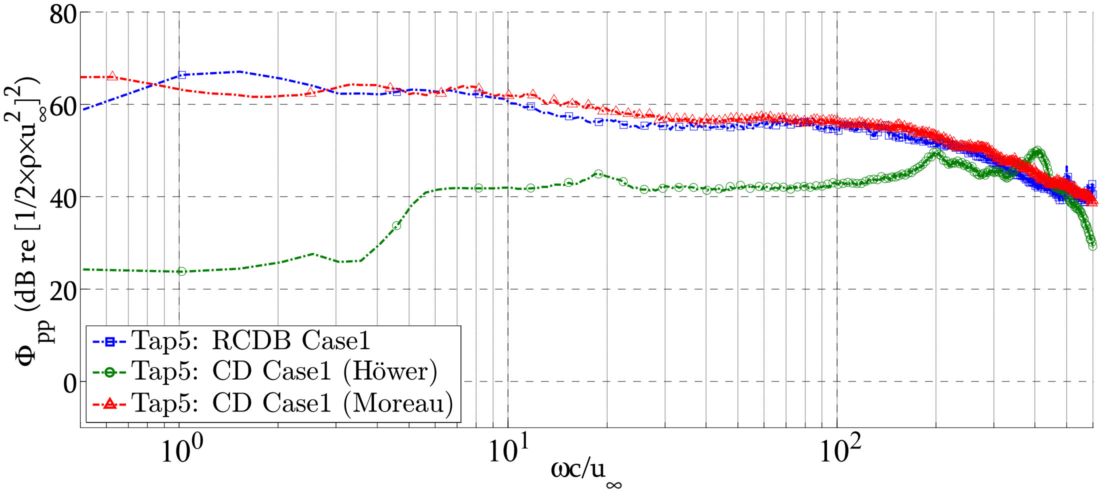

Figure 3.21 RCDB and CD Case 1 (Höwer and Moreau) spectra: Tap5 (x/c=0.087)

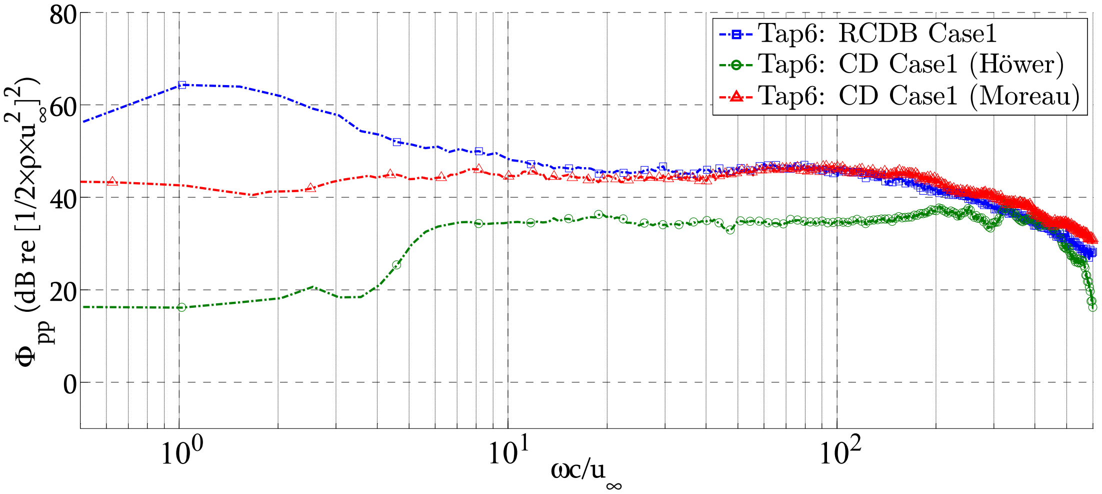

Figure 3.22 RCDB and CD Case 1 (Höwer and Moreau) spectra: Tap6 (x/c=0.149)

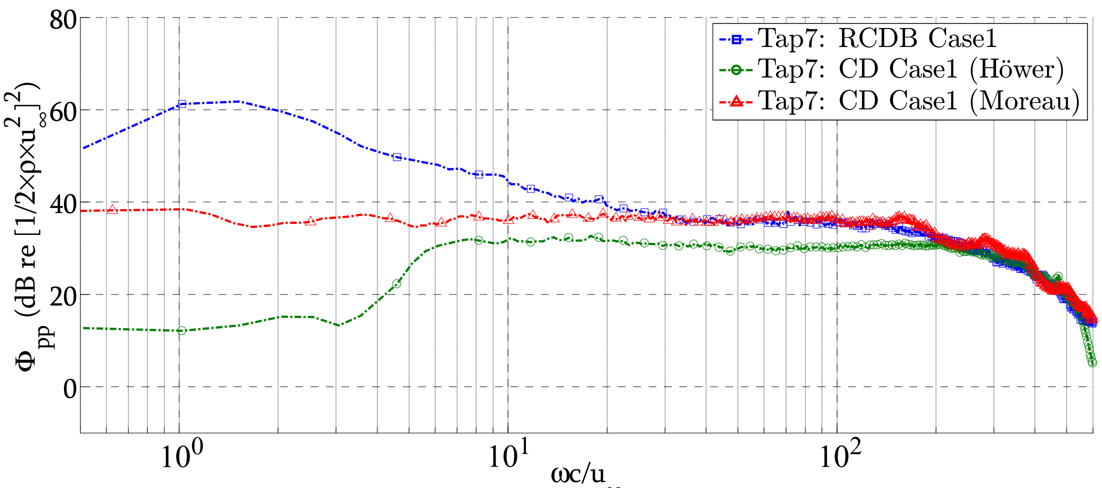

Figure 3.23 RCDB and CD Case 1 (Höwer and Moreau) spectra: Tap7 (x/c=0.403)

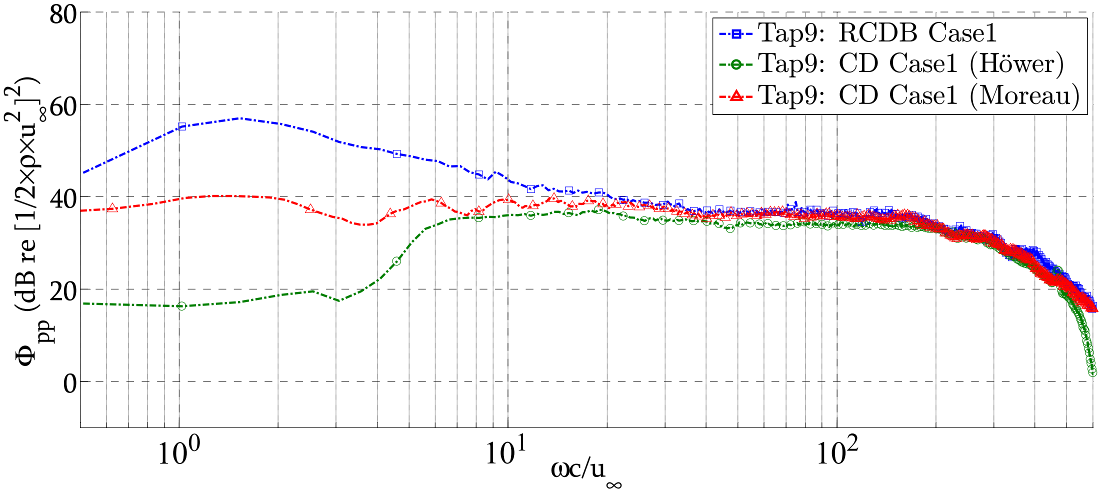

Figure 3.24 RCDB and CD Case 1 (Höwer and Moreau) spectra: Tap9 (x/c=0.534)

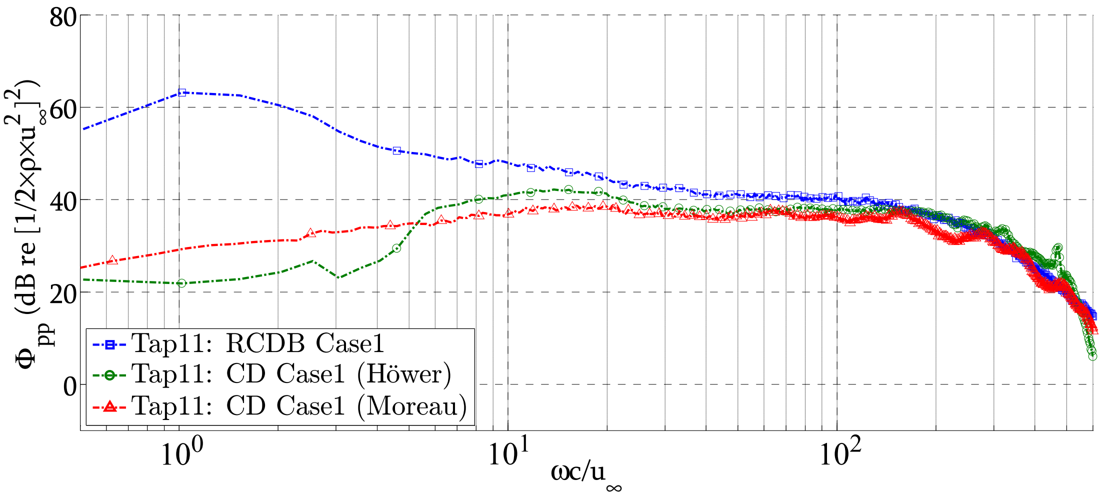

Figure 3.25 RCDB and CD Case 1 (Höwer and Moreau) spectra: Tap11 (x/c=0.679)

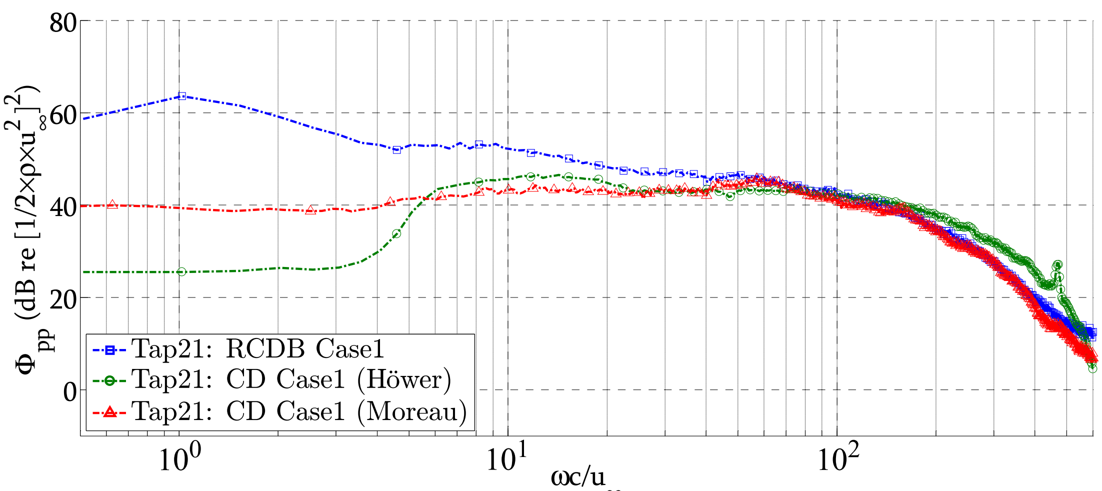

Figure 3.26 RCDB and CD Case 1 (Höwer and Moreau) spectra: Tap21 (x/c=0.858)

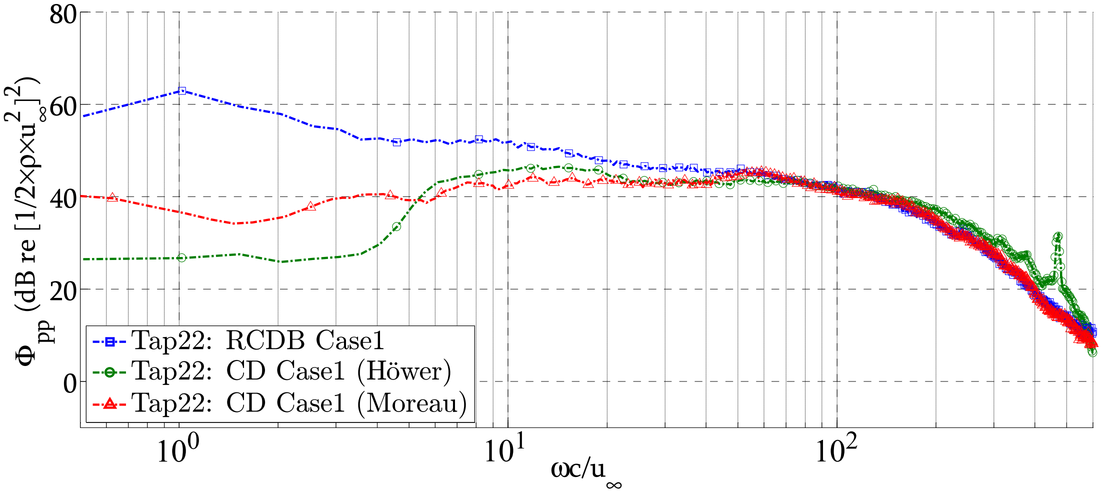

Figure 3.27 RCDB and CD Case 1 (Höwer and Moreau) spectra: Tap22 (x/c=0.881)

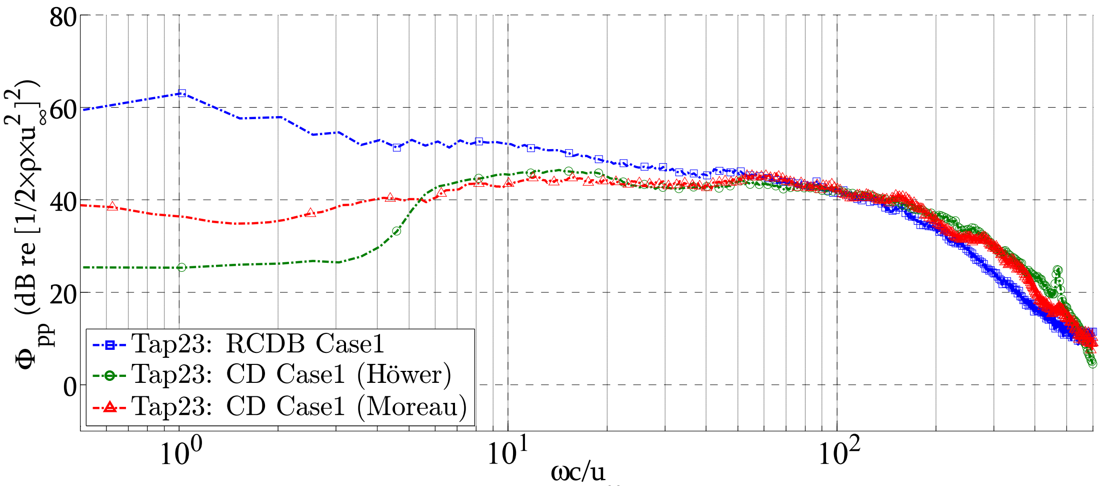

Figure 3.28 RCDB and CD Case 1 (Höwer and Moreau) spectra: Tap23 (x/c=0.899)

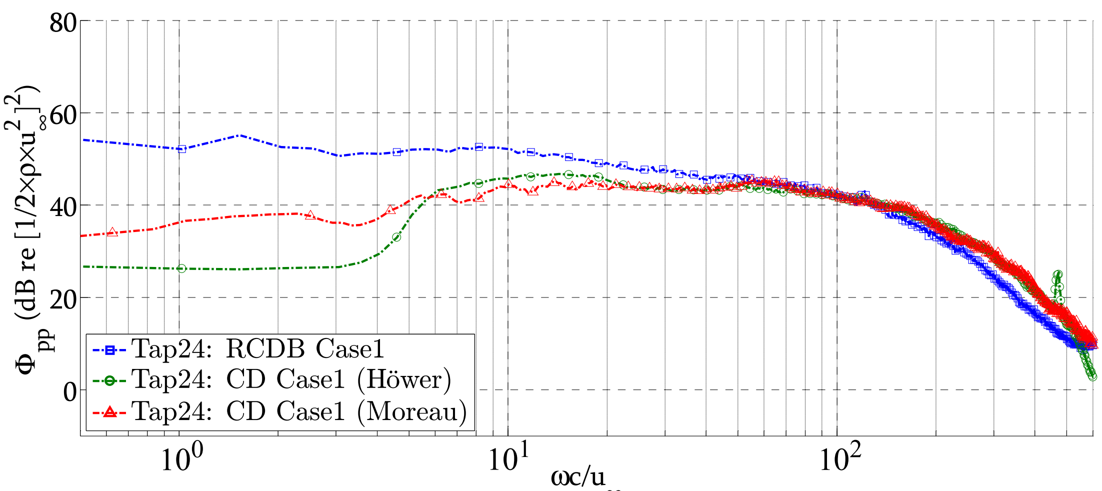

Figure 3.29 RCDB and CD Case 1 (Höwer and Moreau) spectra: Tap24 (x/c=0.922)

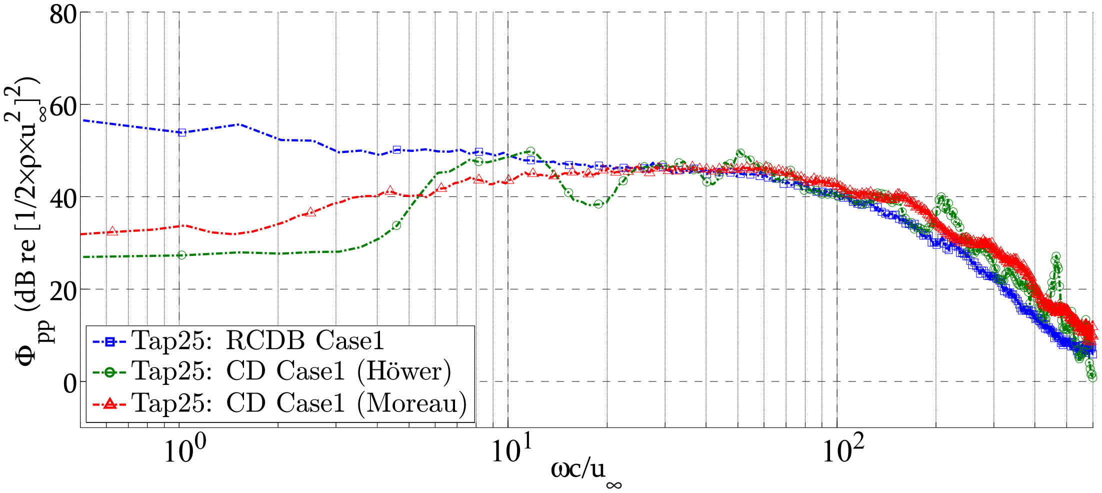

Figure 3.30 RCDB and CD Case 1 (Höwer and Moreau) spectra: Tap25 (x/c=0.978)

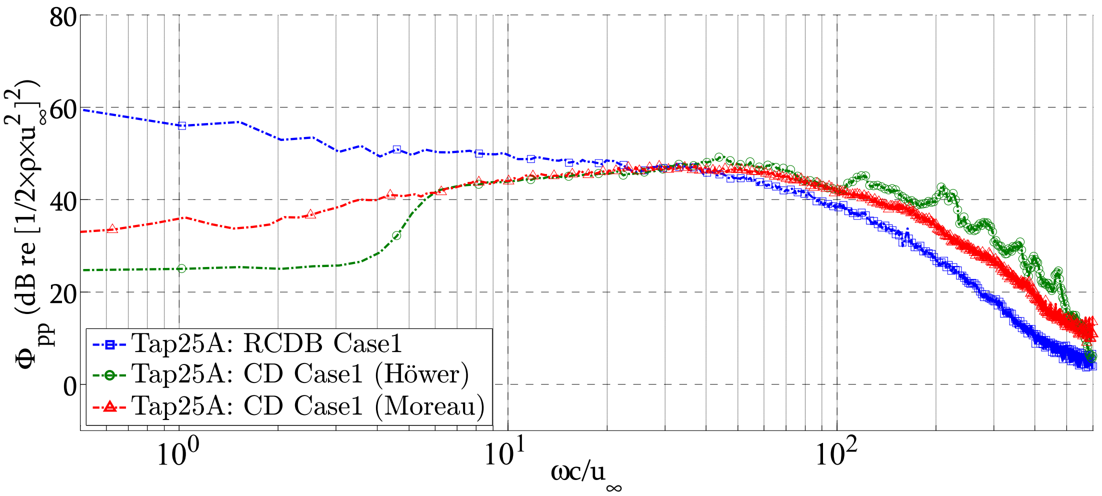

Figure 3.31 RCDB and CD Case 1 (Höwer and Moreau) spectra: Tap25A (y/l=0.45)

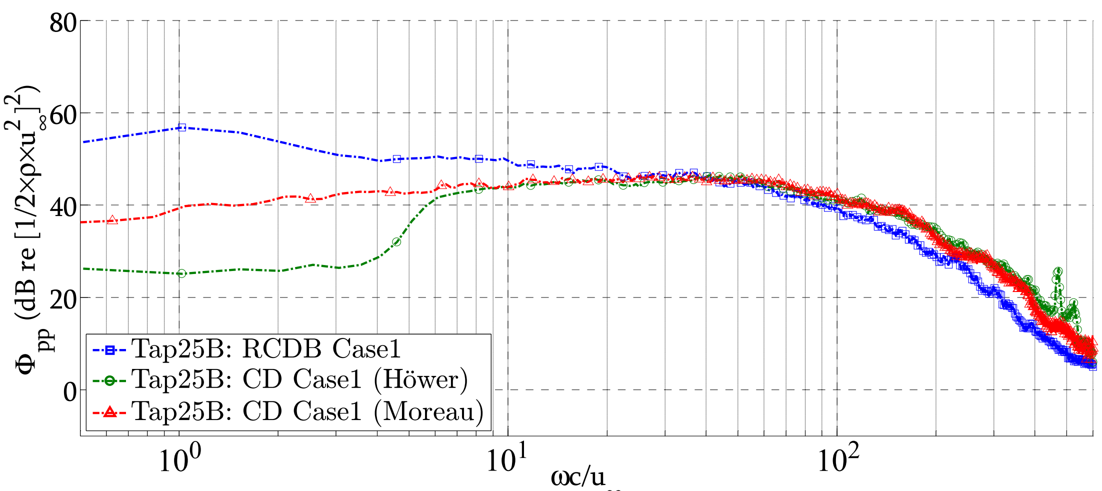

Figure 3.32 RCDB and CD Case 1 (Höwer and Moreau) spectra: Tap25B (y/l=0.48)

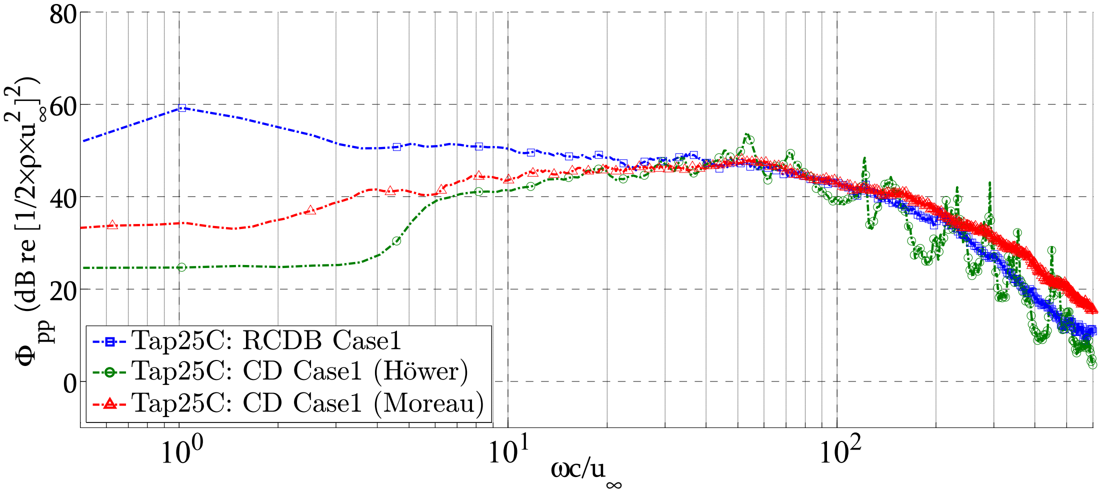

Figure 3.33 RCDB and CD Case 1 (Höwer and Moreau) spectra: Tap25C (x/c=0.58)

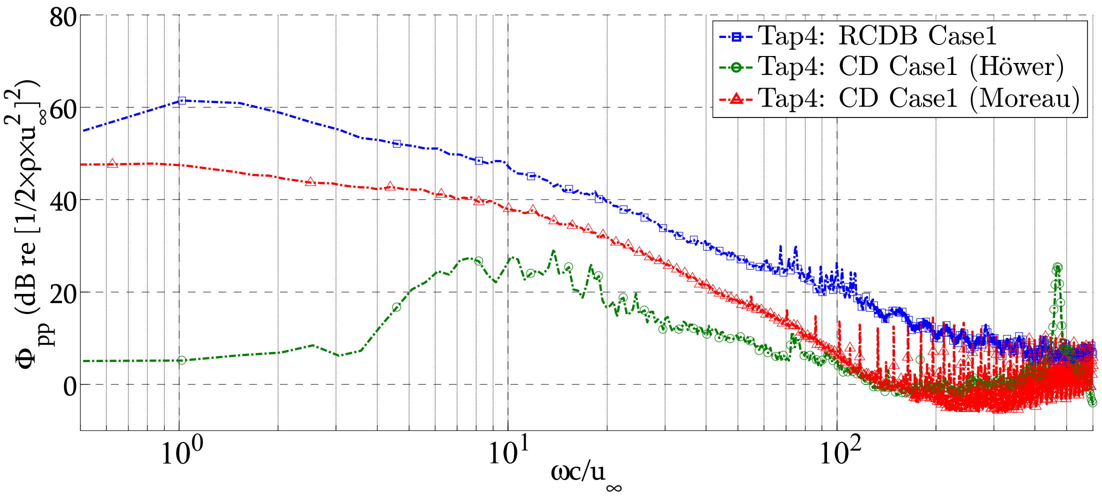

Figure 3.34 RCDB and CD Case 1 (Höwer and Moreau) spectra: Tap4 (x/c=0.067)

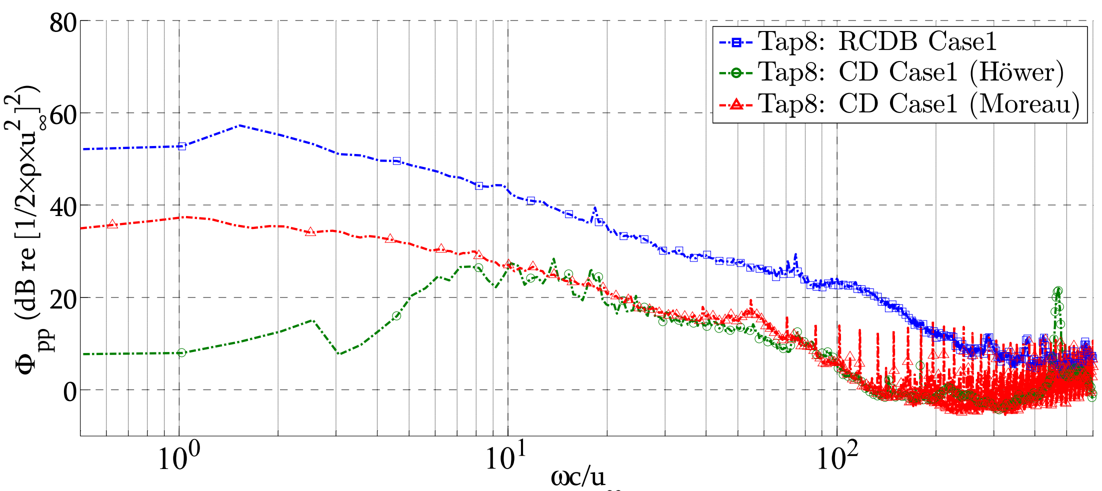

Figure 3.35 RCDB and CD Case 1 (Höwer and Moreau) spectra: Tap8 (x/c=0.400)

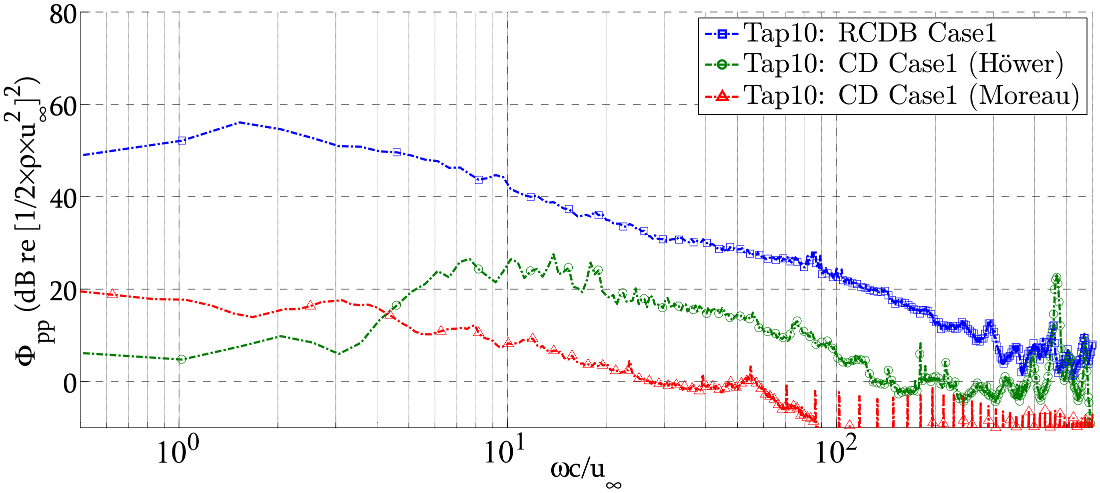

Figure 3.36 RCDB and CD Case 1 (Höwer and Moreau) spectra: Tap10 (x/c=0.530)

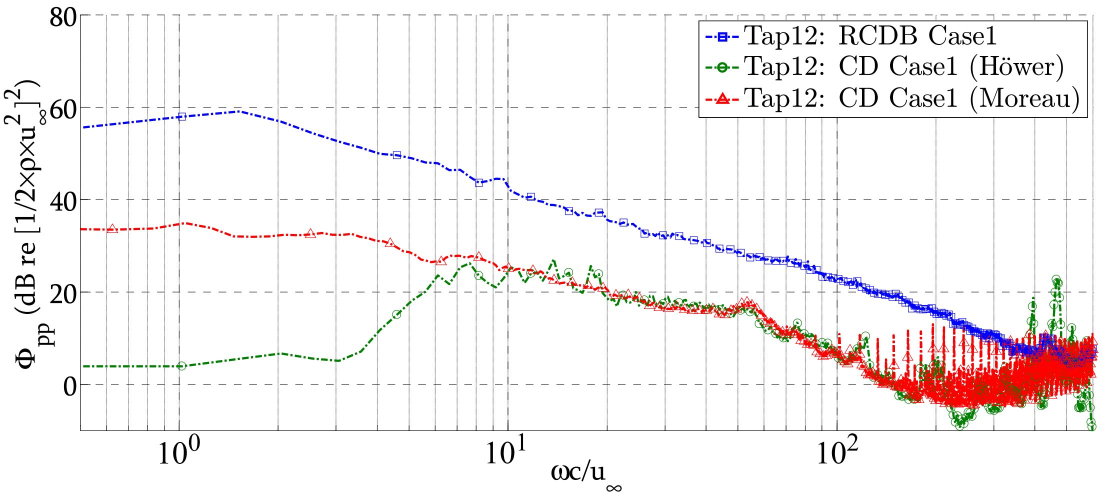

Figure 3.37 RCDB and CD Case 1 (Höwer and Moreau) spectra: Tap12 (x/c=0.675)

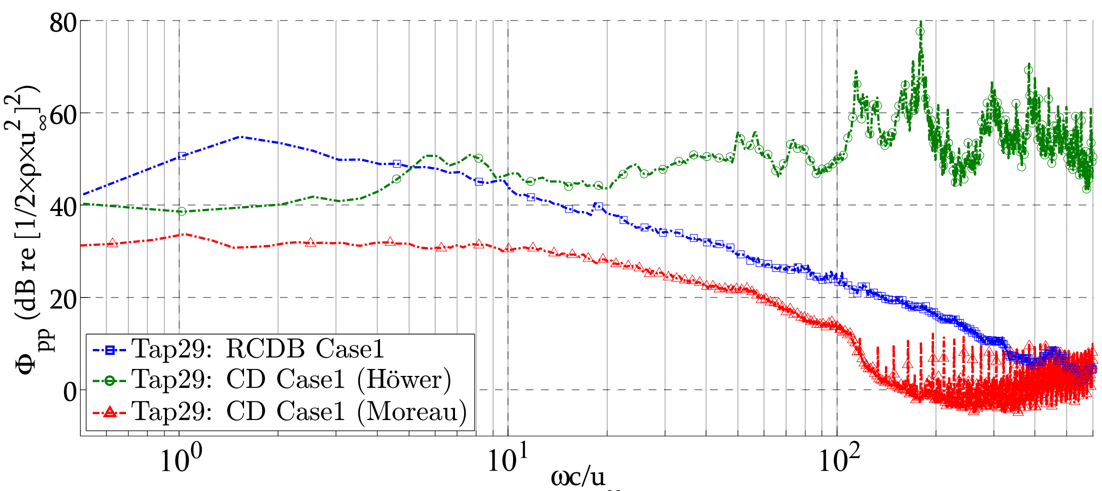

Figure 3.38 RCDB and CD Case 1 (Höwer and Moreau) spectra: Tap29 (x/c=0.929)

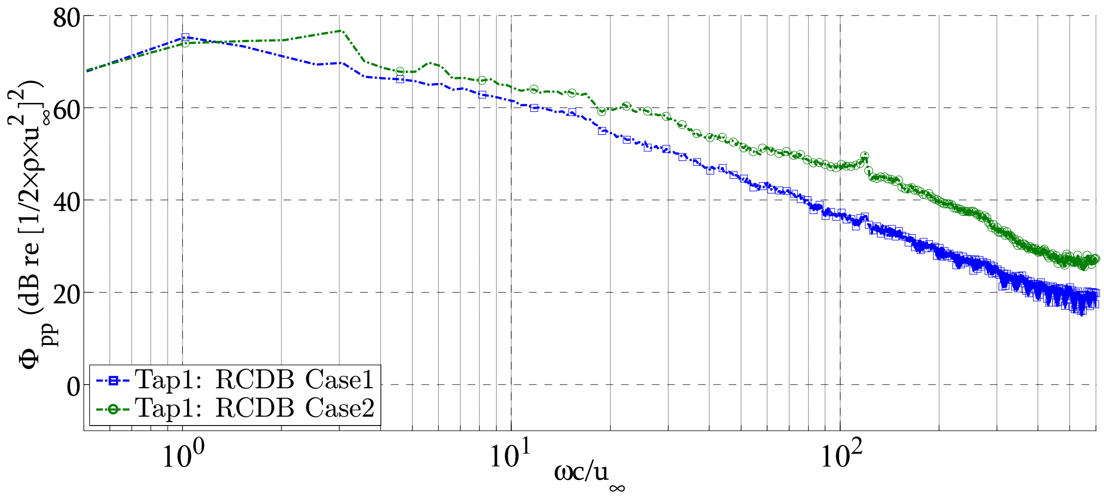

Figure 3.39 RCDB Case 1 and Case 2 spectra: Tap1 (x/c=0.013)

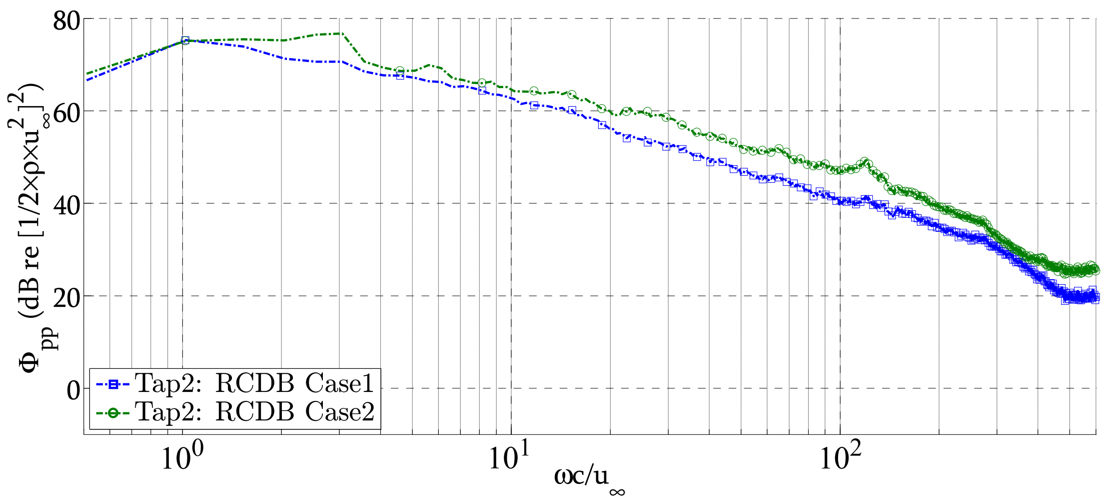

Figure 3.40 RCDB Case 1 and Case 2 spectra: Tap2 (x/c=0.030)

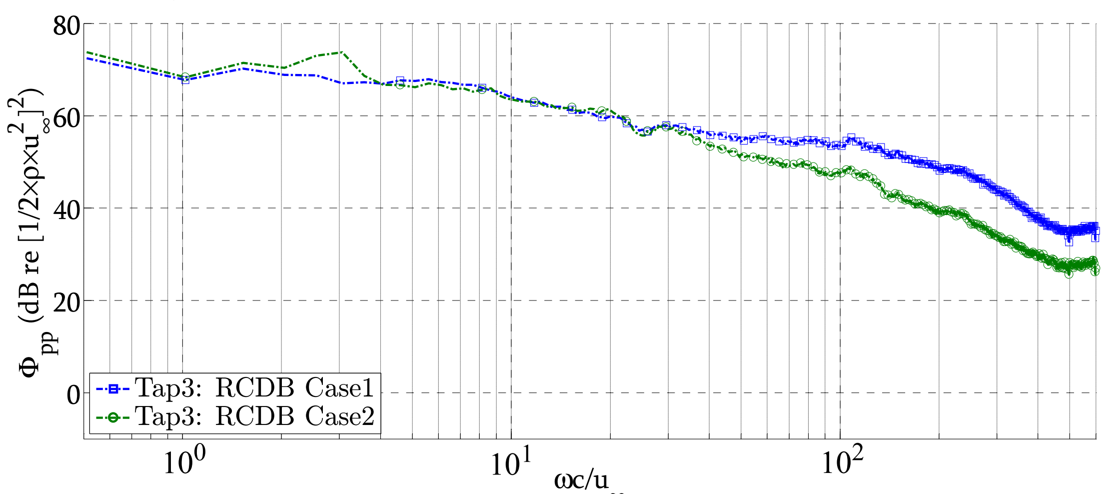

Figure 3.41 RCDB Case 1 and Case 2 spectra: Tap3 (x/c=0.052)

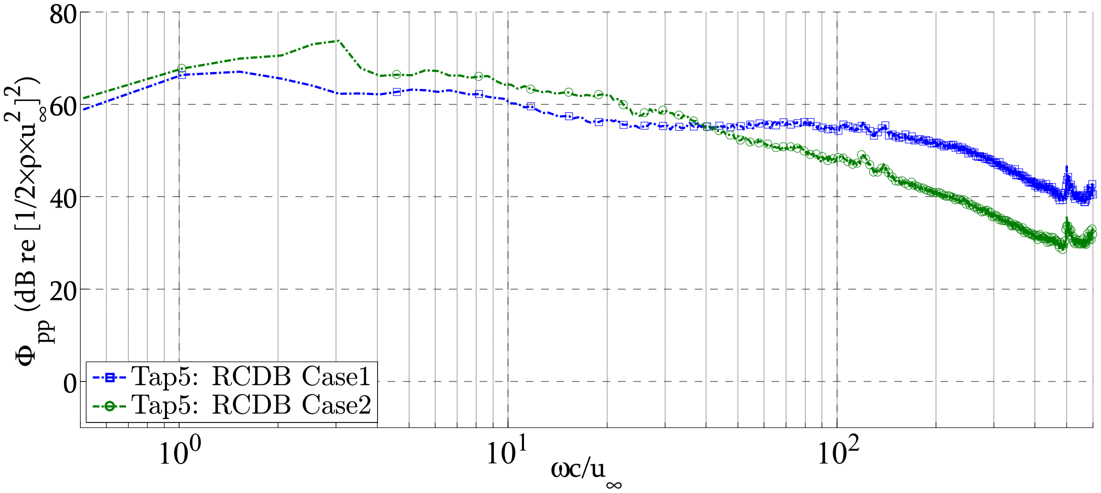

Figure 3.42 RCDB Case 1 and Case 2 spectra: Tap5 (x/c=0.087)

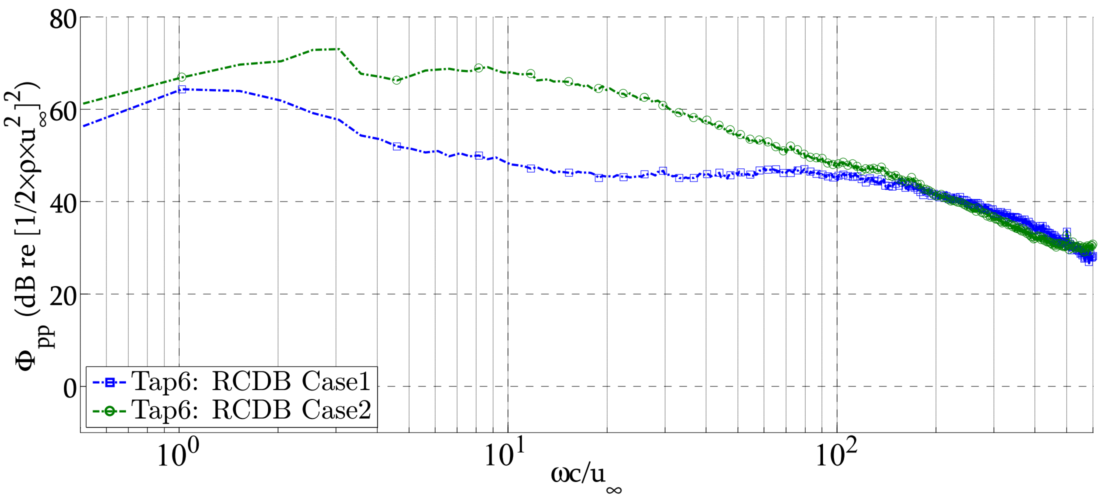

Figure 3.43 RCDB Case 1 and Case 2 spectra: Tap6 (x/c=0.149)

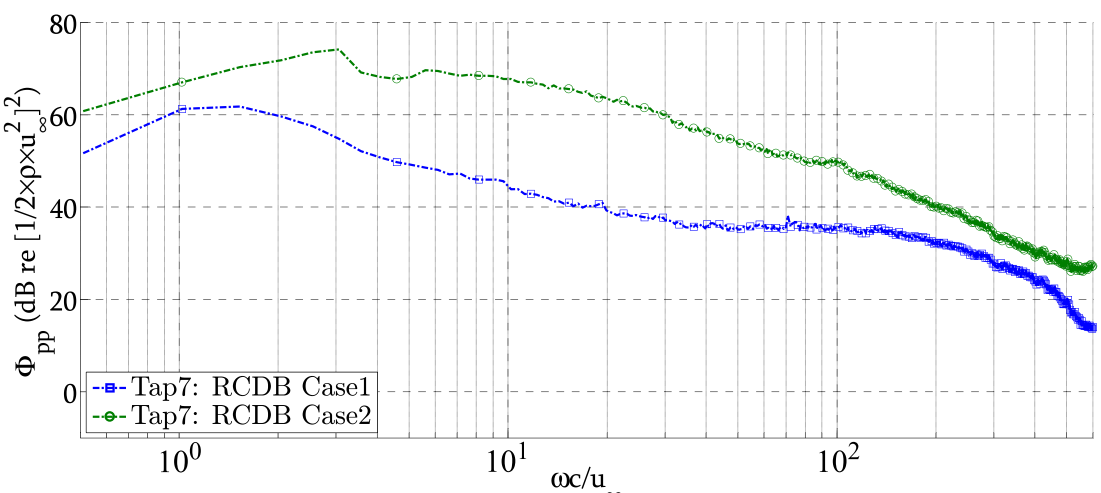

Figure 3.44 RCDB Case 1 and Case 2 spectra: Tap7 (x/c=0.403)

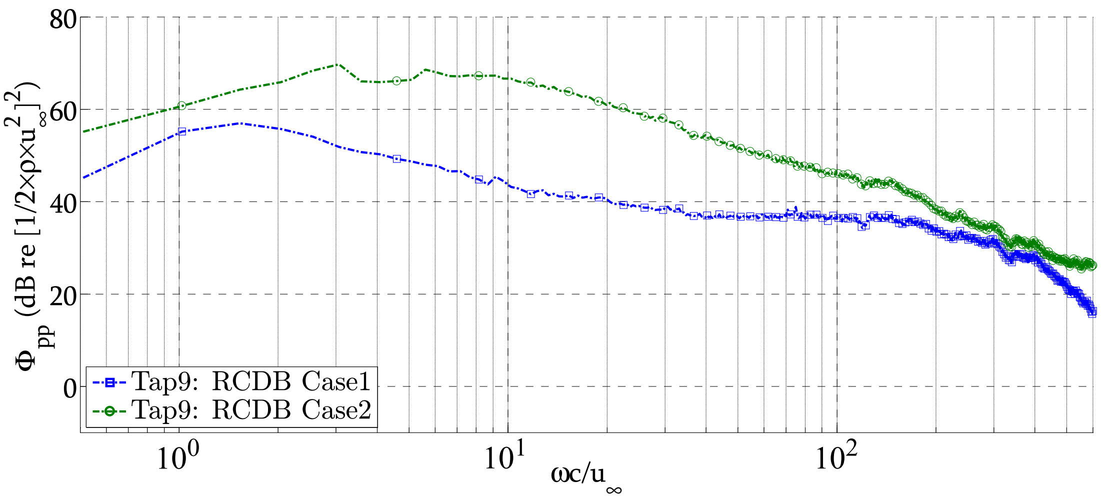

Figure 3.45 RCDB Case 1 and Case 2 spectra: Tap9 (x/c=0.534)

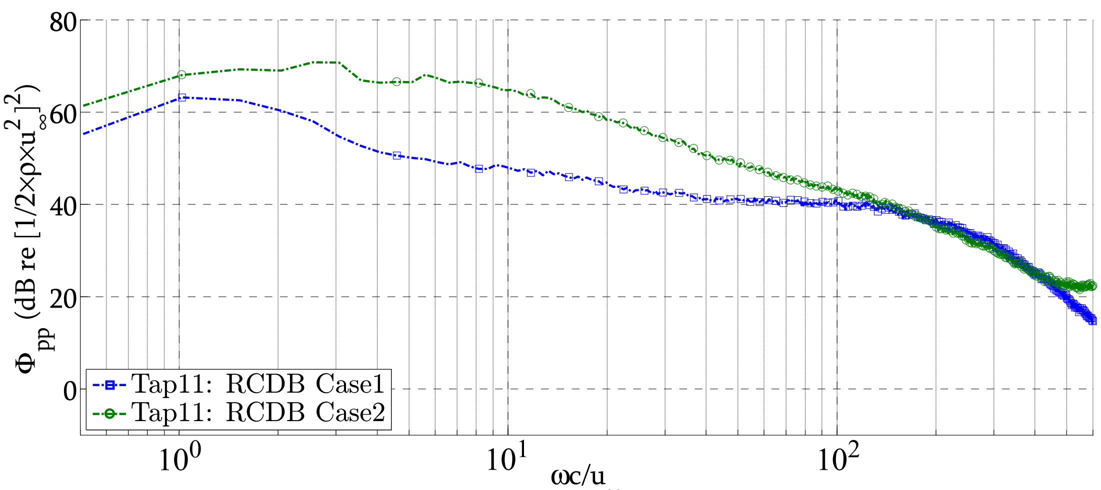

Figure 3.46 RCDB Case 1 and Case 2 spectra: Tap11 (x/c=0.679)

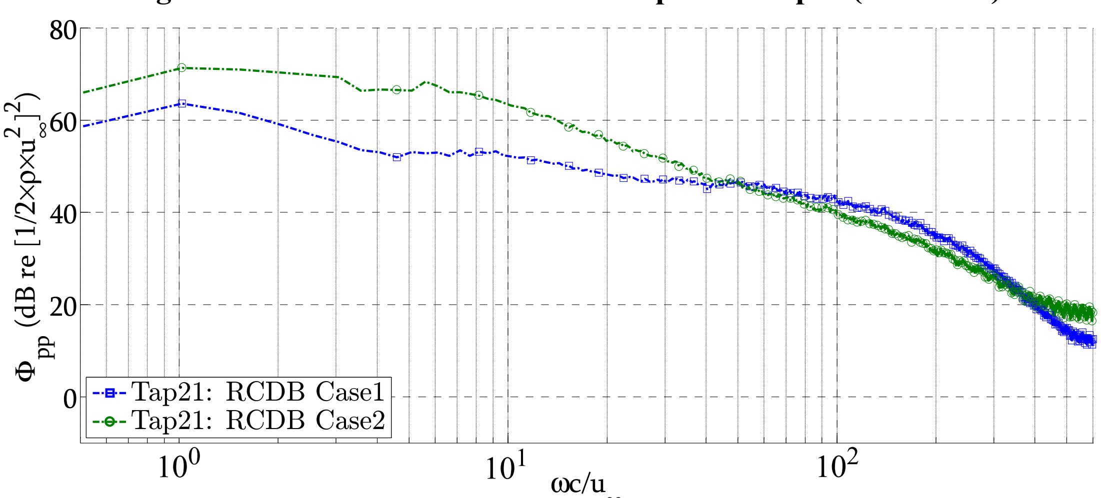

Figure 3.47 RCDB Case 1 and Case 2 spectra: Tap21 (x/c=0.858)

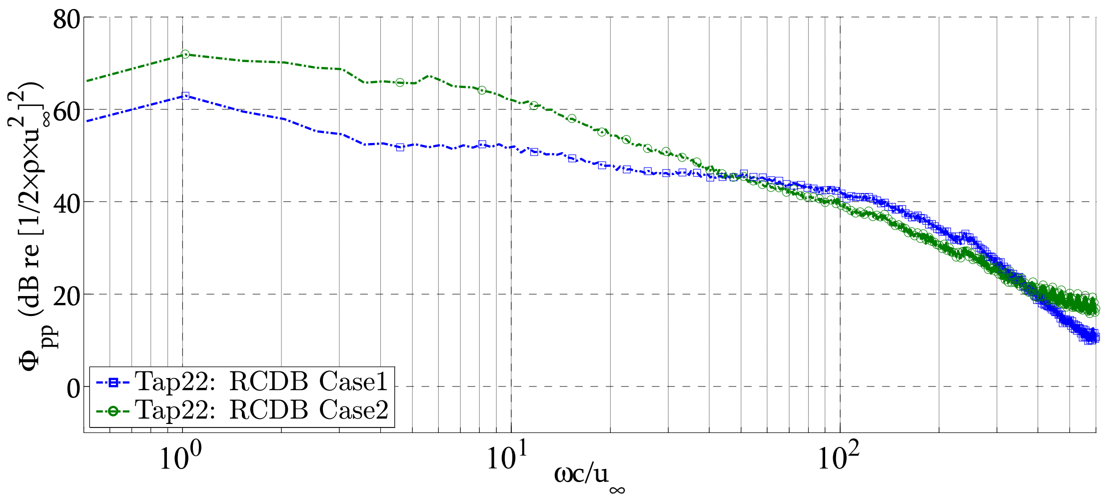

Figure 3.48 RCDB Case 1 and Case 2 spectra: Tap22 (x/c=0.881)

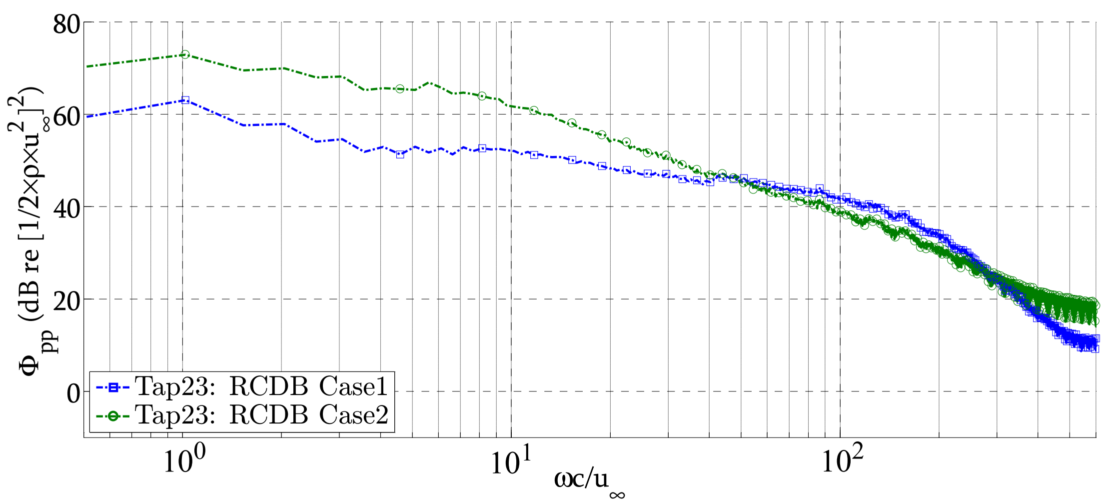

Figure 3.49 RCDB Case 1 and Case 2 spectra: Tap23 (x/c=0.899)

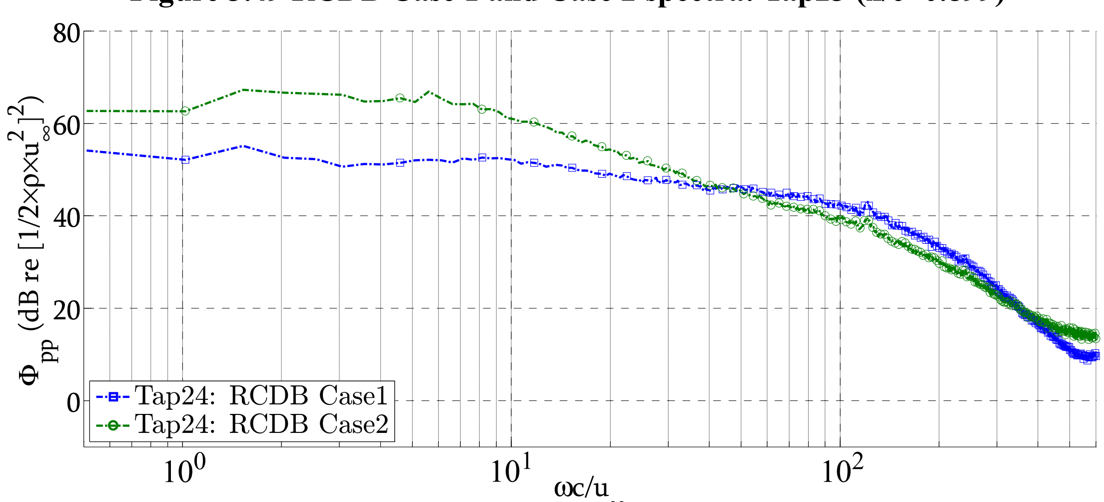

Figure 3.50 RCDB Case 1 and Case 2 spectra: Tap24 (x/c=0.922)

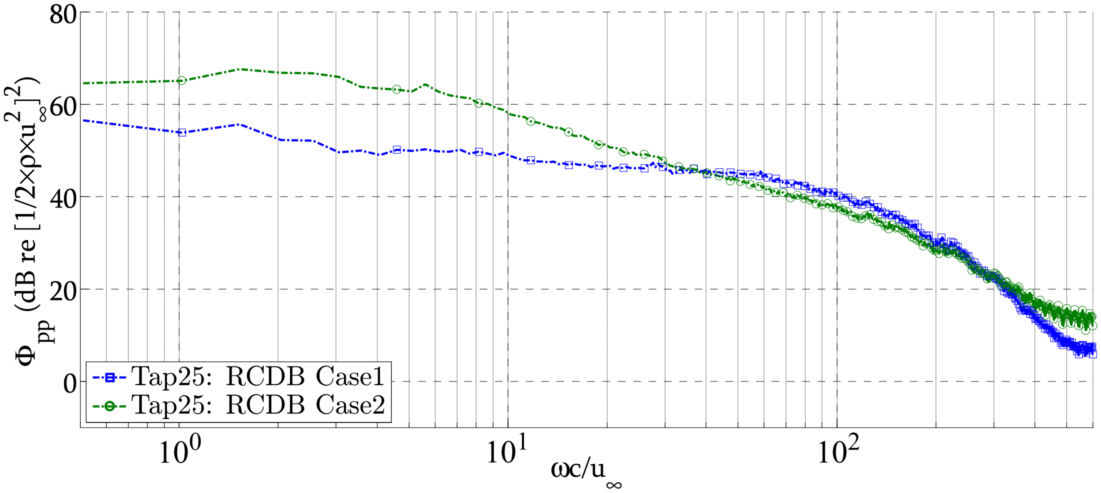

Figure 3.51 RCDB Case 1 and Case 2 spectra: Tap25 (x/c=0.978)

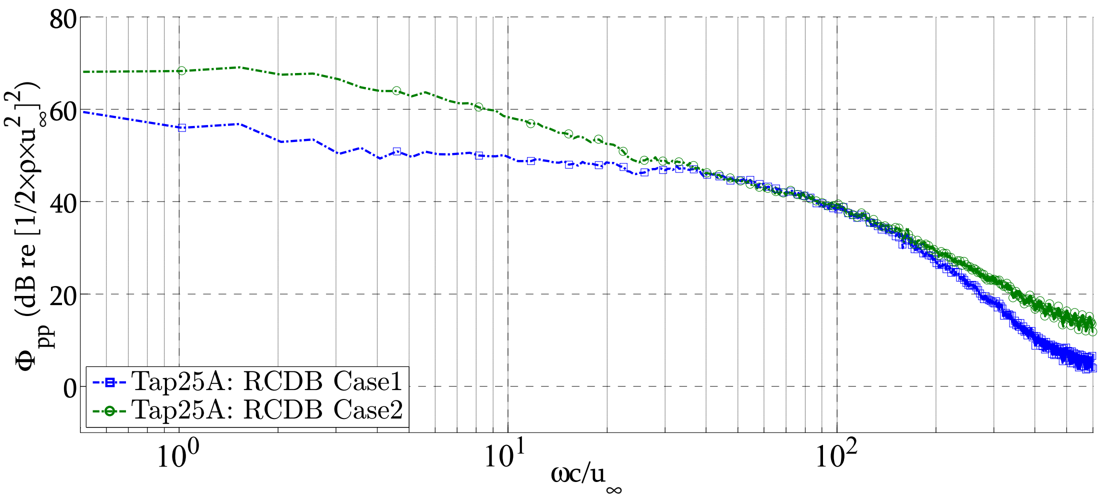

Figure 3.52 RCDB Case 1 and Case 2 spectra: Tap25A (y/l=0.45)

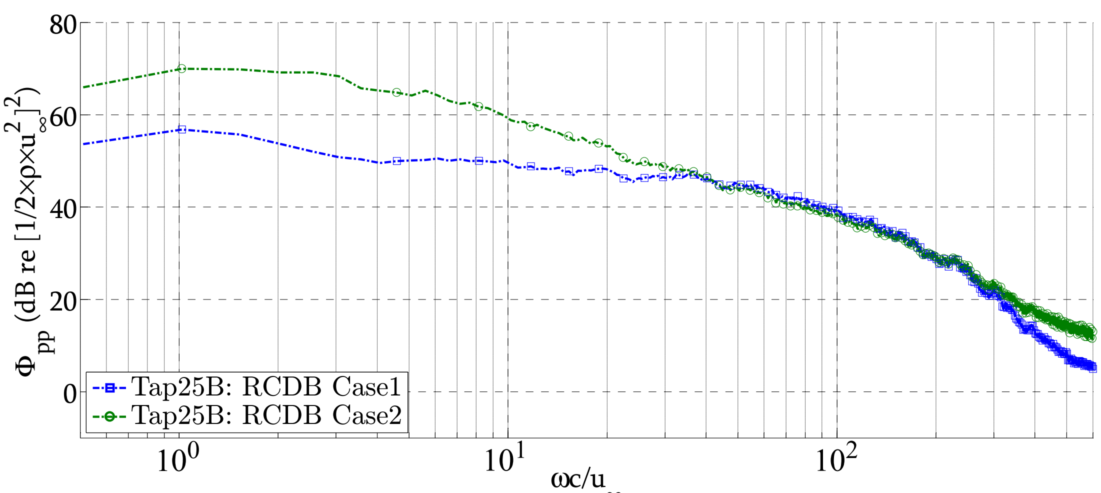

Figure 3.53 RCDB Case 1 and Case 2 spectra: Tap25B (y/l=0.48)

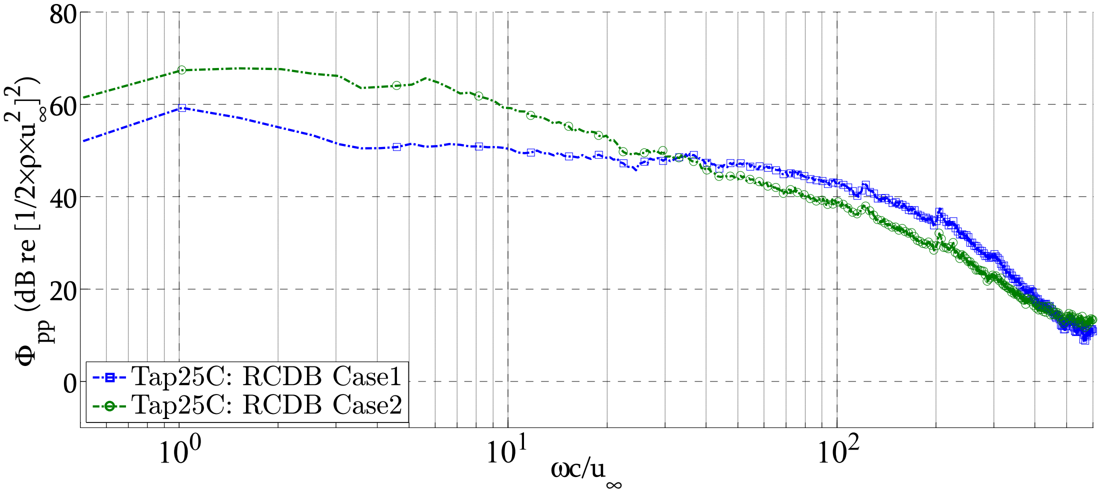

Figure 3.54 RCDB Case 1 and Case 2 spectra: Tap25C (y/l=0.58)

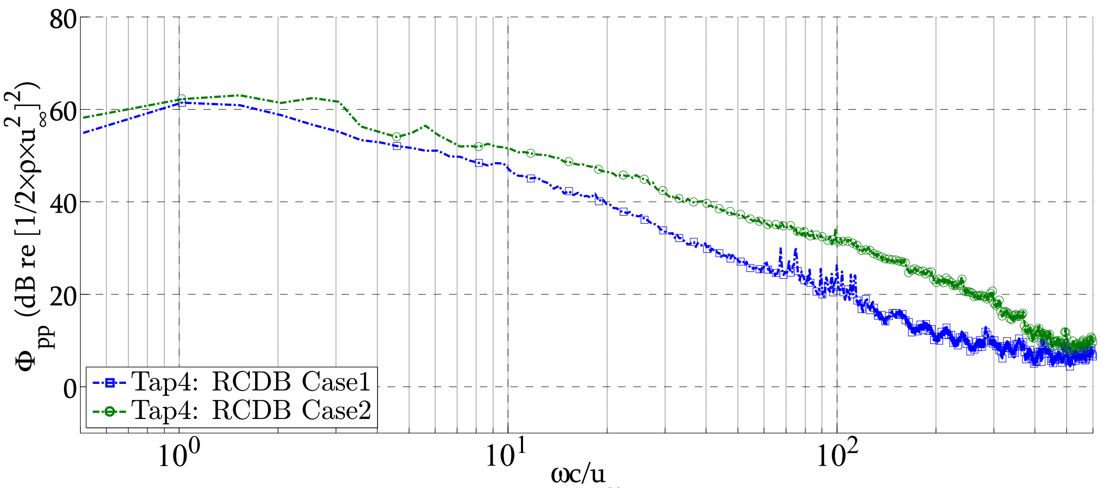

Figure 3.55 RCDB Case 1 and Case 2 spectra: Tap4 (x/c=0.067)

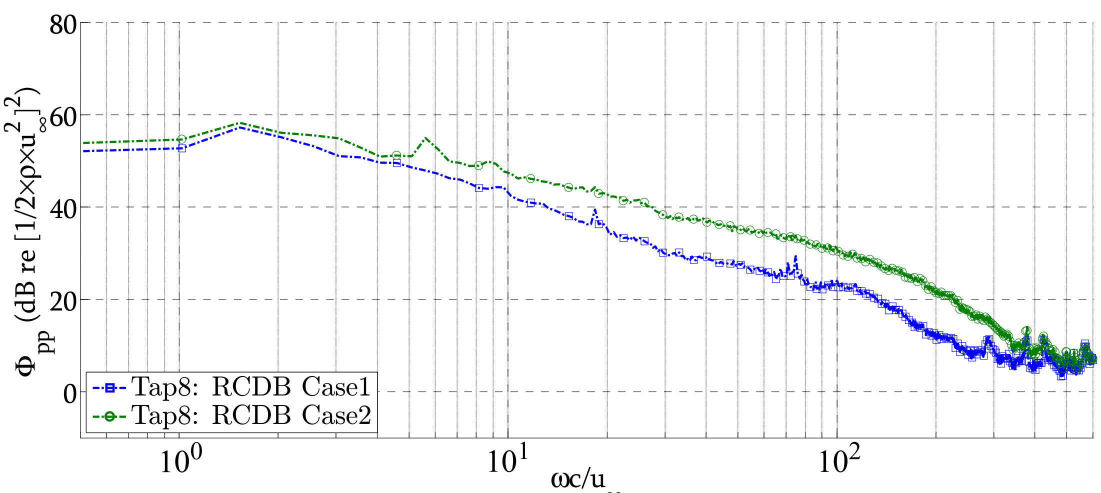

Figure 3.56 RCDB Case 1 and Case 2 spectra: Tap8 (x/c=0.400)

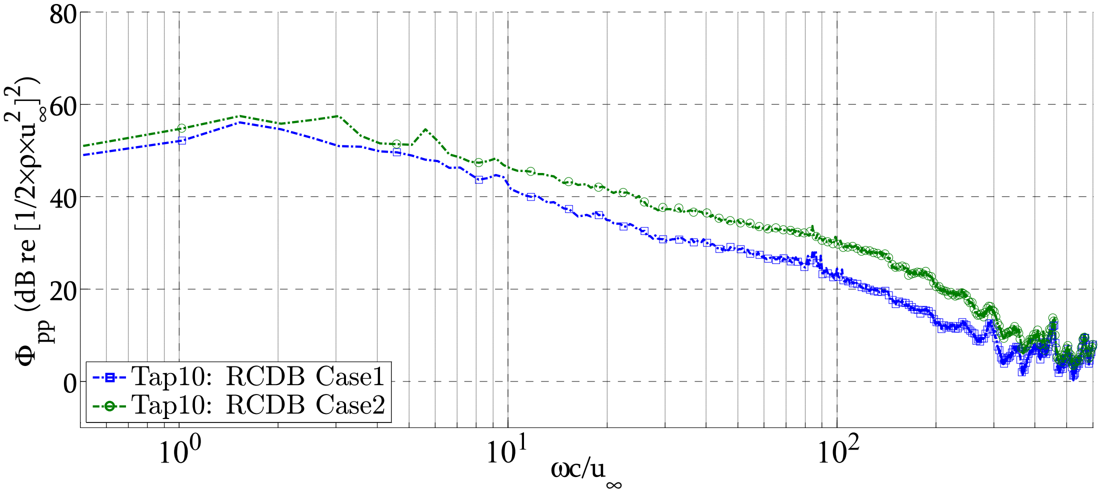

Figure 3.57 RCDB Case 1 and Case 2 spectra: Tap10 (x/c=0.530)

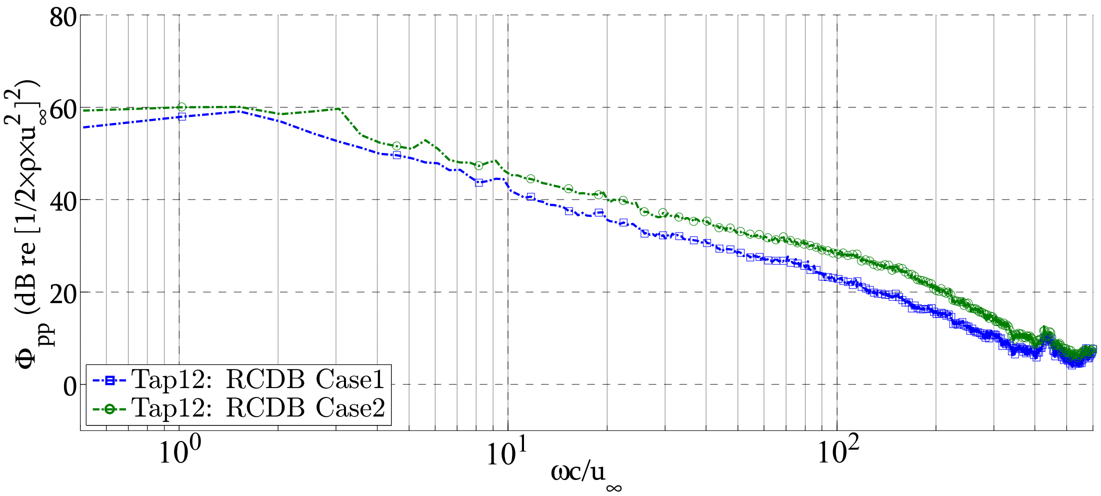

Figure 3.58 RCDB Case 1 and Case 2 spectra: Tap12 (x/c=0.675)

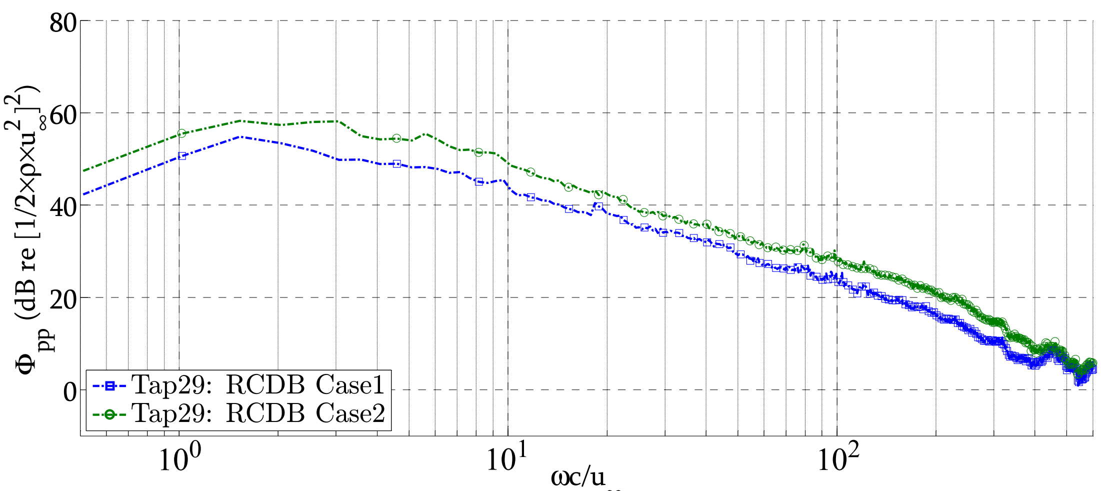

Figure 3.59 RCDB Case 1 and Case 2 spectra: Tap29 (x/c=0.929)

Boundary layer trends across the airfoil surface are better identified by re-representing the previous figures as a collection of regions along the blade. Figure 3.60 shows the forward region of the airfoil - this includes separation and reattachment. The large difference of spectral energy magnitude between Taps 1 and 2 and Taps 3 and 4 from $20 < \omega c/u_{\infty} < 600$ is indicative of the laminar-to-turbulent boundary layer transition; the transition begins near Tap 2. The long decay of Taps 1 and 2 ($5 < \omega c/u_{\infty} < 600$)suggests a viscous dominated boundary region during the transition process. The wall pressure spectrum stabilizes and the streamwise spatial agreement between taps improves in the mid-chord region (Figure 3.61). The shape begins to scale more appropriately to that suggested by Hwang (see Section 1.3) at measurement locations farther downstream. The collapse of the spectra near the trailing edge (Figure 3.62) suggests that the boundary layer is homogenous in the streamwise direction. This observation is of particular use to the aeroacoustic community, where predictions are often based on the spatial averaging of the wall pressure spectra near an airfoil's trailing edge (Blake 1986). spanwise statistics (Figure 3.63) suggest that there is some variation of the boundary layer in the radial direction since the spectral power difference from Tap 25A to Tap 25C is on the order of ~10dB. The pressure side power spectra (Figure 3.64) show a consistent boundary layer across the entire pressure side with a very clear decay rate of ω^{-2} - a viscous dominated boundary layer.

There are a few clear decay rates present among the spectra: the inner scale (high frequency), overlap (mid-range frequencies), and the outer scale (low frequencies). Each scale is characterized by a typical decay rate: an almost constant intensity for the outer scale, a slight decay in the overlap region, and a steep decay within the inner scale. ω^{-5} is a typical decay rate of the inner scale for turbulent boundary layers of any pressure gradient (Hwang et al. 2009). The outer scale and overlap region have decay rates that are dependent of the streamwise pressure gradient. An adverse pressure gradient will cause the pressure fluctuations to decay at a higher rate (Goody and Simpson 2000).

Consider the decay rates of RCDB Case 1 (Figure 3.60 to Figure 3.64), CD Case 1 (Figure 3.65 to Figure 3.69), and RCDB Case 2 (Figure 3.70 to Figure 3.74). It is interesting to note that the spectral decays follow similar trends between the three flow conditions/geometries for corresponding pressure taps. The leading edge region has a large variation between Taps 1-5 for Case 1 flow fields (a function of the boundary layer instability/unpredictability as it transitions from laminar to turbulent); decay rates are similar between corresponding taps of CD and RCDB Case 1 flow fields. The mid-chord region shows similar spectral matching of CD and RCDB Case 1. Tap 6 shows a decay of $\sim\bar{\omega}^{-2.5}$ and Taps 7, 9, and 11 show a decay of $\bar{\omega}^{-5}$ for $200 < \omega c/u_\infty < 600$. The trend continues through the aft region to the trailing edge, where the spectral decay rates and magnitudes match very well for frequencies $50 < \omega c/u_\infty < 600$. RCDB Case 1 has a higher energy for low frequencies ($0.5 < \omega c/u_\infty < 50$) compared to CD. The similarity of the wall pressure spectra across the suction and pressure sides of RCDB and CD Case 1 suggests that a similar wall pressure field exists - further confirmation of matched boundary conditions between the stationary and rotating analog.

It is unclear why the spectra of Case 2 (Figure 3.70 to Figure 3.74) all similarly decay at of a rate $\sim\bar{\omega}^{-2}$ - the interpretation is subject to uncertainty when considering only spectral processing.

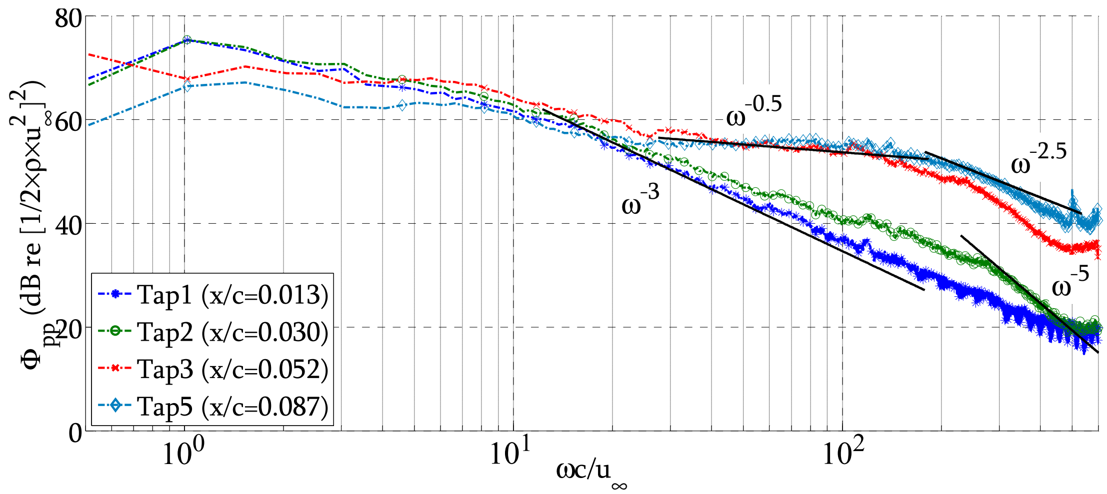

Figure 3.60 RCDB Case 1 fore region

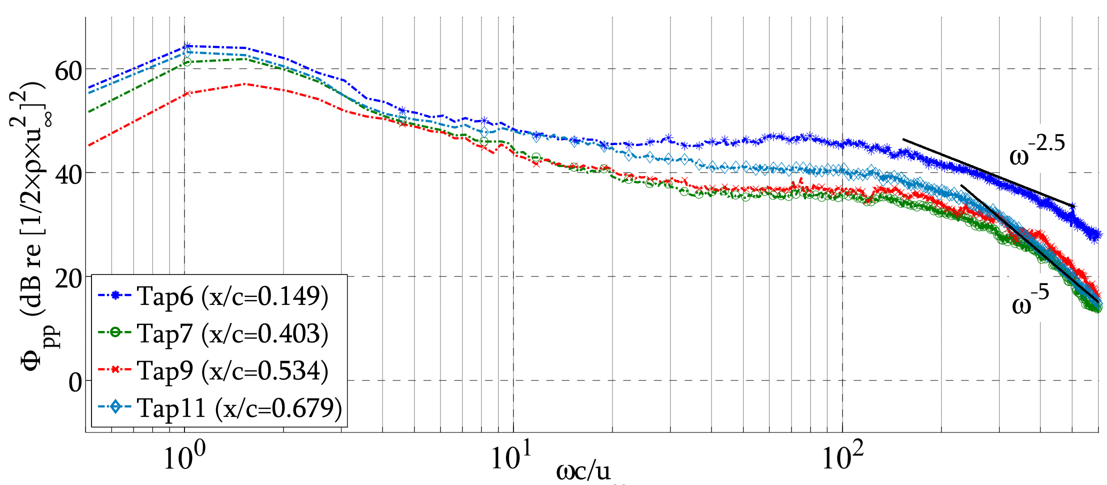

Figure 3.61 RCDB Case 1 mid-chord region

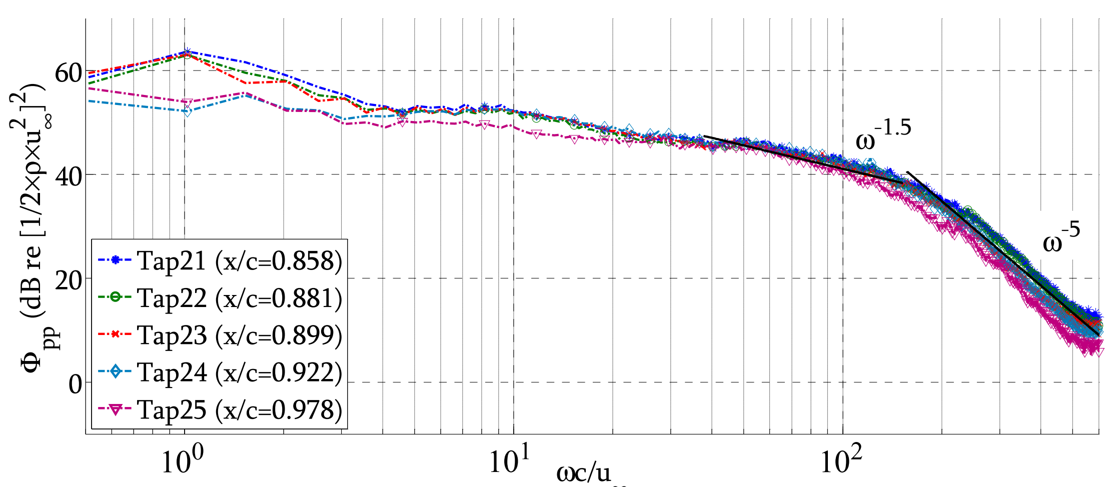

Figure 3.62 RCDB Case 1 aft region

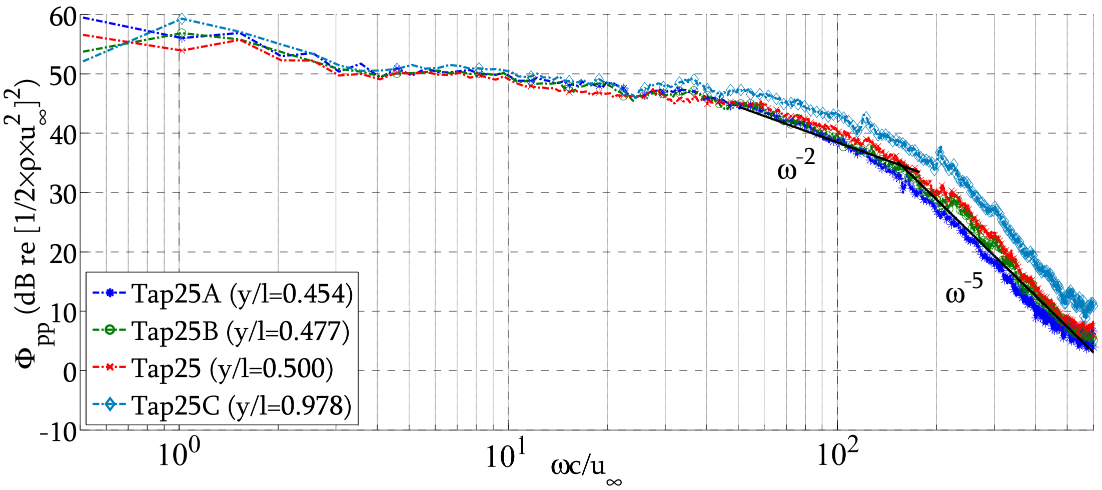

Figure 3.63 RCDB Case 1 trailing edge spanwise region

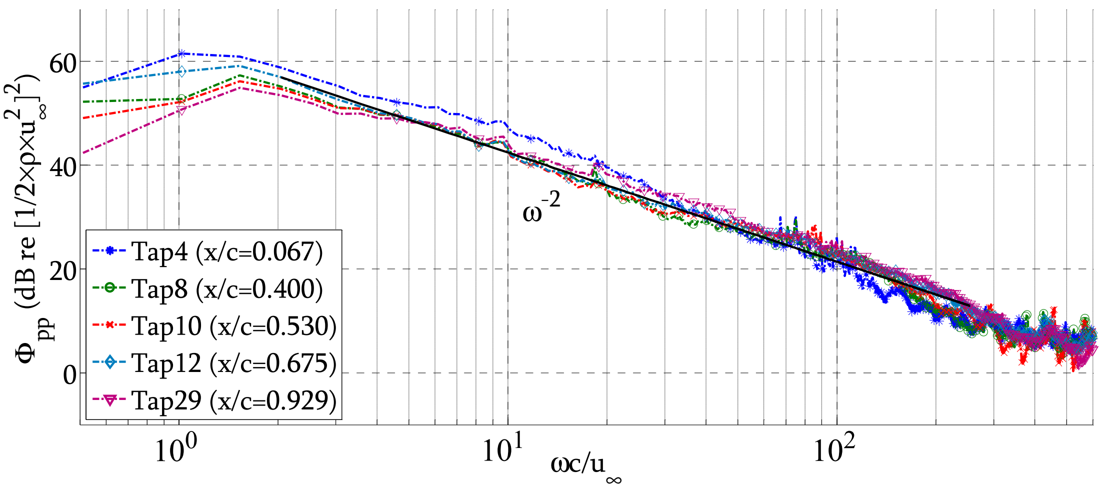

Figure 3.64 RCDB Case 1 pressure side

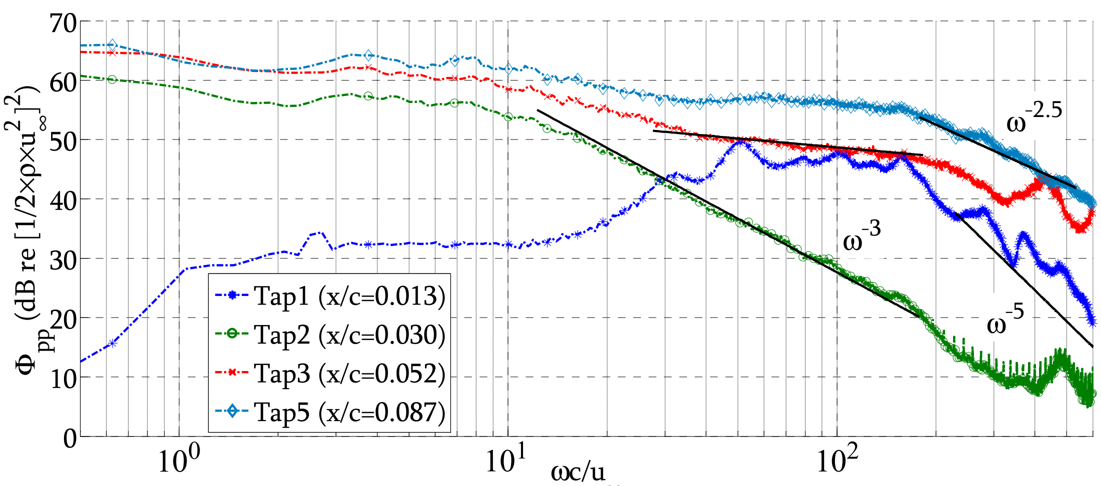

Figure 3.65 CD fore region

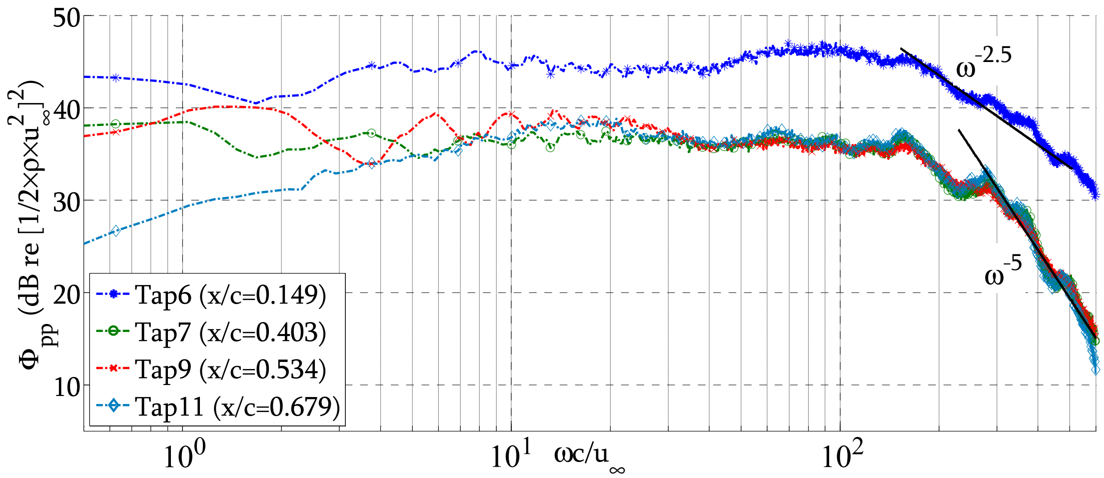

Figure 3.66 CD mid-chord region

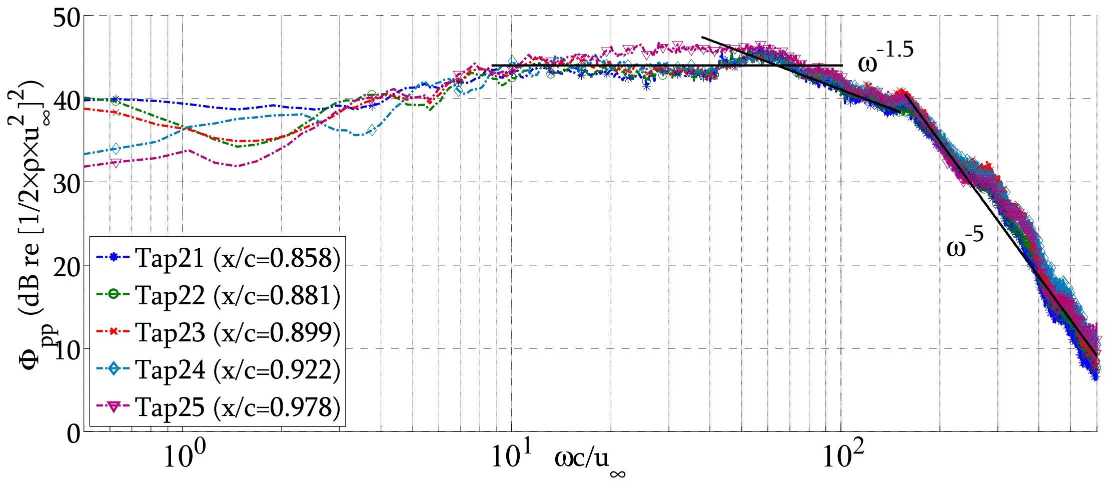

Figure 3.67 CD aft region

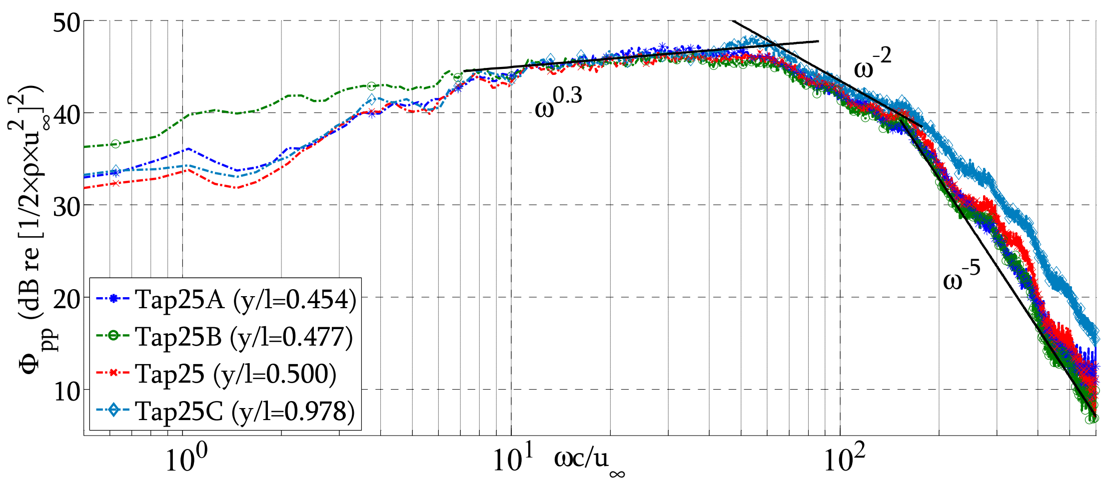

Figure 3.68 CD trailing edge spanwise region

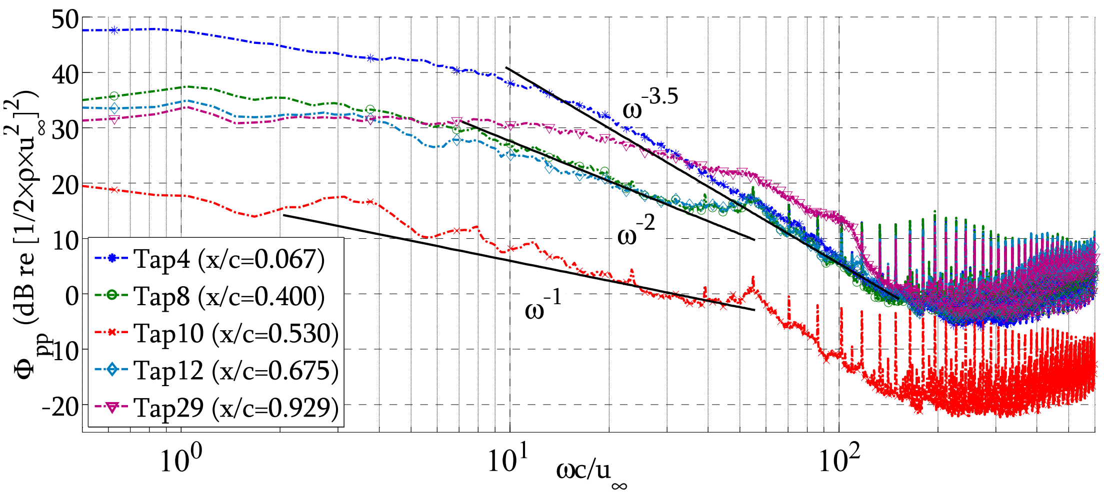

Figure 3.69 CD pressure side

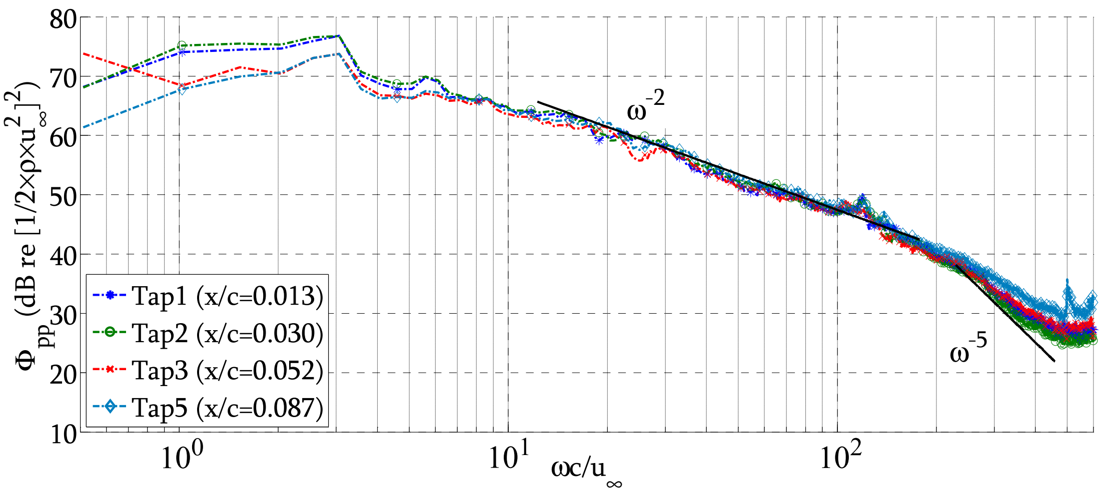

Figure 3.70 RCDB Case 2 fore region

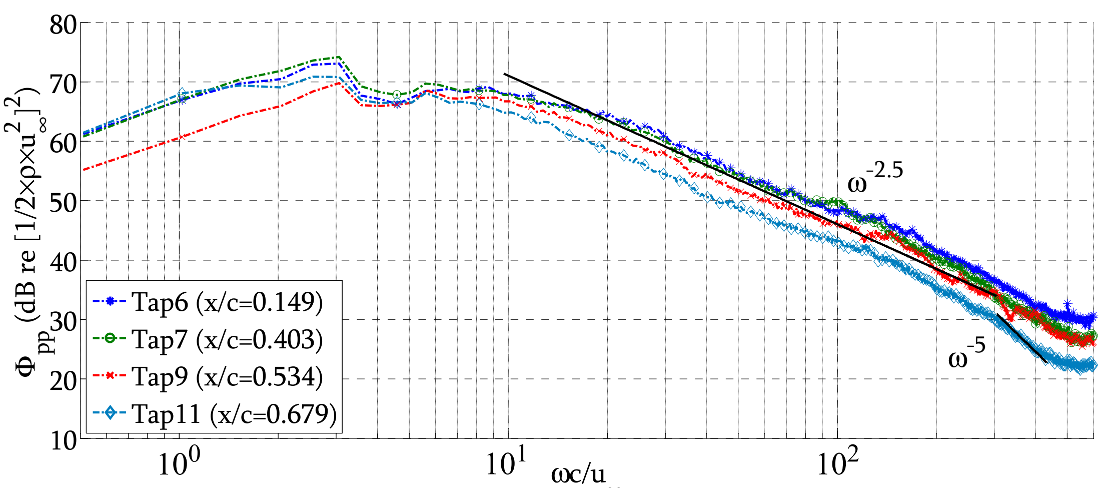

Figure 3.71 RCDB Case 2 mid-chord region

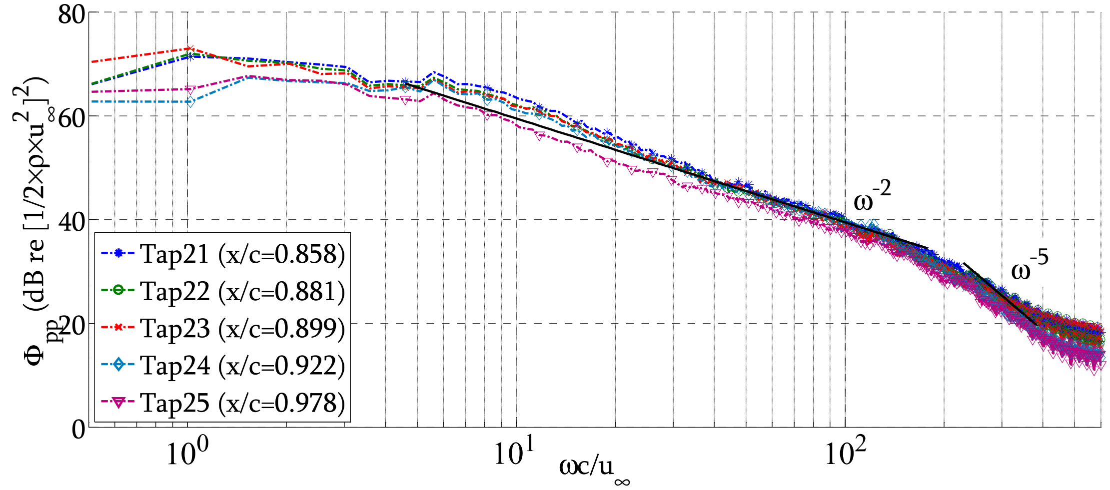

Figure 3.72 RCDB Case 2 aft region

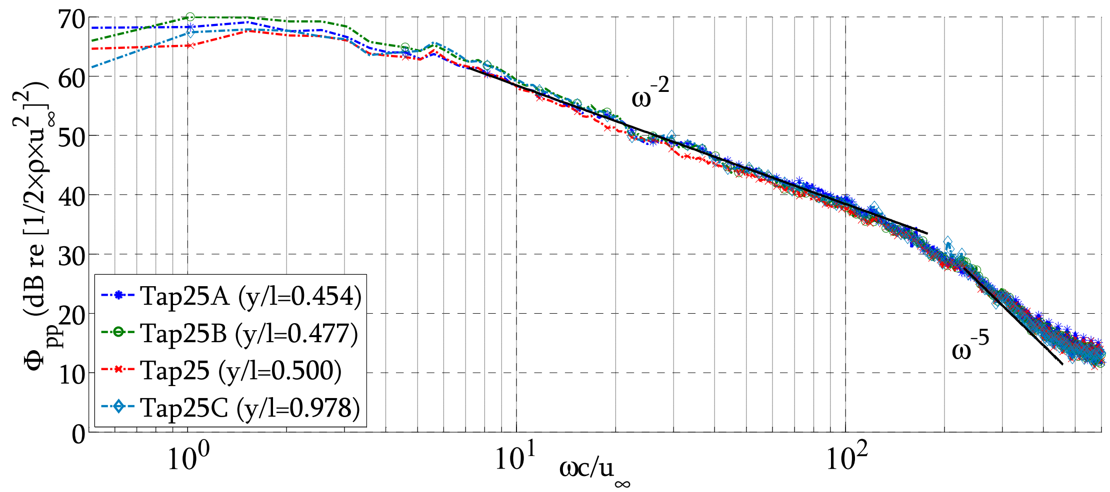

Figure 3.73 RCDB Case 2 trailing edge spanwise region

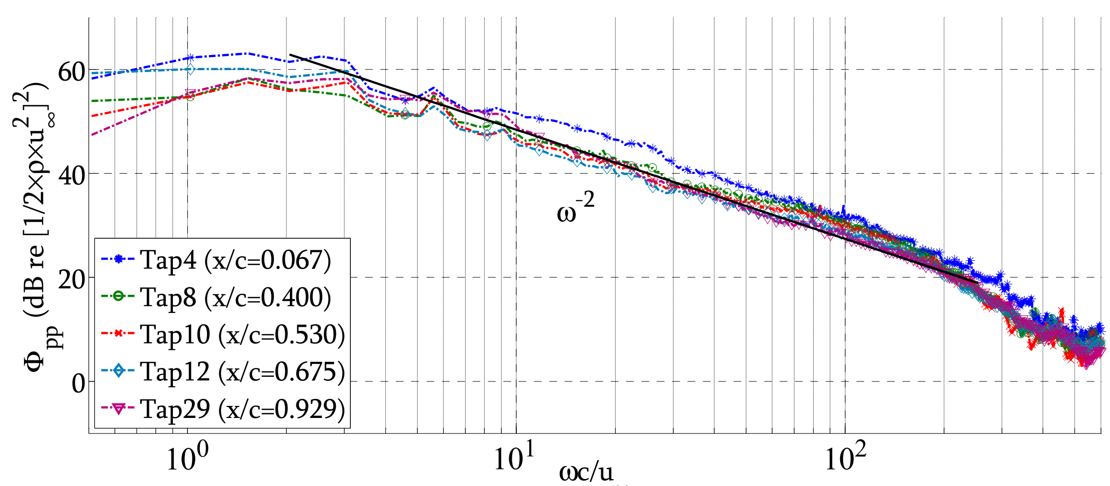

Figure 3.74 RCDB Case 2 pressure side

3.4 Space-Time Correlations

A space-time cross-correlation (R_{pp}) of the fluctuating pressure field between surface taps allows for the "tracking" of a coherent motion. Following the convention of Willmarth and Woolridge (1962) introduced in Section 1.2, this section is designated to calculate some of the useful parameters for predicting acoustic trailing edge noise production: convection velocity, length scales.

The space-time correlations are performed in the trailing edge region only. This is due to geometric constraints - favorable tap spacing in the trailing edge region - and a well established boundary layer in the aft region. Figure 3.75 shows a typical correlation from Tap 21-21, Tap 21-22, Tap 21-23, Tap 21-24, and Tap 21-25. The correlations in Figure 3.75 demonstrate the time-lag (τ) of the boundary layer coherent motions, band-filtered from 200-500Hz (yielding an average frequency of 350Hz). As the streamwise correlation distance (η) is increased, the cross-correlation peak has a time-lad and magnitude decrease. The correlation distance η, defined in Figure 3.76, is the streamwise or spanwise distance associated with the cross-correlation of any two given pressure taps. The speed of the coherent motion is calculated by considering the time lag and the spatial separation - this velocity is known as the convection velocity (U_c). The convection velocity is identified for a set of frequency ranges, each range identifies an eddy of a corresponding wavelength (Willmarth and Woolridge, 1962). Figures 3.77, 3.78, and 3.79 show a small collection of band-filtered space-time correlations for RCDB Case 1, CD, and RCDB Case 1. A more complete set of frequency ranges can be found in Appendix C.1.

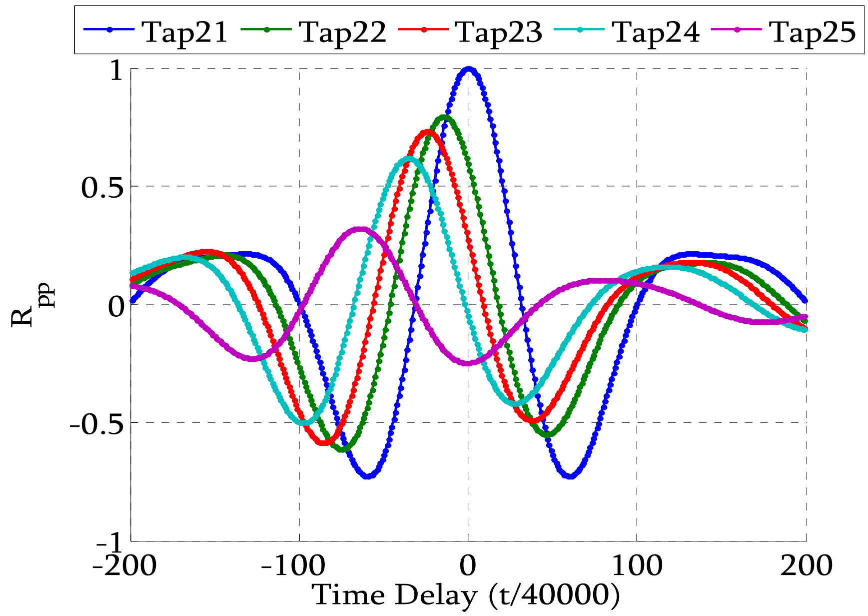

Figure 3.75 Typical space-time correlation (200-500Hz)

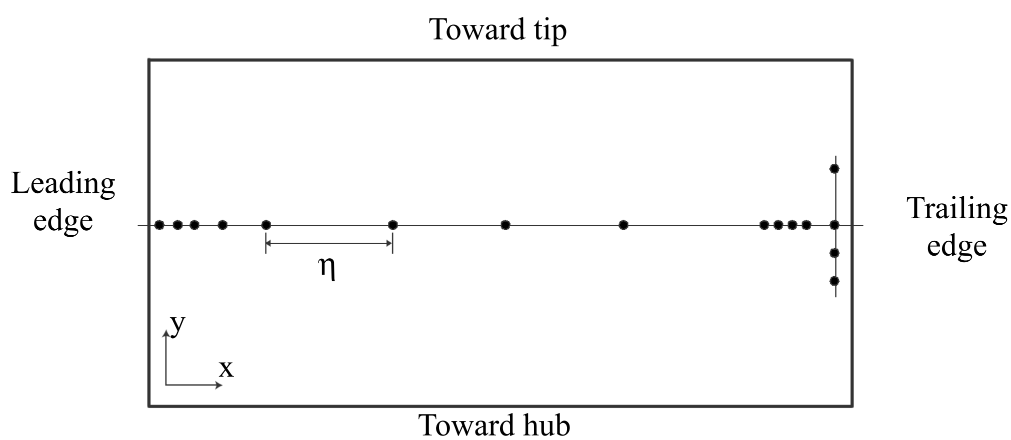

Figure 3.76 Controlled Diffusion surface tap geometry

Figure 3.77 shows the frequency band-filtered correlations of RCDB Case 1 for (a) 400-600Hz, (b) 800-1100Hz, (c) 1300-1700Hz, and (d) 1900-2300Hz. This yields eddy wavelengths (λ_w) following Equation 1.4 of 0.0155m, 0.0091m, 0.0065m, and 0.0043m using average convection velocities inferred from the time-lag of the first three spatial correlations. The convection velocity is averaged spatially from x/c=0.858 to x/c=0.922. Simply, each plot represents the correlation of a given "structure" characterized by the eddy wavelength λ_w. It is seen that correlations are stronger at lower frequencies and deteriorate at higher frequencies as well as at high spatial separation between correlated taps. The weak correlations at high frequency lead to a break-down of U_c calculations; the maximum correlation is no longer in the appropriate range of accepted time delays (note that the typical delay for the correlation of Taps 21-25 is: $0.16 \le tu_\infty / c \le 0.18$). Convection velocity is most accurately calculated for lower frequencies and small tap separation. U_c / u_∞ varies as a function of frequency and has a typical range of 0.5 to 0.7.

Figure 3.78 shows a set of cross-correlations for the CD Case 1 geometry. As in the RCDB Case 1 geometry, the correlations are generally stronger and more stable for smaller tap separations. Convection velocities are higher for higher frequency bands and, because correlations are much weaker over longer separations, the convection velocity is identified as the spatial average over Taps 21-24 (x/c=0.858 to x/c=0.922). The associated λ_w for each plot is 0.0192m, 0.0113m, 0.0073m, and 0.0055m. The stationary airfoil boundary layer's coherent pressure fluctuations travel faster across the airfoil compared to RCDB Case 1; this directly leads to higher eddy wavelengths for the same frequency band. It is interesting to consider that the decay of the pressure fluctuation cross-correlation is a function of convection velocity in addition to the clear frequency dependence - there is a similar trend in the decay of R_{pp} for similar λ_w between the RCDB and CD Case 1. However, it is expected that the stationary airfoil boundary layer has a more stable structure compared to the rotating geometry with similar flow conditions.

The cross-correlations of the off-design operating condition (RCDB Case 2, Figure 3.79) show dramatically different results. From previous spectral information, it is known that the wall pressure field is not consistent with the Case 1 flow field. It is clear that the correlations are much weaker, particularly at high frequencies. The weak correlations make it much more difficult to accurately infer convection velocities and, subsequently, eddy wavelength.

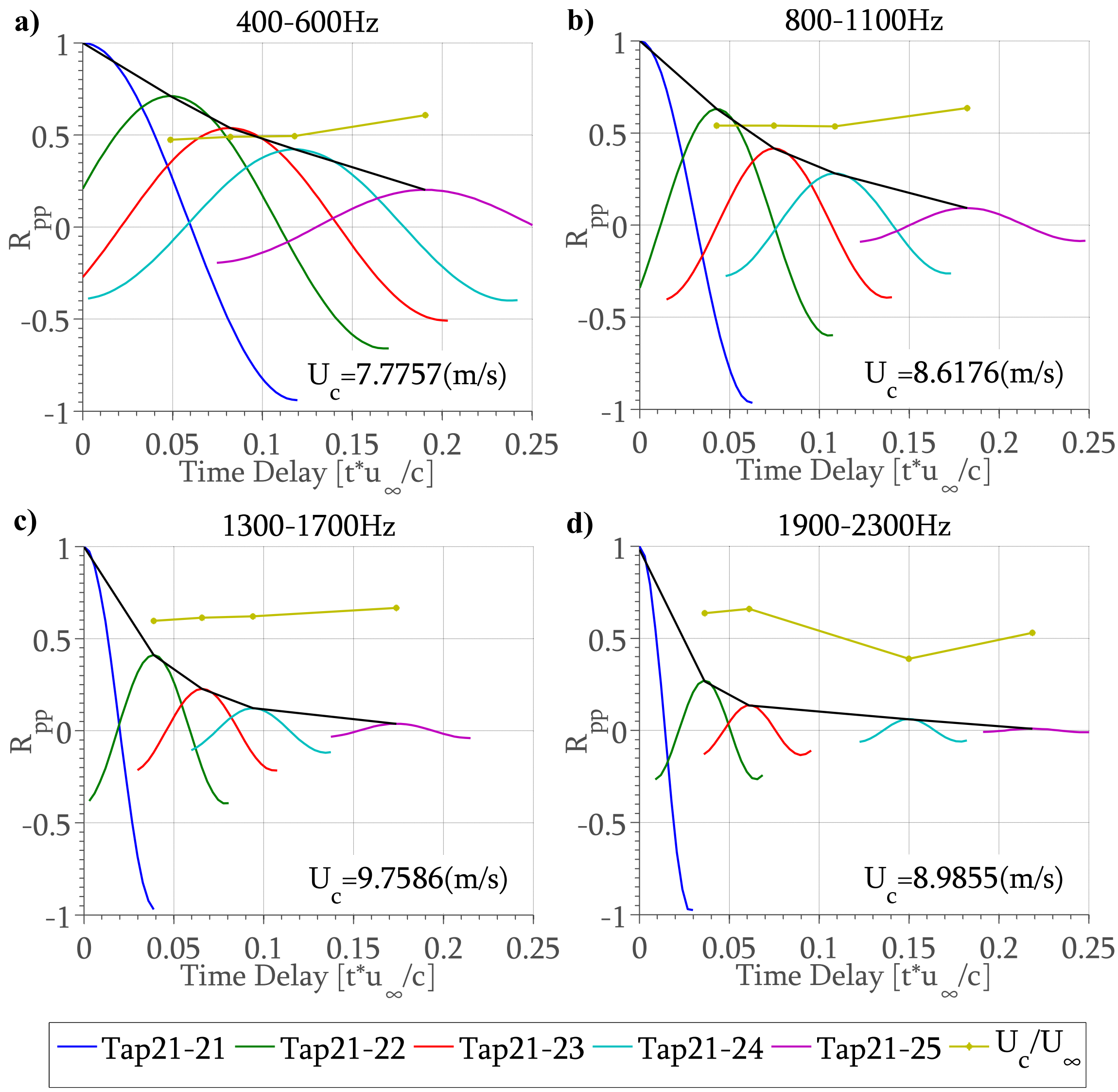

Figure 3.77 Space-time correlations: RCDB Case 1

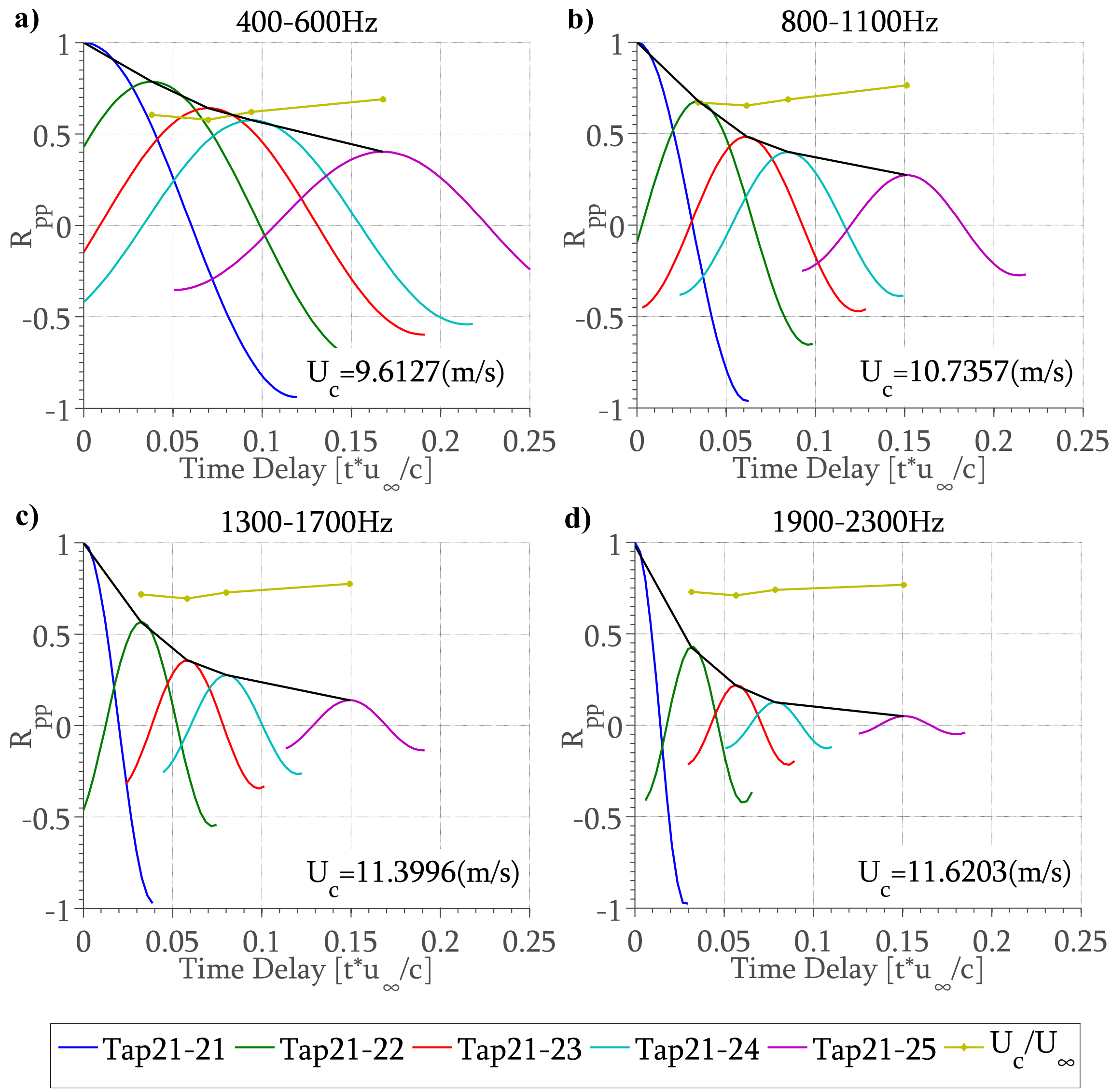

Figure 3.78 Space-time correlations: CD Case 1

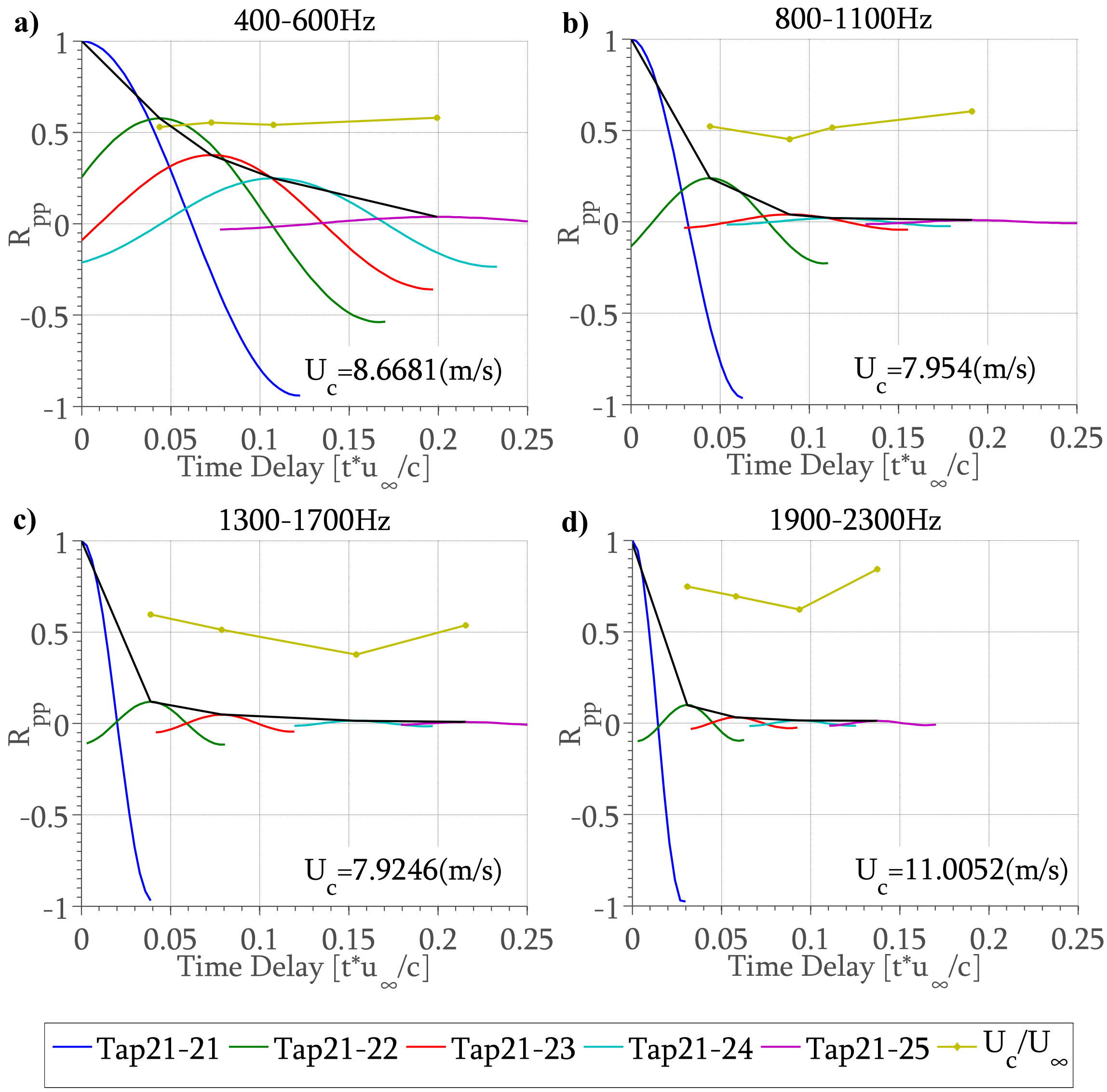

Figure 3.79 Space-time correlations: RCDB Case 2

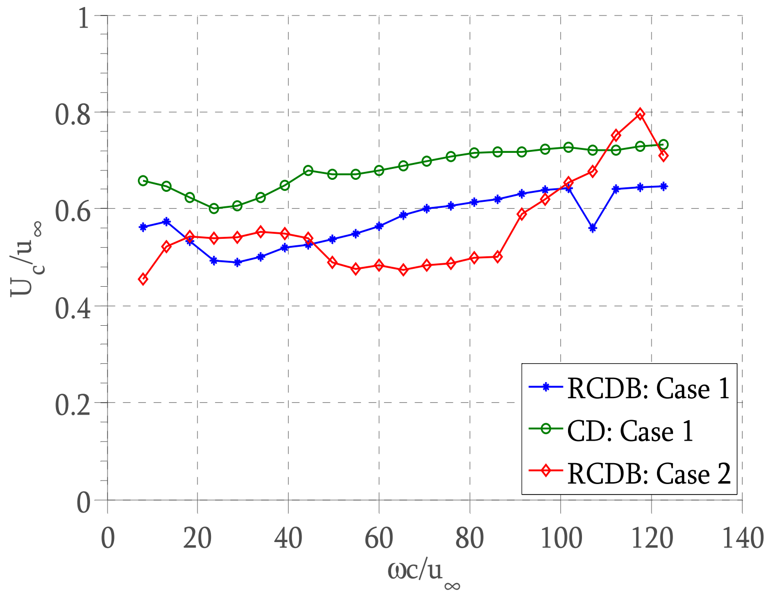

Figure 3.80 Coherent motion convection velocity

Figure 3.80 shows convection velocity as a function of non-dimensional frequency for RCDB and CD Case 1 and RCDB Case 2. It is clear that U_c is a non-linear function of frequency. Interestingly, a similar trend occurs between the CD and RCDB Case 1 geometries. Both show a convection velocity that is a similar function of frequency where the CD Case 1 has a magnitude shift of approximately $0.05 < U_c/u_\infty < 0.1$. The agreement between the RCDB and CD Case 1 convection velocity is very notable - it further reinforces the similarities between the two geometries. As expected, due to difficulties accurately inferring convection velocity, RCDB Case 2 is significantly different from that of Case 1 and the stationary airfoil.

The cross-correlation plots suggested a frequency and spatial dependent systematic decay of the correlated coherent pressure field over the trailing edge region of the airfoil. To quantify this, the cross-correlation is expressed as a function of the normalized eddy wavelength. This follows the convention of Willmarth and Woolridge (1962); the relatively short aft region can benefit from a similar manipulation that Willmarth gave to his canonical flat plate boundary layer. Willmarth's results are reproduced in Figure 3.81. His flat plate boundary layer is characterized by an exponential decay of $10^{-0.3}$. The decay characterization of the canonical flat plate boundary layer is adapted as a distinguishing parameter for the three cases explored in this document. It is important to note that the pressure patterns do not "decay", rather, they evolve to a pattern that is incoherent after some distance downstream.

Figure 3.82 shows the collapse of RCDB Case 1 cross-correlation data. The decay is characterized by a $10^{-0.7}$ exponential decay, where the pressure pattern evolves to a pattern which is not correlatable after nominally four wavelengths. CD Case 1 (Figure 3.83) shows a similar decay pattern - characterized by a rate of $10^{-0.6}$. The slower decay of the CD airfoil boundary layer is an expression of the improved stability of the stationary over the rotating airfoil. Figure 3.84 shows a very steep decay $10^{-1.8}$ for RCDB Case 2. RCDB Case 2 sees a decay of the cross-correlation coherent pressure field after 1-2 wavelengths.

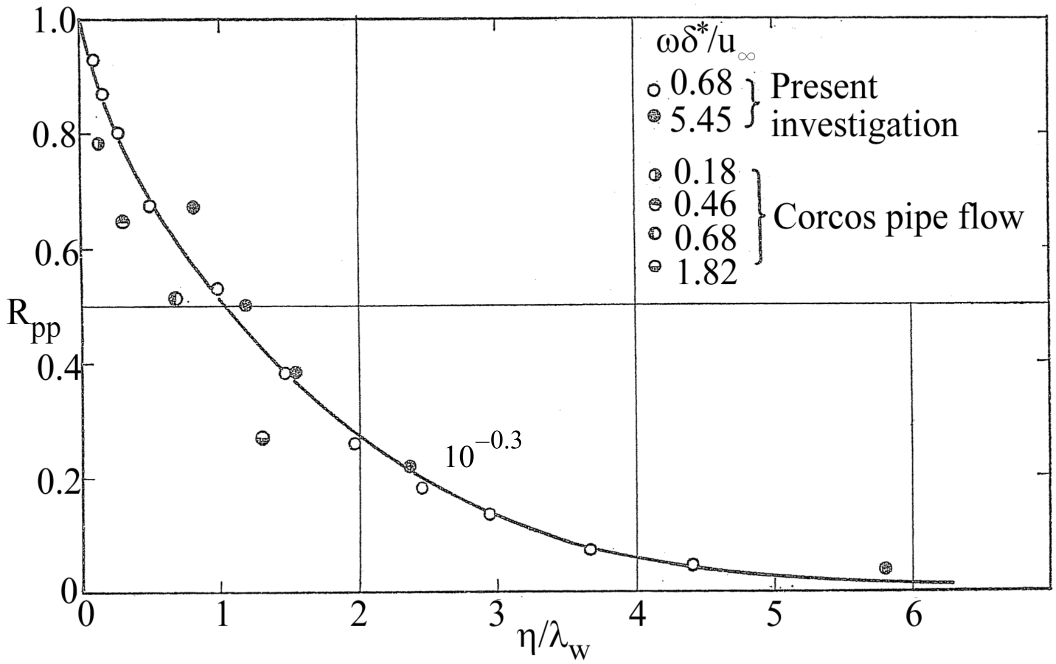

Figure 3.81 Willmarth and Woolridge (1962) decay

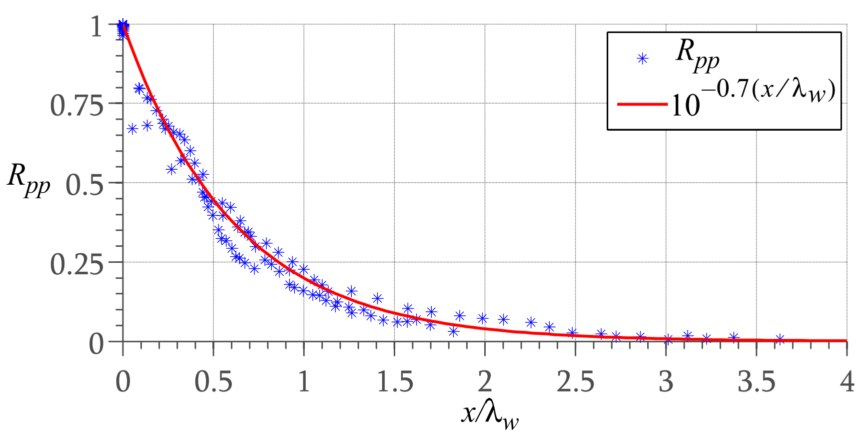

Figure 3.82 RCDB: Case 1 decay

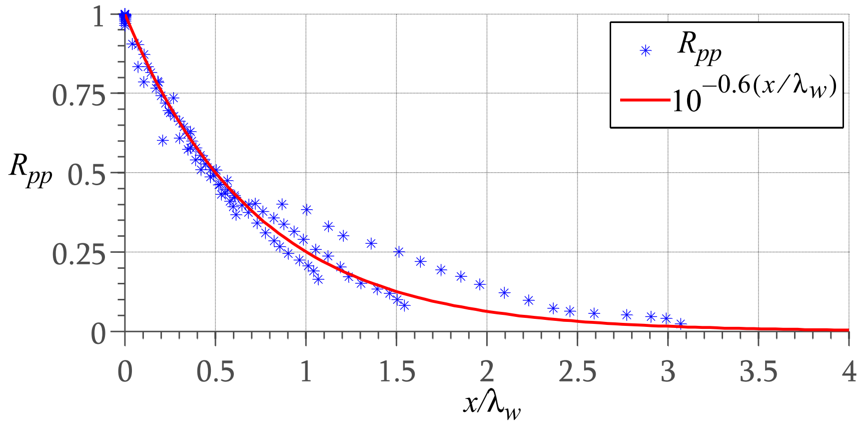

Figure 3.83 CD Case 1 decay

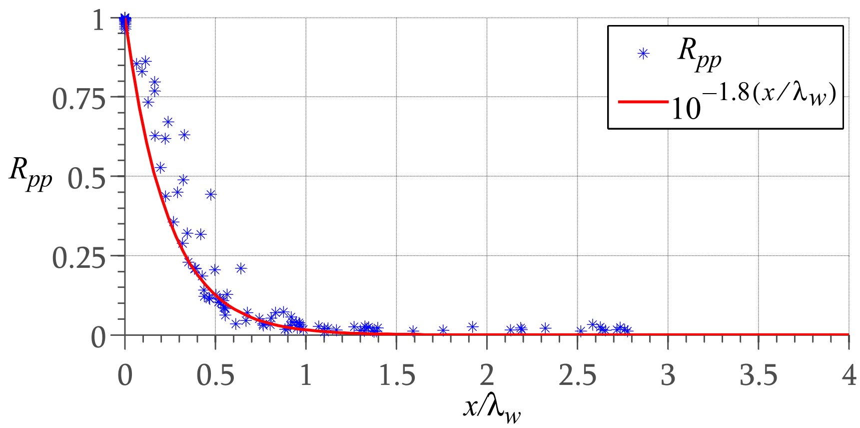

Figure 3.84 RCDB: Case 2 decay

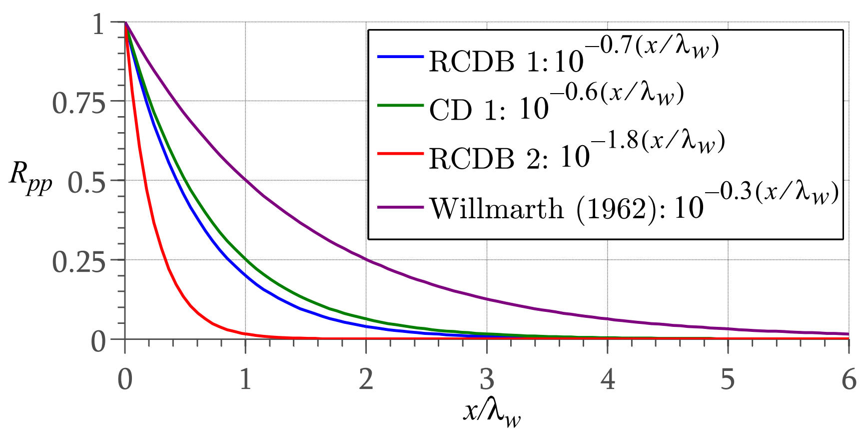

Figure 3.85 Decay comparison

Figure 3.85 shows a comparison of the pressure pattern decay rates between Willmarth's results and the present experiment. It is seen that the RCDB Case 1 and CD Case 1 cross-correlation decay rates are very similar; both wall pressure patterns decay to something incoherent after nominally four wavelengths. The cross-correlation of RCDB Case 2 decays much quicker so that coherent pressure patterns cannot be tracked beyond two wavelengths. The contrasting decay rate of Case 2 distinguishes Case 1 rotting and stationary wall pressure fields as comparatively similar. Additionally, the contrast of the present experimental cross-correlation decay rates to the canonical flat plate boundary layer further reinforces the similarities between RCDB Case 1 and the CD blade as a bounding condition. This is an excellent verification of the stationary-rotating analog.

3.5 Integral Length Scales

Figure 3.86 shows the longitudal (streamwise) cross-correlation (R_{11}) as a function of correlation length, calculated by considering all permutations of tap-to-tap cross-correlations in the trailing edge region. At zero time delay, the correlation R_{11} is purely a function of space; high correlation suggests a wall pressure field that have correlated pressure patterns between taps separated by length η. The integral length scale (Λ_1) is defined as the area under the R_{11} curve (Equation 1.10); Λ_1 is a length scale that identifies a characteristic length to describe the "largeness" of the pressure pattern. The longitudal integral length scale is a useful length scale in the prediction of trailing edge aeroacoustic noise radiation (Blake 1986). It can be seen in Figure 3.86 that there is a slight positive-negative asymmetry, arguing that the cross-correlation is dependent on the direction of the calculation (positive: fore-to-aft or negative: aft-to-fore). The fore-to-aft length scale is 2.949mm, 1.041mm, and 6.612mm for RCDB Case 1, CD Case 1, and RCDB Case 2, respectively.

The aft-to-fore length scale is 3.155mm, 1.074mm and 8.897mm for RCDB Case 1, CD Case 1, and RCDB Case 2, respectively. There is little asymmetry in RCDB and CD Case 1 where RCDB Case 2 is heavily biased in the negative direction. This implies that the boundary layer is uniform in the streamwise direction for RCDB and CD Case 1 and non-uniform for RCDB Case 2.

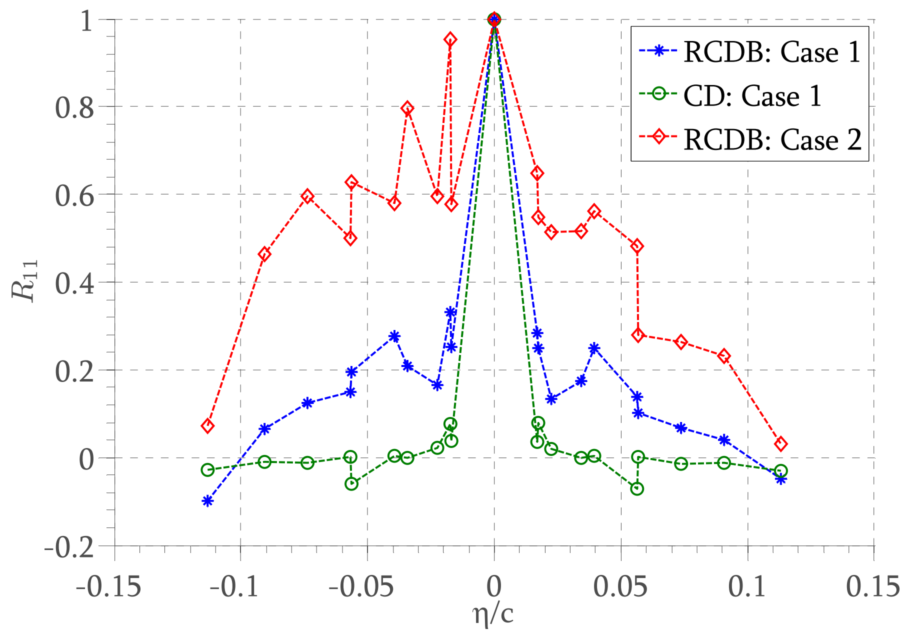

Figure 3.86 Longitudal integral length scale

Note that the connecting lines do not imply trends. The lines exist purely to identify and connect data points from adjacent measurement locations.

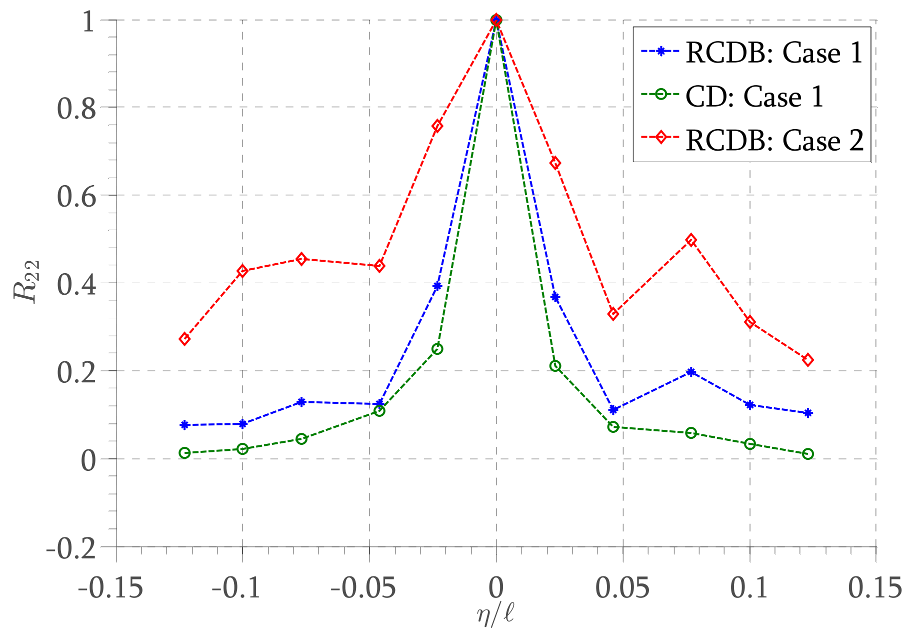

Figure 3.87 Transverse integral length scale
Note that the connecting lines do not imply trends. The lines exist purely to identify and connect data points from adjacent measurement locations.

Figure 3.87 shows the transverse (spanwise) cross-correlation (R_{22}) as a function of correlation length, calculated by considering all permutations of tap-to-tap cross-corrections at zero time delay of the trailing edge spanwise taps. The transverse integral length scale (Λ_2) is defined as the area under the R_{22} curve. The transverse integral length scale is another useful length scale in the prediction of trailing edge aeroacoustic noise radiation. In addition to the streamwise length scale, Λ_2 identifies a length scale associated with the size of the pressure pattern. Again, it can be seen in Figure 3.87 that there is a slight positive-negative asymmetry; the cross-correlation is dependent on the direction of the calculation (positive: hub-to-tip or negative: tip-to-hub). The hub-to-tip length scale is 3.920mm, 2.865mm, and 8.631mm for RCDB Case 1, CD Case 1, and RCDB Case 2, respectively. The tip-to-hub length scale is 4.202mm, 2.713mm and 7.689mm for RCDB Case 1, CD Case 1, and RCDB Case 2 respectively. There is little asymmetry in CD Case

1, suggesting that the boundary is uniform in the spanwise direction. There is mild asymmetry in RCDB Case 1 and Case 2, implying that the boundary layer is non-uniform in the streamwise direction; this is not surprising considering the rotational effects on the flow field.

3.6 Spectral Processing: Coherence and Phase

In addition to the cross-correlation, coherent structures and correlations between pressure taps can be quantified using a spectral coherence function (Equation 1.18). The spectral coherence function represents a statistical value between zero and one - expressing the relationship between two known signals as a function of frequency. This operation produces similar conclusions as the cross-correlation method, but does so with better frequency resolution. The use of the Fast Fourier Transform (FFT) allows calculations to be made in the frequency domain rather than the time domain. Frequency domain calculations are typically less computationally intensive when calculating spectral information and do not rely on filtering algorithms (often poorly tuned) for band-passed frequency results.

Figure 3.88 shows the coherence functions of the trailing-edge pressure taps for the three flow conditions and geometries: (a) RCDB Case 1, (b) RCDB Case 2, (c) CD Case 1. There is generally a higher coherence at lower frequencies; it has already been established that low frequencies propagate farther downstream than high frequencies since the pressure patterns decay spatially as a function of their eddy wavelength. It is seen that correlation is typically highest for adjacent pressure taps and decreases as spatial separation increases; this is a direct result of the evolution of the pressure signal as it propagates downstream. Pressure patterns are created and destroyed across the surface of the airfoil;

but, they are coherent, or trackable, for roughly four wavelengths before they grow or decay into other patterns. RCDB Case 1 shows a plateau from roughly $10 < (\omega c)/u_{\infty} < 40$. This suggests a coherent motion with a strong mid-frequency component; evidence of the plateau is seen, but decays, as spatial separation increases. The CD blade shows a very long coherence in the frequency domain, suggesting that there is a coherent high-frequency pressure signal. The CD blade and RCDB Case 1 coherences are distinguished from RCDB Case 2 by their notably similar spectral decay rates - quantified in the previous section. RCDB Case 2 shows a sharp high coherence peak at low frequencies. This suggests a wall pressure field with prominent low-frequency structures. This supported by the spectral plots that show a shallower decay of high frequency ($100 < (\omega c)/u_{\infty}$) fluctuations compared to RCBD Case 1.

Phase delay is a measure of the delay between sinusoidal components in a random signal as a function of the frequency of the sinusoidal components (Equation 1.19). The phase delay is a useful expression for quantifying the effective frequency resolution of the correlations between pressure taps. Consider Figure 3.89, RCDB Case 1, where the phase of Taps 21-22 is well resolved past $(\omega c)/u_{\infty} = 200$ but Taps 21-25, where η is much larger, the phase factor is only clear to $(\omega c)/u_{\infty} = 90$. This is another way to identify the decay in the pressure pattern after some spatial separation.

Generally, the phase of the flow conditions match well with the conclusions the coherence function yielded. Low frequency content is better defined, as are low spatial separation conditions. RCDB and CD Case 1 (Figure 3.89 and Figure 3.90) show similar phase curves - further reinforcing the similarities between the rotating and stationary geometries. RCDB Case 2 (Figure 3.91) has a much poorer frequency resolution; phase information for Figure 3.91d Taps 21-25 is well resolved to $\omega c/u_\infty \approx 40$ whereas RCDB Case 1 (Figure 3.89d) and the CD blade (Figure 3.90d) resolve phase to $\omega c/u_\infty \approx 100$. This matches the results from the coherence function, indicating a stronger coherent high-frequency component of the pressure signal for the CD blade and RCDB Case 1.

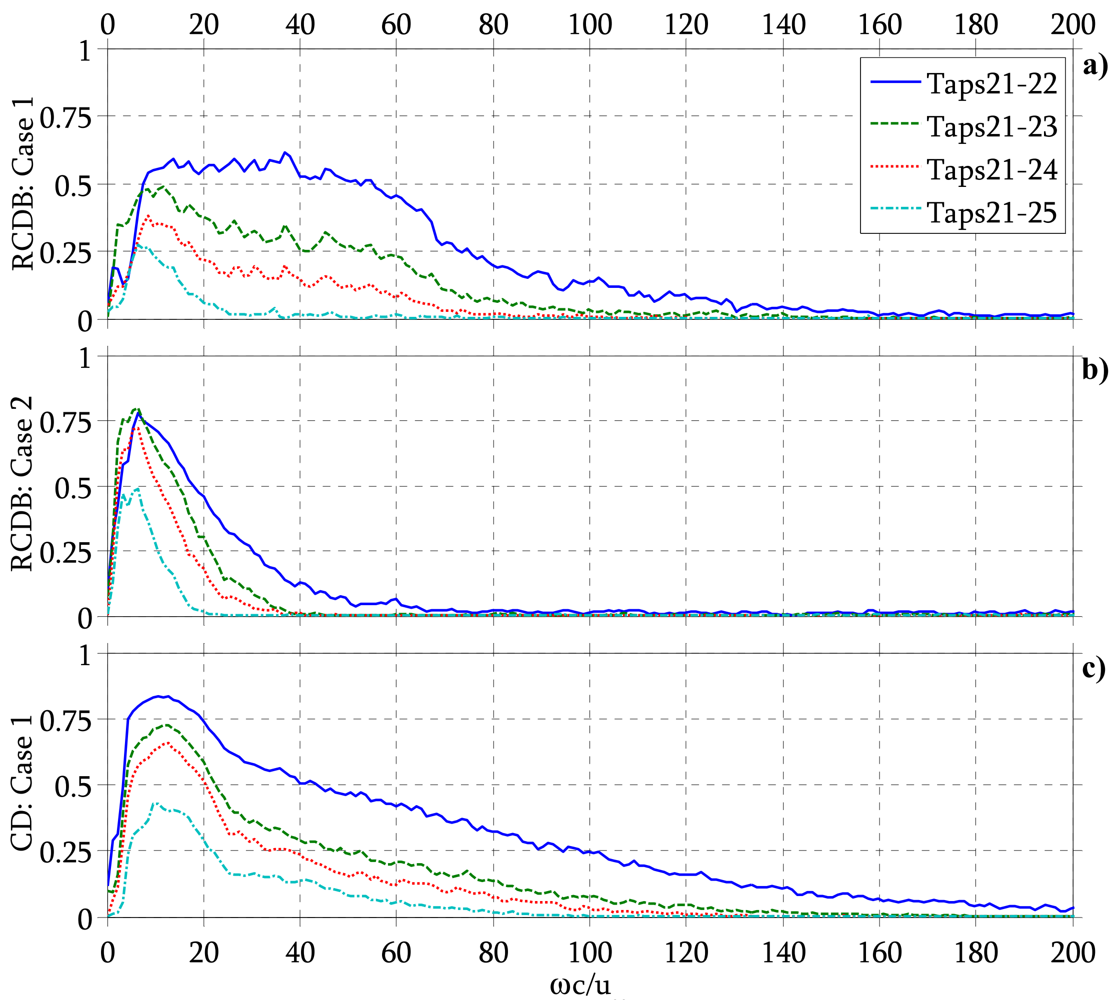

Figure 3.88 Coherence functions

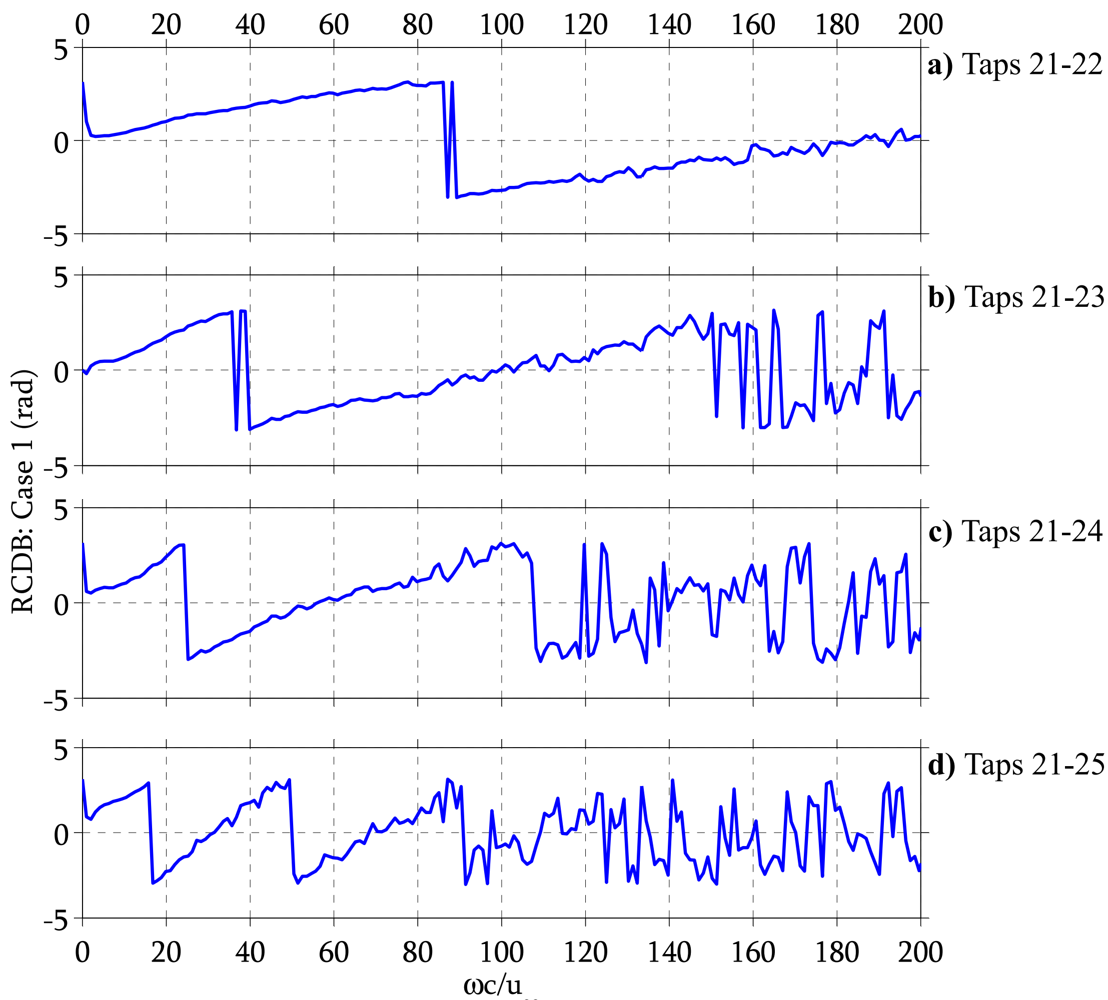

Figure 3.89 Phase RCDB Case 1

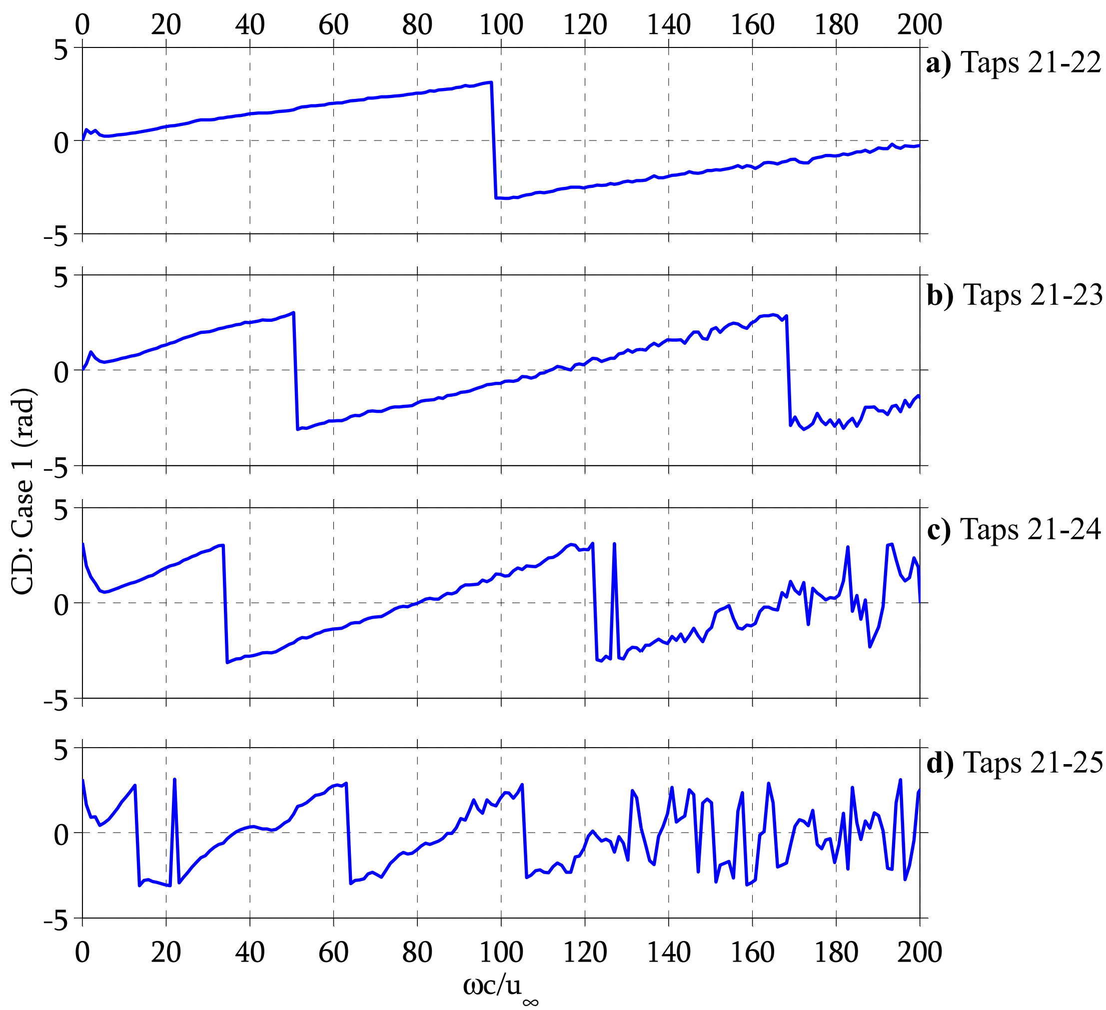

Figure 3.90 Phase CD blade

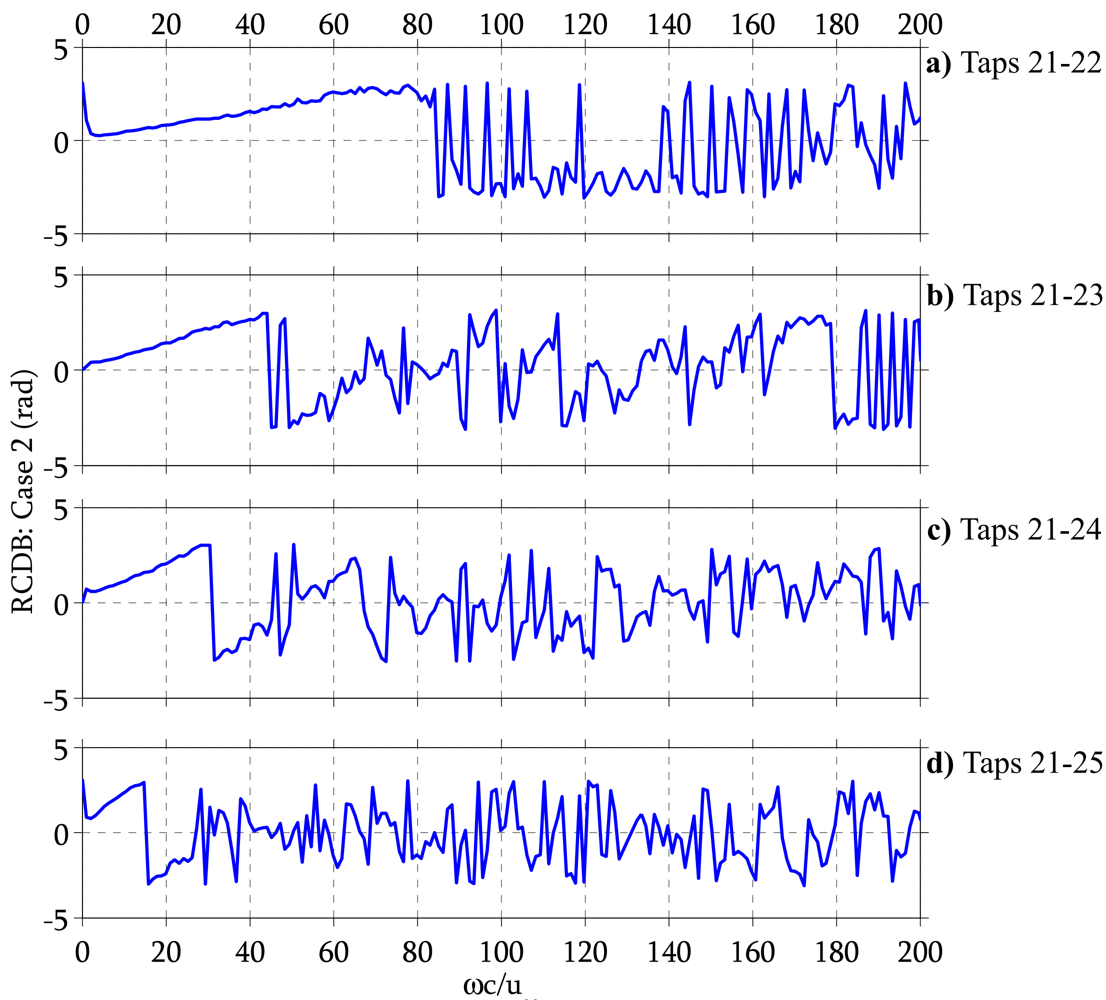

Figure 3.91 Phase RCDB Case 2

Convection velocity can be inferred using the time delay associated with the phase lag of the pressure signals. Linear regions of the phase plot suggest a constant convection velocity over that frequency range. Considering RCBD and CD Case 1, there is a general linear trend, but locally there is significant variation.

Figure 3.92 expresses the convection velocity calculated from the cross-correlation and phase methods for RCDB and CD Case 1. Following Moreau and Roger (2005), the convection velocity is calculated from the phase by:

$$U_c = \frac{2\pi\Delta f\eta}{\Delta\phi} \tag{3.2}$$

where Δf is the width of the frequency bin of the Fourier transform, η is the separation between taps and $\Delta\phi$ is the phase change for a particular frequency bin size. As noted previously, similar trends exist between the RCDB and CD airfoils with a moderate magnitude offset. Additionally, there is a strong similarity between the two methods of calculating convection velocity, particularly with the RCDB. Differences arise from the inherent averaging process in the cross-correlation method (each point represents the center of the band-pass limits - the average frequency). While both methods represent an "average" of the convection velocity, the cross-correlation method averages content for a large frequency range, on the order of 200Hz, whereas the phase calculations average frequency on order of 10Hz. This leads to an unintentional smoothing of the cross-correlation convection velocity. The phase method quantifies transients better and is able to quantify higher frequencies more accurately.

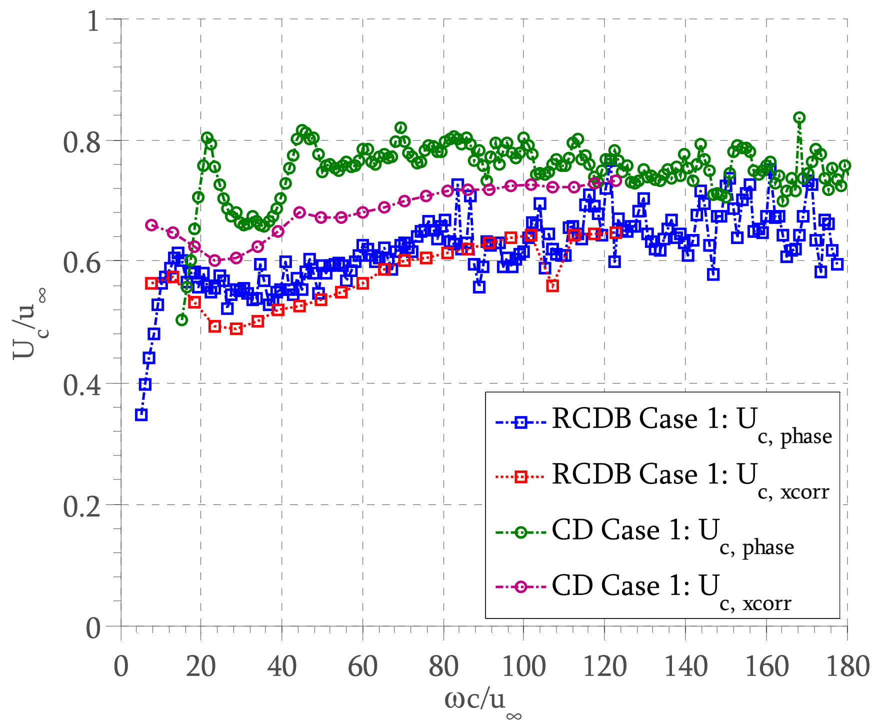

Figure 3.92 Convection velocity comparison CD - RCDB Case 1
Note that the connecting lines do not imply trends. The lines exist purely to identify and connect data points from adjacent measurement

Convection velocity is often a necessary parameter when predicting aeroacoustic noise production. In general, U_c is taken to be a constant value across all frequencies. It is clear from the RCDB and CD airfoils that it is more accurate to describe U_c as a non-linear function of frequency.

3.7 Hot-wire measurements

Trailing edge hot-wire measurements, acquired using the "flying" hot-wire probe, quantify the velocity magnitudes that describe the RCDB wake. The shape and the locations of the defect and shear layer regions supplement the fluctuating surface pressure data by providing velocity data that are used to infer boundary layer shape and size. Wake measurements near the trailing edge are representative of the boundary layer on the blade just before the flow separates off the trailing edge[1]. A schematic of the hot-wire survey and coordinates is shown in Figure 3.93.

Figure 3.94 shows the velocity magnitude and RMS from the hot-wire wake survey of RCDB Case 1. Note that R=0 is the location of the identifiable airfoil trailing edge and the center of the wake moves to higher R values as measurements are acquired in lower z planes - this is a result of non-similar coordinate systems of the hot-wire traverse and airfoil exit velocity. It can be seen that there is a relatively thin wake; at z=1mm the width of the wake is nominally 0.6R/c. The center of the shear layer is identified from the maximum RMS; z=1mm, R/c=0.38; z=3mm, R/c=0.058; z=8mm, R/c=0.088. The width of the wake grows downstream of the airfoil. Velocities higher than the free stream velocity, seen at high and low R, are a direct effect of the fluid accelerating over the airfoil surface, a more extensive survey would yield velocities nearer to the free-stream.

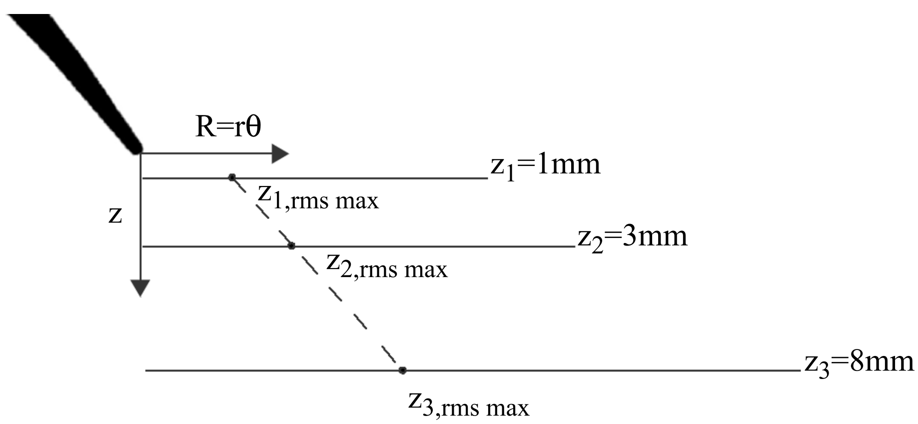

Figure 3.93 Schematic of hot-wire measurements

1. Note that the quantity of hot-wire wake data is limited to three z-rθ surveys. The flying hot-wire survey is time intensive and requires the facility to be shut down and restarted between each discrete location.

Figure 3.95 shows the velocity magnitude and RMS of the RCDB Case 2 wake. It is immediately obvious that there are significant differences between the Case 1 and Case 2 flow conditions. The lack of velocity recovery over the measured regimes suggests that the wake is very thick. A thick wake implies a thick boundary layer at the trailing edge of the airfoil. The thick boundary layer validates and explains some observations from the wall pressure fluctuations. It was previously mentioned that the shape of the C_p curve, suction-side statistics, spectral decay, and correlations were uncharacteristic of the CD blade. The hot-wire measurement provides validation to this observation.

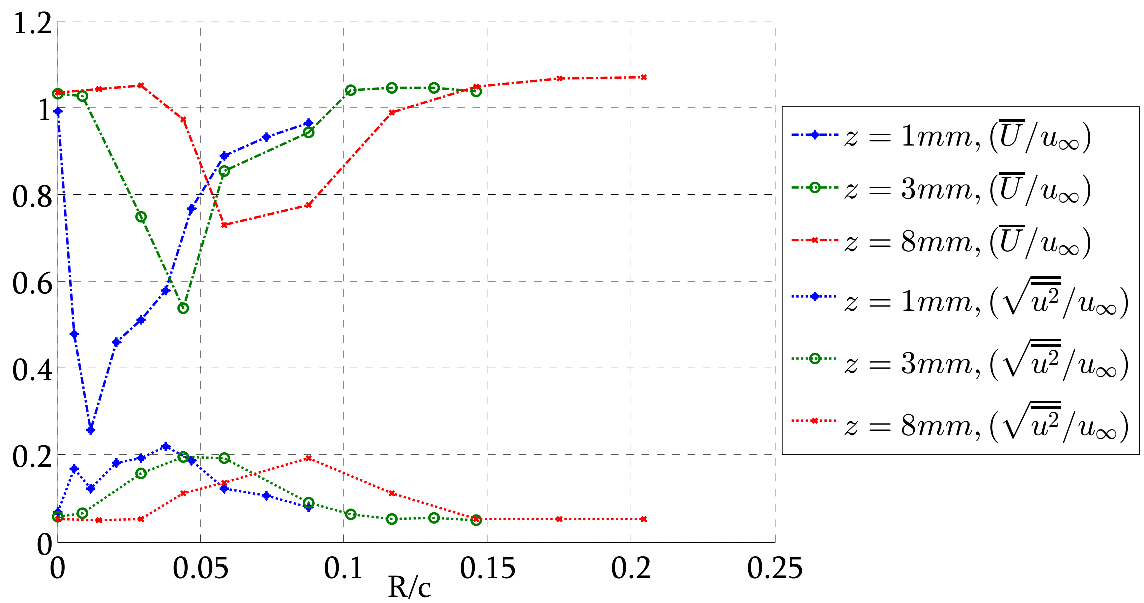

Figure 3.94 Wake Statistics RCDB: Case 1 (*R*=*rθ*)
Note: the line connecting the discrete measurements do not imply intermediate values

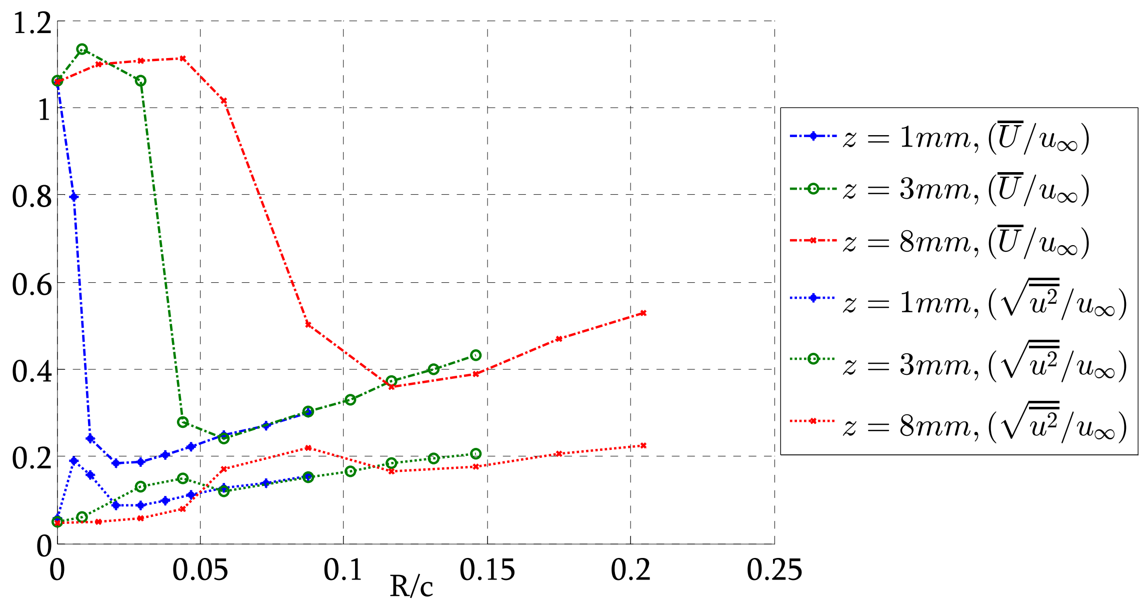

Figure 3.95 Wake Statistics RCDB: Case 2 (*R*=*rθ*)
Note: the line connecting the discrete measurements do not imply intermediate values

It is interesting to compare the pressure spectra and velocity spectra of the trailing edge pressure fluctuations and the wake. Figure 3.96 and Figure 3.97 show the spectra for RCDB Case 1 and Case 2 respectively. Note that the velocity spectra were selected based on the location of the maximum RMS, or the center of the sheared region on the suction side. Note the similarities between the pressure and velocity spectra. Most interesting is the spatial homogeneity of each spectrum. The streamwise pressure spectra near the trailing edge collapse on a common curve and the velocity spectra collapse in the sheared region. Curiously, this spatial homogeneity holds for both RCDB Case 1 and RCDB Case 2. CD data were unavailable to perform a similar comparison.

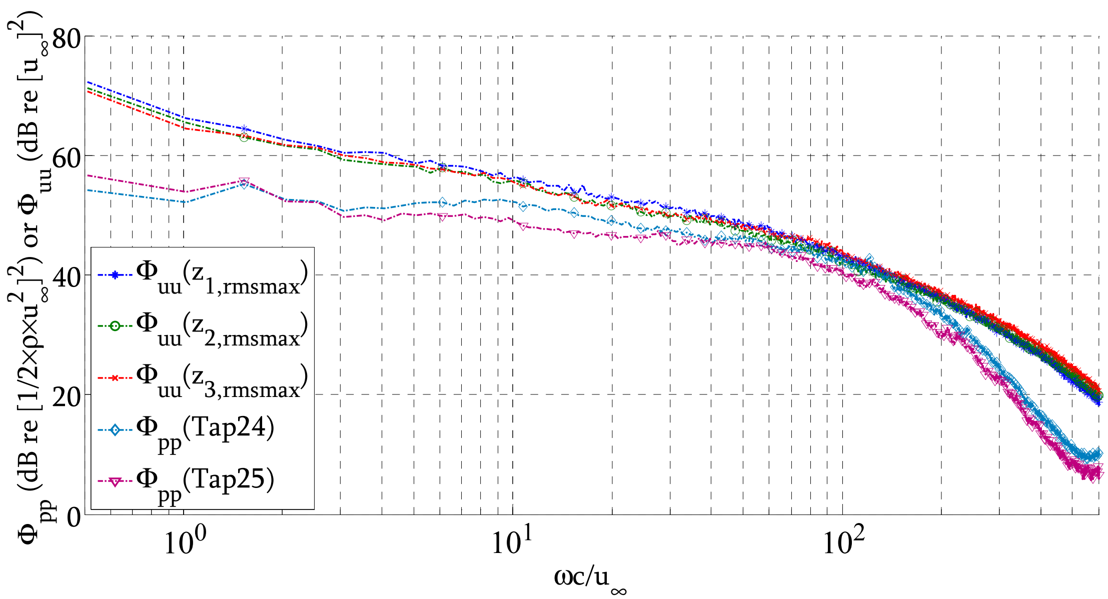

Figure 3.96 Power spectra (u,p) RCDB: Case 1

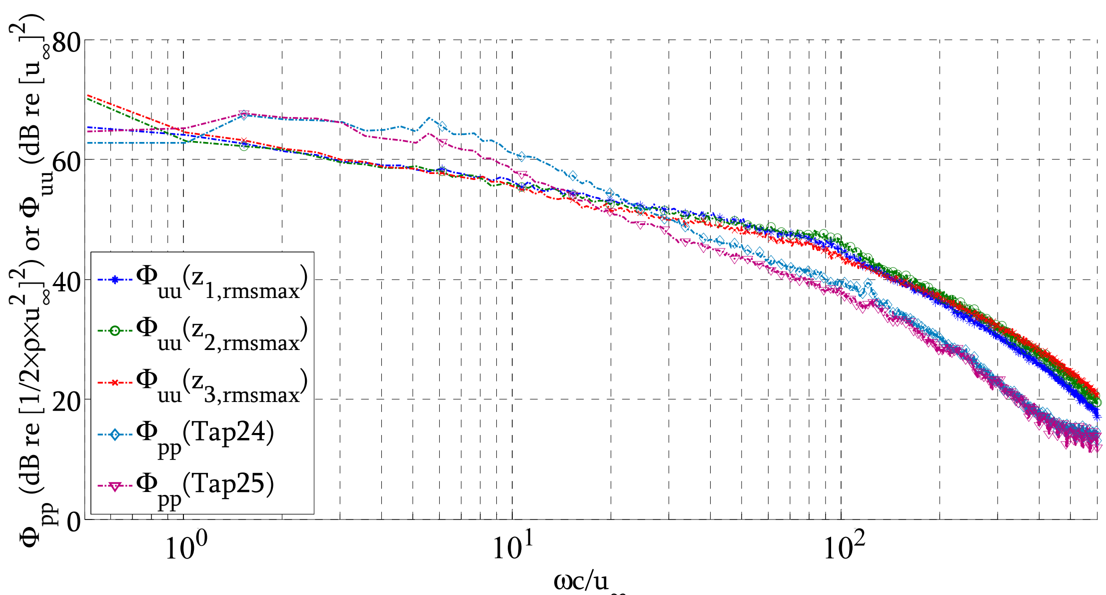

Figure 3.97 Power spectra (u,p) RCDB: Case 2

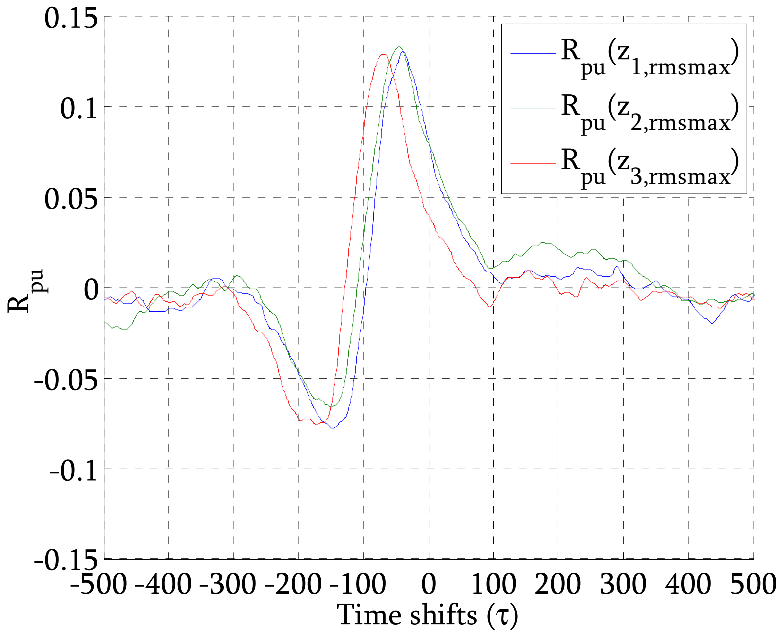

Figure 3.98 Pressure-velocity cross-correlation RCDB: Case 1

Additionally, a preliminary investigation of pressure-velocity cross-correlations was explored (Figure 3.98). Using a similar technique as Section 3.4, the velocity fluctuations of the wake (center of sheared region where RMS is a maximum) are correlated to the trailing edge fluctuating pressure measurements (Tap 25 x/c=0.978). There is a clear time lag between the trailing edge pressure signal and the wake fluctuations; the strength of the correlation is not high, but it is clearly present. Note that Figure 3.98 was calculated over the entire frequency band; filtered frequency bands will yield stronger correlations for a given set of frequencies.

Table 3.1 presents the results from the pressure-velocity cross-correlation. The time delay ($\tau_{measured}$) is measured from the delay in the cross-correlation. A correlation length scale ($\eta_{calculated}$) is calculated using the hot-wire velocity as U_c following Equation 1.2. The distance between the pressure tap and the correlated hot-wire ($\eta_{measured}$) is well resolved from the hot-wire traverse. A time-shift ($\tau_{calculated}$) corresponding to the estimated time delay between the pressure tap and the hot-wire probe is calculated following Equation 1.2 from the known spatial separation and the hot-wire velocity (U_c). The similarity between the estimated and measured time-shifts and spatial separations suggests that the correlation is well-resolved and physical. More detailed measurements would be needed to perform similar analysis as in Section 3.4 and Section 3.6

Table 3.1 Cross-Correlation Results

	$\tau_{measured}$	$\eta_{infered}$(mm)	$\eta_{measured}$(mm)	$\tau_{infered}$
$R_{pu}(z_{1,rmsmax})$	39	9.1	8.6	38
$R_{pu}(z_{2,rmsmax})$	45	11.3	10.85	43.5
$R_{pu}(z_{3,rmsmax})$	68	18.2	17.1	65

4.0 Summary and Conclusions

Measurements were made on a rotating analog (RCDB) of a stationary Controlled Diffusion airfoil. The airfoil shape was reproduced for the rotating blade and the blade's twist (hub to tip) provided a constant angle of attack over the blade span. A method for identifying fluctuating pressures on the surface of the blade was developed using the prior work of Pérennès & Roger (1998) to identify characteristics of the flow structure of the boundary layer along various streamwise and spanwise locations. The development of the the Remote Microphone Probe (RMP) measurements have allowed the similarities and differences between the CD airfoil flow fields to be identified.

The following conclusions are supported by the results of this study. The conclusions are presented in five categories:

1) The characterization of regions along the RCDB and CD blade surface for an incident velocity of 16m/s, a geometric angle of attack of $8°$:

   a) The leading edge region ($0 < x/c < 0.15$) is identified by a boundary layer transition from a laminar to a turbulent state. There is a strong spatial inhomogeneity in the leading edge region due to the boundary layer evolution. These inhomogeneites are expressed by dissimilarities in the leading edge statistics (Section 3.2) and large variations between spectral magnitudes and spectral decay rates (Section 3.3) of the wall pressure field in the streamwise survey.

   b) The mid-chord region ($0.15 < x/c < 0.75$) is identified by adverse pressure gradient boundary layer growth and increasing spatial homogeneity. Statistical moments and spectral magnitudes and decay show modest uniformity in the streamwise direction (Section 3.2 and Section 3.3).

c) The trailing edge region ($0.75 < x/c < 1$) is characterized by a spatially homogenous wall pressure field - similar to a well developed flat plate boundary layer with a mild adverse pressure gradient condition. Space-time correlations and spectral analyses identify a convection velocity, as $0.4 < U_c < 0.65$ for the RCDB and $0.5 < U_c < 0.8$ for the CD blade (Section 3.4 and Section 3.6). The convection velocities are a nonlinear function of the frequency of the fluctuations.

d) The trailing edge spanwise measurements ($x/c = 0.98, 0.45 < y/l < 0.58$) reflect the spanwise uniformity of the boundary layer. Statistical and spectral results demonstrate that the radial variations of the RCDB boundary layer are minimal (Section 3.2).

e) The pressure side wall pressure field of the RCDB is characterized by uniform pressure statistics and a spectral decay that corresponds to a viscous dominated boundary layer (Section 3.2 and Section 3.3).

2) The processed results for the fluctuating pressures of the rotating analog (RCDB) of the Controlled Diffusion blade are found to be in good agreement with the results for the stationary Controlled Diffusion Blade. This conclusion was quantified through a comparison of the mean and fluctuating pressure evaluations (The agreement of the mean values was observed by Neal 2010). Similarities in the following measurements argue for similarities in the wall pressure fluctuations and, as an extension, the boundary layer:

a) The profile of the pressure coefficient (C_p) is well matched for the suction side blade loading. There is a slight magnitude shift for the pressure side (Section 3.1).

b) Fluctuating pressure statistics quantify the agreement of the wall pressures at corresponding tap locations following reattachment of the boundary layer (Section 3.2)

c) The magnitude and decay rates of the pressure spectra for corresponding regions are also well matched (Section 3.3). Space-time correlations and spectral processing of trailing edge fluctuating pressures show similarities in the spatial decay rates and coherence functions, the magnitude of the boundary layer convection velocity is higher for the CD blade but follows a similar trend to that for the RCDB. Pressure patterns decay to zero correlation after ~4 wavelengths (Section 3.4 and Section 3.6)

3) The trailing edge hot-wire wake survey in the present study confirms wake measurements made of the RCDB and CD blade by Neal (2010); the wake profile of the RCDB is very thin, with a notable shedding phenomenon around f=1800Hz. The spectra of the wake survey where the highest velocity RMS values occurred collapsed onto a single curve for each plane surveyed. Correlation between pressure and velocity, although weak, showed agreement between calculated and measured time lags τ and correlation distances η (Section 3.7).

4) The CD/RCDB experiment, when outfitted with unsteady surface pressure sensors, is capable of measuring and calculating pressure spectra and length scales

- streamwise and spanwise - along the airfoil trailing edge. These measurements are designed to provide better predictive capabilities for acoustic noise models as discussed in Section 1.3.

5) An off-design condition (RCDB Case 2), corresponding to an incident velocity of 16m/s and a geometric angle of attack of 15°, was investigated. Principal results relative to RCDB Case 1 (design point) are:

   a) A dissimilar pressure coefficient curve between Case 1 and Case 2 (Section 3.1) - the blade in Case 2 is more highly loaded. The statistical moments have higher magnitudes at all x/c locations (Section 3.2); there are more intense and random pressure fluctuations along the surface of the RCDB Case 2 blade.

   b) RCDB Case 2 has higher spectral power for low frequencies and decays, as a function of frequency, at a much slower rate (Section 3.3).

   c) The coherent motions of the pressure field spatially decay more rapidly in RCDB Case 2. Correlated pressure patterns decay to zero correlation after approximately 2.5 wavelengths as compared with a decay of approximately 4 wavelengths shown by CD and RCDB Case 1 flow fields. Similarly, the maximum frequency of correlated pressure patterns is lower (Section 3.4 and Section 3.6).

   d) Hot-wire measurements indicate a much wider wake for the off-design flow field. This suggests that there is a very thick boundary layer at the separation lip of the blade.(Section 3.7).

APPENDICES

Appendix A: Remote Microphone Probe Development

This appendix will detail the development and implementation of the RMP device.

A.1 RMP Motivation

In order to measure pressure fluctuations with a boundary layer, microphones are typically flush-mounted to the surface of some bounding geometry. Flush-mounting requires the size of the microphone sensor to be sufficiently small but with now noise and high sensitivity. This places limitations on sensor type; conventional condenser-type microphones are too large. Small capacitive and MEMS-Bases microphones have become popular in recent years for their size and improved quality. Considering the geometry of the present experiment, a thin heavily cambered airfoil, it is very difficult to instrument the surface with adequate resolution and accurate sensors. In order to make the necessary measurements, it imperative that the microphones are located at some "remote" distance from the tap itself.

Remote mounting the microphones traditionally embedded in the surface satisfies the need for high spatial resolution measurements for a thin, heavily cambered airfoil. The remote microphone probe (RMP) infers the fluctuating surface pressures by measuring the local pressure fluctuations within a small channel, excited by pressure fluctuations at the start of the channel: the airfoil surface. The associated challenges to fabricate, install and calibrate the RMP system are presented in the following sections.

A.2 Development

Pioneering measurements from (Willmarth and Woolridge 1962) demonstrations the possibilities of using fast-response pressure transducers for characterizing a boundary layer. Additional work of Sheplak et al. (2001), Moreau and Roger (2005), Gerakopulos and Yarusevych (2012), among others extended the use of microphone transducers for the use on an airfoil surface. Each of these modern experiments required a method to characterize frequency and magnitude response of the array of test microphones used within the experiment. Due to the rotating nature of the present experiment, an evolved microphone technique was needed to accurately and precisely, measure the fluctuating pressures along the airfoil surface.

A.2.1 Measurements/calibrations/previous work

Following the work of Sheplak et al. (2001), Moreau and Roger (2005), Boerrigter and Charbonnier (1997), a method to identify frequency response calibrate the microphone sensors was developed. A plane wave tube (PWT) was fabricated following AES standard AED-1ID-1991, ASTM standard E1050-10, and suggestions from the work of Magalotti et al. (1999) and Anderson (2003).

A source driver is located at one end of the PWT while the other is left open to the lab environment. The PWT, with a uniform cross section across the length of the duct, establishes a one-dimensional sound field within the tube when excited by the source driver. Under steady state conditions, the one-dimensional sound field condition is satisfied and the acoustic pressure is uniform over a given cross section of the duct. Microphones placed along the wall of the duct at the same cross section will measure identical acoustic pressures; the microphones measure the field at the same nodal line.

The PWT apparatus in the present experiment is a 12.7mm by 12.7mm square tube 1.5m long. Microphones are located on the same cross section 0.6m from the duct entrance. Following ASTM E1050-10, it is suggested that the length of the tube be sufficiently long enough to prevent non-plane waves. Non-plane waves typically subside by three tube diameters; as such, it is suggested to place microphones at distances greater than three diameters. A schematic of the PWT is shown in Figure A.2.1.

The working frequency range of the PWT is limited by a lower and upper limit; identified by geometric limits. It is recommended that the microphone spacing be greater than one percent of the wavelength of the lowest frequency. In reality the lowest resolvable frequency is determined by the driving speaker (approximately 200Hz). The high frequency limit is generally determined by the physical dimensions of the device following Equation A.1.

$$d < 0.5c/f \qquad \textbf{A.1}$$

where f_u is the upper frequency limit in hertz, c is the speed of sound and l is the largest sectional dimension of the tube. The high frequency limit for the present PWT corresponds to approximately 13.5kHz.

The critical aspect of the PWT is that at a given cross section, or nodal line, the pressure signal is uniform across all surfaces. This idea is fundamental for the use of the PWT as a calibration device. A broadband speaker (Dayton PA130-8) is driven by a high-quality reference amplifier (Behringer A500) to excite the PWT. A broad-spectrum white-noise signal provides sufficient spectral content to infer microphone sensitivity functions from approximately 50Hz to 20kHz.

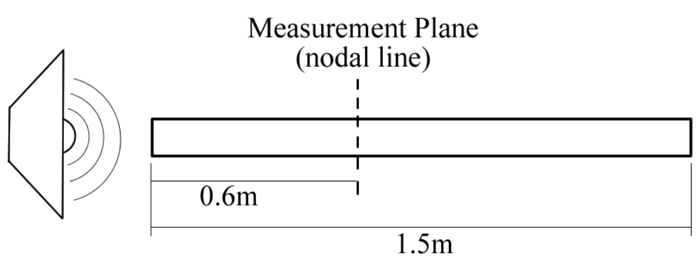

Figure A.2.1 PWT schematic and specifications

A.2.2 Signal processing/Calibrations

Each RMP device is identified as a simple single-input/single-output model where the blade is modeled as a single-input/single-output model with 21 parallel transmissions. Consider the RMP system (Figure A.2.2), where x(t) and y(t) are the input and output of the model. y(t) is the fluctuating pressure measured remotely by the RMP microphone and x(t) is the fluctuating pressure at the surface. The attenuation of the transmitted signal associated with the tubing, and electrical responses is represented by the system response function, or, transfer function $H_{xy}(f)$. Where $H_{xy}(f)$ is the parameter that defines the relationship between the pressure measured at the remote microphone and the pressure measured at the airfoil surface.

The recommended method for calculating $H_{xy}(f)$, following Bendat and Peirsol (1986) is:

$$H_{xy}(f) = \frac{G_{xy}(f)}{G_{xx}(f)} = |H_{xy}(f)|e^{-j\phi(f)} \qquad \textbf{A.2}$$

where G_{xx} and G_{xy} are the auto and cross-spectral densities. The magnitude factor and phase factor can be estimated by

$$|H_{xy}(f)| = \frac{[C_{xy}^2(f) + Q_{xy}^2(f)]^{1/2}}{G_{xx}(f)} \qquad \textbf{A.3}$$

$$\phi(f) = \operatorname{atan}(C_{xy}(f)/Q_{xy}(f)) \qquad \textbf{A.4}$$

where $C_{xy}(f)$ and $Q_{xy}(f)$ are the real and imaginary parts of the cross-spectrum $G_{xy}(f)$

.

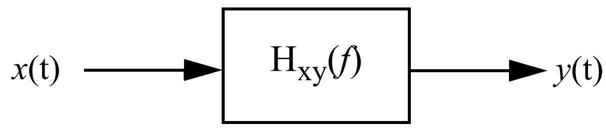

Figure A.2.2 Linear input-output system

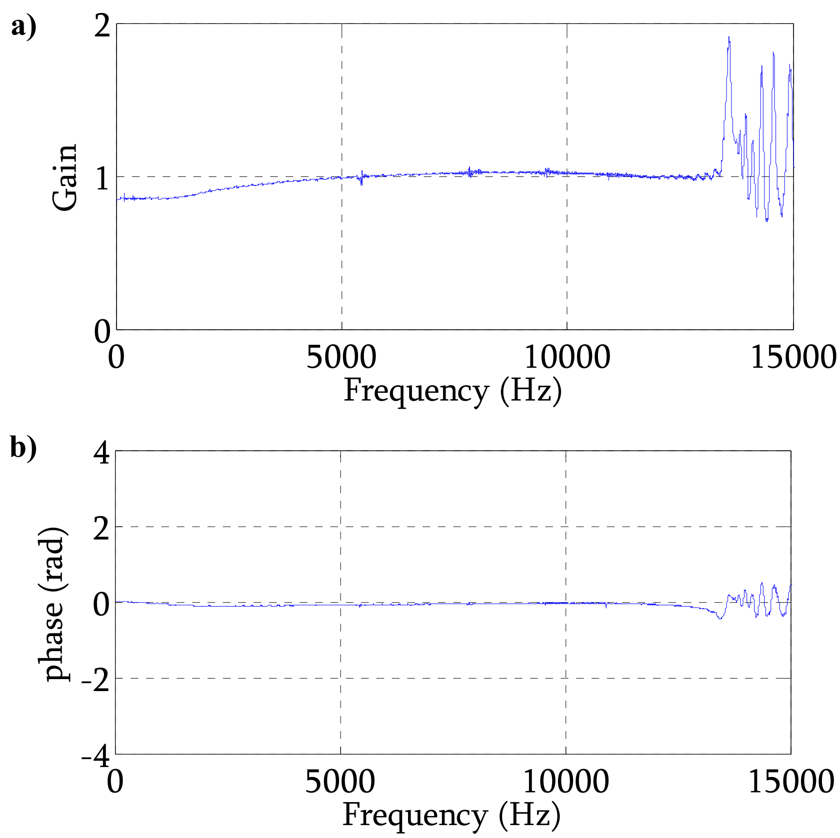

Figure A.2.3 Larson Davis transfer function

The amplitude and phase response of the system are analogous to the 'transfer function' referred to in the engineering community. A sample function generated from a calibration is seen in Figure A.2.3. Figure A.2.3 shows the gain and phase factor for two phase and gain matched reference microphones in the PWT. A gain of 1 and phase of 0 indicates the microphones are paired. Note the breakdown of the calibration around 13.5kHz; a representation of the high frequency limit of the device.

As mentioned in the main text, the PWT was not a suitable device to perform the calibration of the RMP devices. An open-air *in situ* method was developed to allow for more complex geometries. To verify the accuracy of the method, a rig (FIGURE) was developed using known, phase and magnitude matched reference microphones. The reference microphones are held at some distance apart and traversed until their faces are touching at the surface. A calibration routine was performed at each height. Results of the test are shown in Figure A.2.5.

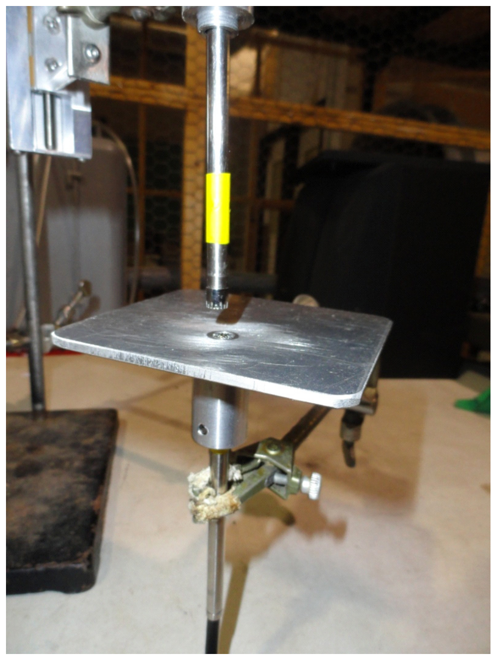

Figure A.2.4 *in situ* verification rig

It is clear from Figure A.2.5 that the *in situ* method is best suited for small microphone separations. Small separations better match wavetube gain and phase response (see Figure A.2.3. Note that there is much higher frequency resolution with the *in situ* method. This is due to a cut-off frequency that is on order or tap separation (f_c>20kHz). Implementation of the RMP device is discussed in the main text (Section 2.2.3)

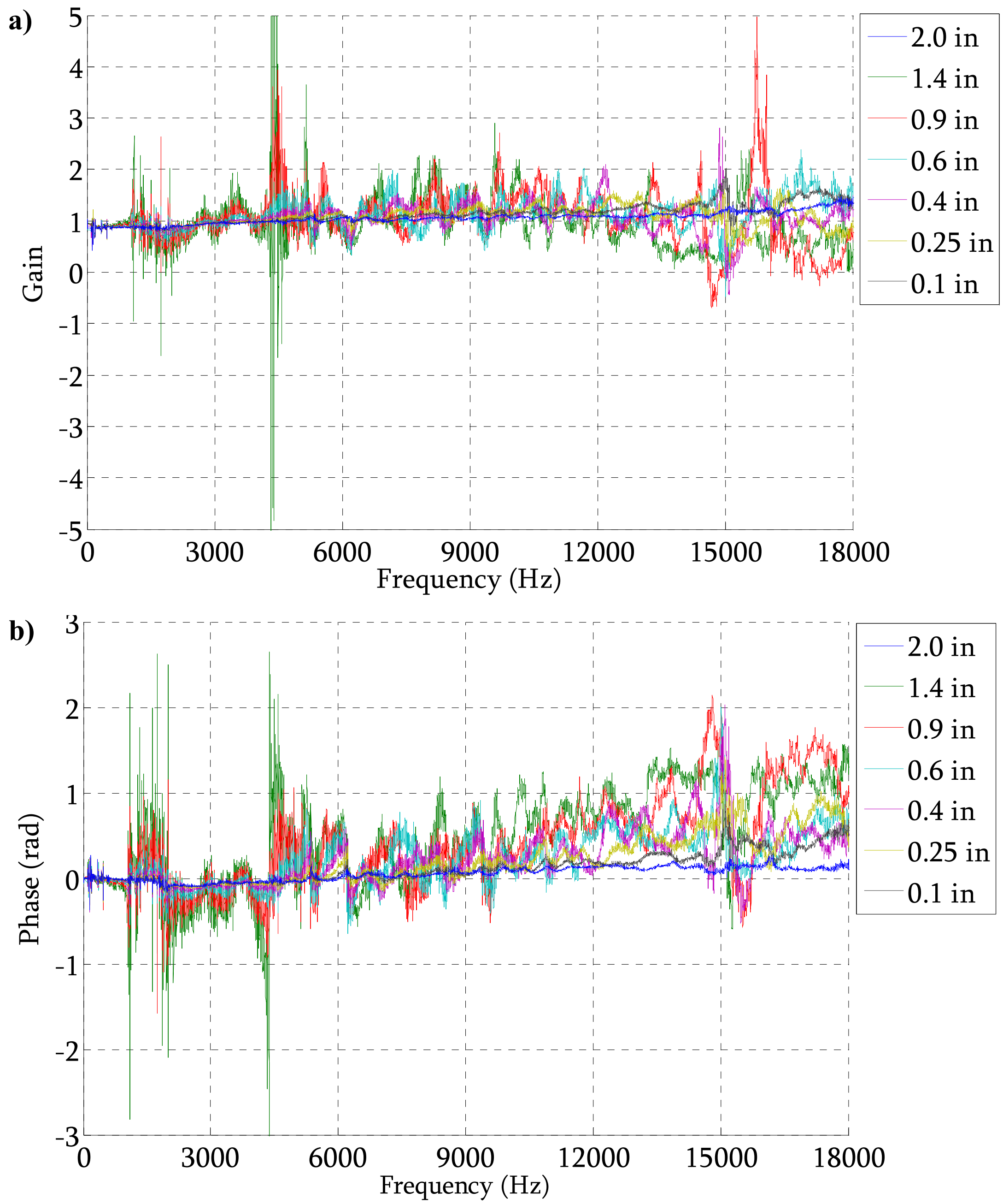

Figure A.2.5 *in situ* verification

A.3 Technical Data Sheets

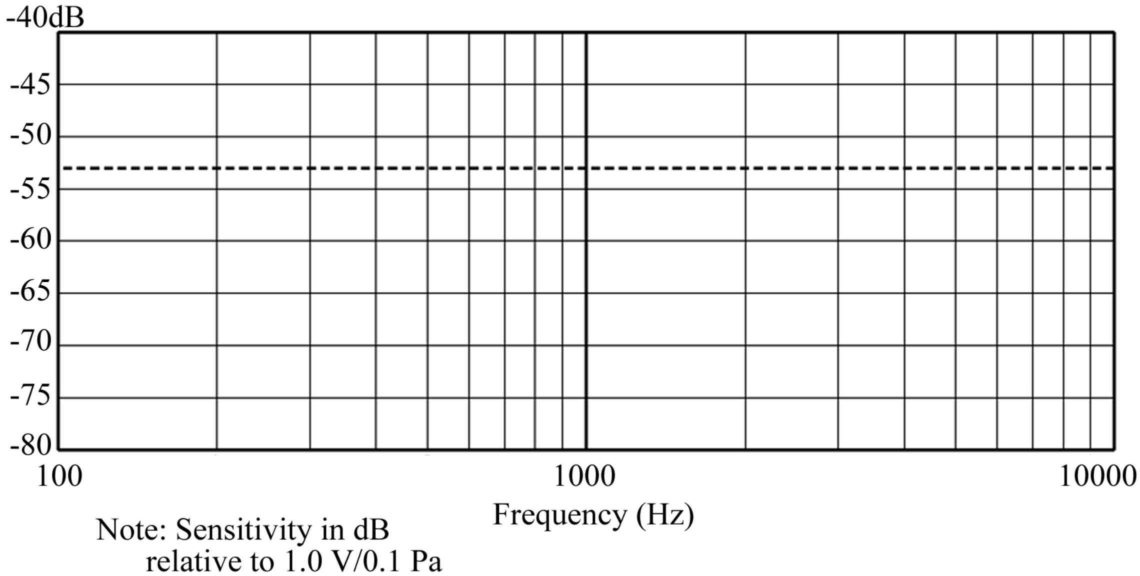

Figure A.3.6 RMP microphone specifications (Knowles FG-23329-C05)

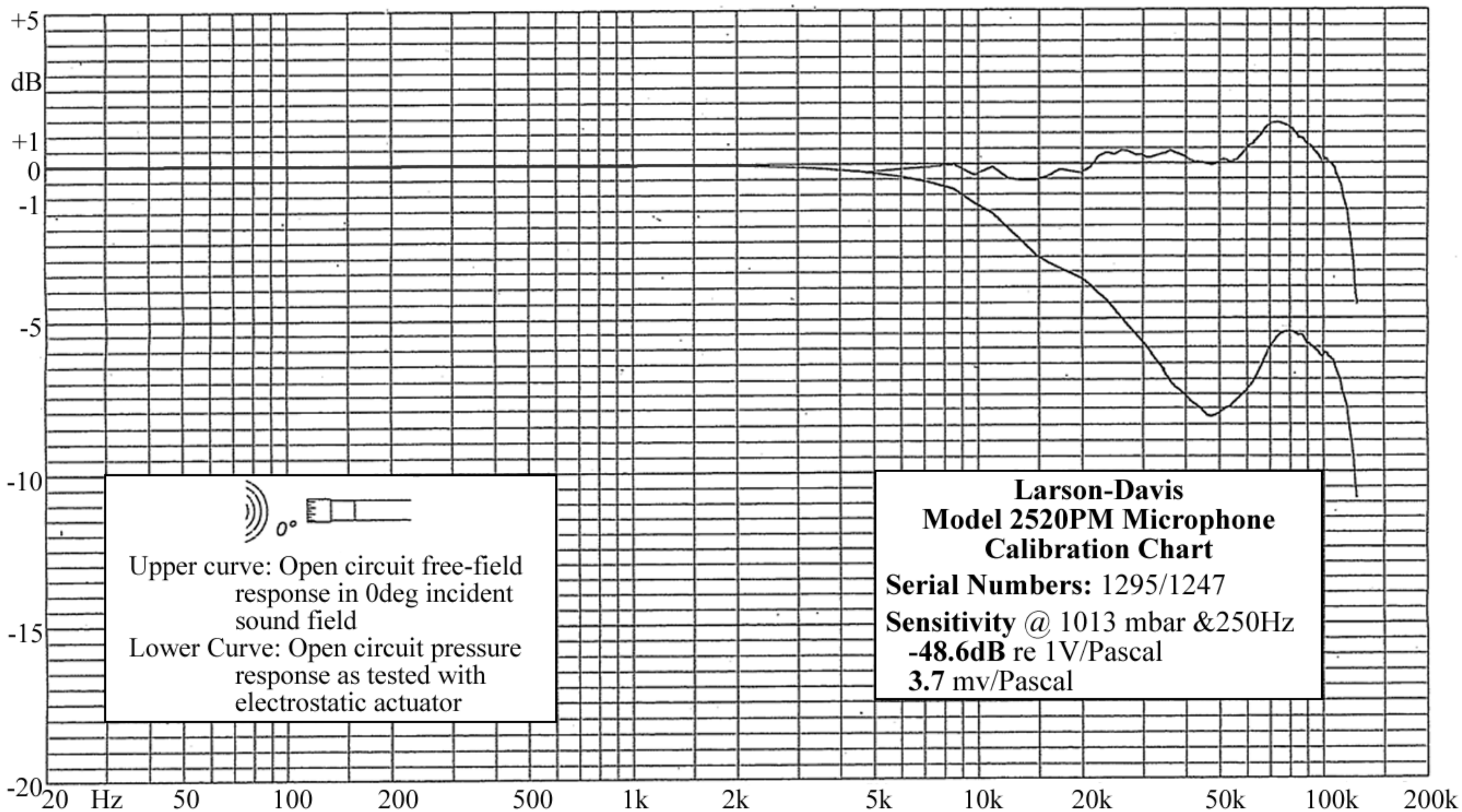

Figure A.3.7 Larson Davis manufacturer specifications

Appendix B: Optimal Noise Cancellation

Correlated tonal noise between the ground-level ambient microphones and RMPs is attenuated using the Optimal Noise Cancellation method suggested and provided by Professor Ahmed Naguib from Michigan State University. “Noise” is identified and removed from the RMPs by considering a correlation between a test microphone (RMP) and a reference microphone (Larson-Davis). High correlations correspond to a pressure signal that is shared by both microphones. Since the two microphones are located in stochastically unique fields, any correlated pressure must correspond to a global acoustic noise source; the signal is attenuated wherever correlations are high (Naguib et al. 1996) Figure B.1. It is expected that if the correlation between two statistically separate microphones is high, there exists a common producer that both microphones measure - noise.

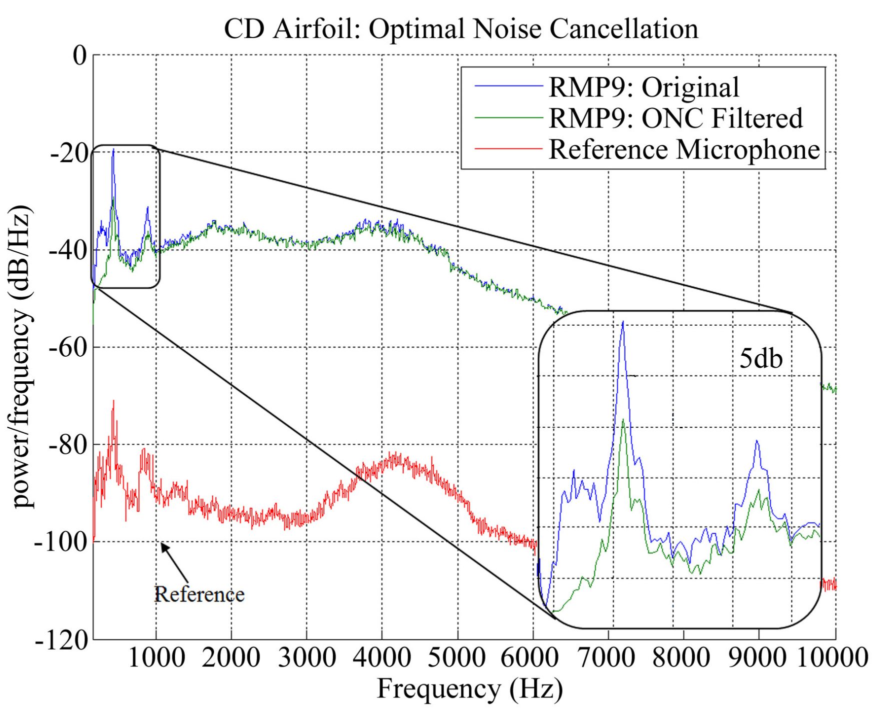

Figure B.1 Sample ONC filter applied to preliminary CD data

Appendix C: Additional Figures

C.1 Cross-correlations

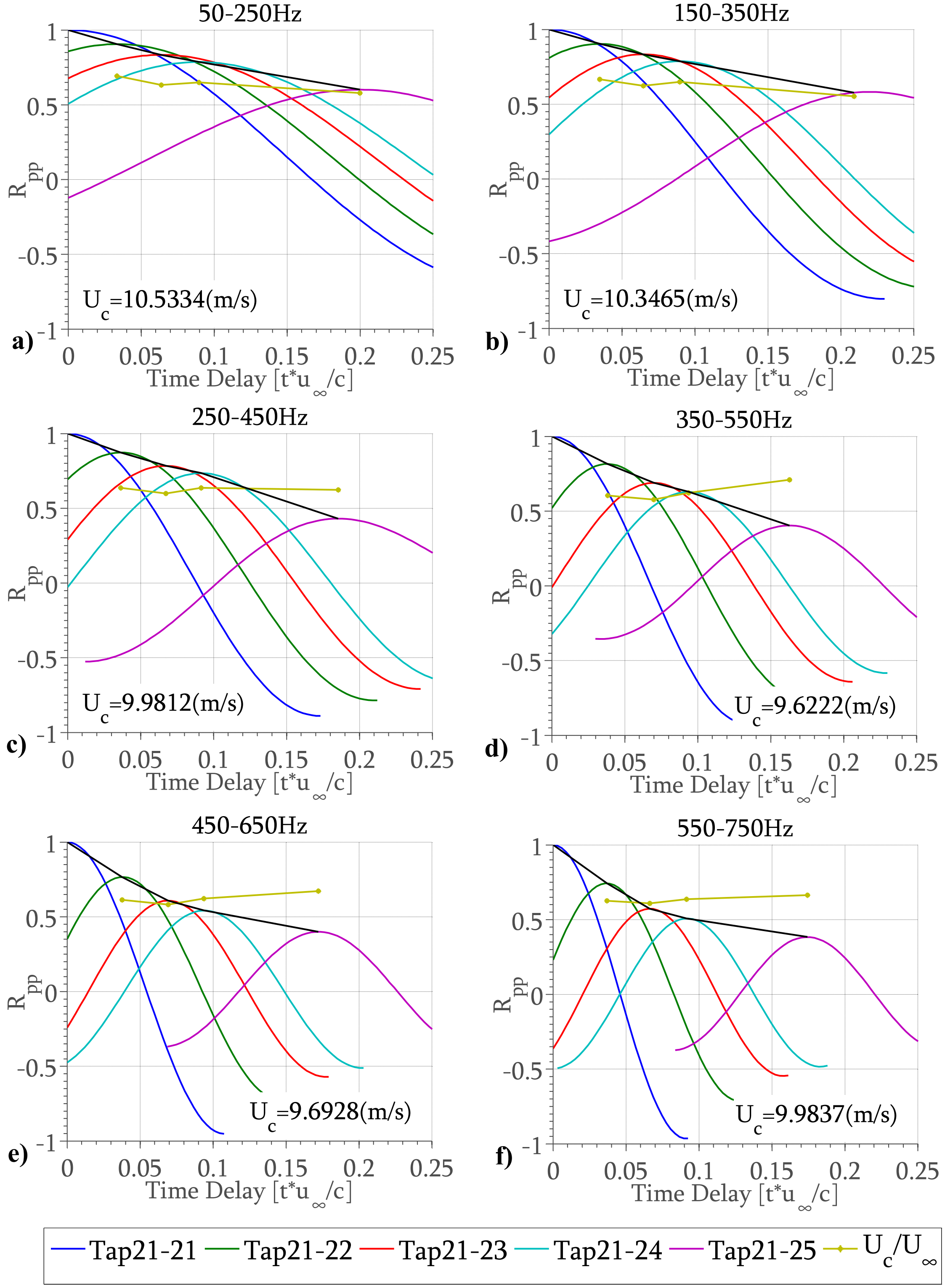

Figure C.1.1 Band-filtered R_{pp} correlations (CD blade)

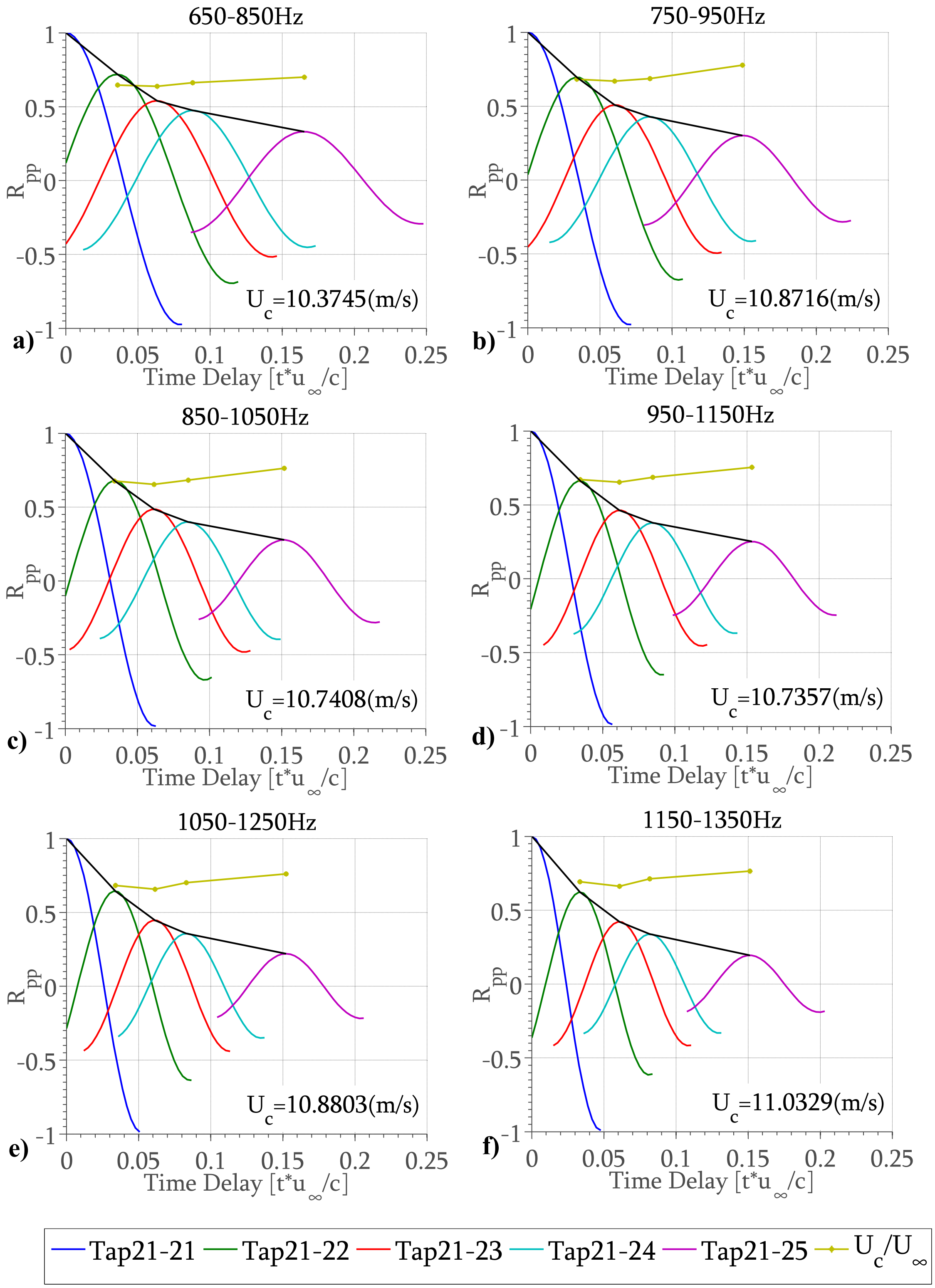

Figure C.1.2 Band-filtered R_{pp} correlations (CD blade)

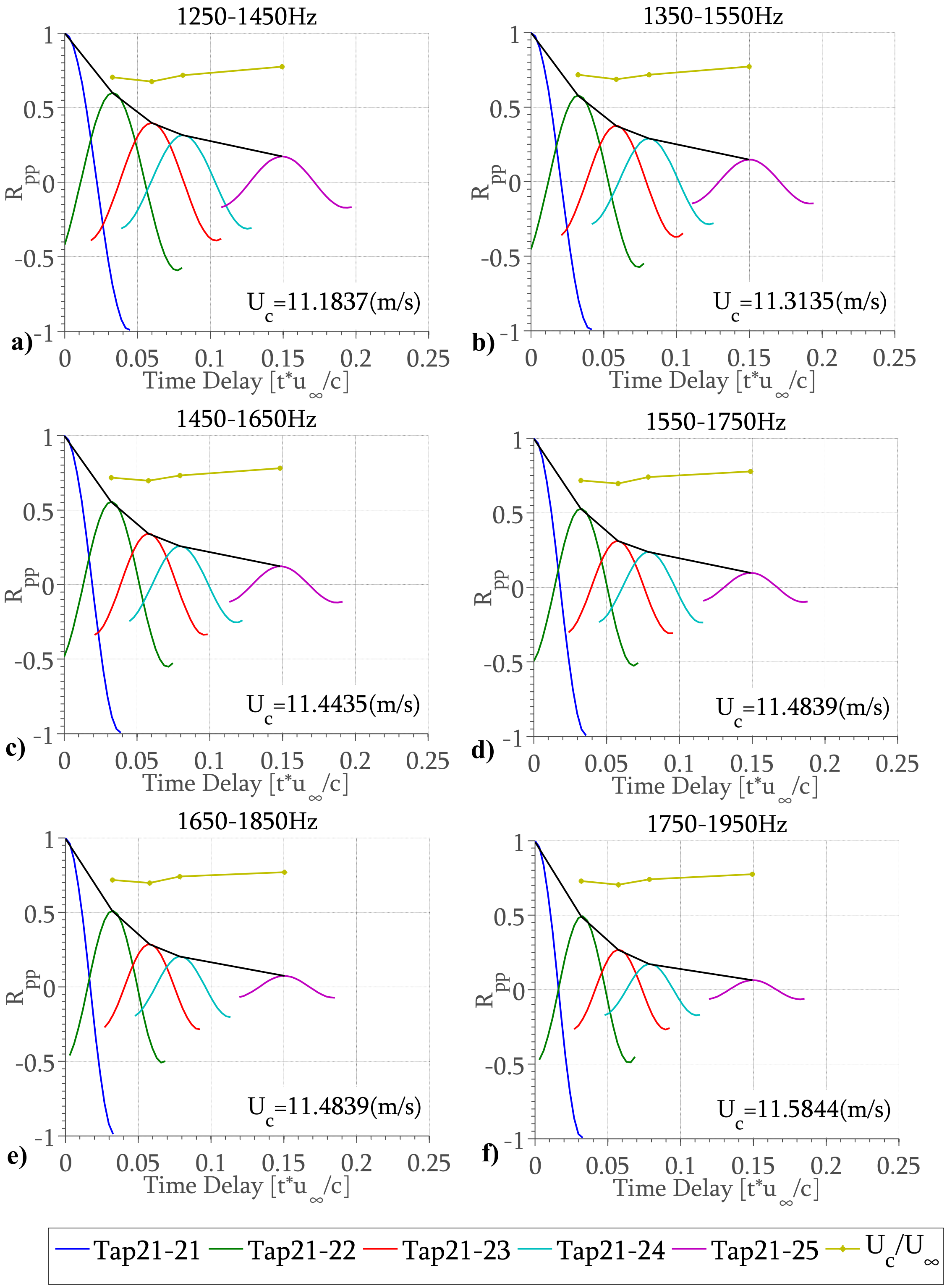

Figure C.1.3 Band-filtered R_{pp} correlations (CD blade)

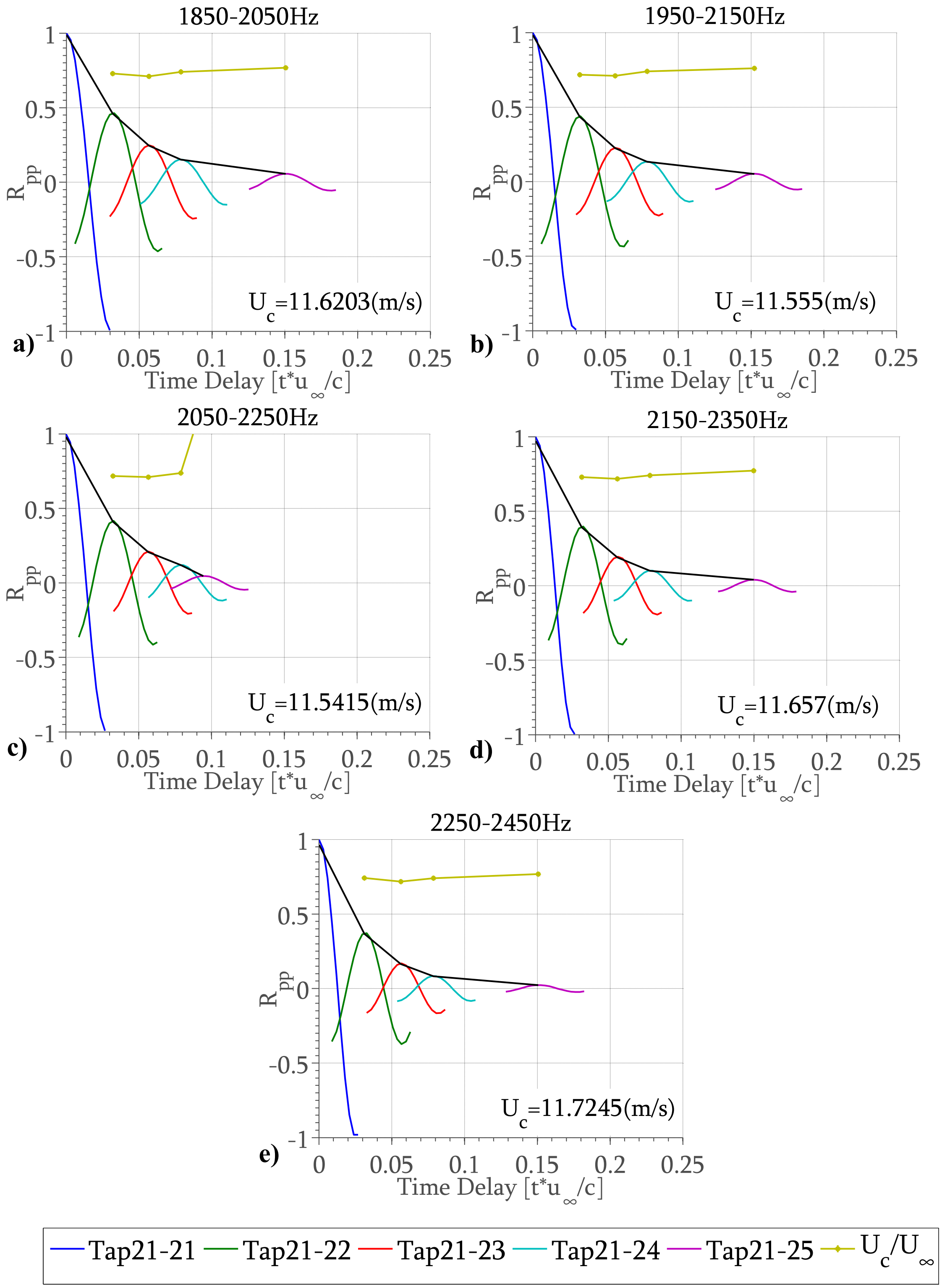

Figure C.1.4 Band-filtered R_{pp} correlations (CD blade)

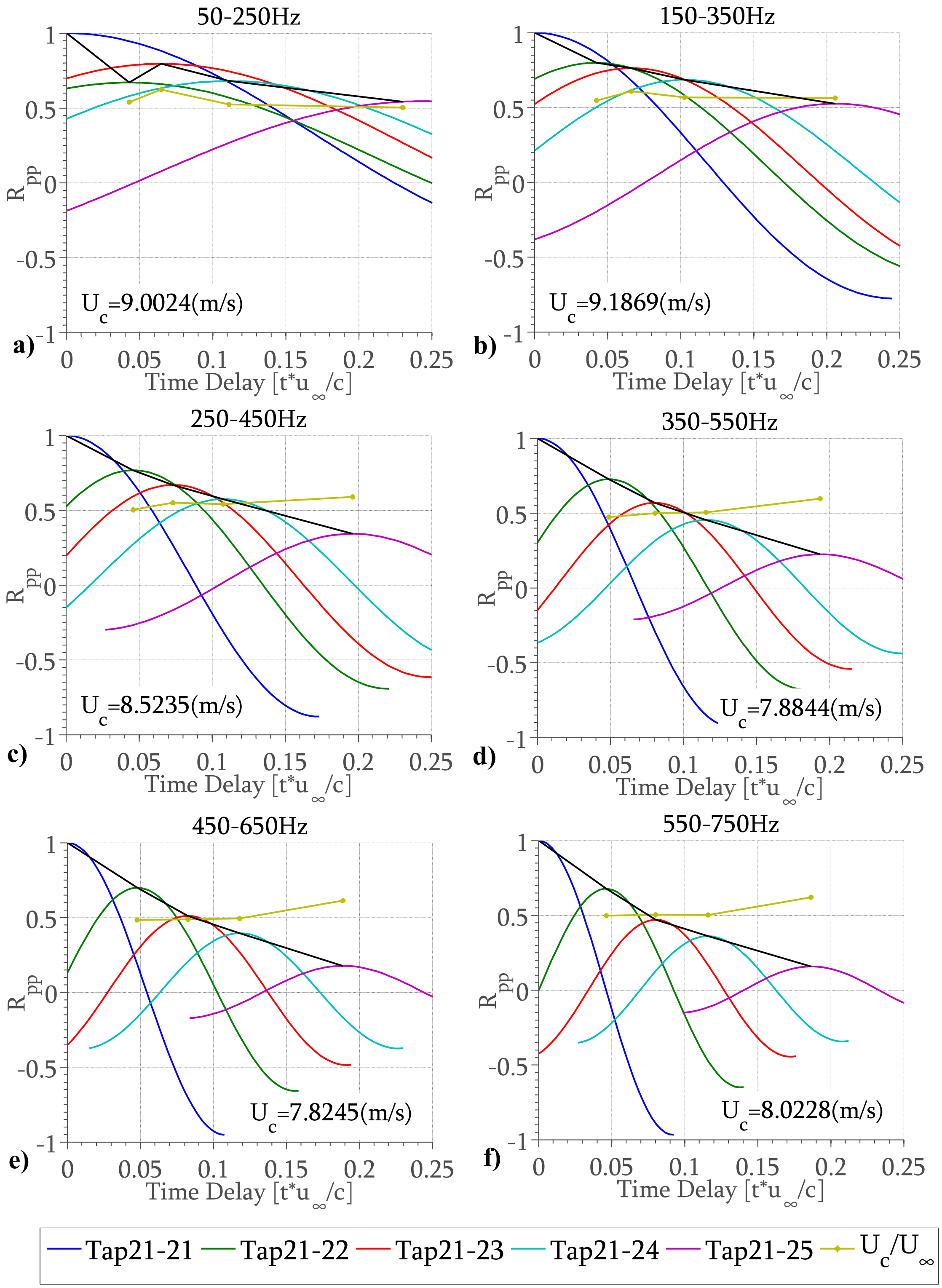

Figure C.1.5 Band-filtered R_{pp} correlations (RCDB Case 1)

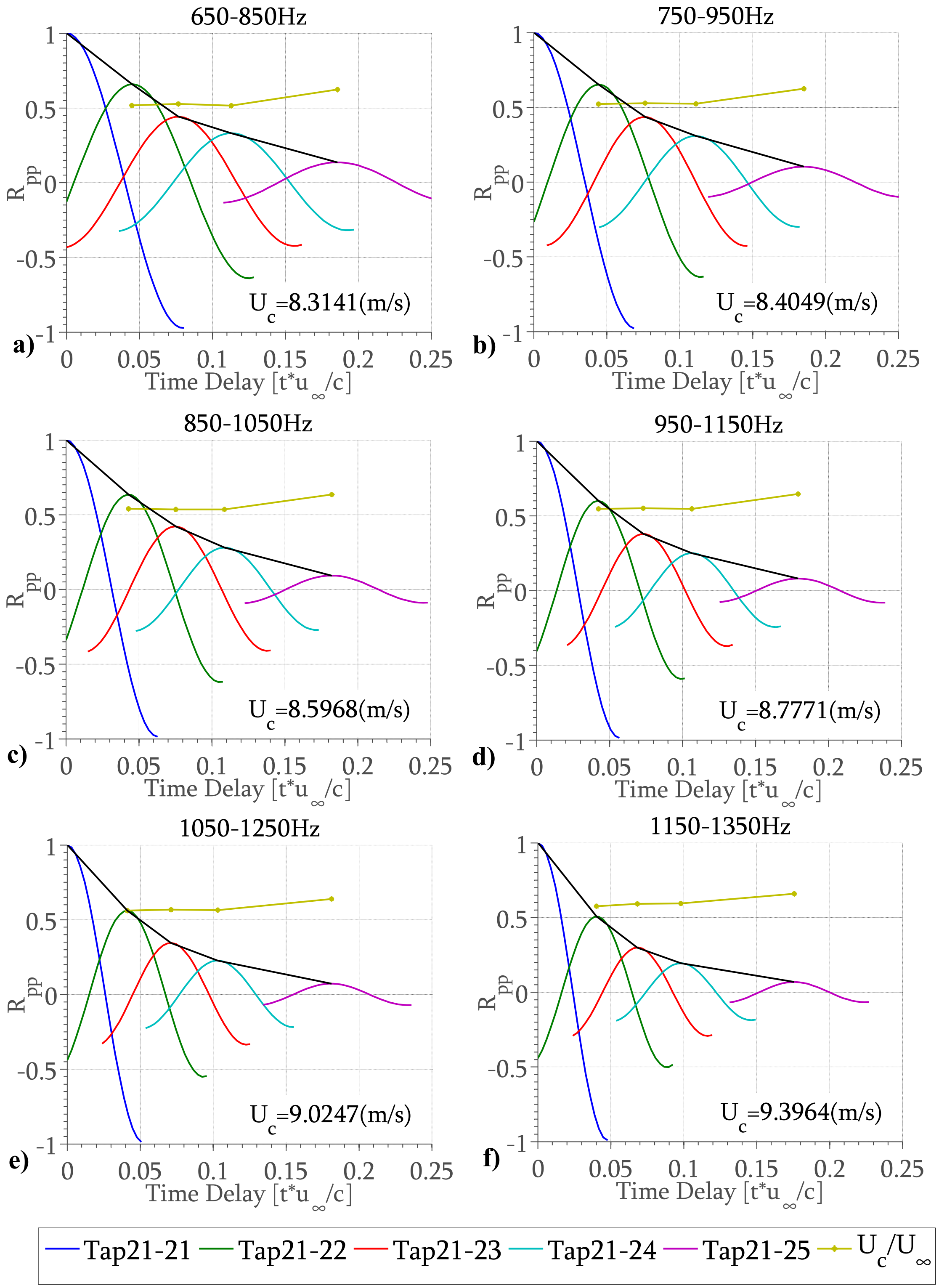

Figure C.1.6 Band-filtered R_{pp} correlations (RCDB Case 1)

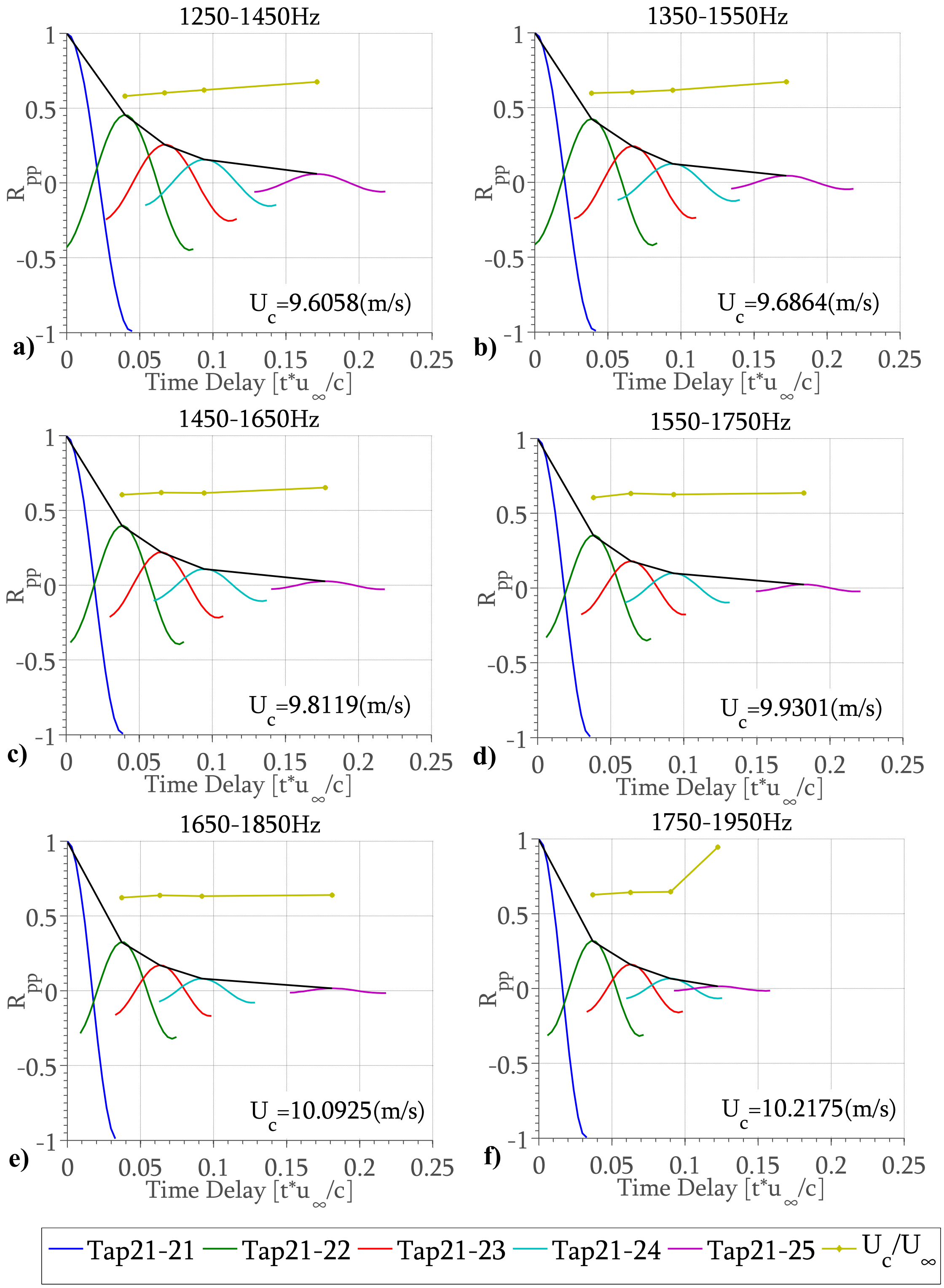

Figure C.1.7 Band-filtered R_{pp} correlations (RCDB Case 1)

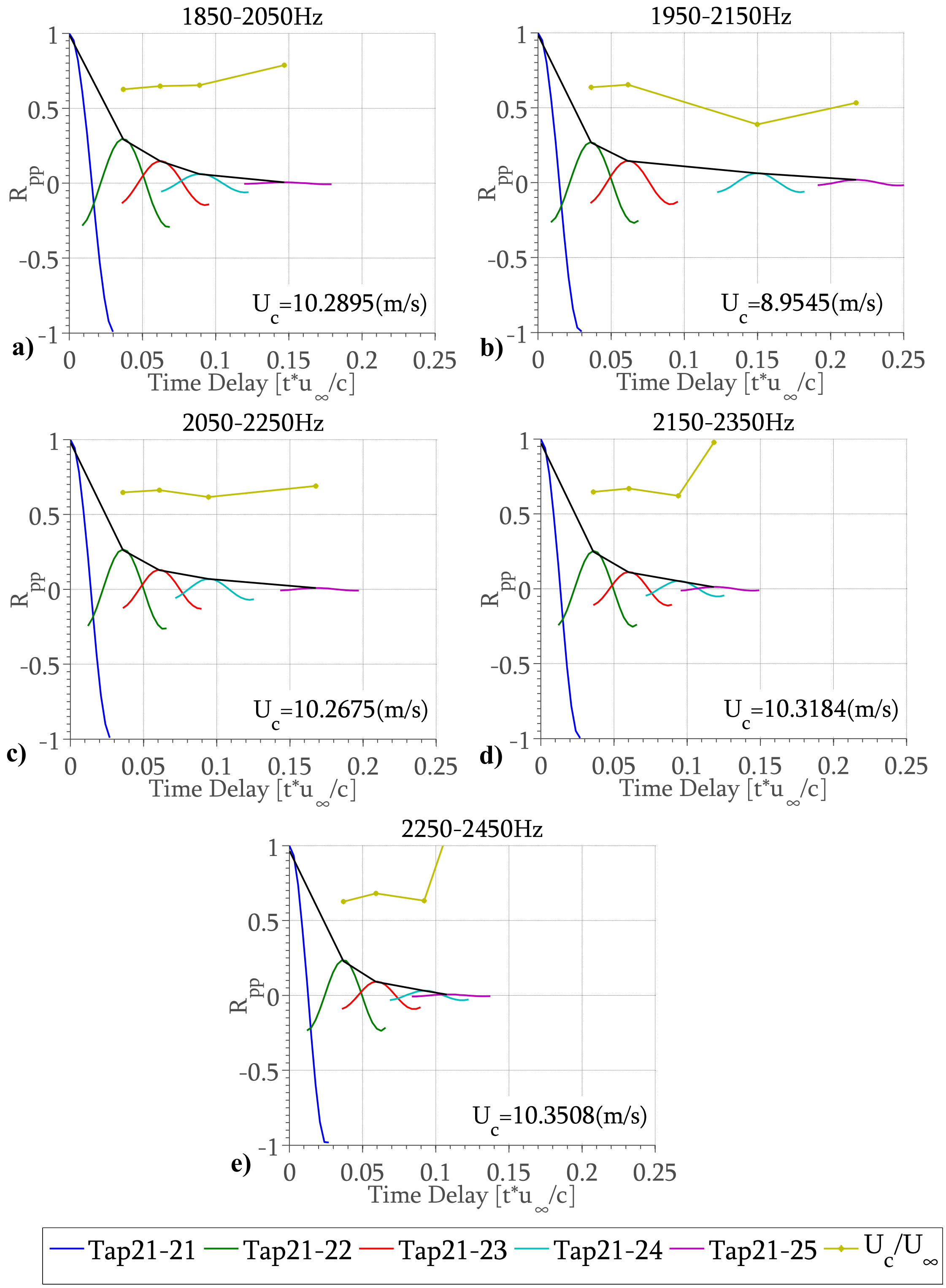

Figure C.1.8 Band-filtered R_{pp} correlations (RCDB Case 1)

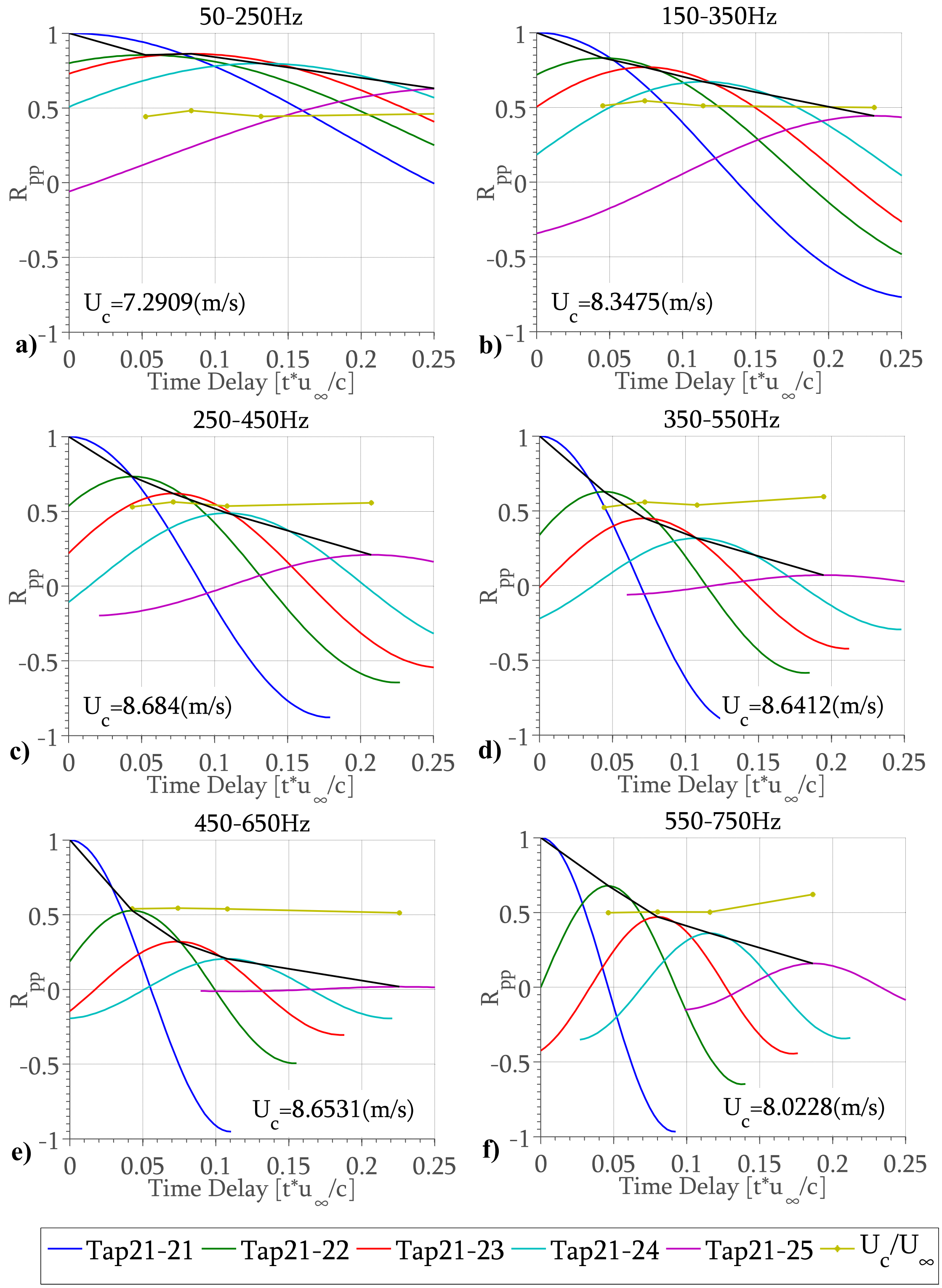

Figure C.1.9 Band-filtered R_{pp} correlations (RCDB Case 2)

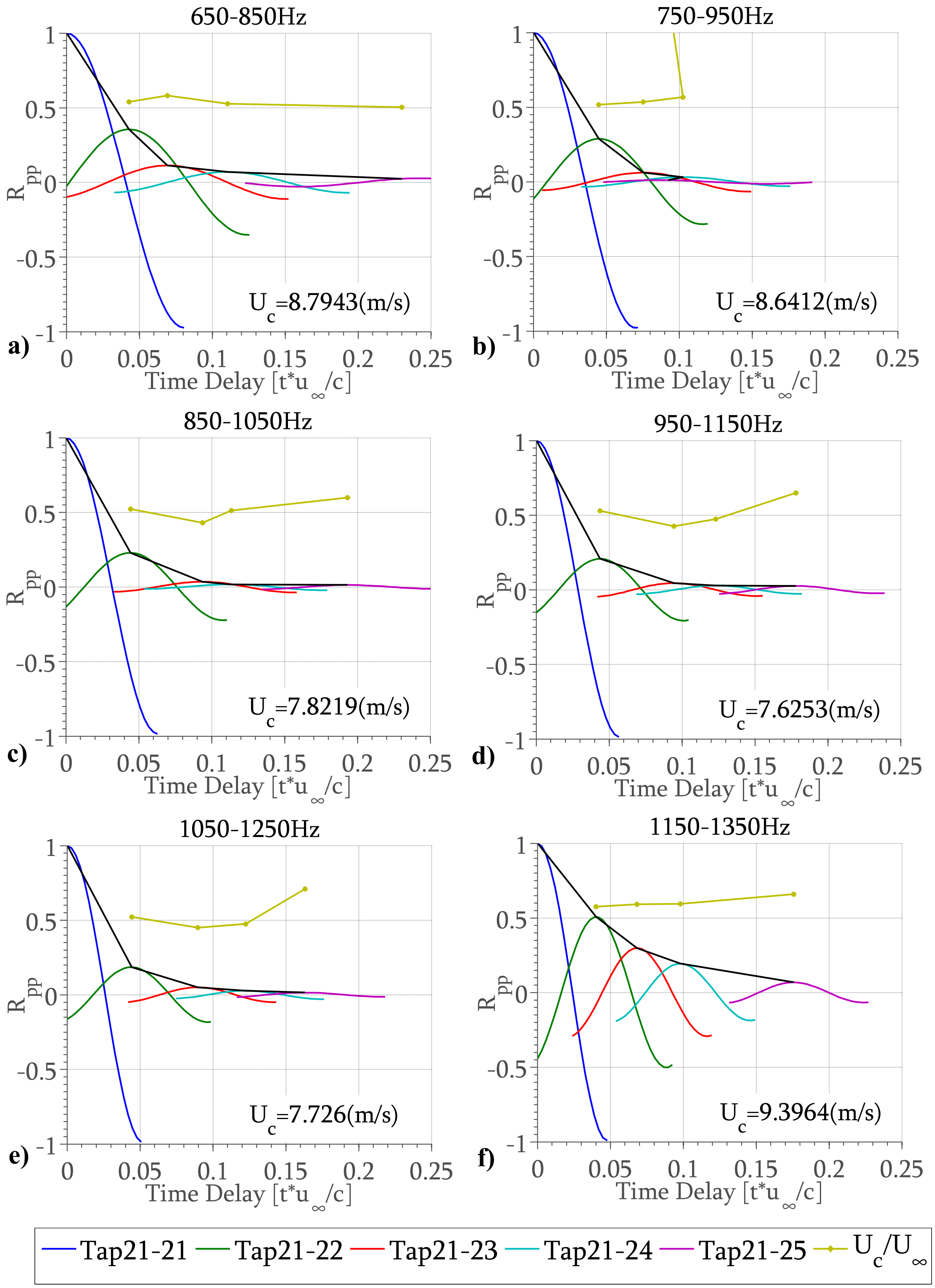

Figure C.1.10 Band-filtered R_{pp} correlations (RCDB Case 2)

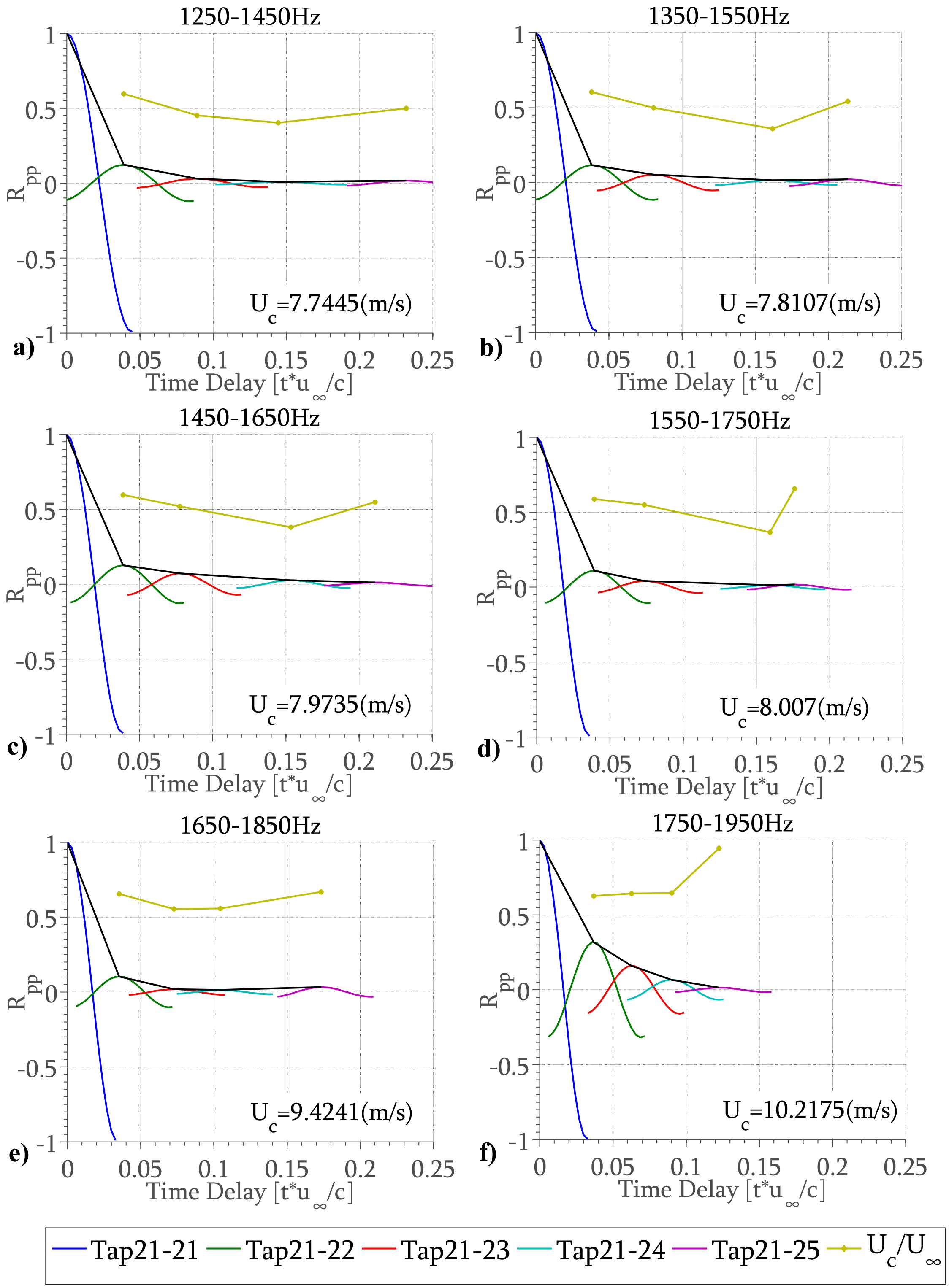

Figure C.1.11 Band-filtered R_{pp} correlations (RCDB Case 2)

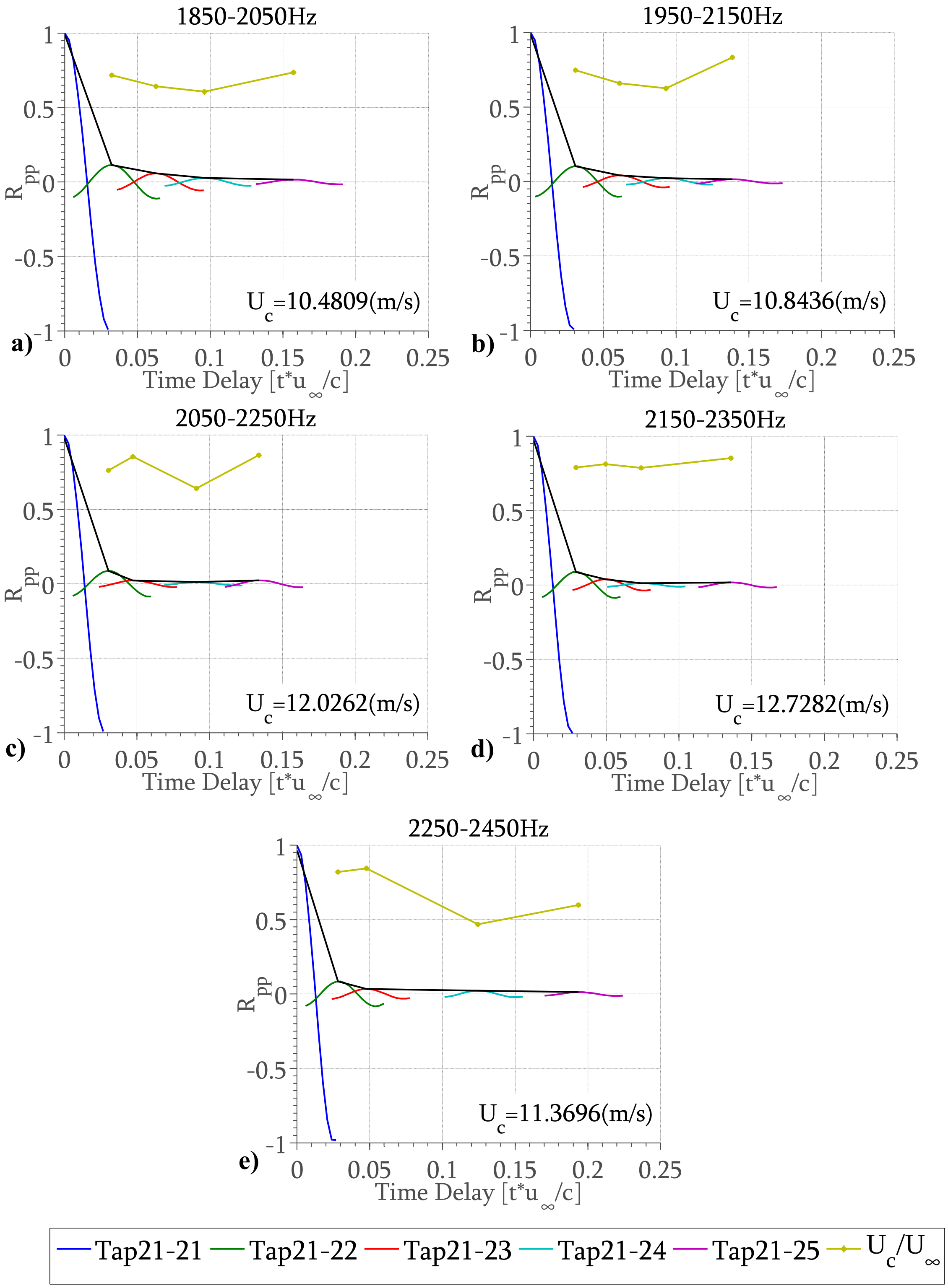

Figure C.1.12 Band-filtered R_{pp} correlations (RCDB Case 2)

C.2 Coherence-Phase

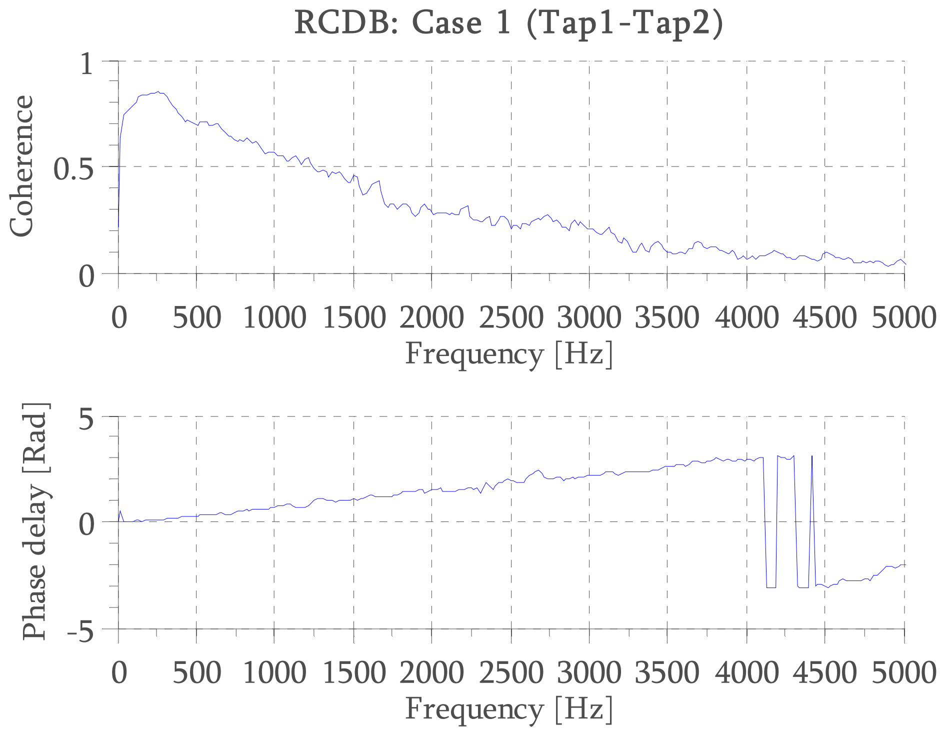

Figure C.2.1 Coherence and Phase (RCDB Case1: Tap1-Tap2)

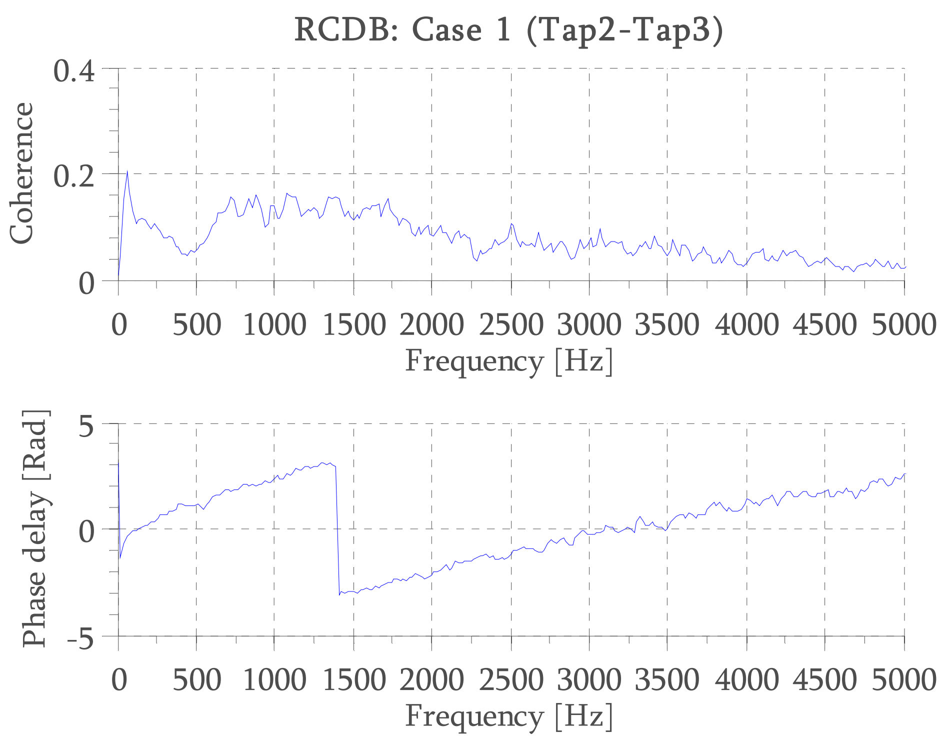

Figure C.2.2 Coherence and Phase (RCDB Case1: Tap2-Tap3)

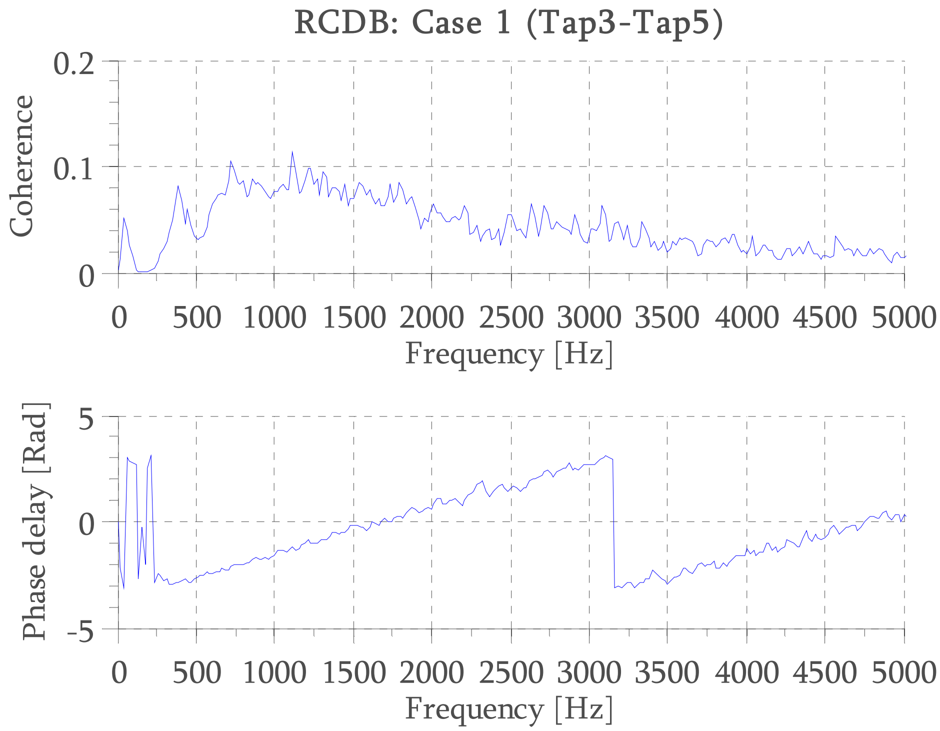

Figure C.2.3 Coherence and Phase (RCDB Case1: Tap3-Tap5)

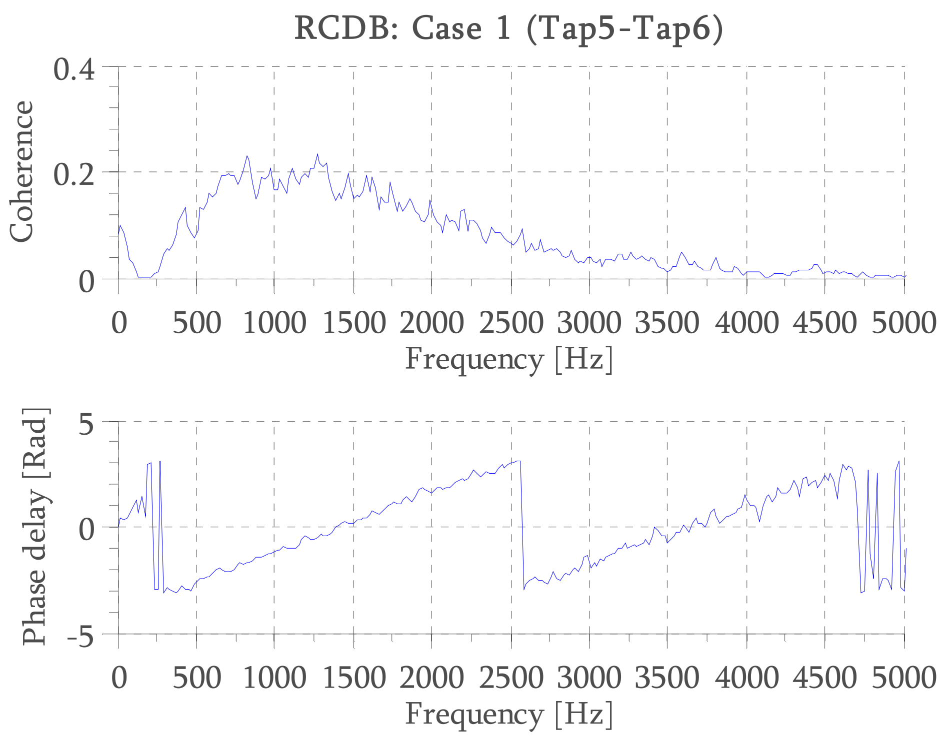

Figure C.2.4 Coherence and Phase (RCDB Case1: Tap5-Tap6)

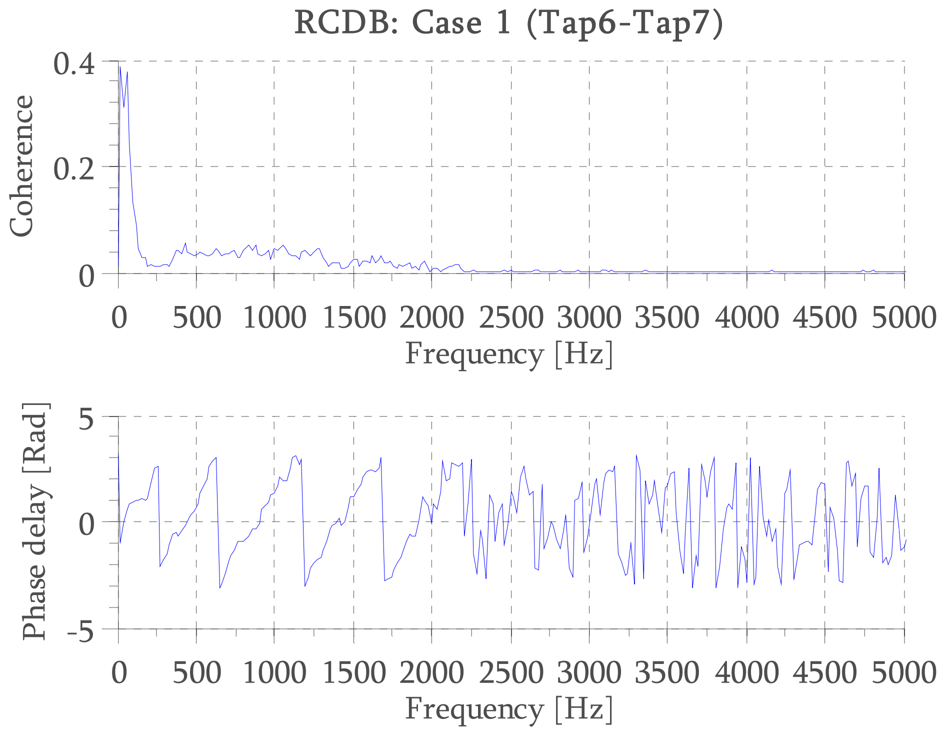

Figure C.2.5 Coherence and Phase (RCDB Case1: Tap6-Tap7)

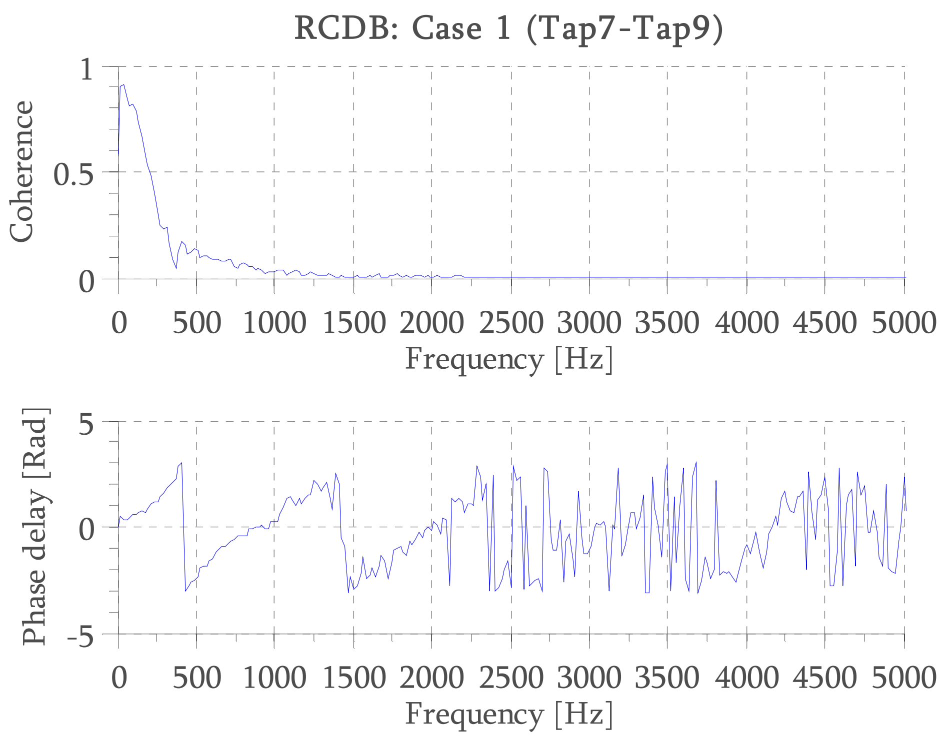

Figure C.2.6 Coherence and Phase (RCDB Case1: Tap7-Tap9)

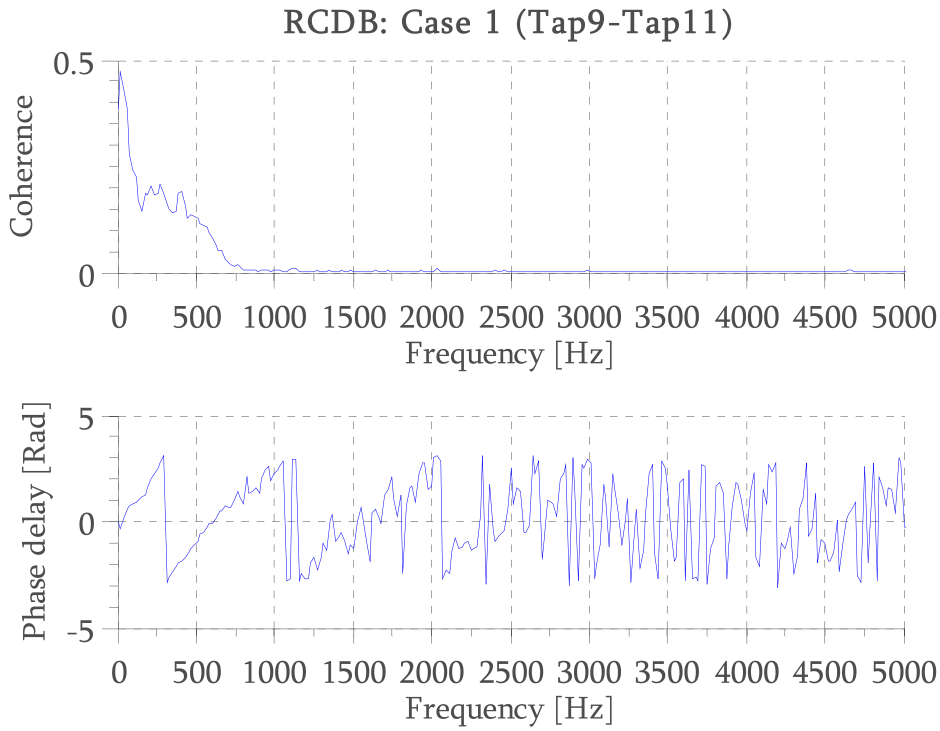

Figure C.2.7 Coherence and Phase (RCDB Case1: Tap9-Tap11)

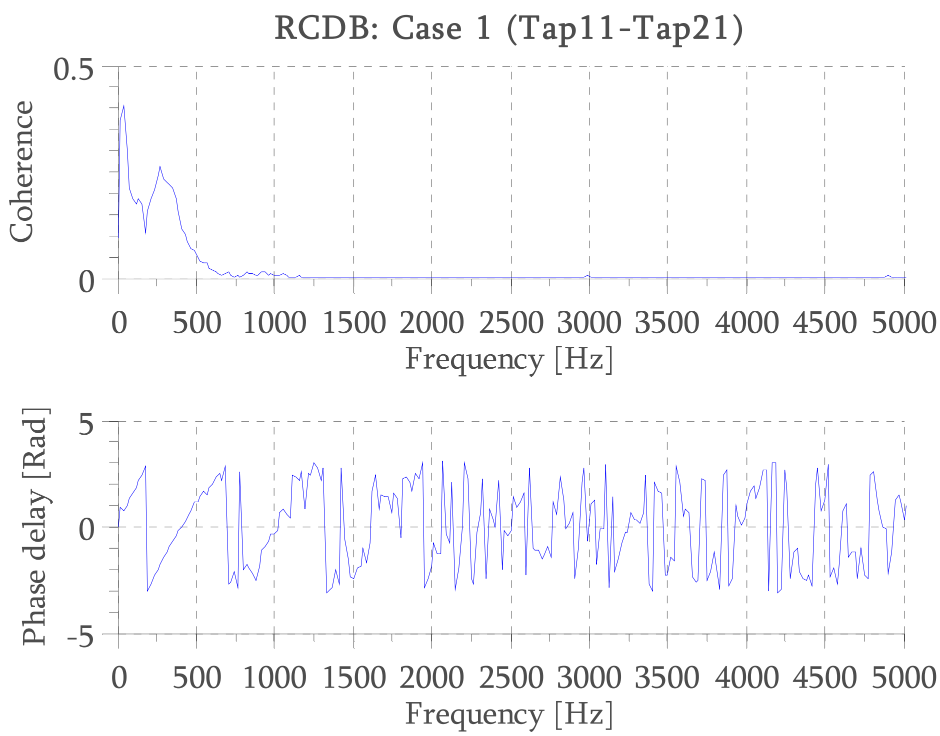

Figure C.2.8 Coherence and Phase (RCDB Case1: Tap11-Tap21)

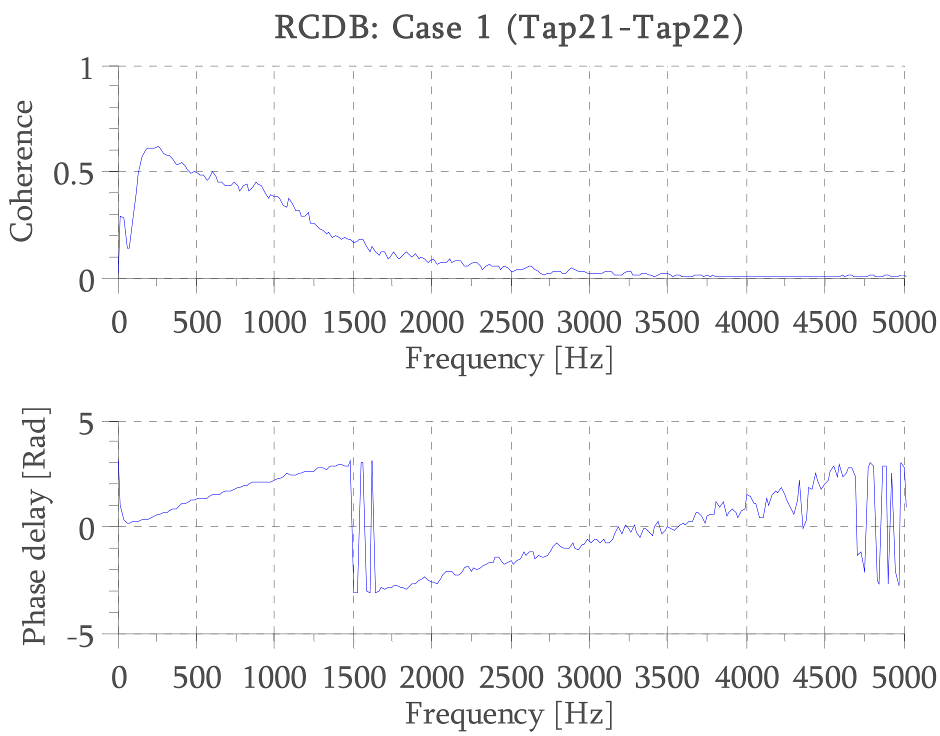

Figure C.2.9 Coherence and Phase (RCDB Case1: Tap21-Tap22)

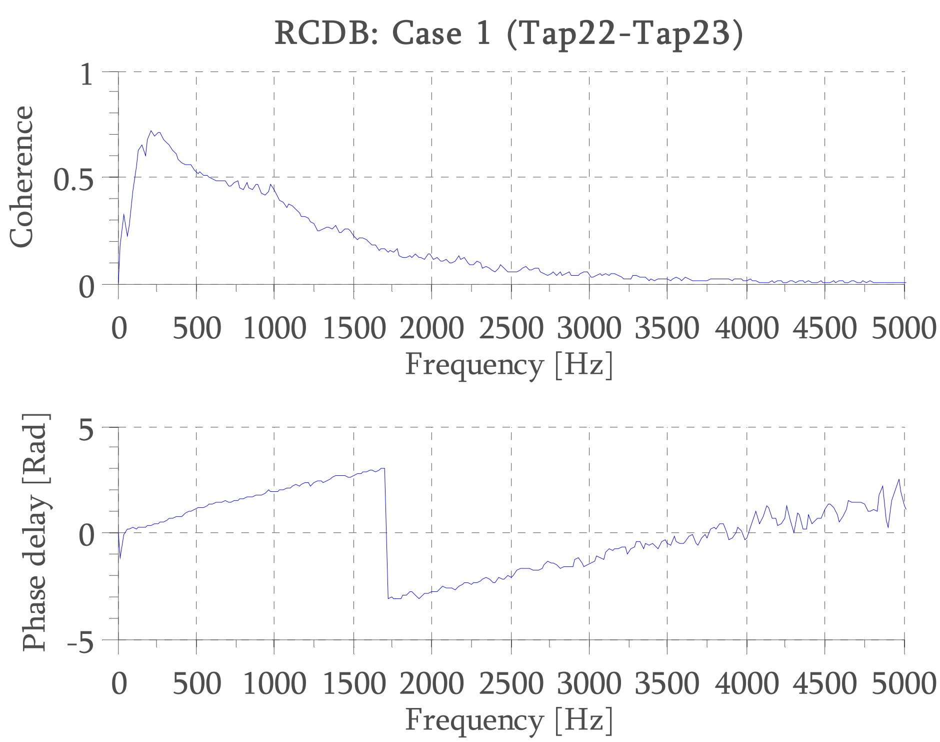

Figure C.2.10 Coherence and Phase (RCDB Case1: Tap22-Tap23)

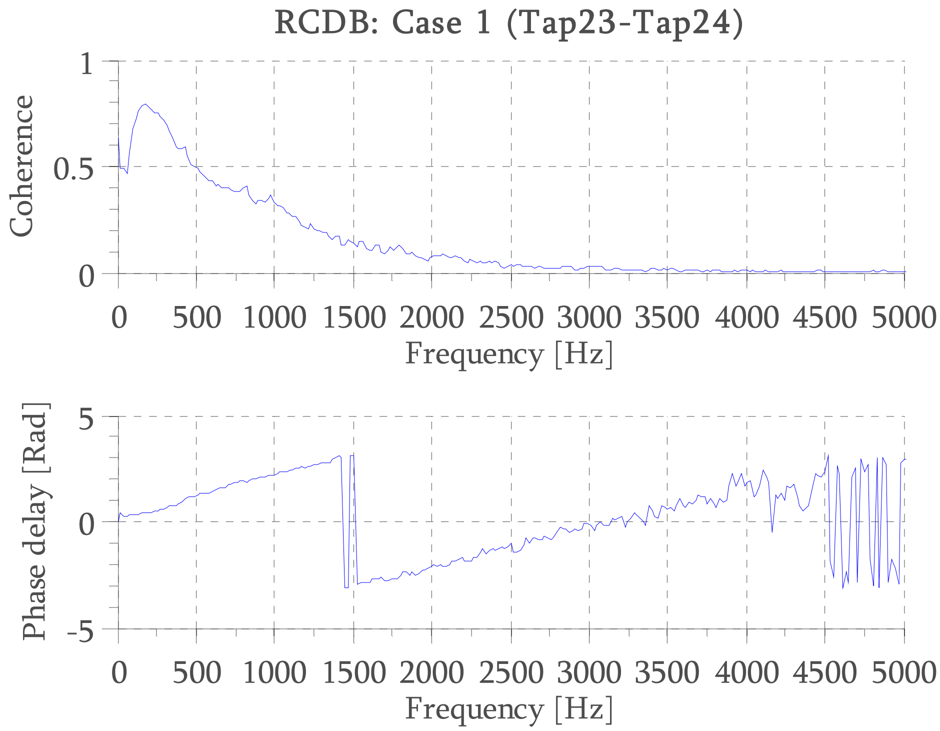

Figure C.2.11 Coherence and Phase (RCDB Case1: Tap23-Tap24)

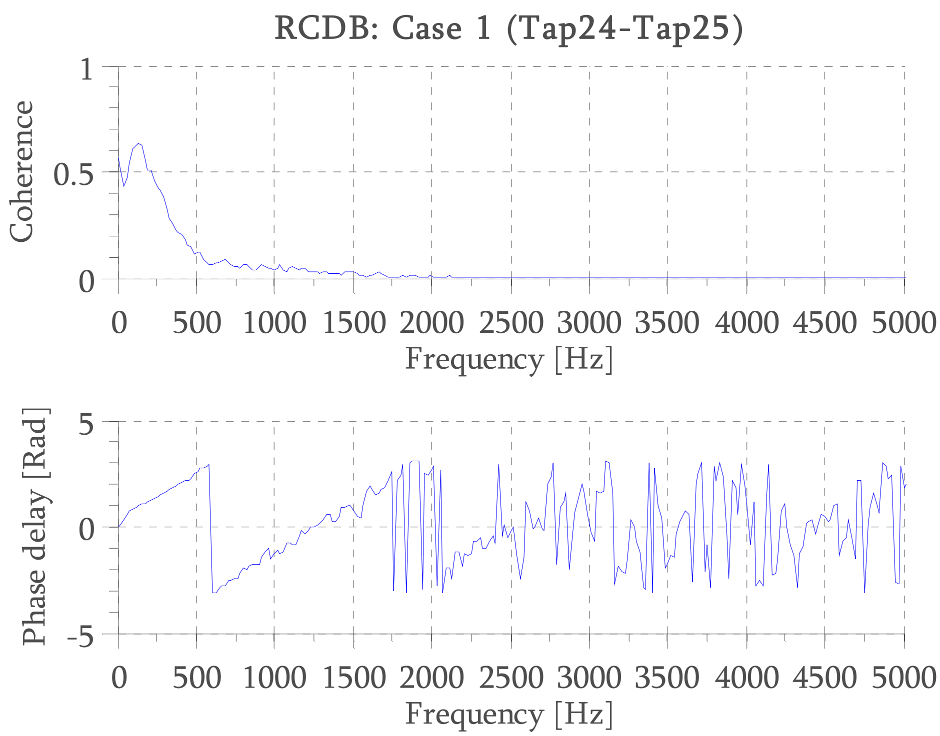

Figure C.2.12 Coherence and Phase (RCDB Case1: Tap24-Tap25)

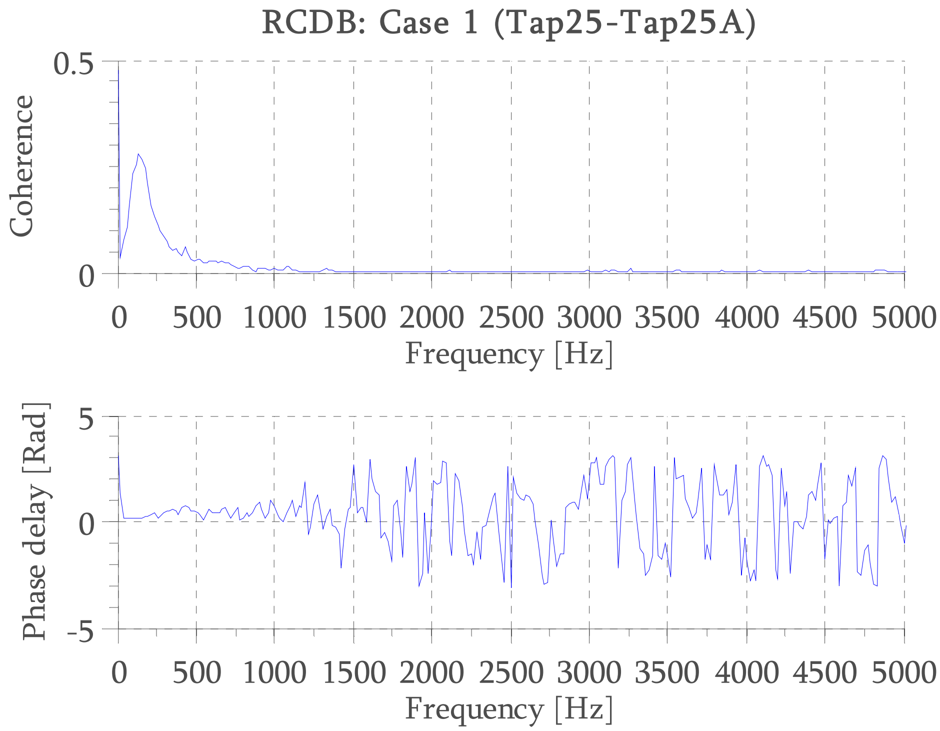

Figure C.2.13 Coherence and Phase (RCDB Case1: Tap25-Tap25A)

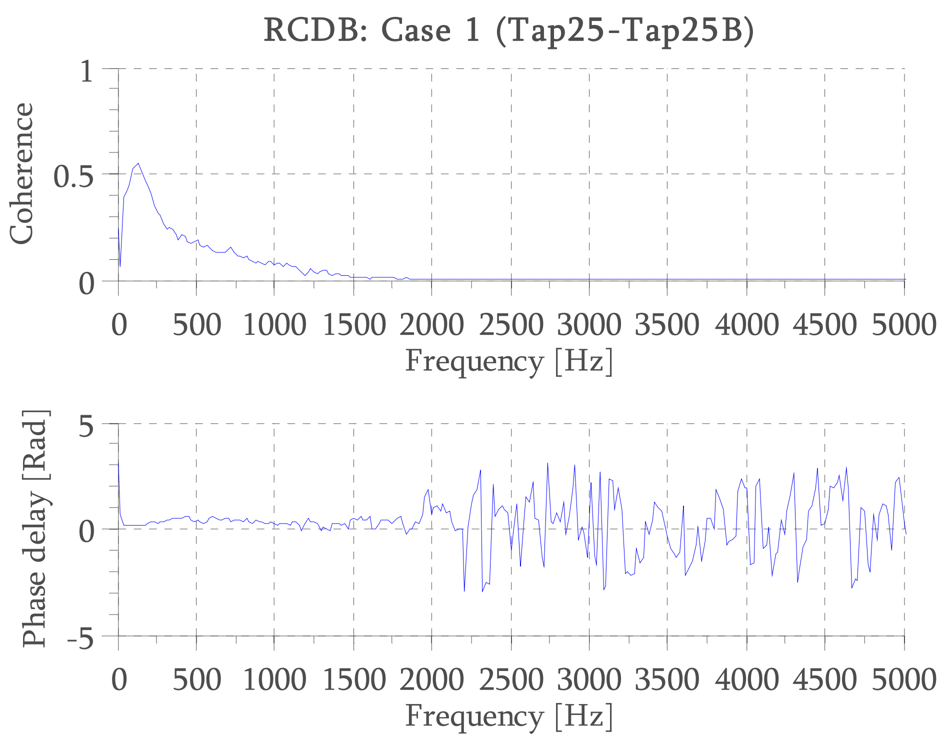

Figure C.2.14 Coherence and Phase (RCDB Case1: Tap25-Tap25B)

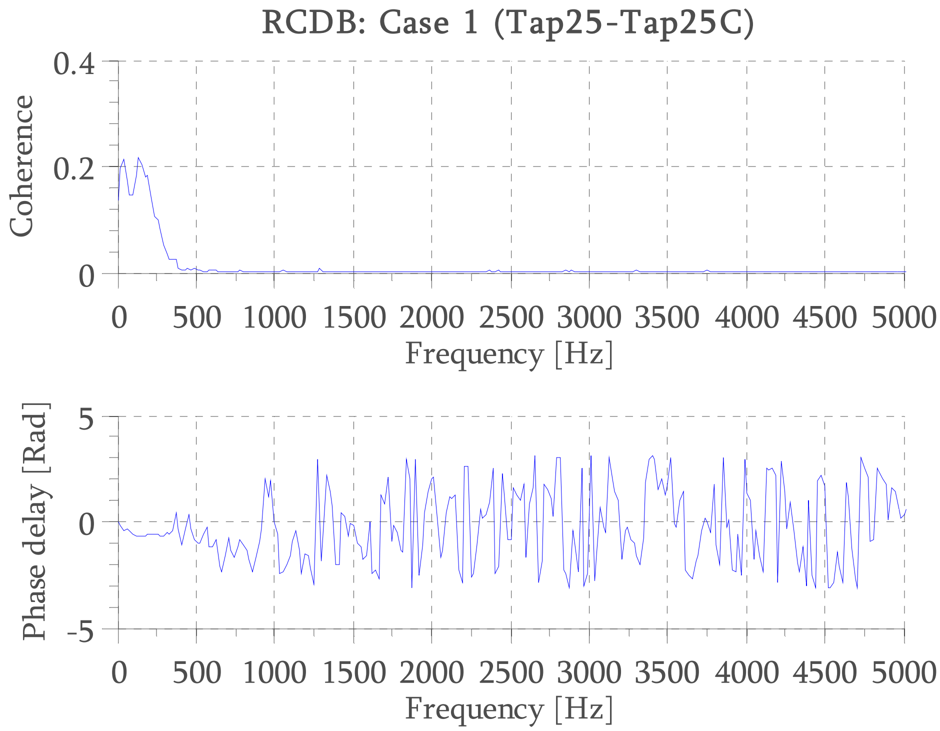

Figure C.2.15 Coherence and Phase (RCDB Case1: Tap25-Tap25C)

REFERENCES

REFERENCES

ANDERSON, B.E. 2003. *Derivation of Moving-Coil Loudspeaker Parameters Using Plane Wave Tube Techniques*. M.S. Thesis, Bringham Young University.

Audio Engineering Society, Inc. 2003. *AES Information Document - Plane wave tubes: design and practice.* AES 1id-1991 (r2003).

BENDAT, J. S., PIERSOL, A. G. 1986. *Random Data: Analysis and Measurement Procedures*. John Wiley and Sons, Inc., New York.

BOERRIGTER, H.L. AND CHARBONNIER, J.M. 1997. "Design and Calibration of an Unsteady Pressure Measurement System. *Instrumentation in Aerospace Simulation Facilities.* ICIASF '97.

BLAKE, W.E. 1986. *Mechanics of Flow-Induced Sound and Vibration II: Complex Flow-Structure Interactions*. Academic Press, Inc., Orlando, FL, 497– 594.

BOUTILIER, M. S. H. AND YARUSEVYCH, S. 2012. Parametric study of separation and transition characteristics over an airfoil at low Reynolds numbers. *Experiments in Fluids*, **52**(6), 1491-1506.

BROOKS, F., STUART, D., AND MARCOLINI, A. 1989. Airfoil self-noise and prediction. *NASA Reference Publication, 1218.*

BULL M. K. 1967. Wall-pressure fluctuations associated with subsonic turbulent boundary layer flow, *Journal of Fluids Mechanics*, **28**(4), 710-754.

BULL, M. K. 1996. Wall-pressure fluctuations beneath turbulent boundary layers: some reflections on forty years of research. *Journal of Sound and Vibration*, **190**(3), 299-315.

CHAMPAGNE, F. H., SLEICHER, C.A. AND WEHRMANN, O.H. 1967. Turbulence Measurements With Inclined Hot-Wires. *Journal of Fluid Mechanics*, **28**, 153-182.

DASSAN, T., PARCHEN, R., GUIDATI, G., AND WAGNER, S. 1997. Comparison of measured and predicted airtoil self-noise with application to wind turbine noise reduction. *The European Wind Energy Conference and Exhibition 1997; Dublin, 6-9 October, 1997.*

DUSEL, M. D. 2005. *An experimental investigation of the aerodynamic shroud with an off-highway engine cooling fan*. M.S. Thesis, Michigan State University.

GERAKOPULOS, R., AND YARUSEVYCH, S. 2012. Novel time-resolved pressure measurements on an airfoil at a low reynolds number. *AIAA Journal*, **50**(5), 1189-1200.

GOODY, M. C., AND SIMPSON, R. L. 2000. Surface pressure fluctuations beneath two- and three-dimensional turbulent boundary layers. *AIAA Journal*, **38**(10), 1822–1831.

GRAVANTE, S. P., NAGIB, H. M., NAGUIB, A. M., AND WARK, C. E. 1998. Characterization of the pressure fluctuations under a fully developed turbulent boundary layer. *AIAA Journal*, **36**(10), 1808-1816.

HELLUM, A. 2006. *Intermittency and the viscous superlayer in a single stream shear layer.* M.S. Thesis, Michigan State University.

HOARAU, C., BORÉE, J., LAUMONIER, J., AND GERVAIS, Y. 2006. Analysis of the wall pressure trace downstream of a separated region using extended proper orthogonal decomposition. *Physics of Fluids*, **18**(5), 055107.

HÖWER, D. 2012. *Unsteady pressure fluctuations on the surface of a controlled diffusion airfoil*. M.S. Thesis, RWTH University.

HOWE, M. 1978. A review of the theory of trailing edge noise. J*ournal of Sound and Vibration*, **61**(3), 437-465.

HOWE, M. S. 2001. Vorticity and the theory of aerodynamic sound. *Journal of Engineering Mathematics*, **41**, 367-400.

HWANG, Y. F., BONNESS, W. K., AND HAMBRIC, S. A. 2009. Comparison of semi-empirical models for turbulent boundary layer wall pressure spectra. *Journal of Sound and Vibration*, **319**(1-2), 199-217.

LAKSHMINARAYANA, B. 1996. *Fluid dynamics and heat transfer of turbomachinery.* John Wiley and Sons, Inc., New York.

MAGALOTTI, R., ZUCCATTI, C., PASINI, P. 1999. Building a Plane-Wave Tube: Experimental and Theoretical Aspects. *J. Audio Eng. Soc.* **47**(7/8), 596-601.

MOREAU, S., AND ROGER, M. 2005. Effect of airfoil aerodynamic loading on trailing edge noise sources. *AIAA Journal,* **43**(1), 41-52.

MORRIS, S.C., AND FOSS, J.F. 2001. An aerodynamic shroud for automotive cooling fans. journal of fluids engineering, **123**, 287.

MUNSON, B. R., YOUNG, D. F., AND OKIISHI, T. H. 1998. *Fundamentals of Fluid Mechanics*. 3rd, John Wiley and Sons, Inc., New York.

NAGUIB, A. M., GRAVANTE, S. P., AND WARK, C. E. 1996. Extraction of turbulent wall-pressure time-series using an optimal filtering scheme. *Experiments in Fluids*, **22**, 14-22.

NEAL, D. R. 2010. *The effects of rotation on the flow field over a controlled-diffusion airfoil*. Ph.D. Dissertation, Michigan State University

NEAL, D.R., AND FOSS, J.F. 2007. The application of an aerodynamic shroud for axial ventilation fans. *Journal of Fluids Engineering*, **129**, 764.

OBERAI, A. A., HUGHES, T. J. R., AND ROKNALDIN, F. 2002. Computation of trailing-edge noise due to turbulent flow over an airfoil. *AIAA Journal*, **40**(11), 2206-2216.

PÉRENNÈS, S., AND ROGER, M. 1998. Aerodynamic noise of a two-dimensional wing with high-lift devices. *Pages 772-782 of: AIAA/CEAS Aeroacoustics Conference, 4th(19th AIAA Aeroacoustics Conference), Toulouse, France.*

POPE, S.B. 2000. *Turbulent Flows*. Cambridge University Press, New York.

ROGER, M., AND MOREAU, S. 2004. Broadband self noise from loaded fan blades. *AIAA Journal*, **42**(3), 536-544.

SINGER, B. 2000. Simulation of acoustic scattering from a trailing edge. *Journal of Sound and Vibration*, **230**(3), 541-560.

SHEPLAK, M., PADMANABHAN, A., SCHMIDT, M. A., AND BREUER, K. S. 2001. Dynamic calibration of a shear-stress sensor using stokes-layer excitation. *AIAA journa*l, **39**(5), 819–823.

WILLMARTH W.W., AND WOOLRIDGE C.E. 1962. Measurements of the fluctuating pressure at the wall beneath a thick turbulent boundary layer. *Journal of Fluid Mechanics*, **14**(2), 187-210.